Title
Electron-Nuclear Interactions in Natural Photosynthetic and Biomimetic Model Systems

Author
Arsenault, Eric Alan

Publication Date
2021

Peer reviewed|Thesis/dissertation

Electron-Nuclear Interactions in Natural Photosynthetic and Biomimetic Model Systems

by

Eric Alan Arsenault

A dissertation submitted in partial satisfaction of the

requirements for the degree of

Doctor of Philosophy

in

Chemistry

in the

Graduate Division

of the

University of California, Berkeley

Committee in charge:

Professor Graham R. Fleming, Chair
Professor Daniel M. Neumark
Professor Markita P. Landry

Fall 2021

Electron-Nuclear Interactions in Natural Photosynthetic and Biomimetic Model Systems

Abstract

Electron-Nuclear Interactions in Natural Photosynthetic and Biomimetic Model Systems

by

Eric Alan Arsenault

Doctor of Philosophy in Chemistry

University of California, Berkeley

Professor Graham R. Fleming, Chair

This dissertation presents the application of two-dimensional electronic-vibrational (2DEV) spectroscopy to a progression of natural photosynthetic and biomimetic model systems where electron-nuclear interactions exert a significant influence on the overall functionality.

In the introduction, we start by describing the unique aspects of the 2DEV spectroscopic method, including improved frequency resolution and the capability to track electronic-vibrational correlations, which are leveraged in the work presented in the subsequent chapters. Following this, the first half of this dissertation (Chapters 2-4) covers applications of 2DEV spectroscopy to light-harvesting complex II (LHCII) under various excitation conditions, as well as the development of theoretical models to aid in the understand of the observed spectra. Together, these experiments unveil the critical role of electronic-vibrational (or vibronic) mixing in facilitating efficient, ultrafast excitation energy transfer (EET) over the entire photosynthetically active region of the solar spectrum. Specifically, vibronic mixing is seen to facilitate EET over moderately large energy gaps, thus largely influencing the potential energy landscape, and ultimately bridging the spatial domains of groups of electronically coupled chlorophylls. In order to more deeply understand the mechanisms of vibronic mixing at play in the natural system, we describe the subsequent development of a model vibronic heterodimer system. This model, although still basic in comparison to LHCII, allows for a more critical examination of the observed 2DEV spectral features and strongly suggests that non-Condon effects are central to the EET mechanism in the complex.

In the second half of this dissertation (Chapters 5-7), emphasis is placed on the photochemistry and photophysics relevant to photosynthetic reaction centers, rather than light-harvesting complexes. In particular, the application of 2DEV spectroscopy to the photosystem II reaction center (PSII-RC) is able to clearly distinguish, for the first time, the initial charge separation step which triggers the light to energy conversion process in the photosynthetic engine of green plants and algae. These experiments also reveal the role of exciton-charge transfer mixing as a potential mechanism for ensuring efficient charge sepa-

ration in the PSII-RC. The charge separated species formed in this step ultimately triggers water splitting—leading to the production of molecular oxygen—which is responsible for life on earth as we know it. Specifically, this process is facilitated by the favorable energetics of an intervening proton-coupled electron transfer (PCET) reaction. However, studying this process directly in the natural system is difficult. In the remaining chapters, 2DEV spectroscopy is first used to study proton transfer in a model system, Indigo Carmine (a derivative of the well-known dye, Indigo). In this experiment, the long-debated mechanism of excited state intramolecular proton transfer is clarified and the role of the solvent in promoting this reaction is investigated. Additionally, this work distinguishes how proton transfer manifests in 2DEV spectra and serves to lay the groundwork for the subsequent investigation of a biomimetic model system for the PCET reaction in PSII. In the study of the biomimetic species, the observation of a non-equilibrium reaction pathway allows for nuanced insight into the complex dynamics and synergistic molecular motions involved in photoinduced PCET.

We conclude with a discussion of future pursuits of the elusive relationship between electrons and nuclei in both natural and bioinspired photosynthetic systems, as well as promising improvements and other applications for the emerging method of 2DEV spectroscopy.

For my Mom.

"You have no choice you have to pay times price
But you can use the price to buy you something nice"

—Jeffrey Lewis

Contents

List of Figures

List of Tables

Acknowledgments

I truly could not be where I am without all the people who have helped, encouraged, and guided me.

The Berkeley community in particular has fostered a brilliant and supportive atmosphere—making it a truly special place. I would like to give a huge thank you to Prof. Graham Fleming—for being a tremendous advisor and always pushing me to grow, yet giving me the latitude to get there in my own way. As I now take a moment to reflect on my time in your group, I am realizing just how far I have come and how enjoyable the journey has been. And thank you to the entirety of the Fleming group—past and current. A special thanks to Prof. Yusuke Yoneda—you are truly an experimental tour de force and possess a work ethic unparalleled. Working with you was an absolute pleasure. Thank you to Sara Ricks—always swooping in to save the day during a moment of crisis. You are a lifeline for the lab. Thank you to all of my collaborators—especially Prof. Thomas Moore and Dr. Masakazu Iwai. Without you, so many of these projects would not be possible. You have both taught me so much and so patiently answered my many questions. Thank you to the Berkeley Department of Chemistry—especially Prof. Eran Rabani and Prof. Richard Saykally for your guidance. I am also grateful for the support I have received from the Berkeley Fellowship for Graduate Study and the National Science Foundation Graduate Research Fellowship (Grant No. DGE 1752814).

I am only at this point in my scientific journey, however, because of all those who have inspired and supported me over the years—especially Prof. Stewart Novick, Prof. Daniel Obenchain, Mrs. Okamoto, and Mrs. Elperina. Thank you for showing me that I could succeed. Prof. Daniel Obenchain—I am so grateful for you. After all of these years, I still learn so much from you and rely on your advice.

Of course, thanks upon thanks to my family and friends. Thank you for being constants, for listening to me complain, for providing some *balance*—Mom, Dad, Emily, Luke, and Will, the keeper of the Wish Box. And Isabel, I am so grateful for you. Thank you for putting up with me, for being life away from lasers, for hikes and all of that stuff, for doing this all with me. You have been an endless source of perspective and laughter. Finally, thank you to Jeffy for teaching me the wonders of playing catch (and also that sometimes it is okay to bark at strange behavior).

Thank you all for helping me along the way.

Chapter 1

Introduction

1.1 Molecular Mechanisms in Photosynthetic Systems

Photosynthesis is the process by which light energy from the sun is converted into chemical energy—providing the energetic grounds on which life on earth is supported.[1] On a molecular level, however, the way that sunlight is captured and converted into more useful forms of energy is far from understood. Particularly, it is profoundly difficult, both experimentally and theoretically, to untangle the highly interacting molecular networks in these photosynthetic systems. For example, the spectral signatures of light-harvesting pigments, such as chlorophyll (Chl), are often nearly indistinguishable which makes questions regarding the pigment contributions, as well as the underlying mechanistic function (driven by quantum mechanical interactions) difficult to answer. In many cases, the governing photochemical and photophysical mechanisms also depend highly on the intricate choreography between the electronic and nuclear degrees of freedom (DOF) of the relevant molecular actors—as will be discussed explicitly in the following chapters. From a theoretical perspective, accounting for the interaction between the electronic and nuclear DOF is challenging, especially as the dimensionality of the system Hamiltonian grows exponentially with the number of nuclear DOF explicitly treated. Even more so, very few experimental methods are capable of directly interrogating the evolution of electron-nuclear interactions. To this end, two-dimensional electronic-vibrational (2DEV) spectroscopy was recently realized.[2] 2DEV spectroscopy is unique in comparison to other multidimensional spectroscopies in that it employs highly non-degenerate (visible) pump and (infrared) probe pulses, therefore allowing for electron and nuclear correlations to be followed directly.

In Chapter 2, we apply 2DEV spectroscopy to study the excitation energy transfer (EET) dynamics of light-harvesting complex II (LHCII)[3]—the most abundant membrane protein on earth.[4] LHCII is the major antenna complex of green plants and algae which serves to harvest solar light and ultimately transfer this excitation energy towards the photosynthetic reaction center where the initial step in light-energy conversion occurs. Despite the importance of LHCII, the underlying mechanisms that drive efficient, robust EET in the

complex are not fully understood. Most notably, the origin of long-lived oscillatory features in earlier ultrafast spectroscopic measurements of LHCII[5] has remained an open question. In this chapter, we demonstrate how the oscillatory structures present in the 2DEV spectra of LHCII unveil the role of vibronic interactions in facilitating energy flow within this pigment-protein complex. Specifically, vibronic mixing is seen to promote EET over moderately large energy gaps, ultimately bridging the spatial domains of groups of electronically coupled Chls. Further, these experiments distinguish the importance of light absorption by vibronic states energetically above the dominant electronic (Q_y) states.

Building on this work, Chapter 3 applies 2DEV spectroscopy to study the role of the highest-lying mixed vibronic Q_y-Q_x states (spanning 520-570 nm) in LHCII.[6] Contrary to the commonly accepted idea that green light is of little importance for photosynthesis, it has been shown by Terashima et al. that for in vivo systems, additional green light in the presence of strong white light illumination actually has the ability to drive photosynthesis more efficiently than additional red light.[7] In this chapter, we interrogate the states responsible for green light absorption in LHCII. We find that this spectral region is dominated by states of Chl *b* character—suggesting that Chl *b* enhances the ability of green plants and algae to harvest light across the photosynthetically active region of the solar spectrum.[7–10] The dynamics of these states also reveal the continued importance of vibronic mixing in promoting ultrafast EET across the absorption spectrum of LHCII.

As discussed in Chapters 2 and 3, vibronic states play a critical role in the function of LHCII. However, a deeper understanding of the employed mechanism(s) of vibronic mixing is lacking. For example, in Chapter 2, a basic theoretical model is put forth to understand the manifestation of EET in the 2DEV spectra of a molecular complex, however, vibronic effects are not treated. In order to address these uncertainties, Chapter 4 presents a more complete model for an electronically/vibronically coupled heterodimer for which two distinct mechanisms of vibronic coupling can be systematically tuned.[11] In particular, this model includes the coupling of an additional low-frequency vibrational mode to site-exciton states in a heterodimer system which can induce vibronic mixing through Franck-Condon activity (which couples the nuclear mode to the site energies) or through Herzberg-Teller activity (which introduces a nuclear dependence on the electronic coupling through the transition dipole moment of a single chromophore). The model results demonstrate the impact that these distinct mechanisms of vibronic mixing have on both the EET dynamics and observable features in 2DEV experiments. Finally, we end this chapter with a discussion comparing these theoretical results with the 2DEV experiments discussed in Chapter 2. Through this comparison, we are able to directly assign the dominant vibronic coupling mechanism in LHCII as arising from Herzberg-Teller activity.[12]

Up until this point, the focus has been placed on the primary light-harvesting step in the natural system. However, a logical next question is: What happens once this excitation energy is transferred from a light-harvesting complex to a photosynthetic reaction center? The remaining chapters will focus on this question. In Chapter 5, we present the first 2DEV spectroscopic study of the photosystem II reaction center (PSII-RC). PSII is crucial for oxygenic life on earth—as it provides oxygen as a product of water splitting.[1, 13, 14] The

PSII-RC is specifically the component of PSII that undergoes the primary photoinduced electron transfer step which triggers the above mentioned water splitting reaction.[15–17] However, the excited state charge separation dynamics of the PSII-RC has been a matter of vivid debate because the absorption spectra of the embedded chromophores significantly overlap and hence it is extremely difficult to distinguish transients. Here, we show how the simultaneous resolution along both the visible excitation and infrared detection axis afforded by 2DEV spectroscopy is crucial in allowing for the character of the excitonic states and interplay between them to be clearly distinguished. In particular, this chapter demonstrates that the initial electron acceptor in the PSII-RC is Phe_{D1}, rather than P_{D1}, regardless of excitation wavelength. Further, we find evidence for extensive exciton-charge transfer mixing throughout the excited state manifold which likely serves as an efficient means to facilitate the charge separation process in the PSII-RC.

Investigating the subsequent reactions in PSII triggered by charge separation in the PSII-RC, however, still poses a significant challenge. 2DEV spectroscopy, though, offers a promising avenue for studying the dynamics of such complex photosynthetic systems. In order to make progress towards the future interrogations of such reactions, we turn towards studies of model molecular systems in Chapters 6 and 7. Following the electron transfer process in the PSII-RC, the resulting highly oxidizing Chl ($P_{680}{}^{+}$) oxidizes the water splitting CaO_5Mn_4 catalytic cluster through a proton-coupled electron transfer (PCET) relay.[18, 19] Chapter 6 presents a 2DEV spectroscopic study of a model proton transfer reaction[20]—the first step towards understanding the dynamics of PCET and ultimately water splitting in PSII. In particular, we focus on the excited state proton transfer (ESPT) reaction of Indigo Carmine (InC) (a form of the well-known dye Indigo that is soluble in polar solvents), which itself has been a matter of debate.[21–26] Through a comparison of the excited state dynamics of InC in a protic solvent, D_2O, and an aprotic solvent, deuterated dimethyl sulfoxide (dDMSO), we clarify the intricate relationship between the solvent-solute interaction and ESPT reaction.[27] We find that the ability of protic solvents to form intermolecular H-bonds with InC enables ESPT and facilitates a rapid non-radiative $S_1 \rightarrow S_0$ transition. Beyond these findings, this chapter also reveals for the first time how the correlation between the electronic and nuclear DOF accompanying proton transfer manifests in 2DEV spectra.

With an understanding of how 2DEV spectra reveal proton transfer reactions, we are well positioned to study the more complex evolution of PCET. In Chapter 7, we present a study of the photoinduced PCET dynamics of a biomimetic model system.[28] While PCET is crucial to the favorable energetics of water splitting in PSII, a full understanding of the mechanism is still lacking due to the complex non-equilibrium dynamics arising from the strongly coupled electronic and nuclear DOF. In this chapter, we provide a nuanced picture of the complex dynamics and synergistic motions involved in photoinduced PCET. We find that PCET along a non-equilibrium reaction pathway cannot be described as a single kinetic step. Rather, the electron transfer component of the reaction only reaches completion following significant nuclear rearrangement. Based on this work, it seems highly likely that all PCET systems will require substantial rearrangement to complete the transfers, as they all involve substantial changes in electronic structure.

In Chapter 8, we finish by sketching the path forward in elucidating the complex molecular choreography of photosynthetic systems—including investigations of the PSII core complex and a biomimetic system designed to undergo one-electron two-proton transfer. In the remainder of the current chapter (adapted from Ref. [29]), we will focus on the background of 2DEV spectroscopy, as well as the various aspects which distinguish this method from other multidimensional spectroscopies.

1.2 Two-Dimensional Electronic-Vibrational Spectroscopy

A comparison of 2DEV spectroscopy with the degenerate third-order two-dimensional infrared[30–33] and two-dimensional electronic[34–36] spectroscopies (2DIRS and 2DES, respectively) can aid in clarifying the distinguishing features of each method. An immediate difference is that while the degenerate spectroscopies measure quantities related to autocorrelation functions of transition frequency fluctuations or cross-correlations between transitions arising from the same types of DOF, 2DEV spectra contain cross-correlations of the fluctuating electronic and vibrational energy gaps, i.e. disparate DOF. These cross-correlation functions can be characterized by the evolution of the center line slope (CLS) of the spectral features.[37, 38] Because 2DEV features involve different types of transition moments, electronic and vibrational, the spectra can be very sensitive to electronic and vibronic mixing through substantial alteration to the infrared transition moments. This is distinct from degenerate spectroscopies where features are depend only on one type of transition moment. The result is that weak transitions not readily apparent in one-dimensional or two-dimensional electronic spectra can become prominent in 2DEV spectra.

Degenerate spectroscopies also contain a diagonal along which is displayed the absorption spectrum and in 2DIR spectra, includes the anharmonic splitting. 2DEV spectra, on the other hand, are intrinsically off-diagonal. Here, the detection of vibrational features spreads out the electronic excitation along the detection axis, often giving remarkably improved resolution in the electronic spectrum. The comparison of diagonal and off-diagonal features and of diagonal and anti-diagonal widths has long been of value in 2DES and 2DIRS, as has comparison of rephasing and non-rephasing spectra.[39–41] 2DEV spectra, being entirely off-diagonal and exhibiting rather little rephasing, do not allow such comparisons.[42] Recording spectra as a function of waiting time in 2DES or 2DIRS generally results in spectra that have an intuitive appearance, such as the growth of off-diagonal features resulting from EET in molecular complexes, for example. In 2DEV spectra, however, the evolution of the spectra with waiting time is not always intuitive. This is clearly apparent in the same example as just given, where the entire 2DEV spectrum becomes increasingly symmetric around the excitation axis as EET proceeds. In 2DIR spectra of chemical exchange systems, the spectra do become symmetric, as a result of the reversibility of the exchange process[39], but only unidirectional transfer is required in 2DEV spectra.

All two-dimensional spectroscopies gain spectral resolution by spreading out the peaks into a second dimension. The good spectral resolution in 2DEV spectra along the detection (infrared) axis is not surprising, but in many 2DEV spectra, enhanced resolution along the excitation (visible) axis as compared to linear absorption or two-dimensional electronic spectra is also noticeable. This will be discussed below.

1.3 Origin of the 2DEV Spectroscopic Signal

2DEV spectroscopy is a four-wave mixing process where the interactions of the three pulses (in this case two visible and one infrared) with the sample produce the third-order nonlinear signal (pulse sequence shown in Figure 1.1). This signal can be understood as arising from the third-order polarization which, within a perturbative framework, is given by the convolution of the third-order response function, $S^{(3)}(t_1, t_2, t_3)$, with the electric field of the incident pulses, $E(t)$[43]

$$P^{(3)}(t_1, t_2, t_3) = \int_0^\infty \int_0^\infty \int_0^\infty S^{(3)}(t_1, t_2, t_3) E(t - t_3 - t_2 - t_1) \tag{1.1}$$

$$E(t - t_3 - t_2) E(t - t_3) dt_1 dt_2 dt_3. \tag{1.2}$$

Considering that the electric field of the pulse sequence is given by

$$E(t) = \sum_{j=1}^{3} A_j(t - t_j) e^{-i\omega_j(t-t_j) + i\mathbf{k}_j \cdot \mathbf{r} + i\phi_j} + c.c. \tag{1.3}$$

where A_j, ω_j, $\mathbf{k}_j$, and ϕ_j are the temporal envelope, carrier frequency, wavevector, and phase of the jth pulse, respectively, the third-order polarization is a complicated quantity as a result of the many contributing signal pathways.

Typically, degenerate or near-degenerate two-dimensional spectroscopies utilize phase matching conditions to spatially separate the desired signal pathways from the others inherently generated through the light-matter interactions. In practice, these conditions are enforced through the physical geometry (e.g. boxcar geometry) of the incident beams.[34] However, what distinguishes 2DEV spectroscopy in this regard is that there is approximately an order of magnitude difference between the wavelengths of the highly nondegenerate visible excitation pulses and the infrared detection pulse. This severely limits the practical experimental geometries by which this type of spectroscopy can be performed in order to obtain a background-free signal.[44] Rather, the implementation of phase cycling with a pump-probe geometry ($\mathbf{k}_1 = \mathbf{k}_2 \neq \mathbf{k}_3$) is the most useful means for isolating the 2DEV signal. In the pump-probe geometry, the third-order signal intensity is given by

$$I^{(3)}(t_1, t_2, \omega_3) = \left| E_3(\omega_3) \left(1 + \tilde{S}^{(3)}_{113}(t_1, t_2, \omega_3) + \tilde{S}^{(3)}_{223}(t_1, t_2, \omega_3) + \tilde{S}^{(3)}_{123}(t_1, t_2, \omega_3) \right) \right|^2 \tag{1.4}$$

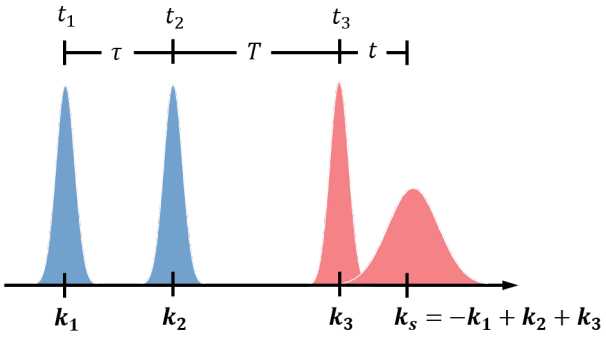

Figure 1.1: 2DEV spectroscopic pulse sequence. The blue pulses, $\mathbf{k}_1$ and $\mathbf{k}_2$, indicate electronically-resonant excitation interactions and the red pulse, $\mathbf{k}_3$, indicates a vibrationally-resonant detection interaction. Finally, $\mathbf{k}_s$ represents the emitted signal following the three previous light-matter interactions occurring at t_1, t_2, and t_3. The relative delay between fields are denoted as τ, T (termed the waiting time), and t. We note that τ and t are interchangeably referred to as $t_{\text{exc.}}$ and $t_{\text{det.}}$, respectively, throughout the following chapters.

where $E_3(\omega_3)$ is the infrared probe filed which also serves as the local oscillator, $\tilde{S}^{(3)}_{113}(t_1, t_2, \omega_3)$ and $\tilde{S}^{(3)}_{223}(t_1, t_2, \omega_3)$ are the pump-probe background signals, and $\tilde{S}^{(3)}_{123}(t_1, t_2, \omega_3)$ is the 2DEV signal. Here,

$$S^{(3)}_{jk3}E_3(\omega_3) = \int_0^\infty \int_0^\infty \int_0^\infty e^{-i\omega_3 t_3} S^{(3)}(t_1, t_2, t_3) E_j(t - t_3 - t_2 - t_1) \\ E_k(t - t_3 - t_2) E_3(t - t_3) dt_1 dt_2 dt_3 \tag{1.5}$$

is the Fourier transform over t_3 of the convolution of the third-order response function with the electric fields of the pulses. The intensity can be rewritten as

$$I^{(3)}(t_1, t_2, \omega_3; \Delta\phi_{12}) \propto \left| \left(1 + \tilde{S}^{(3)}_{113}(t_1, t_2, \omega_3) + \tilde{S}^{(3)}_{223}(t_1, t_2, \omega_3)\right) E_3(\omega_3) \right|^2 \\ + \left| \left(\tilde{S}^{(3)}_{123}(t_1, t_2, \omega_3)\right) E_3(\omega_3) \right|^2 + 2\text{Re}\left[e^{i\Delta\phi_{12}} \tilde{S}^{(3)}_{123}(t_1, t_2, \omega_3) \left(\tilde{S}^{(3)}_{113}(t_1, t_2, \omega_3) \right.\right. \\ \left.\left. + \tilde{S}^{(3)}_{223}(t_1, t_2, \omega_3) E_3(\omega_3) \right)^* \right] |E_3(\omega_3)|^2 \tag{1.6}$$

where the dependence of $\tilde{S}^{(3)}_{123}(t_1, t_2, \omega_3)$ on the interpulse phase difference between the two pump pulses has been shown explicitly—the 2DEV signal acquires an overall phase prefactor while the largest undesirable signals do not. In this way, the 2DEV signal can be effectively isolated by repeating the measurement n times with values of $\Delta\phi_{12}$ stepped by $2\pi/n$ and

summing the results[45, 46]

$$\begin{aligned}\frac{1}{n}\sum_{j=1}^{n-1} e^{-i(2/n)} \left| E_3(\omega_3)\left(1+\tilde{S}^{(3)}_{113}(t_1,t_2,\omega_3)+\tilde{S}^{(3)}_{223}(t_1,t_2,\omega_3)+\tilde{S}^{(3)}_{123}(t_1,t_2,\omega_3)\right)\right|^2 \\ = 2\tilde{S}^{(3)}_{123}(t_1,t_2,\omega_3)\mathrm{Re}\left[\left(1+\tilde{S}^{(3)}_{113}(t_1,t_2,\omega_3)+\tilde{S}^{(3)}_{223}(t_1,t_2,\omega_3)\right)^*\right]|E_3(\omega_3)|^2 \\ \backsimeq 2\tilde{S}^{(3)}_{123}(t_1,t_2,\omega_3)\,|E_3(\omega_3)|^2\,. \end{aligned} \tag{1.7}$$

While the cross-terms between the pump-probe and 2DEV signals cannot be completely suppressed, these terms scale quadratically with the third-order field and thus are negligible compared to the desired signal which scales linearly with the third-order field. The isolation of the 2DEV signal is completed following division by a reference field (identical to the probe field). Finally, to obtain the absorptive 2DEV spectrum, a Fourier transform along t_1 of the signal is performed. Often, however, further processing is done in order to achieve a higher quality spectrum.

The details regarding how the 2DEV experiment is realized in practice are described in the following chapters.

1.4 The 2DEV Spectrum

Two main defining features emerge as apparently unique to 2DEV spectra: 1) improved spectral resolution along both the electronic and vibrational frequency axes and 2) the ability to correlate the electron and nuclear dynamics as a function of waiting time. In this section, we will focus on the former. To recognize the origin of this phenomenon, it is necessary to consider that the requirement for observing a peak in a 2DEV spectrum is that the conditional probability $P(\omega_e;\omega_v)$ is non-zero where ω_e is the electronic excitation energy and ω_v the vibrational detection frequency. The consequence of this highly specific condition manifests significantly in systems with multiple closely-lying electronic/vibronic states. In such systems, there is often a certain degree of spectral congestion as a result of the many closely spaced levels which makes resolving them difficult with electronic spectroscopies where the conditional probability $P(\omega_e;\omega'_e)$(where ω_e is the electronic excitation energy and ω'_e the electronic detection frequency) is comparatively more relaxed. A graphical demonstration of the effect of the condition $P(\omega_e;\omega_v)$ is shown in Figure 1.2 where there is a noticeable enhancement of the spectral resolution in the 2DEV spectrum along the excitation axis (Figure 1.2b-d) versus the corresponding linear absorption spectrum (Figure 1.2a) where states ε_1-ε_4 are indistinguishable. While it is more obvious that infrared detection allows for the signatures of various electronic states to be dispersed along the detection axis as a result of the vibrational frequency dependence on the given electronic manifold (2DEV spectroscopic features pointed out with the black arrow in Figure 1.2b), this is not necessarily the cause of enhanced resolution along the excitation axis. Rather, this enhancement can occur even if there is little difference in the characteristic vibrational frequencies of given

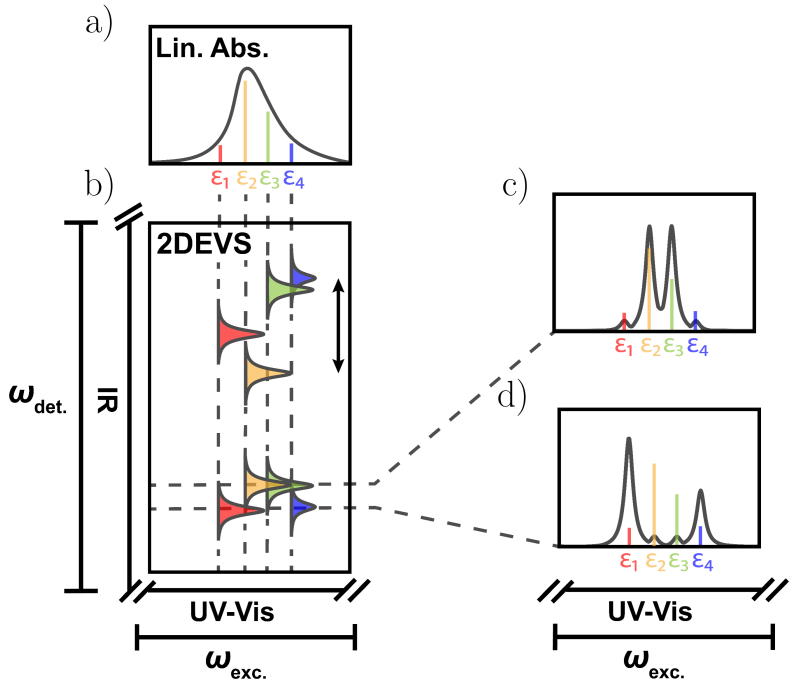

Figure 1.2: a) Representative linear absorption spectrum for a system with many closely space, unresolvable, electronic/vibronic levels labeled ε_1-ε_4. b) Associated cartoon 2DEV spectrum depicting the dependence of the detected vibrational structure on the given electronic state which can vary substantially (see top portion highlighted with black arrow to show the frequency spread) or only slightly (see bottom portion of spectrum). c) and d) Slices through the 2DEV spectrum at a fixed detection frequency emphasizing the improved frequency resolution along the excitation axis. Also shown in the figure is how the dependence of features on both the electronic and vibrational transition moments can amplify certain states with respect to the linear absorption spectrum (see the intensity of the red versus blue features).

electronic/vibronic states. Such a phenomenon is highlighted in Figure 1.2c and 1.2d which show slices through the 2DEV spectrum at fixed detection frequencies. In this case, the condition $P(\omega_e;\omega_v)$ essentially results in a gap between 2DEV peaks. In practice, this effect is not always quite as dramatic, however, it is still striking and will be apparent in the spectra presented in Chapters 2-5.

1.5 The Center Line Slope

In many cases, the ability of 2DEV spectra to correlate the electron and nuclear dynamics as a function of waiting time is the defining factor which allows for connections to be drawn between spectroscopic observables and the actual underling photochemical or photophysical mechanism(s) of a system. This aspect of the method will be particularly apparent in Chapters 2, 6, and 7.

The theory underpinning the description of the CLS as representing a cross-correlation of the fluctuating parts of the electronic and vibrational energy gaps for individual molecules in solution has recently been developed by Cho and Fleming.[38] In this case the CLSs for a ground state bleach (GSBs) and an excited state absorption (ESA) feature are given by

$$\mathrm{CLS}_{\mathrm{GSB}}(T) = \frac{\langle \delta\omega_{eg}(T)\delta\omega_{gg'}(0)\rangle}{\langle \delta\omega_{eg}^2\rangle} \tag{1.8}$$

and

$$\mathrm{CLS}_{\mathrm{ESA}}(T) = \frac{\langle \delta\omega_{eg}(T)\delta\omega_{ee'}(0)\rangle}{\langle \delta\omega_{eg}^2\rangle} \tag{1.9}$$

where subscripts gg' and ee' refer to vibrational excitation frequencies in the ground and excited states, respectively. These expressions describe the correlation of the electronic and vibrational frequencies via coupling of their transition frequencies to the same solvent motions. If the solvent-solute interaction can be described by the interaction of the solute dipole moment and the solvent electric field, then the fluctuating part of the potential energy difference is given by

$$\delta V_{eg}(q) = -\Delta\mu_{eg} \cdot E_{\mathrm{sol.}}(q) \tag{1.10}$$

where q is the bath coordinate and $\Delta\mu_{eg} = \mu_e - \mu_g$ is the difference in dipole moment between the excited and ground electronic states. Similarly, for the vibrational Stark effect, the vibration frequencies will fluctuate as

$$\delta F_i V_i(q) = -\delta\mu_i \cdot E_{\mathrm{sol.}}(q) \tag{1.11}$$

where $i = e, g$ such that $\delta\mu_i$ is the vibrational Stark tuning rate of the jth normal mode in the ground or excited electronic state. Here, the F operators connect the solvent-solute interaction to the frequency shifts of the specific modes. With these various approximations in place, the cross-correlation functions in Equations 1.8 and 1.9 can be simplified to

$$\langle \delta\omega_{eg}(T)\delta\omega_{gg'}(0)\rangle = \langle E_{\mathrm{sol.}}(q(T)) \cdot [\Delta\mu_{eg}(T)\delta\mu_g(0)] \cdot E_{\mathrm{sol.}}(q(0))\rangle/\hbar^2 \tag{1.12}$$

and

$$\langle \delta\omega_{eg}(T)\delta\omega_{ee'}(0)\rangle = \langle E_{\mathrm{sol.}}(q(T)) \cdot [\Delta\mu_{eg}(T)\delta\mu_e(0)] \cdot E_{\mathrm{sol.}}(q(0))\rangle/\hbar^2, \tag{1.13}$$

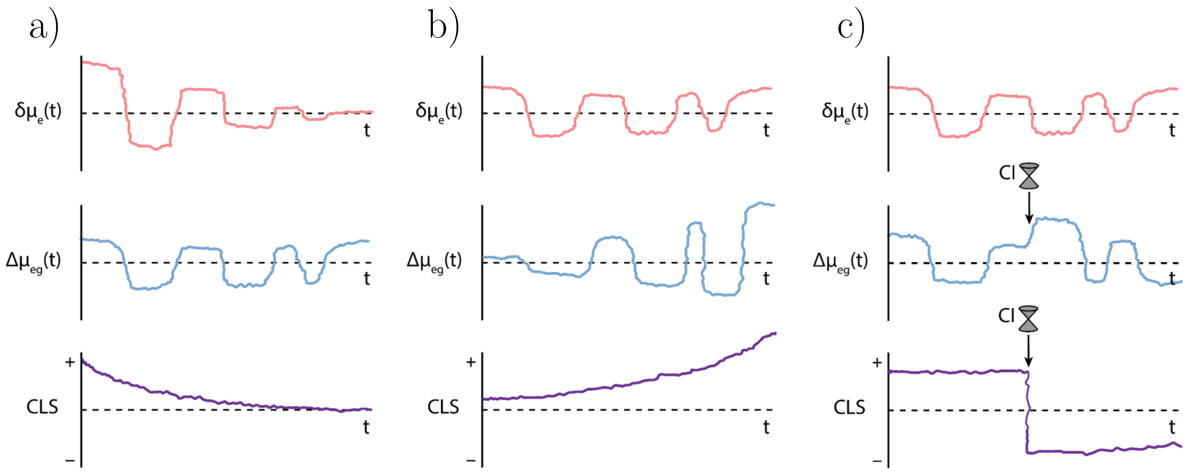

Figure 1.3: Illustration of the origins of various forms of center line slope (CLS) evolution, in this case for an excited state absorption feature, guided by the formalism presented in Ref. [38]. Correlations between the fluctuations of $\delta\mu_e$ and $\Delta\mu_{eg}$ are shown when a) $\delta\mu_e$ dominates leading to an exponential decay in the CLS indicative of vibrational dephasing, b) $\Delta\mu_{eg}$ dominates as a result of electronic structure evolution, for example, which can lead to an exponential rise or decay and be positive or negative (the example above is for the scenario when $\Delta\mu_{eg}$ increases and the correlation is positive), and c) when a sudden change in $\Delta\mu_{eg}$ occurs as a result of a relaxation through a conical intersection (CI), for example (the illustrated example is for the case when the electronic dipole moment reverses direction above and below the CI).

respectively. The quantities $\Delta\mu_{eg}\delta\mu_g$ and $\Delta\mu_{eg}\delta\mu_e$ are dyadic products of the two vector Stark tuning rates.

Within this formalism, we can understand how correlations between the electronic and vibrational DOF manifest in the two-dimensional lineshape. Figure 1.3 contains cartoon representations of how various relations between $\delta\mu_e$ (where we note this example is for an excited state vibration) and $\Delta\mu_{eg}$ can drive the CLS dynamics. For example, Figure 1.3a illustrates the most straightforward dynamical case when solvation dynamics, driven by $\delta\mu_e$, dominate. Observing this CLS behavior is expected mainly in unreactive systems, when changes in $\Delta\mu_{eg}$ will not overwhelm the electron-nuclear correlation. However, the more interesting scenarios are rather when $\Delta\mu_{eg}$ is the prevailing influence over the correlation (Figure 1.3b and c). Starting with Figure 1.3b, this cartoon depicts how a gradual increase of $\Delta\mu_{eg}$ results in an increase in the CLS. For clarity of the illustration, $\delta\mu_e$ is shown not to vary, but this is a noted simplification. Regardless, it now becomes clear how changes in the 2DEV lineshape for reactive systems can be utilized to connect spectroscopic dynamics (e.g. peak amplitudes) with the underlying mechanistic function of the system. Examples of this

type of CLS behavior will be presented in Chapters 6 and 7. Finally, Figure 1.3c provides an example of how a change in $\Delta\mu_{eg}$ as a result of rapid radiationless relaxation (i.e. involving a conical intersection) can influence both the sign and magnitude of the CLS. A change in the sign of the CLS can occur when there is a reversal in the dipole moment as a result of significant nuclear rearrangement.[20, 47] This sensitivity to molecular geometry along a potential surface, is again, a significant advantage when the goal is to understand condensed phase molecular dynamics. This dynamically behavior in the CLS will be exemplified in Chapter 6.

In this section, only the CLS dynamics of single molecular systems have been considered. For coupled molecular systems, the calculation of the CLS behavior is sufficiently complex that more insight is gained via numerical simulations of specific models. An elaboration on the modeling of CLS dynamics in such systems is reserved for Chapter 2.

Chapter 2

The Influence of Vibronic Mixing on the Ultrafast Energy Flow of LHCII

2.1 Introduction

Excitation energy transfer (EET) within light-harvesting complex II (LHCII) lies at the heart of green plant and algae photosynthetic light-harvesting.[1] LHCII can comprise up to 50% by weight of the grana membrane, the site of water splitting by Photosystem II.[48] The complex is generally found as a trimer with each monomer containing eight chlorophyll (Chl) *a* and six Chl *b* molecules along with four carotenoid molecules.[49] The empirical Hamiltonian developed by Novoderezhkin and van Grondelle accounts for a wide range of linear spectroscopic measurements and forms the basis for theoretical and experimental studies of the EET dynamics and mechanism.[50] The spatial arrangement of the Chls and experimental linear absorption spectrum along with the exciton energy levels from the Novoderezhkin and van Grondelle Hamiltonian are shown in Figure 2.1 (exciton energy levels are colored to match pigments in Figure 2.1a that have the most substantial contribution).

From the earliest ultrafast spectroscopic measurements on LHCII, it was clear that rapid Chl *b* to Chl *a* transfer occurred[51, 52] and as multidimensional spectroscopy has developed, models of EET within LHCII have advanced significantly.[5, 53–57] At the same time, long-lived oscillatory features were observed, initially in the Fenna-Matthews-Olson complex[58] and later in LHCII.[5] Since then, the origin of these oscillations has been extensively debated.[59–71] Beyond this debate lies an even more challenging question—how does the observation of these beats spectroscopically connect to the mechanistic function of natural light-harvesting? For example, the assignment of beats as vibronic in origin does not necessarily demonstrate that electronic-vibrational mixing influences energy transport. In response to such a question, the mechanistic role of vibronic coupling in facilitating EET has also received significant theoretical attention, however, the conclusions can vary widely as there remains no uniform treatment of electronic-vibrational mixing.[64–72] To this end, recent work has expressed how certain aspects of vibronic mixing must be treated carefully,

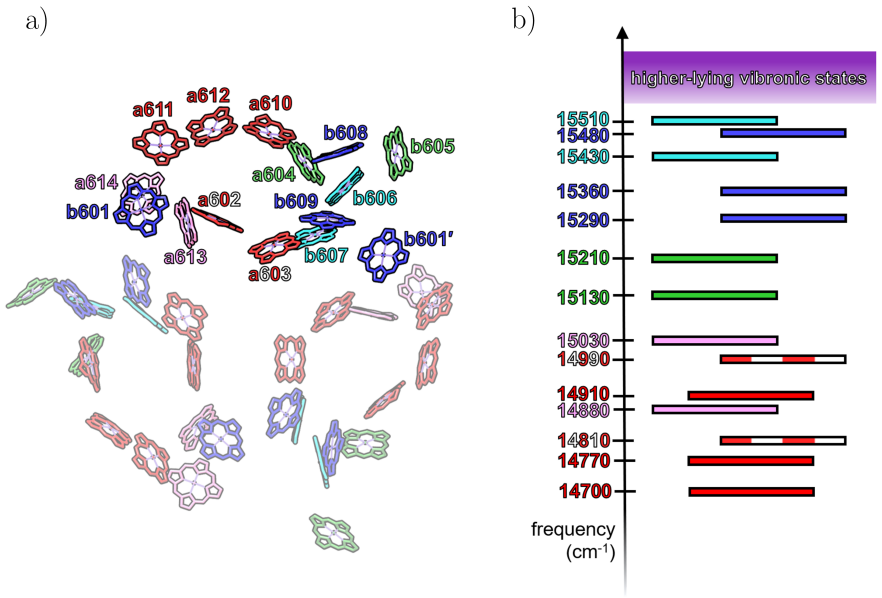

Figure 2.1: a) Pared-down LHCII trimer from 2.72 Å X-ray crystal structure.[49] Chl *a* and Chl *b* pigments in one monomer are labeled (note: a prime indicates a pigment located in a different monomer). b) Excitonic states of LHCII, which are colored to match the pigments with dominate contributions, based on the Novoderezhkin and van Grondelle Hamiltonian.[50] Excitonic states colored with pink, red and white, or red have predominately Chl *a* character, while those labeled with light blue or blue have predominantly Chl *b* character. The corresponding frequencies are based on past experimental work.[5]

namely Yeh et al. illuminated the need to synchronously treat electronic energy fluctuations and vibrational relaxation in mixed electronic-vibrational systems[67], while Zhang et al. highlighted the potential for disconnect between spectral signatures and system dynamics by showing that both Condon and non-Condon coupling can lead to prolonged oscillatory features, but only non-Condon effects led to enhancements in electronic-vibrational energy transfer.[64] The commonly employed technique of two-dimensional electronic spectroscopy (2DES) often lacks the spectral resolution to untangle the complex, congested spectra of relevant systems—making it challenging to discern whether or not an oscillatory feature is electronic, vibrational, or vibronic in nature.[66] Although recent work has successfully unveiled the presence of vibronic coupling in natural and artificial light-harvesting systems[73–79], the newly developed technique of two-dimensional electronic-vibrational (2DEV) spectroscopy[2, 37, 42, 47, 53, 80–86], by focusing on vibrational transitions in the final light-matter interaction, has the potential to provide significantly improved experimental input into the interplay of electron and nuclear dynamics in ultrafast energy (and charge) transfer. Several aspects of 2DEV spectroscopy are significant in this regard. The improved spec-

tral resolution along the detection (infrared) axis enables features that are not discernible in degenerate (all electronic) spectra to be resolved. A further advantage of this extreme two-color technique is that in certain cases (e.g. the work presented in this chapter), the spectral dynamics will be completely free of beats that are purely vibrational in origin, as will be discussed below (it should be noted that this is also possible to achieve with certain polarization schemes in 2DES[87]). This allows for the issue of the origin of oscillatory features to be easily distinguished, thus emphasis can be shifted to the actual role that these beats may serve. Finally, the center line slopes (CLSs) of the spectral features being related to a cross-correlation of vibrational and electronic dipoles, as opposed to the autocorrelation relationship of conventional, degenerate multidimensional spectroscopies, contains unique information on the mixing and dynamics of specific levels.

This chapter examines the sub-picosecond (<700 fs) energy transfer dynamics of LHCII at 77 K with 2DEV spectroscopy. Throughout, comparisons to a basic heterodimer model, featuring two electronically coupled monomers, each with one electronic degree of freedom (DOF) and one vibrational DOF, will be used to create an intuitive picture for much of the phenomena that control the observed spectral dynamics. Specifically, evidence for the direct participation of higher-lying vibronic states during the EET process will be discussed, in addition to the assignments of oscillatory signals, observed in both the peak intensities and CLS dynamics. The assignments provide a deeper understanding of the interplay between different sites in LHCII—directly connecting the intricate energetic, spatial, and vibronic landscapes of this pigment-protein complex. We will conclude by discussing the likely role of non-Condon effects in the EET dynamics of LHCII, which demonstrates the important next step towards determining the actual mechanistic function that quantum beats may serve during EET.

2.2 Results and Discussion

Manifestation of EET in 2DEV Spectra

In a 2DEV experiment, visible pump pulses prepare an ensemble of electronic/vibronic states that evolve as a function of waiting time, T, and are then tracked with an infrared (IR) probe pulse. The resulting data are presented as (visible) excitation frequency-(IR) detection frequency correlation plots at given waiting times. Another way to describe a 2DEV experiment is in terms of more traditional pump-probe spectroscopy—2DEV spectroscopy is the two-dimensional analog to a one-dimensional visible pump-IR probe experiment, where the resulting 2DEV spectra will have spectral resolution along both the excitation and detection axes, as opposed to the visible pump-IR probe experiment, which will only have spectral resolution along the detection axis. A more detailed description of the technique can be found in previous work.[2]

In this chapter, we have chosen to probe modes in the higher frequency region (1525-1715 cm^{-1}), which do not explicitly promote energy transfer, but rather serve as spectators that

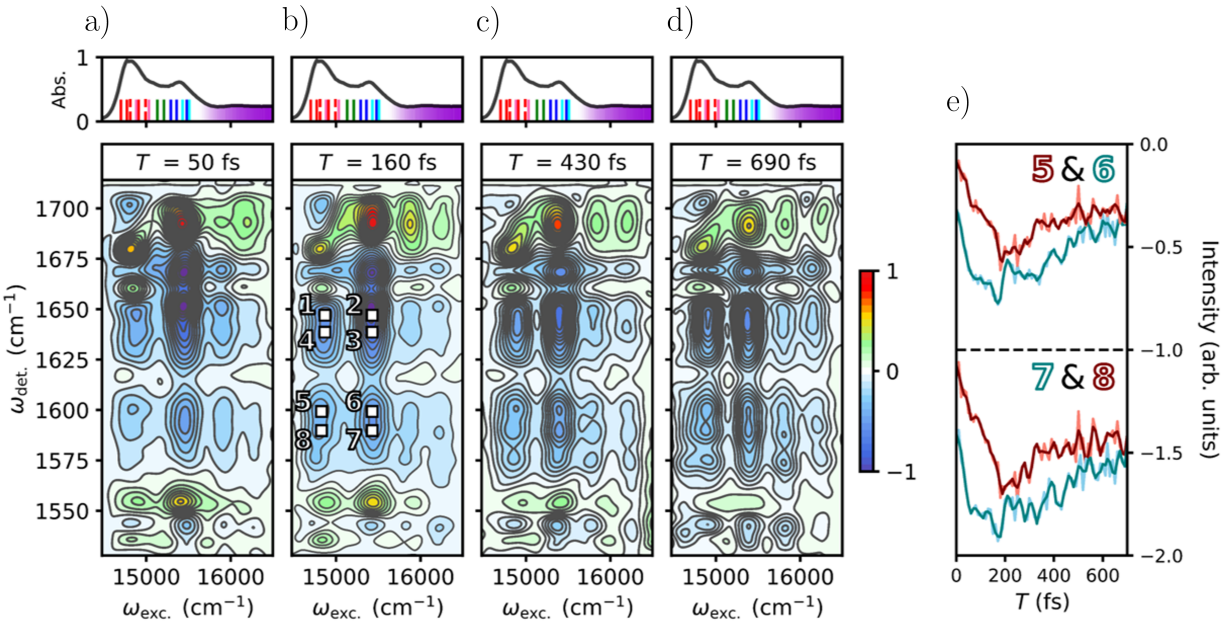

Figure 2.2: a)-d) 2DEV spectra of LHCII at waiting times of $T = 50$ fs, 160 fs, 430 fs, and 690 fs, respectively. Positive features indicate ground state bleaches and negative features indicate excited state absorptions (ESAs). The intensities of all spectra have been normalized to $T = 0$ fs. Contour lines are drawn in 6.6% intervals. The region of the linear absorption spectrum of LHCII (at 77 K) that was excited during this experiment (the Q_y bands), along with the excitonic states described in Figure 2.1, has been placed at the top of each of the 2DEV spectra in a)-d). The grouping of red and pink lines distinguishes the excitonic band of mainly Chl *a* character, while the grouping of blue lines distinguishes the excitonic band of mainly Chl *b* character. The purple continuum highlights the region of the absorption spectrum composed of the higher-lying vibronic states of mixed Chl character. In b), ESA features of interest have been labeled. e) Example of the observed oscillatory intensities, for ESAs five through eight. The intensity dynamics for seven and eight have been offset for clarity. The unfiltered intensities are shown in light red and blue, while the data in dark red and blue has been subjected to a 1200 cm^{-1} cutoff filter, in order to highlight the lower frequency oscillations of interest.

report on the energy transfer dynamics. These modes were chosen specifically because in the case of Chl, these modes are highly local and thus not anharmonically coupled to the lower frequency modes (<1500 cm^{-1}).[88] One major advantage of probing in this region, as opposed to the lower frequency region, which is energetically closer to the exciton energy gaps, is that since there is no anharmonic coupling between low and high frequency vibrational modes, the dynamics observed via probing the higher frequency modes are free from

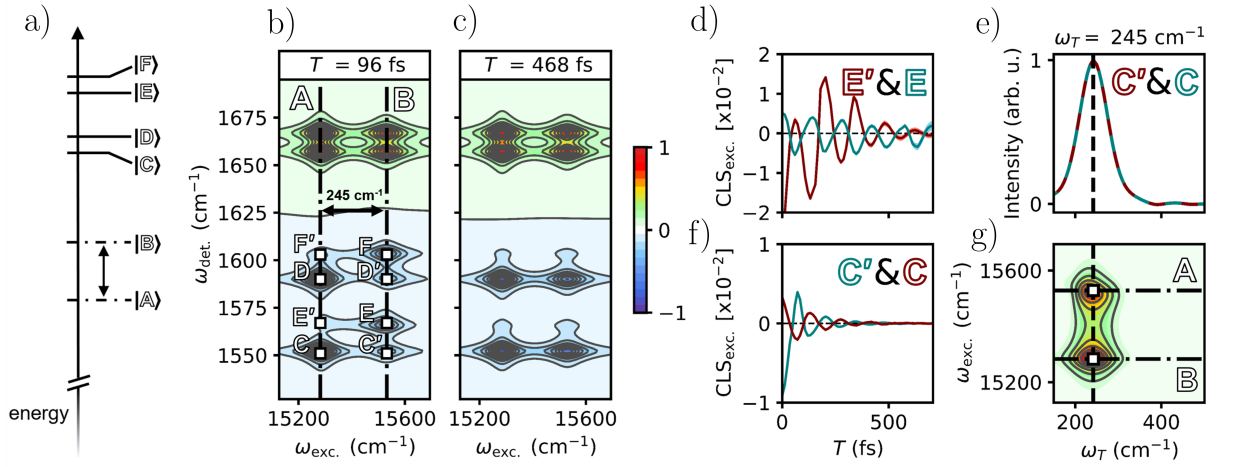

Figure 2.3: a) Energy level diagram for the six excitonic states of the heterodimer model, where the ground state manifold has been omitted for clarity. b)-c) 2DEV spectra for the model at $T = 96$ fs and $T = 468$ fs. Positive features indicate ground state bleaches and negative features indicate excited state absorptions. All spectra have been normalized to $T = 0$ fs. Contour lines are drawn in 8.3% intervals. Features of interest have been labeled C, D, E, F, C′, D′, E′, and F′. The two bands along the excitation axis have been marked by dashed-dotted black lines and labeled by the excitonic state that they originate from (A and B). The $|A\rangle$ to $|B\rangle$ energy gap has also been labeled. d) and f) Center line slope dynamics along the excitation axis ($CLS_{exc.}$) of certain features, colored according to the peak labels in the top right corner of each plot. e) Magnitude of the cross-power spectrum of the CLSs of features C′ and C, where the oscillatory frequency of 245 cm^{-1} is marked by a dotted black line (a peak in the cross-power spectrum indicates a shared frequency). g) Intensity beat map along the excitation axis of features C′ and C, where the oscillatory frequency of 245 cm^{-1} is marked by a dotted black line and the involved excitation frequencies are labeled and marked by black dotted-dashed lines.

the modulation effects caused by the creation of low(er) frequency vibrational wavepackets. The practical translation of this is that any observed beats in the 2DEV spectra will only be electronic/vibronic in origin. A control 2DEV experiment performed on cresyl violet, which was chosen because it is well known to exhibit very strong vibrational coherences with well-characterized frequencies in 2DES experiments[89, 90], is provided in Appendix A.1. For the same reason explained above, no vibrational coherences are observed in the 2DEV spectra of cresyl violet when the higher frequency modes are probed.

Selected 2DEV spectra of LHCII are shown in Figure 2.2. Along the excitation axis, the features centered around 14800 cm^{-1} and 15500 cm^{-1} correspond to the excitonic bands with mainly Chl *a* character and mainly Chl *b* character, respectively, while the two bands above

15600 cm^{-1} correspond to vibronic transitions that involve both Chl *a* and *b*. Prominent in the spectra are two sets of excited state absorption (ESA) quartets labeled one through four and five through eight in Figure 2.2b, where only the latter will be the focus of discussion (assignments of the other features not discussed here can be found in Ref. [53]). The same unique quartet structure is pronounced in the heterodimer model (Figure 2.3b and 2.3c). The assignment of these quartets in the model is straightforward and translates easily to the experimental spectra of LHCII (model parameters chosen to be comparable to those expected for LHCII, see Appendix A.2 for more details). In the heterodimer model, electronic coupling between two monomers, each with one electronic DOF and one vibrational DOF, leads to the formation of six excitonic states (Figure 2.3a). Excitonic states $|A\rangle$ and $|B\rangle$, which have mainly electronic character, are excited initially, resulting in the appearance of an A excitonic band and B excitonic band along the excitation axis. The other four excitonic states have mainly vibrational character and as such, $|C\rangle$ and $|D\rangle$ form the manifold of A excitonic states, whereas $|E\rangle$ and $|F\rangle$ form the manifold of B excitonic states. Thus, ESAs labeled C and D are transitions within the A excitonic band (between $|A\rangle \rightarrow |C\rangle$ and $|A\rangle \rightarrow |D\rangle$ in Figure 2.3a, respectively), whereas ESAs denoted E and F are transitions within the B excitonic band (between $|B\rangle \rightarrow |E\rangle$ and $|B\rangle \rightarrow |F\rangle$ in Figure 2.3a, respectively). The remaining ESAs—C′, D′, E′, and F′—are a manifestation of $|B\rangle$ to $|A\rangle$ or $|A\rangle$ to $|B\rangle$ EET and are cross peak-type features. For example, if $|B\rangle$ is initially excited, the B excitonic band will appear along the excitation axis, however, $|B\rangle$ to $|A\rangle$ EET during the waiting time will cause frequencies specific to the manifold of A excitonic states to appear in the B excitonic band along the detection axis because $|A\rangle \rightarrow |C\rangle$ or $|A\rangle \rightarrow |D\rangle$ will be the probed transitions, as opposed to $|B\rangle \rightarrow |E\rangle$ or $|B\rangle \rightarrow |F\rangle$. An increasing degree of mirror symmetry between bands along the excitation axis (Figure 2.3b and 2.3c) in 2DEV spectroscopy indicates population transfer. Returning to LHCII, spectral assignments now become much easier.

At $T = 50$ fs (Figure 2.2a), the intensity of ESA five, located in the mainly Chl *a* band at 1600 cm^{-1}, and seven, located in the mainly Chl *b* band at 1590 cm^{-1}, are greatest, whereas ESA six and especially eight are barely distinguishable. At longer waiting times (Figure 2.2b-d), the formation of four distinct ESAs at positions five through eight becomes increasingly evident as six and eight grow in. This indicates that ESAs five and seven have mainly Chl *a* and *b* character, respectively. Thus, ESAs six and eight are cross peaks indicative of EET between states of mainly Chl *a* and mainly Chl *b* character.

Shifting attention to higher excitation frequencies in the LHCII spectra, direct evidence for the participation of higher-lying vibronic states during EET appears in much the same way as for the Q_y states. The detection frequencies in the higher-lying vibronic bands mirror those in the lower-lying Chl *a* and *b* bands, as excitation initially populating the higher-lying vibronic states is rapidly transferred to the lower-lying Chl *a* and *b* states. At longer waiting times (Figure 2.2b-d), more population is funneled to the lower energy Chl *a* and *b* states, counterintuitively causing these higher-lying vibronic bands to grow in.

One particularly revealing feature along the detection axis is the ground state bleach at 1690 cm^{-1}—highly specific to Chl *b*—present in the higher-lying vibronic bands.[53] This directly shows that these bands have mostly Chl *b* character and indicates that EET directly

from the higher-lying vibronic states → Chl *a* states is not the predominant pathway of energy flow. Rather, transfer from the higher-lying vibronic states → lower-lying Chl *b* states → Chl *a* states contributes most to the vibronic energy funnel mechanism. Clearly, the nuclear DOF play an important role in LHCII, as the participation of the higher-lying vibronic states allows for an extension of efficient light-harvesting into a higher excitation frequency regime.

Center Line Slope Dynamics

2DEV spectroscopy offers another unique way to further elucidate both the complex energy transfer dynamics and the role of the nuclear DOF during the dynamics in the form of center line slopes (CLSs). In a 2DEV experiment, the CLS is a sensitive measure of the correlation between the nuclear and electronic DOF. Throughout, we will focus on CLSs along the excitation axis, $\mathrm{CLS}_{\mathrm{exc.}}$ (CLSs along the detection axis contain identical information). As described previously, the CLSs of asymmetric features are best determined based on conditional averages, $f(\omega_{\mathrm{exc.}})$, given by[80]

$$f(\omega_{\mathrm{exc.}}) = \frac{\int d\omega_{\mathrm{det.}}\, P(\omega_{\mathrm{exc.}}, \omega_{\mathrm{det.}})\, \omega_{\mathrm{det.}}}{\int d\omega_{\mathrm{det.}}\, P(\omega_{\mathrm{exc.}}, \omega_{\mathrm{det.}})} \tag{2.1}$$

where $\mathrm{P}(\omega_{\mathrm{exc.}}, \omega_{\mathrm{det.}})$ is the spectral area that encloses the peak and is calculated at each $\omega_{\mathrm{det.}}$ in $\mathrm{P}(\omega_{\mathrm{exc.}}, \omega_{\mathrm{det.}})$. The $\mathrm{CLS}_{\mathrm{exc.}}$ is then extracted from a linear fit of the conditional averages of the peak intensity versus $\omega_{\mathrm{det.}}$.[80] The CLS is a dynamical quantity and is calculated as a function of waiting time. To understand how energy transfer manifests in the CLS, we return to the model. Shown in Figure 2.3d and 2.3f are the $\mathrm{CLS}_{\mathrm{exc.}}$ of the lower frequency ESA quartet. The oscillatory behavior of the CLSs is striking and results from $|\mathrm{B}\rangle$ to $|\mathrm{A}\rangle$ transfer, made unmistakable by the fact that the oscillation frequency is equal to the energy gap between these two excitonic states. Using the model ESAs C and C′ as an example, the frequency relationships between this pair of CLSs can be more clearly evaluated by calculating the magnitude of the cross-power spectrum, given by the magnitude of the conjugate Fourier transform of one CLS multiplied by the Fourier transform of the other (Figure 2.3e), where by taking the magnitude, only frequency relationships are retained. The cross-power spectrum of the C and C′ CLSs demonstrate that these features share a common frequency of 245 cm^{-1} ($|\mathrm{B}\rangle$ to $|\mathrm{A}\rangle$ energy gap). It is worth noting here that the CLS has one major advantage in characterizing energy transfer because, as we have shown, it is free of the population dynamics that greatly complicate cross-peak amplitudes. Therefore, when applied to electronically coupled systems, the CLS is an electronic/vibronic coherence-specific measurement. Turning back to LHCII, Figure 2.4 compares the $\mathrm{CLS}_{\mathrm{exc.}}$ dynamics of several spectral features. The $\mathrm{CLS}_{\mathrm{exc.}}$ dynamics of each feature clearly exhibit long-lived (>700 fs), strongly oscillatory correlations between the electronic and nuclear DOF—a signature of EET in 2DEV spectroscopy. LHCII, obviously a far more complicated system than the heterodimer model, has an abundance of EET pathways and energy gaps, which translates

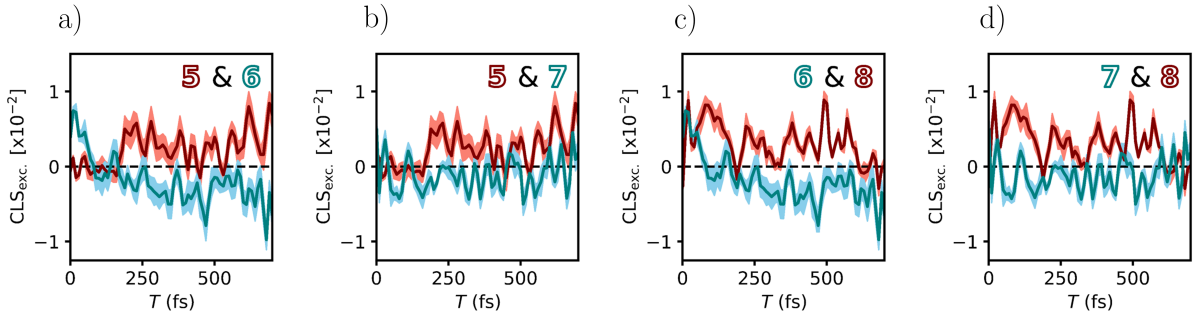

Figure 2.4: Time domain center line slope (CLS) dynamics along the excitation axis of features five through eight. Pairings have been made to emphasize the striking complementary behavior. The pairs of features shown are a) five and six, b) five and seven, c) six and eight, and d) seven and eight. The CLSs are colored according to the peak labels in the top right corner of each plot. Shaded light red or blue regions around each CLS indicate the standard error from the linear fits used to calculate the $\mathrm{CLS}_{\mathrm{exc.}}$.

directly to the presence of many oscillatory frequencies in the CLS dynamics. By simultaneously taking advantage of 1) the sensitivity of the CLS to EET, 2) a spectrally resolved excitation axis (the E in 2DEV), 3) the high spectral resolution along the detection axis (the V in 2DEV), 4) the observation of EET-driven intensity beats in the ESA features, and 5) the fact that the probed modes will not be modulated by purely vibrational coherences, the origin of the oscillatory features can be unambiguously determined.

Assignments and Discussion of Oscillatory Frequencies

We will now demonstrate how to extract information pertaining to the specific excitonic levels involved in the EET process. Starting with the model, by taking slices along the excitation axis at a detection frequency of 1555 cm^{-1} (through ESAs C and C′), and then performing a Fourier transform along the waiting time, an intensity beat frequency map can be created (Figure 2.3g). In the beat frequency map are two peaks, each with a beat frequency of 245 cm^{-1}, at the A and B band excitation frequencies. This same frequency appears in the cross-power spectrum of the corresponding C and C′ CLSs (Figure 2.3f) and in both cases it appears as a result of EET between $|\mathrm{B}\rangle$ and $|\mathrm{A}\rangle$. However, if we did not already know the origin of the oscillatory frequency, by observing it in the cross-power spectrum between C and C′, we would learn that it originates from EET. To facilitate an assignment of the specific states involved, we would next look for the excitation frequencies in the intensity beat map of C and C′ that have an energy gap equal to that oscillatory frequency. In 2DEV spectra, those excitation frequencies are the origin of the oscillatory feature. This procedure can be applied to the experimental 2DEV spectra of LHCII (particularly using ESAs seven

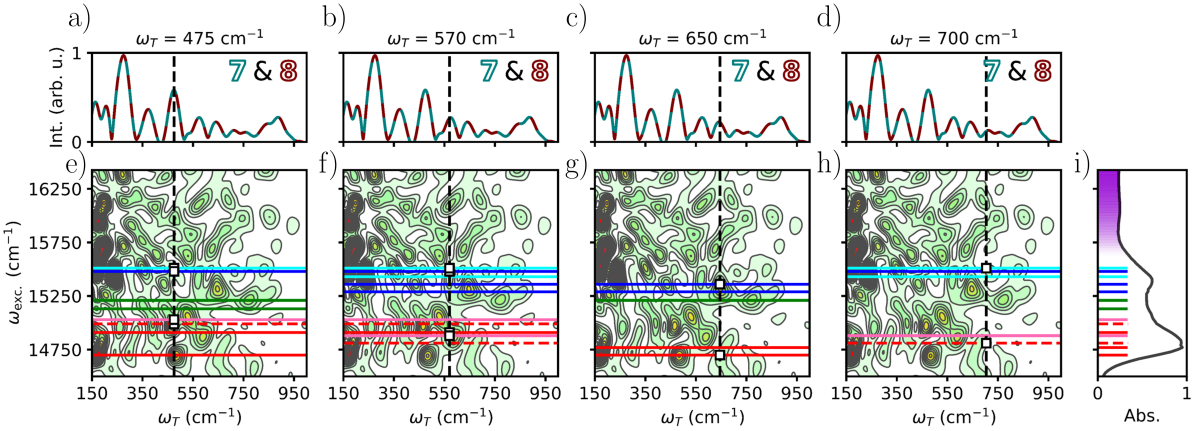

Figure 2.5: a)-d) Magnitude of the cross-power spectrum between the $CLS_{exc.}$ of excited state absorption (ESA) seven and of ESA eight (peaks in the cross-power spectrum indicate shared frequencies). e)-h) Power spectrum along the excitation axis at a detection frequency of 1590 cm^{-1} (through ESAs seven and eight, i.e. a Fourier transform of Figure 2.6). Only peaks that survived the noise floor were plotted in e)-f) such that contour levels are drawn in 4% intervals starting from the top of the noise floor. The contour levels indicate peak intensity, where intensity is shown to increase as the colormap changes from green to red. Vertical dashed black lines indicate certain beat frequencies of interest: 475 cm^{-1}, 570 cm^{-1}, 650 cm^{-1}, and 700 cm^{-1}. Horizontal lines in e)-h) highlight excitonic states (colored according to Figure 2.1) that fall along the beat frequencies of interest—the most important intersection points are accentuated by the white squares. i) For clarity, the linear absorption spectrum of LHCII at 77 K is shown along with the excitonic states detailed in Figure 2.1.

and eight), in order to assign the origin of oscillatory features (Figure 2.5). In our analysis below, we have chosen to focus on the 475-700 cm^{-1} region because towards the lower beat frequency region, the concurrent loss of frequency resolution and large number of closely spaced excitonic states makes explicit assignment of these beats difficult. Therefore, the oscillatory frequencies that will be discussed are 475 cm^{-1}, 570 cm^{-1}, 650 cm^{-1}, and 700 cm^{-1} (marked by vertical dashed lines in Figure 2.5), which have been assigned to EET between excitonic states of mainly Chl *a* character and states of mainly Chl *b* character. To make more site-specific assignments of the origins of these beats, the energy levels from Figure 2.1b (color coded to match) were overlaid on the intensity beat map. For example, the beat frequency of 650 cm^{-1} (Figure 2.5c and 2.5g) is shared by excitation frequencies of ∼15360 cm^{-1} (b601′-b608-b609) and ∼14700 cm^{-1} (a610-a611-a612), which have an energy gap of 660 cm^{-1}. This indicates that the beat frequency of 650 cm^{-1}, found in both the peak intensity and CLS dynamics, originates from b601′-b608-b609 → a610-a611-a612 transfer. However, unlike the model, also evident in the beat frequency map is the participation of excitation

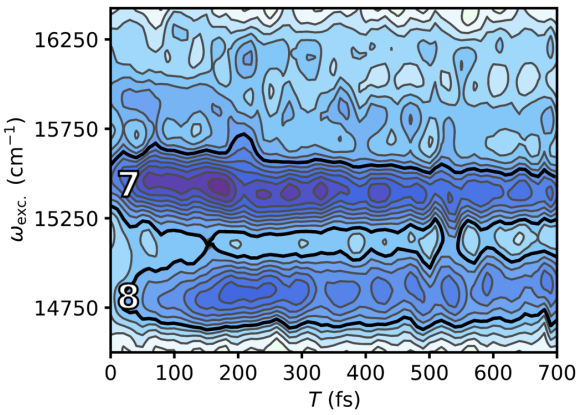

Figure 2.6: Spectral evolution along the excitation axis through excited state absorptions seven and eight, at a detection frequency of 1590 cm^{-1}, plotted as a function of waiting time. The colormap used here is identical to that in Figure 2.2.

frequencies in addition to those that have an energy gap matching the beat frequency. This is an indication that other states are involved in that particular energy transfer process. For example, there is evidence for the participation of higher-lying vibronic states, which have already been established as energetically-connected to the lower-lying Chl states. The beat frequency of 650 cm^{-1} appears at the higher vibronic level excitation frequencies as a result of these states rapidly populating the lower-lying b601′-b608-b609 state that then undergoes b601′-b608-b609 → a610-a611-a612 transfer. Additionally, the presence of other excitation frequencies that nearly match those in Figure 2.1b result from the complexity of the energetic landscape of LHCII—in addition to transfer between excitonic states of Chl *b* character to those of mainly Chl *a* character, intradimer, intratrimer, dimer to trimer, and dimer to dimer Chl *a* to Chl *a* or Chl *b* to Chl *b* energy transfer can occur.[50, 91] Through the same analysis, the beat frequency of 700 cm^{-1} (Figure 2.5d and 2.5h), common to excitation frequencies of ∼14810 cm^{-1} (a602-a603) and ∼15510 cm^{-1} (b606-b607), is assigned to b606-b607 → a602-a603 transfer. Lower frequency beats, 475 cm^{-1} (Figure 2.5a and 2.5e) and 570 cm^{-1} (Figure 2.5b and 2.5f), are more difficult to assign due to the participation of many excitation frequencies, but 475 cm^{-1} is a compelling candidate for either b606-b607 → a613-a614 or b601′-b608-b609 → a602-a603 transfer and 570 cm^{-1} for either b601′-b608-b609 → a610-a611-a612 or b601′-b608-b609/b606-b607 → a613-a614 transfer.

While the model successfully accounts for many of the features in the 2DEV spectra of an electronically coupled system (including the emergence of ESA quartets, as well as peak amplitudes and CLSs that oscillate at the frequency of the excitonic energy gaps), it is still an enormous simplification of the actual spectrum of LHCII. The full understanding

of electronic-vibrational dynamics is nontrivial and would require the inclusion of multiple vibrational DOF. This is clearly evident as demonstrated in Figure 2.6, which shows the spectral evolution of ESAs seven and eight along the excitation axis (where a Fourier transform along the waiting time would create the intensity beat map introduced earlier in Figure 2.5e-h). Upon inspection of Figure 2.6, spectral modulation of ESAs seven and eight can be observed. The oscillatory features at the blue edge of eight are in phase with those at the red edge of seven and nearly completely out of phase with those at the blue edge of seven. Similar behavior is seen if slices are taken along the excitation axis through peaks five and six. The previous observation of this type of spectral modulation by Prall et al. in a metal bridged phthalocyanine dimer was only accurately modeled by allowing for a nuclear modulation of the energies and interaction between participating electronic states, or in other words, by incorporating non-Condon effects, rather than simpler wavepacket dynamics.[92] The mechanism behind this type of behavior is driven by an opposite dependence of two electronic states on a common nuclear coordinate, as well as a nuclear dependence on the coupling between the two states. The observation of the spectral modulation effects depicted in Figure 2.6 suggests a significant degree of mixing between the electronic and nuclear DOF in LHCII and inspection of Table 2 in Ref. [93] shows that Chl *a* does indeed possess vibrations of very similar frequencies to those observed here and that all those observed have reasonable Huang-Rhys factors, making their likely involvement in mixing Chl *a* and *b* levels stronger.

2.3 Conclusion

2DEV spectroscopy provides a powerful way to untangle the connection between congested electronic spectra and complex ultrafast dynamics, such as EET. The connection of oscillatory features to specific excitation wavelengths allows their assignment to specific site states in LHCII, enabling a mapping of evolution in energy space to that in physical space. Our analysis reveals the critical role of the nuclear DOF in facilitating ultrafast energy transfer over moderately large energy gaps. In order to fully understand the role of non-Condon effects in photosynthetic light-harvesting, the manifestation of these effects in this newly developed technique will need to be developed, however, this chapter provides an important framework for elucidating the actual mechanistic role of vibronic interactions in these systems.

2.4 Experimental Methods

Sample Preparation

The isolation of thylakoid membranes was performed by using sucrose cushion[94] as described below. Deveined leaves were homogenized in 25 mM Tricine-KOH (pH 7.8), 400 mM NaCl, 2 mM $MgCl_2$, 0.2 mM benzamidine, and 1 mM ε-aminocaproic acid at 4 °C

using a Waring blender for 30 s with max speed. The homogenate was filtrated through 4 layers of Miracloth, and the filtrate was centrifuged at 27000 × g for 10 min at 4 °C. The pellet was resuspended in 25 mM Tricine-KOH (pH 7.8), 150 mM NaCl, 5 mM $MgCl_2$, 0.2 mM benzamidine, and 1 mM ε-aminocaproic acid. The suspension was loaded on sucrose cushion containing 1.3 M sucrose with 25 mM Tricine-KOH (pH 7.8), 15 mM NaCl, and 5 mM $MgCl_2$, which was overlaid on 1.8 M sucrose with 25 mM Tricine-KOH (pH 7.8), 15 mM NaCl, and 5 mM $MgCl_2$, and centrifuged at 131500 × g for 30 min at 4 °C using a SW 32 Ti rotor (Beckman Coulter). Thylakoid membranes sedimented in 1.3 M sucrose cushion were collected and washed with 25 mM Tricine-KOH (pH 7.8), 15 mM NaCl, and 5 mM $MgCl_2$, and centrifuged at 27000 × g for 15 min at 4 °C. The pellet was resuspended in 25 mM Tricine-KOH (pH 7.8), 0.4 M sucrose, 15 mM NaCl, and 5 mM $MgCl_2$, and centrifuged at 27000 × g for 10 min at 4 °C. The pellet was resuspended and used as purified thylakoid membranes.

The purified thylakoid membranes were resuspended in 25 mM HEPES-NaOH (pH 7.8) and centrifuged at 15300 × g for 10 min at 4 °C. The pellet was resuspended in 25 mM HEPES-NaOH (pH 7.8) at 2.0 mg Chl/mL and solubilized with 4% (w/v) n-dodecyl-α-D-maltoside (α-DM; Anatrace) for 30 min with gentle agitation on ice. The unsolubilized membranes were removed by centrifuging at 21000 × g for 5 min at 4 °C. The supernatant was filtrated through 0.22 μm filter using Durapore Ultrafree filters centrifuged at 10000 × g for 3 min at 4 °C. The 200 μL of filtered solubilized fraction was used for gel filtration chromatography using the ÄKTAmicro chromatography system with a Superdex 200 Increase 10/300 GL column (GE Healthcare) equilibrated with 25 mM HEPES-NaOH (pH 7.8) and 0.03% (w/v) α-DM at room temperature. The flow rate was 0.9 mL/min. The proteins were detected at 280 nm absorbance. The fraction separated from 10.0 to 10.3 mL contained trimeric LHCII proteins.

For the experiments, the maximum optical density of the LHCII sample in the visible was ∼0.9 with a path length of 200 μm at 77 K (Optistate DN2, Oxford Instruments).

Spectroscopic Measurements

Below we describe the 2DEV experimental setup[2] used in this chapter. A Ti:Sapphire oscillator and regenerative amplifier (Vitara-S, Legend Elite, Coherent) pumped a home-built visible non-collinear optical parametric amplifier (NOPA) and mid-IR OPA. The visible pump spectrum was centered at ∼15565 cm^{-1} and spanned 14350∼16775 cm^{-1}. As the experiments were performed in a partially collinear pump-probe geometry, a pulse shaper (Dazzler, Fastlite) was employed to generate the visible pump pulse pair and then control the relative initial time delay, $t_{exc.}$, (scanned from 0-100 fs in ∼2.4 fs steps) and phase (the desired 2DEV signal was isolated with a 3×1 phase cycling scheme) between the pair.[45, 46] The pulse shaper was also used to compress the visible pulses (∼10 fs) and set the pump energy (∼270 nJ). The visible pulses were focused into the sample to a spot size of 250 μm with a $f = 25$ cm silver coated 90° off-axis parabolic mirror. To remove the optical frequency

of the pump, the data was collected in the fully rotated frame with respect to $t_{\text{exc.}}$. A Fourier transform was performed along $t_{\text{exc.}}$ to recover the excitation dimension of the spectra.

The mid-IR OPA produced an IR probe spectrum centered at ∼1620 cm^{-1}. To account for shot-to-shot energy fluctuations in the IR, the probe beam was normalized by a reference. The IR probe and reference pulses had an energy of ∼100 nJ and duration of ∼50 fs. Both IR pulses were focused into the sample to a spot size of 200 μm with a $f = 15$ cm gold coated 90° off-axis parabolic mirror. After the sample, the IR probe and reference were dispersed with a spectrometer (Triax 180, Horiba) onto a dual-array 64 element HgCdTe detector (Infrared Systems Development).

Except for the NOPA, the entire setup was purged with dry air, free of CO_2 (Perkins Balston FTIR Purge Gas Generator).

Data Processing

To emphasize the lower frequency oscillations for presentation in the text, the data in Figure 2.4-2.6 was subjected to a Savitzky-Golay filter[95] (essentially a ∼1200 cm^{-1} cutoff filter). An unfiltered version of Figure 2.5 is provided in the Appendix A.3, which shows that filtering has no impact on the results discussed in this chapter.

Chapter 3

The Role of Mixed Vibronic Q_y-Q_x States in Green Light Absorption of LHCII

3.1 Introduction

The fact that leaves are green and the majority of spectroscopic studies on optically active pigment-protein complexes (PPCs) are performed on in vitro systems has led to the misunderstanding that green light has little efficacy on photosynthesis. However, on the contrary, it has been shown by Terashima et al. that for in vivo systems, green light in the presence of strong illumination actually has the ability to drive photosynthesis more efficiently than red light.[7] In this chapter, we explore the states absorbing green light and their dynamics in light-harvesting complex II (LHCII).

Overall, the success of the photosynthetic apparatus begins with the design and function of the PPCs which harvest solar light, the primary step in photosynthesis.[1] In green plants and algae, LHCII serves as the major antenna complex, which transfers excitation energy towards the photosynthetic reaction center.[1] LHCII, in trimeric form as it is generally found, is composed of 24 chlorophyll (Chl) *a*, 18 Chl *b*, and 12 carotenoid (Car) pigments.[49] Spatially, these pigments are held within the protein environment in such a way that electrostatic interactions between nearby pigments promote the formation of delocalized excitonic states, leading to intricately tuned spatial and energetic landscapes. Together, these pigments, preferentially arranged over billions of years of evolution[96, 97], harvest light with a quantum efficiency of near unity.[1]

Understanding how the excitation energy transfer (EET) dynamics of LHCII are mapped across the spatial and energetic degrees of freedom (DOF) of the complex has been the focus of significant, sustained attention.[3, 5, 50, 52–57, 91, 98–104] This effort has increasingly led to a deeper understanding of Chl-Chl interactions, which predominately manifest energetically in the red edge of the LHCII absorption spectrum (excitonic Q_y bands of mainly

Chl *a* and Chl *b* character give rise to the two peaks centered around 14800 cm^{-1} and 15500 cm^{-1} in Figure 3.1a, respectively).[52] Recent work has also more closely considered the role of Car-Chl interactions, which arise largely at higher energies, i.e. at the blue edge of the LHCII absorption spectrum (peak shoulder rising around 19000 cm^{-1} in Figure 3.1a).[101, 102] However, over 3000 cm^{-1} of the spectrum, namely the Chl vibronic Q_y-Q_x region energetically connecting the Chl Q_y states and the Car states[105], remains little studied. This is not particularly surprising, despite the estimated integrated absorption of the vibronic Q_y-Q_x region being nearly 75% of that of the Q_y region in LHCII, because these states have low oscillator strength and are highly mixed in multiple ways, thus making them challenging to study. Namely, the states of LHCII that span this spectral region have varying degrees of i) mixed inter-pigment electronic character, ii) mixed intra-pigment electronic character (Q_y/Q_x character), and iii) vibronic character (mixed electronic-vibrational states). The understated importance of the vibronic Q_y-Q_x states in light-harvesting is also perpetuated by the context in which the complex is typically studied—in vitro—rather than in vivo. In fact, previous work has shown that absorption of the vibronic Q_y-Q_x states of Chl is enhanced in leaves relative to isolated LHCII, as well as other minor PPCs, to such an extent that the spectrum is essentially uniform over the full photosynthetically active region (PAR).[8–10, 106] This phenomenon, termed the detour effect, is caused by the highly light scattering environment within the leaf which effectively increases the optical path length of incident green light, therefore, increasing the likelihood of absorption.[9, 106] The result is that such a significant increase in the light-harvesting contribution of the vibronic Q_y-Q_x region occurs such that these states rival the contribution from the Q_y electronic region.[7, 106] Through an analogous mechanism, yet on even larger scale, green light is also crucial in stimulating photosynthesis in the lower portions of the canopy where red and blue light have been filtered out by the top layers.[106] It is worth noting here that this comparison is in terms of quantum efficiency rather than overall energy efficiency.[107, 108] This is to say that the additional energy over the Q_y region contained by the photons absorbed by the vibronic Q_y-Q_x region is unable to be utilized by photosynthesis because the energy required to drive charge separation in the photosynthetic reaction center is equivalent to that of a red, rather than green, photon.[108] However, in vivo, green light drives photosynthesis more successfully in chloroplasts *throughout* the leaf and plant (despite diminished energy efficiency). This is because of the improved quantum efficiency of the vibronic Q_y-Q_x states due to the detour effect and the fact that the photons absorbed by these states ultimately penetrate deeper into the mesophyll of a given leaf and the canopy of a whole plant than do the red photons, which are more readily absorbed by the Q_y electronic states arising from PPCs residing nearer to the surface of the leaf. However, the lack of spectral assignments or insight into the EET dynamics of the Chl vibronic Q_y-Q_x states has long hindered a complete understanding of their in role photosynthetic light-harvesting.

In this chapter, we utilize recent advances in multidimensional spectroscopy, namely the advent of two-dimensional electronic-vibrational (2DEV) spectroscopy[2], to study the origin and involvement of these highly mixed states—inaccessible to more conventional spectroscopies. A major advantage of this technique is the improved spectral resolution, afforded

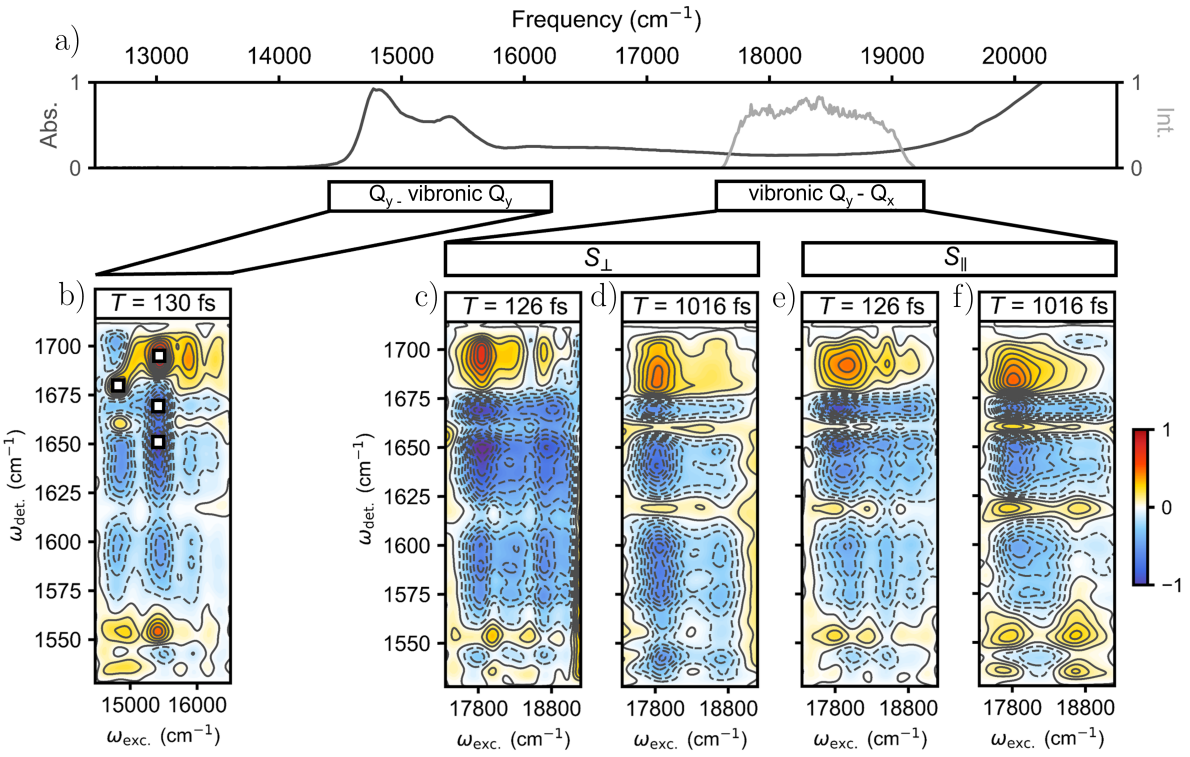

Figure 3.1: a) Linear absorption spectrum of LHCII at 77 K, along with the spectrum of the visible pump pulses employed in this chapter (light gray). b) Representative 2DEV spectrum of the Q_y band of LHCII at $T = 130$ fs, prior to significant Chl $b \rightarrow$ Chl a transfer. Throughout, ground state bleach (GSB) features are positive (red) features and excited state absorption (ESA) features are negative (blue) features. Four regions have been marked in the spectra with white squares—one GSB in the predominately Chl a excitonic band (centered around 14800 cm^{-1}) and one GSB and two ESA in the predominately Chl b excitonic band (centered around 15500 cm^{-1}). c)-d) Perpendicular PA 2DEV spectra of the vibronic Q_y-Q_x bands of LHCII at 77 K at waiting times of $T = 126$ fs and 1016 fs. e)-f) Parallel PA 2DEV spectra of the vibronic Q_y-Q_x bands of LHCII at 77 K at waiting times of $T = 126$ fs and 1016 fs.

by infrared (IR) detection, which has successfully allowed for insight into ultrafast energy transfer, charge transfer, and proton transfer dynamics.[3, 20, 47, 53, 84, 109] IR detection also inherently makes this technique especially sensitive to the mixing of vibronic states because such mixing significantly alters vibrational transitions moments. Additionally, the further sensitivity provided by polarization-dependent 2DEV spectroscopy has been demonstrated in the spectral assignments of monomeric Chl a and b[81], as well as in unveiling the

role of vibronic coupling in a solar cell dye.[84]

Here, building on previous applications of this technique, particularly to LHCII[3, 53], we apply polarization-dependent 2DEV spectroscopy to study the origin of the highest-lying mixed vibronic Q_y-Q_x states (spanning 520-570 nm) arising from Chl-Chl interactions in LHCII, in order to gain mechanistic insight into their function in photosynthetic light-harvesting. In doing this, we present direct evidence that this spectral region is dominated by Chl *b* character, which together with previous in vivo studies indicates that Chl *b* enhances the ability of green plants and algae to harvest green light.[7–10] Following more definitive assignments, we discuss the role of these states in the EET dynamics of LHCII at 77 K. Namely, we show that relaxation from the higher-lying states of mainly Chl *b* character to the lower-lying Q_y states occurs on a timescale of <90 fs (within our instrument response function), demonstrating how mixing between the electronic and nuclear DOF of Chl *b* drives the ultrafast EET dynamics of LHCII and extends efficient light-harvesting throughout the PAR. Further, we find that relaxation from the $Q_x \rightarrow Q_y$ states of Chl *b* occurs on a timescale of ∼200 fs (based on the timescales of an oscillatory component associated directly with these states). Such a timescale for $Q_x \rightarrow Q_y$transfer in Chl *b* agrees well with recent theoretical work on monomeric Chl *b*[110], which suggests that the observed Q_x states arise from more highly localized Chl *b* pigments. The ability of polarization-dependent 2DEV spectroscopy to follow the pathways of energy flow for such highly mixed states of LHCII offers a direction towards a deeper understanding of photosynthetic light-harvesting across the solar spectrum.

3.2 Results and Discussion

2DEV spectroscopy, a two-color multidimensional spectroscopic experiment, features visible pump pulses that prepare an ensemble of electronic/vibronic states that evolve during the waiting time, T, and are tracked via an IR probe pulse.[2] The data is presented in the form of excitation frequency-detection frequency correlation plots that map how the electronic/vibronic states evolve with considerable frequency resolution—made possible by IR detection.

The 2DEV measurements were performed in two different polarization schemes—one in which the visible pump pair and IR probe were all vertically polarized, $S_V(\omega_{\text{exc.}}, T, \omega_{\text{det.}})$, and one in which the visible pump pair was horizontally polarized while the IR probe was vertically polarized, $S_H(\omega_{\text{exc.}}, T, \omega_{\text{det.}})$. These were combined to generate the perpendicular and parallel polarization-associated (PA) 2DEV spectra, given by[111, 112]

$$S_\perp(\omega_{\text{exc.}}, T, \omega_{\text{det.}}) = 3S_H(\omega_{\text{exc.}}, T, \omega_{\text{det.}}) - S_V(\omega_{\text{exc.}}, T, \omega_{\text{det.}}) \tag{3.1}$$

and

$$S_\parallel(\omega_{\text{exc.}}, T, \omega_{\text{det.}}) = 2S_V(\omega_{\text{exc.}}, T, \omega_{\text{det.}}) - S_H(\omega_{\text{exc.}}, T, \omega_{\text{det.}}), \tag{3.2}$$

respectively. The perpendicular or parallel distinction indicates the angle between the electronic transition dipole moment (TDM) of states initially populated by the visible pump pair

and the vibrational TDM of the probed mode on the states populated during the waiting time, T, that will be amplified in the respective PA spectra. As will be shown below, PA 2DEV spectra are particularly useful for separating the evolution of different states (e.g. states of Q_x or Q_y character) in highly congested, complex spectra.

Along with the linear absorption spectrum of LHCII (Figure 3.1a), Figure 3.1 shows a representative 2DEV spectrum obtained via exciting the Q_y bands (14350-16775 cm^{-1}) of LHCII (Figure 3.1b), discussed in detail in previous work[3, 53], along with PA 2DEV spectra of a portion of the vibronic Q_y-Q_x region (17545-19230 cm^{-1}) of the LHCII spectrum (Figure 3.1c-f). In the 2DEV spectrum of the Q_y bands of LHCII at $T = 130$ fs, multiple distinct bands along the excitation axis are evident. Bands centered around 14800 cm^{-1} and 15500 cm^{-1} correspond to the excitonic states of mainly Chl *a* and Chl *b* character, respectively, while the bands above 15600 cm^{-1} correspond to higher-lying vibronic Q_y transitions originating from mainly Chl *b*.[3, 53] It is clear from comparing the bands of mainly Chl *a* and Chl *b* character at $T = 130$ fs, prior to significant Chl *b* $\rightarrow$ Chl *a* transfer, that there are differences in the vibrational structure, as particular modes have predominately Chl *a* or *b* character.

Four distinct spectral regions have been marked in Figure 3.1b in order to assign and track the dynamics of the vibronic Q_y-Q_x region. Of the four detection frequencies of interest, two are ground state bleach (GSB) features (red, positive features), at 1680 cm^{-1} and 1690 cm^{-1}, assigned to Chl *a* and Chl *b*, respectively, and two are excited state absorption (ESA) features (blue, negative features). These two ESA features, at 1650 cm^{-1} and 1670 cm^{-1}, are notably dominant in the Chl *b* band. Previously, the ESA around 1650 cm^{-1} was assigned to have predominately Chl *b* character from more localized chromophores, supported by a singular value decomposition analysis that revealed that this region of the spectrum decayed on a timescale of a few picoseconds, a characteristic timescale of transfer from more localized Chl *b* intermediate states to Chl *a*.[53] Although an assignment for the feature at 1670 cm^{-1} was not totally conclusive, the spectral regions around 1650 cm^{-1} and 1670 cm^{-1} evolved on similar timescales and it is clearly a dominant ESA in the band of mainly Chl *b* origin, suggesting that the 1670 cm^{-1} band also has significant character from more localized Chl *b* states.

A comparison of the predominantly Chl *a* and Chl *b* bands in the Q_y region (Figure 3.1b) versus the PA 2DEV spectra in the vibronic Q_y-Q_x region at $T = 126$ fs (Figure 3.1c and 3.1e) shows that across the spectrum, detection frequencies assigned either completely or predominantly to Chl *b*—the GSB at 1690 cm^{-1} and ESAs at 1650 cm^{-1} and 1670 cm^{-1}—dominate the spectral structure along the detection axis. After about a picosecond (Figure 3.1d and 3.1f), there is noticeable decay of these three peaks, as a peak at 1680 cm^{-1}, the GSB of Chl *a*, grows in. Immediately, the dominance of Chl *b* excited states in this region of the LHCII spectrum is clearly demonstrated.

In order to gain a more quantitative understanding of the composition of this region of the LHCII absorption spectrum (Chl *a* versus Chl *b* character and Q_y versus Q_x character), it is helpful to view the PA 2DEV spectra in a different way. The best visualization of the dynamics is in the form of a plot of excitation frequency versus waiting time at a fixed detection

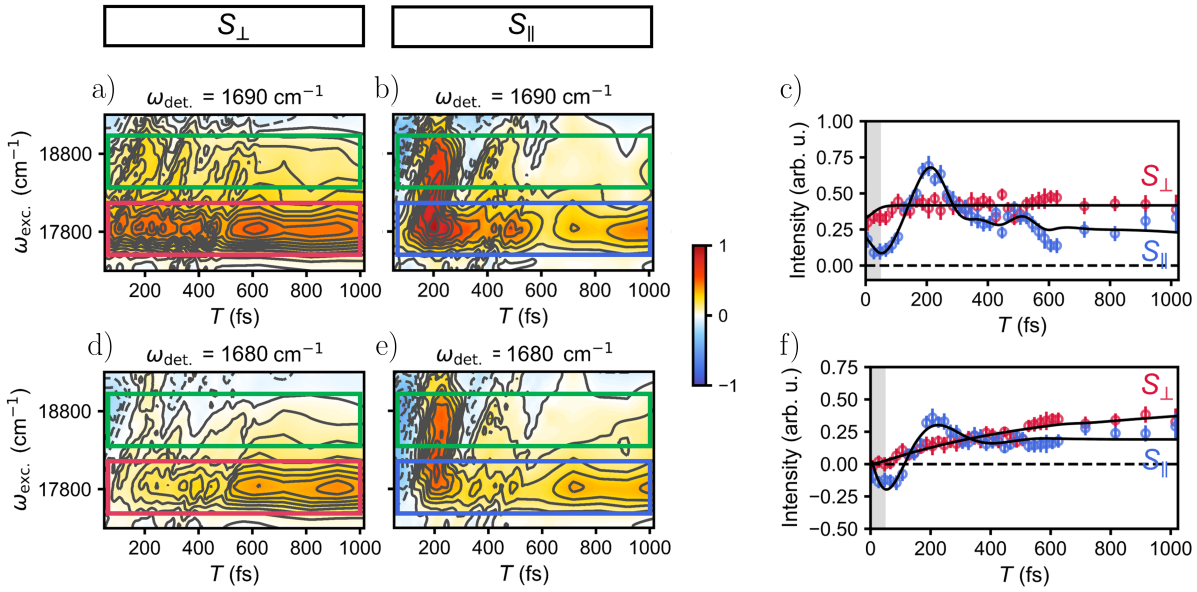

Figure 3.2: a)-b) Perpendicular and parallel PA spectral evolution as a function of waiting time along the excitation axis at a fixed detection frequency of 1690 cm^{-1} (indicative of Chl *b* population). Ground state bleach features are positive (red) features and excited state absorption features are negative (blue) features. The frequency region centered around 17800 cm^{-1} is boxed in red for the perpendicular PA component ($S_\perp$) and blue for the parallel PA component ($S_\parallel$). Throughout, green boxes indicate the higher frequency region centered around 18700 cm^{-1}. c) Peak amplitude dynamics at a detection frequency of 1690 cm^{-1} along 17800 cm^{-1} (through the center of the corresponding boxed regions of the same color). Error bars indicate the estimated errors in the peak amplitude based on the standard deviation of the signal amplitude at each waiting time. The black lines indicate the fits of the peak amplitude dynamics (provided in Table B.1). The gray shaded region indicates the region where pulse overlap effects occur. d)-e) Same as described for a)-b) except at a detection frequency of 1680 cm^{-1} (indicative of Chl *a* population). f) Same as c) except at a detection frequency of 1680 cm^{-1}.

frequency (Figure 3.2a, 3.2b, 3.2d, and 3.2e). To construct these plots, slices through the 2D spectra will be taken at a fixed detection frequency along the excitation axis and plotted as a function of the waiting time. The benefits of this visualization are twofold. First, setting the detection regions specific to either Chl *a* or Chl *b* modes will allow for a high degree of spectral sensitivity, facilitating the assignment of pigment contributions in this region. Secondly, if the detection frequency is fixed on a highly localized mode, as will be done here, then this mode serves as an anchor point to assess the relative orientation between the TDM of this vibrational mode and the TDM of the populated excited state(s). To see how this

can be used to interrogate the electronic character of this region, we will discuss how various electronic state configurations manifest in the set of $S_{\parallel}$ and $S_{\perp}$ spectra. The relevant cases that we will consider are 1) a system containing coupled electronic states and 2) and system containing non-interacting electronic states. In the first case, the electronic TDMs are inherently complementary as a result of the electronic mixing between the states. Therefore, even though one PA component selectively enhances the signal originating from one mixed electronic state and suppresses that from the other, while the opposite holds for the other PA component (depending on the angle between the electronic TDMs and the TDM of the localized vibrational mode), the mixing between electronic states essentially ensures complementary dynamics in the two PA components. By complementary we mean that the parallel and perpendicular PA components inherently contain aspects of the same information. This phenomenon arises in principle for exactly the same reason as the observation of oscillatory anisotropy signals driven by energy transfer in anthracene dimers, for example.[113] But, what if the $S_{\parallel}$ and $S_{\perp}$ spectra are not complementary in nature, but rather contain entirely unrelated information? In order to understand such a counterintuitive concept, we need to consider the second system—one which contains non-interacting electronic states. In this scenario, such non-complementary behavior arises if the non-interacting electronic states have nearly orthogonal TDMs which themselves fall either parallel or perpendicular to the TDM of the localized detection mode. Importantly, these electronic states must belong to the same molecule to ensure that the vibrational mode remains as a fixed point of reference. For example, now we see how the signals specific to the electronic state with a TDM parallel to the TDM of the localized mode become selectively isolated in the parallel PA component, while completely suppressed in the orthogonal PA component (which in turn isolates the other electronic state). It is this second case that is relevant to this chapter where we see that the $S_{\parallel}$ and $S_{\perp}$ spectra do not appear complementary in nature at all. Here, because the electronic states are non-interacting, the dynamics associated with each state are "locked" into its associated PA component and therefore no complementary dynamics will be observed in the two orthogonal PA components. As we will discuss, this case, defined generally above, is satisfied by the Q_y and Q_x states of Chl and can be utilized to very effectively determine the character and isolate the dynamics of various electronic states in highly congested spectral regions.

Specifically, to assess the character of this region, the GSB detection frequencies will be set to 1690 cm^{-1} (Figure 3.2a and 3.2b) and 1680 cm^{-1} (Figure 3.2d and 3.2e), to track Chl *b* and Chl *a* character, respectively. The analysis here will focus on the region centered around 17800 cm^{-1} (Figure 3.2; highlighted by red and blue boxes in $S_{\perp}$ and $S_{\parallel}$, respectively), but much of what is found here can be easily extrapolated to the higher frequency around 18700 cm^{-1} (Figure 3.2; highlighted by green boxes). Monitoring the peak amplitude of the Chl *b* GSB evolution around 17800 cm^{-1} reveals the immediate appearance of this feature in both $S_{\perp}$ and $S_{\parallel}$. This is shown more explicitly in Figure 3.2c, which shows the evolution of the Chl *b* GSB peak amplitude at an excitation frequency of 17800 cm^{-1}. Prominent in Figure 3.2a-c is a remarkable overall lack of complementarity—indicating that these signals arise from approximately orthogonal, non-interacting electronic states. This observation is partic-

ularly notable because the electronic structure of Chl in the Q-band region, described using the Gouterman model[114], contains contributions from the both the Q_y (S_1) and Q_x (S_2) electronic transitions which have nearly orthogonal polarization directions.[115] Therefore, these PA 2DEV spectra are effectively isolating two distinct, overlapping sets of features arising from the vibronic Q_y and Q_x states of Chl *b*. The assignments of which PA 2DEV spectra correspond to which electronic states is reserved for later in the discussion. To confirm the dominance of Chl *b*, analysis of the spectral evolution at the Chl *a* GSB detection frequency, 1680 cm^{-1}, reveals that in both the $S_{\parallel}$ and $S_{\perp}$ spectra (Figure 3.2d and 3.2e), there is essentially no Chl *a* character initially. This is more clearly demonstrated in Figure 3.2f which shows that both the parallel and perpendicular PA components of the Chl *a* GSB peak amplitude along 17800 cm^{-1} have initial intensities of zero. In addition, a clear rise can be observed in the perpendicular component with a timescale of 600±200 fs, which agrees well with other previously observed Chl *b* $\rightarrow$ Chl *a* transfer timescales.[54, 57, 91] A more in-depth analysis of the parallel component for this feature of Chl *a* is difficult as there is a degree of spectral congestion even with IR detection. For example, there is an overlapping negative oscillatory ESA signal in this same detection region clearly visible in the higher frequency region in Figure 3.2e which obscures the dynamics of this band. This overlap makes it difficult to determine if there is some small amount of Chl *a* character in this region or if there is some rapid Chl *b* $\rightarrow$ Chl *a* transfer in less than 200 fs. The clearly observed oscillatory behavior in the parallel component of the 2DEV spectra will be discussed below, in addition to how it facilitates assignments of Chl *b* Q_x versus vibronic Q_y character in the PA spectra.

Figure 3.3a, 3.3b, 3.3d, and 3.3e present the evolution of the excited state frequency distributions along the excitation axis as a function of waiting time at fixed detection frequencies of 1670 cm^{-1} and 1650 cm^{-1}. The focus of the ESA analysis will be at a detection frequency of 1670 cm^{-1}, rather than at 1650 cm^{-1}, because there is less spectral congestion in this region, although the evolution between these two detection frequencies is nearly identical (Figure 3.3a and 3.3d versus Figure 3.3b and 3.3e). We note that this is further evidence that these two ESAs have similar origins, i.e. a large degree of character from Chl *b* pigments likely only weakly coupled to neighboring chromophores. For the analysis, focus will be on the spectral region around 17800 cm^{-1} because the energy levels in this region clearly participate more strongly in facilitating transfer to Chl *a* and therefore play a more significant role in the dynamics. Additionally, analysis of the 17800 cm^{-1} region is free of the overlapping positive feature present in the 18700 cm^{-1} band around 200 fs which likely belongs to a different, briefly populated excited state. For both of these ESAs, the parallel PA spectra have a significant oscillatory component, as was also seen for the GSB features, and is largely absent in the perpendicular PA spectra for all four detection frequencies. This suggests that the underlying origin of these features is the same, i.e. $S_{\parallel}$ selectively isolates a specific electronic state responsible for both the GSB and ESA features. This may also indicate that these features in part arise from the formyl group specific to Chl *b*, as then the TDM of these excited state vibrational modes should have a similar orientation to the ground state vibrational mode of Chl *b* (also related to the formyl group). Unfortunately, ex-

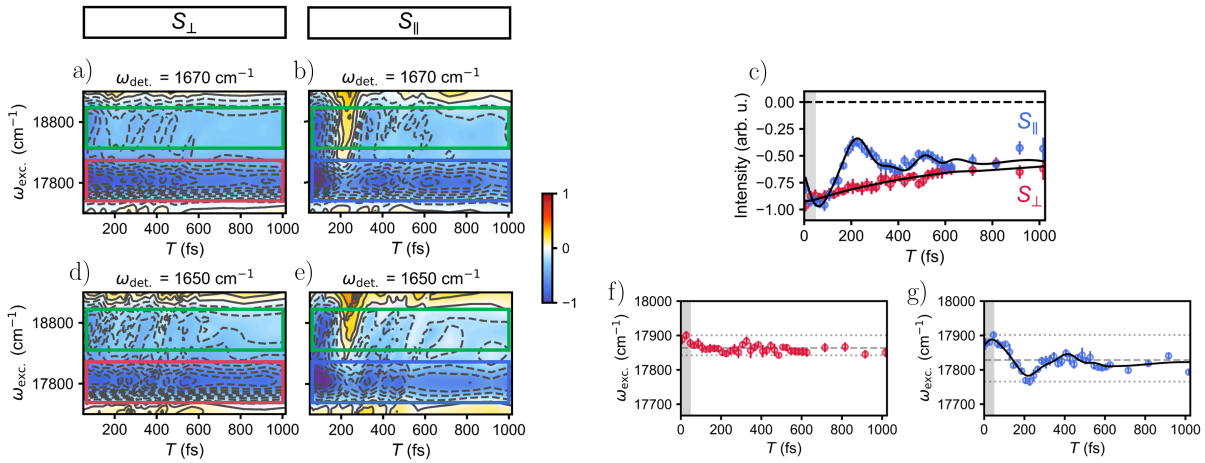

Figure 3.3: a)-b) Perpendicular and parallel PA spectral evolution as a function of waiting time along the excitation axis at a fixed detection frequency of 1670 cm^{-1}. Ground state bleach features are positive (red) features and excited state absorption features are negative (blue) features. The frequency region centered around 17800 cm^{-1} is boxed in red for the perpendicular PA component ($S_\perp$) and blue for the parallel PA component ($S_\parallel$). Throughout, green boxes indicate the higher frequency region centered around 18700 cm^{-1}. c) Peak amplitude dynamics at a detection frequency of 1650 cm^{-1} along 17800 cm^{-1} (through the center of the corresponding boxed regions of the same color). Error bars indicate the estimated errors in the peak amplitude based on the standard deviation of the signal amplitude at each waiting time. The black lines indicate the fits of the peak amplitude dynamics (provided in Table B.1). The gray shaded region indicates the region where pulse overlap effects occur. d)-e) Same as described for a)-b) except at a detection frequency of 1650 cm^{-1}. f)-g) Evolution of excited state frequency distribution of the perpendicular and parallel PA spectra, respectively, at a detection frequency of 1670 cm^{-1}. The error bars (1σ intervals) indicate the uncertainty in the position of the peak maximum, determined by a Gaussian fit of the peak in the range provided in the y-axis of the plot. The dashed gray line indicates the average center frequency, while dotted gray lines indicate the minimum and maximum frequencies. Again, the gray shaded region indicates the region where pulse overlap effects occur. The black line in g) indicates the fit of the evolution of the frequency distribution (provided in Table B.2).

plicit assignments of these vibrational coordinates are not yet possible due to the complexity of the electronic structure problem for this multichromophoric system. However, we hope that these spectroscopic observables will provide future guidance for more robust models of photosynthetic light-harvesting in green plants and algae. Experimentally, the attribution of the origin of the oscillatory signal to a specific electronic state of Chl *b* is further supported by the fact that not only do the ESA and GSB both show oscillations in $S_\parallel$, but a fit of the

ESA at 1670 cm^{-1} along 17800 cm^{-1} (Figure 3.3c; shown in blue) recovers frequencies of 106±5 cm^{-1} and 240±10 cm^{-1}, while a fit of the GSB recovers identical frequencies within error: 111±7 cm^{-1} and 240±20 cm^{-1} (error indicates 1σ interval, see Table B.1 for complete fit results). The finding of identical frequencies strongly indicates that $S_{\parallel}$ isolates the same electronic component responsible for both the GSB and ESA detection signals, especially because no such dynamics are observed in any of the perpendicular PA spectra.

Before discussing the origin of these oscillations and spectral composition of this region, we see that the amplitude of the 1670 cm^{-1} ESA along 17800 cm^{-1} in $S_{\perp}$ undergoes a monoexponential decay on a timescale of 600±200 fs (Figure 3.3c; shown in red), in agreement with the observed rise in the Chl *a* GSB. Again, this timescale falls within the range of observed Chl *b* → Chl *a* transfer. However, there is clearly a longer timescale component (>1 ps, beyond the duration of the experiment) to the ESA signal because the peak amplitude has yet to fully decay by one picosecond. This is as expected because this feature likely has a significant degree of character from more localized Chl *b* pigments which undergo Chl *b* → Chl *a* transfer on a timescale of a few picoseconds.[50]

To explain the oscillatory peak dynamics, a few possibilities emerge: 1) protein motion is modulating the distance between Chl pigments and therefore modulating the electronic coupling and TDM orientations, 2) rapid Chl *b* vibronic Q_y-Q_x → Chl *b* Q_y transfer occurs and is followed by energy transfer between the lower-lying Chl *a* and Chl *b* Q_y states, or 3) the oscillatory signal arises directly from the initially populated electronic states. The first option can be excluded immediately because if this oscillatory were to involve the protein environment, it would not have such a significant polarization dependence. This then leaves two options. The most straightforward way to distinguish between the two and verify the origin of this signal is to track how the optical frequency distribution of this region changes during the waiting time, which is essentially tracking the evolution of the excited state(s) in this region. Dynamical changes in the frequency distribution indicate that the excited state(s) are still populated, which would indicate that the dynamics being observed originate from the higher-lying states rather than from the lower-lying Q_y states. Figure 3.3g presents a plot of how the maximum peak position of the band centered around 17800 cm^{-1} in $S_{\parallel}$ evolves as a function of waiting time. The peak maximum as a function of waiting time was determined via fitting with a Gaussian function. It is evident that the frequency distribution changes *dynamically* along the waiting time. Actually, a fit of this peak evolution reveals oscillatory frequencies of 92±6 cm^{-1} and 240±20 cm^{-1} (error indicates 1σ interval, see Table B.2 for complete fit results), which are in agreement within error to those present in the peak amplitude. From the fits, the dominant 92±6 cm^{-1} frequency component was found to decay on a timescale of 250±50 fs, similar to the timescales of the same component in the ESA and GSB peak amplitudes (190±30 fs and 140±30 fs, respectively). As a control, we show the frequency distribution evolution for the same ESA feature in $S_{\perp}$ (Figure 3.3f). Clearly, no such oscillatory behavior is observed (just as none was observed in the peak amplitudes for this PA component) suggesting, again, that the states isolated in the $S_{\parallel}$ component exhibit distinct behavior. Overall, the lack of dynamics in the frequency distribution of the ESA feature in $S_{\perp}$ coupled with the observed monoexponential decay assigned to Chl *b* → Chl

a transfer indicates that ultrafast relaxation from these states to the lower-lying Chl *b* Q_y states occurs within our time resolution (90 fs).

We assign the character of the spectral features isolated in the $S_{\|}$ spectra of Chl *b* to the Q_x states. This assignment is based on the following:

1) the observed oscillations originate from a state in the region 17800-18500 cm^{-1}, which spans the expected range for the Q_x transition of Chl *b*[116],

2) the oscillatory behavior appears in both the GSB and ESA peaks isolated in the $S_{\|}$ spectra, which is distinct from the previously observed behavior of Q_y bands[3, 53],

3) this excitation persists in this state for ∼200 fs which is in agreement with recent theoretical work on $Q_x \rightarrow Q_y$ transfer in Chl *b*[110], yet is a timescale which is at odds with both our previous measurements involving the higher-lying vibronic Q_y states of Chl *b* and the observed dynamics of the $S_{\perp}$ spectra presented in this chapter where ultrafast transfer to the lower-lying Chl Q_y states occurs within 90 fs.[3]

Clearly, the $S_{\|}$ and $S_{\perp}$ spectra capture distinct states that are orthogonal and noninteracting, therefore, we assign the character of the spectral features isolated in the $S_{\perp}$ spectra of Chl to the vibronic Q_y states. Our assignments and corresponding timescales are summarized in Figure 3.4.

As a final comment regarding the assignments, we note that the agreement between the observed 200 fs timescale and the calculated timescale of internal conversion for Chl *b* is consistent with the fact that experimental evidence indicates that the states isolated in the $S_{\|}$ component are likely more localized states of Chl *b*. We would like to point out that, even though our data suggests that these features arise from more localized pigments, we do not rely on previous 2DEV spectroscopic experiments on monomeric Chls to facilitate assignments due to the sensitivity of the TDMs pigment-pigment and pigment-protein interactions. For example, it has been shown previously that even a change in the site energy of a dimer by only 100 cm^{-1} can lead to a ∼30° change in the angle between the electronic TDMs.[55]

Though we conclude that the oscillatory signal originates from the Q_x state of Chl *b*, it remains difficult to assign the mechanistic origin of this signal, especially as the peak evolution analysis of the Chl *b* GSB feature was hindered due to lower signal, it is likely that these oscillatory signals result from coupling between low frequency chlorin ring distortions and the Q_x state. Such a phenomenon has been found to occur in other cases for Chls, where the lifting of the electronic TDM out of the ring results in a coupling and subsequent increase in intensity of the chlorin ring distortion modes.[117, 118] We expect that, in order to see such a pronounced oscillation, there would likely also have to be some anharmonic coupling between the high frequency modes probed and this low frequency mode.[119] The identical, in-phase peak amplitude dynamics between the GSB and ESA of Chl *b* character is also particularly notable, and may suggest that the observed dynamics arise from non-Condon type coupling.[120] The presence of such a non-Condon effect may help to facilitate

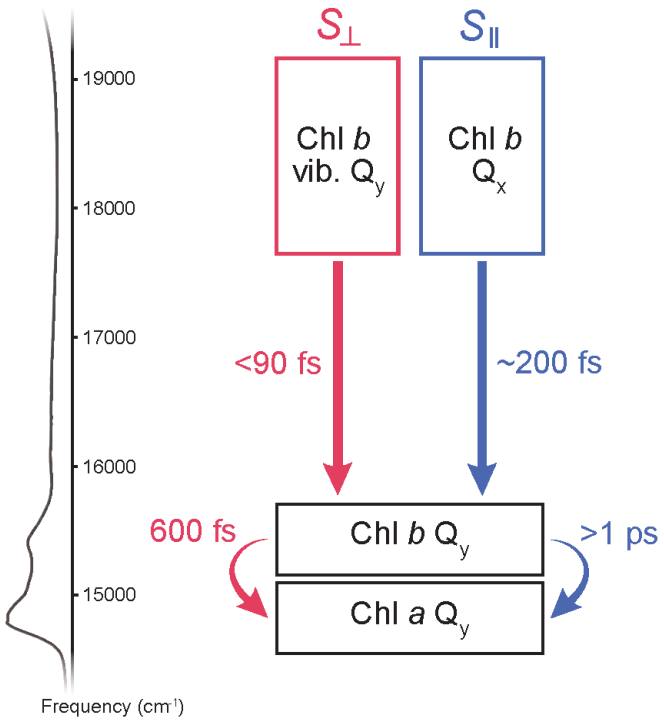

Figure 3.4: The region spanning 17545-19230 cm^{-1} is dominated by Chl *b* character. Polarization-dependent 2DEV measurements reveal distinct, overlapping excited states of Chl *b* in this region, which are assigned as the vibronic Q_y states (isolated in the $S_\perp$ spectra) and the Q_x states (isolated in the $S_\parallel$ spectra). These states also exhibit vastly different dynamics. The Chl *b* vibronic Q_y states were found to undergo relaxation within the Chl *b* Q_y manifold in <90 fs followed by Chl *b* $\rightarrow$ Chl *a* transfer on a timescale of 600 fs, while the Chl *b* Q_x states were found to undergo internal conversion on a timescale of 200 fs, followed by much slower Chl *b* $\rightarrow$ Chl *a* transfer on a timescale of >1 ps (beyond the duration of the experiment).

rapid internal conversion, therefore further improving quantum efficiency across the PAR. However, further theoretical efforts are required to support such a conclusion.

3.3 Conclusion

Understanding the origin and function of the highly mixed vibronic Q_y-Q_x bands of the LHCII spectrum, which energetically connect the lowest lying Chl Q_y and Car states, is a crucial piece in the complete understanding of the intricate spatial and energetic structure

of this photosynthetic antenna complex, as well as the light-harvesting abilities of green plants and algae. With the aid of IR detection, we show that the states spanning the green portion of the vibronic Q_y-Q_x region of the LHCII spectrum have significant Chl *b* character. The initial amplitudes of the Chl *b* GSB indicates that this region has both substantial Chl *b* Q_x character (selectively amplified in $S_{\parallel}$) and Chl b vibronic Q_y character (selectively amplified in$S_{\perp}$). A comparison of the spectra around 17800 cm^{-1} versus 18700 cm^{-1}, shows that the higher frequency region still has Chl *b* vibronic Q_y character, although it is weaker (Figure 3.2a; region highlighted in the red box versus green box), as well as significant Chl *b* Q_x character, as there is only a slight reduction between the relative signal strengths (Figure 3.2b; region highlighted in blue box versus green box). Additionally, the spectral dynamics of the ESA associated with the Chl *b* vibronic Q_y states indicate that ultrafast relaxation within the Chl *b* vibronic Q_y manifold occurs within our time resolution (90 fs). However, a fraction of the excitation was seen to remain in the Chl *b* Q_x bands for over 200 fs (based on the oscillatory feature associated with these states). The agreement between this timescale for Chl *b* $Q_x \rightarrow Q_y$ transfer in LHCII and recent theoretical work on monomeric Chl *b*[110], suggests that the observed Q_x states arise from more localized Chl *b* pigments. The oscillatory feature likely results from electronic-vibrational coupling between the Q_x transition and low frequency chlorin ring distortions, although a definitive assignment remains difficult. Ultimately, the addition of polarization control to 2DEV spectroscopy enables the observation of different states in parallel versus perpendicular detection without a change in excitation frequency. This lack of reciprocity between the polarization components enables a new way of probing the level structure and dynamics of highly congested and mixed spectra of molecular complexes. These results also highlight the critical role of electron-nuclear mixing in the extension of efficient light-harvesting across the PAR, as well as a distinct difference between Chl *a* versus Chl *b* pigments in light-harvesting. From an in vivo perspective, the significant enhancement in the absorption of these vibronic Q_y-Q_x states arising from the diffusive nature of the leaf environment (i.e. the detour effect), coupled with the fact that green photons therefore penetrate deeper into the mesophyll[7–10, 106], indicates that Chl *b* is responsible for both harnessing green light and evenly distributing photosynthetic activity throughout the leaf.

3.4 Experimental Methods

Sample Preparation

The isolation of thylakoid membranes was performed by using sucrose cushion[94] as described below. Deveined leaves were homogenized in 25 mM Tricine-KOH (pH 7.8), 400 mM NaCl, 2 mM $MgCl_2$, 0.2 mM benzamidine, and 1 mM ε-aminocaproic acid at 4 °C using a Waring blender for 30 s with max speed. The homogenate was filtrated through 4 layers of Miracloth, and the filtrate was centrifuged at 27000 × g for 10 min at 4 °C. The pellet was resuspended in 25 mM Tricine-KOH (pH 7.8), 150 mM NaCl, 5 mM $MgCl_2$, 0.2

mM benzamidine, and 1 mM ε-aminocaproic acid. The suspension was loaded on sucrose cushion containing 1.3 M sucrose with 25 mM Tricine-KOH (pH 7.8), 15 mM NaCl, and 5 mM $MgCl_2$, which was overlaid on 1.8 M sucrose with 25 mM Tricine-KOH (pH 7.8), 15 mM NaCl, and 5 mM $MgCl_2$, and centrifuged at 131500 × g for 30 min at 4 °C using a SW 32 Ti rotor (Beckman Coulter). Thylakoid membranes sedimented in 1.3 M sucrose cushion were collected and washed with 25 mM Tricine-KOH (pH 7.8), 15 mM NaCl, and 5 mM $MgCl_2$, and centrifuged at 27000 × g for 15 min at 4 °C. The pellet was resuspended in 25 mM Tricine-KOH (pH 7.8), 0.4 M sucrose, 15 mM NaCl, and 5 mM $MgCl_2$, and centrifuged at 27000 × g for 10 min at 4 °C. The pellet was resuspended and used as purified thylakoid membranes.

The purified thylakoid membranes were resuspended in 25 mM HEPES-NaOH (pH 7.8) and centrifuged at 15300 × g for 10 min at 4 °C. The pellet was resuspended in 25 mM HEPES-NaOH (pH 7.8) at 2.0 mg Chl/mL and solubilized with 4% (w/v) n-dodecyl-α-D-maltoside (α-DM; Anatrace) for 30 min with gentle agitation on ice. The unsolubilized membranes were removed by centrifuging at 21000 × g for 5 min at 4 °C. The supernatant was filtrated through 0.22 μm filter using Durapore Ultrafree filters centrifuged at 10000 × g for 3 min at 4 °C. The 200 μL of filtered solubilized fraction was used for gel filtration chromatography using the ÄKTAmicro chromatography system with a Superdex 200 Increase 10/300 GL column (GE Healthcare) equilibrated with 25 mM HEPES-NaOH (pH 7.8) and 0.03% (w/v) α-DM at room temperature. The flow rate was 0.9 mL/min. The proteins were detected at 280 nm absorbance. The fraction separated from 10.0 to 10.3 mL contained trimeric LHCII proteins.

The maximum optical density of the LHCII sample in the investigated visible range was ∼0.25 with a path length of 200 μm at 77 K (Optistate DN2, Oxford Instruments).

Spectroscopic Measurements

Below we describe the 2DEV experimental setup[2] used in this work. A home-built visible non-collinear optical parametric amplifier (NOPA) and mid-IR OPA were pumped by a Ti:Sapphire oscillator (Vitara-S, Coherent) and regenerative amplifier (Legend Elite, Coherent). The NOPA was tuned such that the center frequency of the visible pump pulse spectrum was set to ∼18415 cm^{-1} and spanned 17545∼19230 cm^{-1}. A prism pair in combination with a pulse shaper (Dazzler, Fastlite) were used to compress the visible pulses (∼35 fs). The energy of the visible pump pulses was ∼160 nJ and a f = 25 cm silver coated 90° off-axis parabolic mirror was employed to focus the visible pulses into the sample to a spot size of 250 μm. The mid-IR OPA was tuned to produce an IR probe spectrum with a center frequency of ∼1620 cm^{-1}. The mid-IR pulse was split by a 50:50 ZnSe beam splitter, forming probe and reference beams, where the probe was normalized by the reference, in order to account for shot-to-shot energy fluctuations in the IR source. The IR probe and reference pulses both had an energy of ∼100 nJ and duration of ∼60 fs. Both IR pulses were focused into the sample to a spot size of 200 μm with a f = 15 cm gold coated 90° off-axis parabolic mirror. After the sample, the IR probe and reference were dispersed with

a spectrometer (Triax 180, Horiba) onto a dual-array 64 element HgCdTe detector (Infrared Systems Development).

As the 2DEV experiments were performed in a partially collinear pump-probe geometry, the pulse shaper was also employed to generate the visible pump pulse pair and to control the relative phase (where the 2DEV signal was isolated with a 3×1 phase cycling scheme)[45, 46] and initial time delay, $t_{\text{exc.}}$, (scanned from 0-100 fs in ∼2.4 fs steps) between the pulses. To remove the optical frequency of the pump, the data was collected in the fully rotated frame with respect to $t_{\text{exc.}}$. The visible pulse pair was directed towards the sample via a retroreflector on a motorized delay stage used to control the waiting time, T, between the pump pair and probe pulses. In this work, polarization-dependent 2DEV spectra were collected as a function of waiting time in 10 fs increments from 0 fs to 625 fs and in 100 fs increments from 715 fs to 1015 fs. 100 scans were averaged for each waiting time with 80 laser shots acquired per individual scan. The relative polarization between the pump pulses and the probe pulse was controlled with a $\lambda/2$ waveplate in the pump beam line.

Except for the NOPA, the entire setup was purged with dry air, free of CO_2 (Perkins Balston FTIR Purge Gas Generator).

Data Processing

For correct visualization, all data presented in this work have been adjusted for a small residual positive chirp of ∼0.1 $\frac{\text{fs}}{\text{cm}^{-1}}$ in the visible pump pulses, which were unable to be fully compressed to the transform limit by the pulse shaper and prism pair.

Chapter 4

Vibronic Coupling Mechanisms in Energy Transfer Dynamics and 2DEV Spectra

4.1 Introduction

Elucidating the mechanisms of quantum mechanical energy transfer has fundamental implications for the way we understand natural light-harvesting and develop artificial analogs.[121] Previous experimental studies on natural systems[5, 58, 122] have been unable, however, to clearly establish the mechanism of energy transfer that leads to quantum efficiencies approaching unity[1] and have launched long-standing debates obfuscating the role of observed electronically and/or vibrationally coherent phenomena in the transfer process.[3, 60–63, 65, 66, 68–71, 74, 75, 77–79, 123, 124] It has been postulated that these coherent processes may not actually serve any purpose in the overall energy transfer mechanism.[125, 126] This ambiguity largely surrounds the lack of consistent treatment of electronic-vibrational coupling in energy transfer models, which we address through a simplified heterodimer model in this paper. It has been shown that explicit details of the vibronic coupling mechanism can have a large influence on the overall dynamics.[64, 67, 127, 128] Also contributing to the uncertainty is that the distinguishing features between vibronic mixing mechanisms in coupled systems can be subtle in electronic spectroscopies[64, 72, 92]—and are only further obscured in the complex, congested spectra of experimental realizations.

Recently, two-dimensional electronic-vibrational (2DEV) spectroscopy has emerged as a candidate experimental technique that can directly observe the correlated motion of electronic and nuclear degrees of freedom (DOF) and their role in energy transfer.[2] Indeed, initial studies on photosynthetic complexes, such as light-harvesting complex II (LHCII), showed promise in utilizing this technique to unravel the dynamics of energy transfer between different chromophores owing to the improved spectral resolution and structural details afforded via probing vibrational modes.[53] Subsequent 2DEV measurements have shown ev-

idence of vibronic mixing in and its facilitation of ultrafast energy transfer in LHCII.[3] In the latter, the 2DEV spectra showed rich vibrational structure corresponding to the dominant electronic excitations which exhibited oscillatory dynamics reminiscent of non-Condon effects found in previous transient absorption measurements.[92, 120, 129] These oscillations were also found to be present at slightly higher-energy excitations to vibronically mixed states. In this case, the clear similarity in the quantum beating patterns between these higher-lying states and the dominant, more electronically mixed excitations, was speculated to be indicative of rapid energy relaxation due to vibronic mixing. Here we develop a strategy to simulate these general effects in 2DEV spectra and connect them to vibronic coupling mechanisms of energy transfer. Further 2DEV studies on LHCII, involving excitation well-beyond the dominant absorption bands, showed the same rapid energy relaxation, but with a significant polarization-dependence.[6] With polarization control, the dynamics of vibronic excitations, exhibiting much more rapid energy transfer, were disentangled from purely electronic excitations with significantly slower energy transfer. Not only does this polarization-dependence isolate the role of vibronic mixing on the rate of energy transfer, it potentially rules out the role the protein environment has on enhancing rapid energy transfer and suggests a predominant contribution from *intra*molecular modes to the underlying energy transfer mechanism.

To date, theoretical work regarding the 2DEV signals of coupled systems, while informative, has been restricted to systems that have a only have a single vibrational mode per monomeric unit.[80, 83, 86] An interpretation of the origin of the vibronic coupling observed in these recent findings is, therefore, lacking. Particularly, the relative infancy of 2DEV spectroscopy makes assigning vibronic mixing to direct electron-nuclear coupling or non-Condon effects in the experiments difficult as this requires the development of multimode models. Previous modelling efforts to understand these effects in dimeric systems have been informative, but limited to linear spectroscopy or homodimer systems.[72, 130, 131] In this paper, we bridge this gap between vibronic coupling mechanisms and analysis of the experimental measurements by directly simulating the 2DEV spectra of a minimal model of a vibronically coupled heterodimer while controlling various vibronic coupling mechanisms. By utilizing a model system, we are able to isolate the role that different vibronic coupling mechanisms have on the structure of the excitonic states that are electronically excited in typical experiments and show how that structure is identifiable in 2DEV spectroscopy both statically and dynamically. We further compare these signatures to the diabatic population dynamics, which demonstrates the ability to directly link the mechanism of energy transfer with spectral observables and connects model systems to potential ab initio simulations for which only simple observables like the populations are available.

The remainder of this paper is organized as follows. In Section 4.2, we introduce a model vibronic heterodimer and the formalism we use for computing linear absorption and 2DEV spectra. We analyze the static and dynamical signatures of vibronic coupling in the spectra in Sections 4.3 and 4.4, respectively. Concluding remarks and directions for future work are provided in Section 4.5.

4.2 Theory

In this section, we introduce a minimal vibronically coupled heterodimer model and the theoretical formalism by which we simulate spectra. We utilize an open quantum system approach to describe the heterodimer in contact with a thermal bath given by the total Hamiltonian, $H = H_S + H_B + H_{SB}$, where H_S is the system Hamiltonian of the heterodimer, H_B is the bath Hamiltonian, and H_{SB} is the system-bath Hamiltonian describing their interactions. This approach offers an exact description of the most strongly-coupled system DOF with a simple treatment of relevant environmental effects that induce dissipation and dephasing in the system.

Model Hamiltonian

The system, which is depicted in Figure 4.1a, is comprised of two chromophores (herein referred to as sites A and B) each consisting of a local ground and excited electronic state and local intramolecular modes. These chromophores, in the context of natural light-harvesting, could be considered distinct pigments in a protein or two of the same pigments with different protein binding properties that statically change the characteristics of the local Hamiltonians. We restrict the system Hamiltonian to the ground state (G) and singly-excited state manifold, thus containing three electronic states of the form,

$$\begin{aligned} H_S = &(h_A^g + h_B^g)\,|G\rangle\langle G| + (h_A^e + h_B^g + \epsilon)\,|A\rangle\langle A| \\ &+ (h_A^g + h_B^e + \Delta E + \epsilon)\,|B\rangle\langle B| + J(AB + \text{h.c.}), \end{aligned} \tag{4.1}$$

where we have implied a Kronecker product structure of the A and B local Hamiltonians applying on their local vibrational subspace. The electronic state $|A\rangle$ ($|B\rangle$) refers to the state when site A (B) is excited and site B (A) is in its ground state. Here, the ground state is uncoupled to and energetically separated from the excited states by an excitation energy, ϵ, which may be removed without loss of generality. The excited states comprise a two-level system in the electronic subspace that has an energy difference denoted by ΔE and an electronic coupling denoted by J. In this two-level subsystem it is useful to consider the excitonic gap, which is equivalent to a Rabi frequency given by $\hbar\Omega_R = \sqrt{\Delta E^2 + 4J^2}$ that determines the timescale of electronic oscillations between the excited states.

Each site has a ground (g) and excited (e) state where the local Hamiltonians acting on the site vibrational subspaces have the form

$$h_I^i = \frac{\hbar\omega_{I,i,f}}{2}\left[p_{I,f}^2 + \left(q_{I,f} - \delta_{ie}\sqrt{2S_f}\right)^2\right] + \delta_{IA}\frac{\hbar\omega_{I,s}}{2}\left[p_{I,s}^2 + \left(q_{I,s} - \delta_{ie}\sqrt{2S}\right)^2\right] \tag{4.2}$$

where $I = A, B$ denotes the chromophore site, $i = g, e$ denotes the electronic state of the site, δ_{ij} denotes the Kronecker delta, and the q and p are the position and momentum operators, respectively of high-frequency, f, and low-frequency, s, modes. Each site contains one high-frequency ($\omega_{I,i,f}/\Omega_R \gg 1$) local intramolecular modes with a distinct site- and

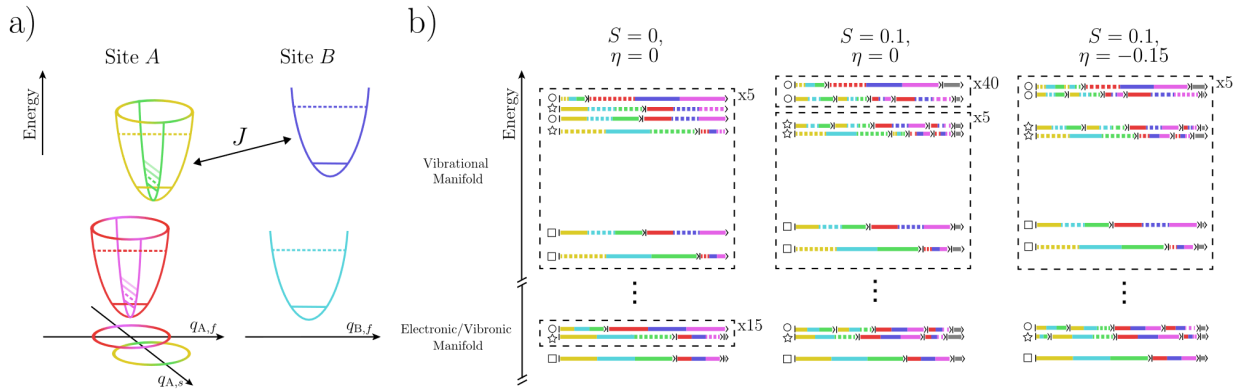

Figure 4.1: a) Schematic of the model consisting of two sites, A and B, each with one electronic DOF and one high-frequency vibrational mode. For site A (B), the high-frequency mode is shown in red (light blue) in the ground state and yellow (dark blue) in the excited state. Horizontal lines in each harmonic potential indicate vibrational levels where dashed lines, specifically, indicate one vibrational quantum. Site A includes an additional low-frequency mode, shown in pink in the ground state and green in the excited state with line-markings corresponding to different vibrational excited states. b) Simplified eigenenergy level diagram arising from electronic coupling, J, between the excited state manifolds of sites A and B for each of the three models considered here. For simplicity, the ground state manifold has been omitted and only the three lowest excitonic states in the excited electronic/vibronic manifold, as well as the corresponding vibrational levels have been illustrated. The relative site contributions for these levels are also shown by the length of each ket, "$|\ \rangle$", with site-specific color-coding following a). Dashed lines indicate a vibrational excitation. Site contributions of $<5\%$ are grouped together and denoted in gray. Shapes on the left hand side of the energy levels in the electronic/vibrational denote the main excited state absorption (ESA) transitions while shapes in the vibrational manifold denote the states to which the main ESA excitations are excited by vibrational pulses.

electronic-state-dependent frequency. These high-frequency modes are slightly displaced in the excited states and thus have a small, but non-zero Huang-Rhys factor, S_f, which we will consider fixed throughout this study in accord with the chosen parameter of Ref. [3] for comparison. Vertical excitations and electronic transitions are, however, still dominated by transitions that leave the vibrational states of these modes unchanged. Coupled to site A only is also a low-frequency mode that is nearly-degenerate with the excitonic gap, $\omega_{A,s} \approx \Omega_R$, which was chosen to enhance the effects of vibronic mixing. In practice, this mode could be considered an intramolecular mode with significant local site electron-phonon coupling. This mode is also shifted in the excited state of the A chromophore with a non-zero Huang-Rhys factor, S, however due to the resonance with the excitonic gap, this displacement induces significant vibronic mixing by coupling different vibrational states in vertical excitations

from the ground state or electronic transitions between the A and B sites. Thus, S can be varied to tune the strength of the vibronic coupling mechanism through what we herein refer to as Franck-Condon (FC) activity. Since the low- and high-frequency modes are well separated energetically they can be assumed uncoupled to good approximation. We note that for the work in this chapter, two vibrational levels per high-frequency mode and four vibrational levels for the low-frequency mode were required for convergence. Additionally, we have restricted the model to the ground- and singly- excited vibrational state manifold with respect to the subspace of the high-frequency modes for a total system Hilbert space dimension of 36.

The electronic coupling is considered to arise from a dipole-dipole interaction between the excited states of the two chromophores,

$$J = \frac{\kappa}{r^3}\mu_A\mu_B, \tag{4.3}$$

where $\mu_{A(B)}$ is the magnitude of the transition dipole moment (TDM) for the A (B) site, r is the distance between the two chromophores, and κ is a factor accounting for the relative orientation of the chromophores. We assume here that the distance, relative orientation, and TDM of the B chromophore are fixed ($r = r_0$, $\kappa = \kappa_0$, and $\mu_B = \mu_{B0}$, respectively), while the TDM of the A chromophore depends linearly on the low-frequency mode,

$$\mu_A(q_{A,s}) = \mu_{A0}\left(1 + \sqrt{2}\eta q_{A,s}\right), \tag{4.4}$$

where μ_{A0} is the static contribution to the dipole moment. The mode-dependence arises as a non-Condon effect, that is,

$$\sqrt{2}\mu_{A0}\eta = \left(\frac{\partial \mu_A}{\partial q_{A,s}}\right), \tag{4.5}$$

where η is a dimensionless parameter controlling the strength of this effect. We note that because the electronic states have the same symmetry there is no strict symmetry requirement here for the HT active mode.[130, 132] Under this assumption, the electronic coupling obtains the form

$$J(q_{A,s}) = J_0\left(1 + \sqrt{2}\eta q_{A,s}\right), \tag{4.6}$$

where J_0 is the electronic coupling arising from the static contributions of the TDM at a fixed distance and orientation, $J_0 = \kappa_0\mu_{A0}\mu_{B0}/r_0^3$, and the non-Condon effect is given by $\sqrt{2}J_0\eta q_{A,s}$. We consider here a system in the electronically coherent regime ($\Delta E = J_0$), which is typical for energy transfer dynamics in these chromophoric systems. Since η is a dimensionless parameter and it enters directly in the TDM, it can be varied to systematically study Herzberg-Teller (HT) activity in this system.

The chromophoric system here is assumed to be weakly coupled to a set of environmental modes that describe the short- and long-range fluctuations of the environment. In particular

we consider two sets of baths, an electronic set and a vibrational set, which are assumed to be independent due to disparity of the frequency of modes that couple to the separate electronic or vibrational DOF. The electronic baths independently couple to the electronically excited states through a dipolar coupling

$$(H_B + H_{SB})_{\text{el}} = \sum_{I,n} \frac{\hbar\omega_{I,n}^{\text{el}}}{2} \left[\left(p_{I,n}^{\text{el}}\right)^2 + \left(q_{I,n}^{\text{el}} - \frac{g_{I,n}^{\text{el}}}{\sqrt{2}} V_I \right)^2 \right], \tag{4.7}$$

where V_I $(I = A, B)$ are the dimensionless system dipole

$$V_I = \left(1 + \delta_{IA}\sqrt{2}\eta q_{I,s}\right) \langle I|I\rangle \tag{4.8}$$

and the vibrational baths independently couple to the nuclear modes of the system

$$\begin{aligned}(H_B + H_{SB})_{\text{vib}} = \sum_{I,n} \Bigg\{ & \frac{\hbar\omega_{I,n}^{f}}{2} \left[\left(p_{I,n}^{f}\right)^2 + \left(q_{I,n}^{f} - g_{I,n}^{f} q_{I,f} \right)^2 \right] \\ & + \delta_{IA} \frac{\hbar\omega_{I,n}^{s}}{2} \left[\left(p_{I,n}^{s}\right)^2 + \left(q_{I,n}^{s} - g_{I,n}^{s} q_{I,s} \right)^2 \right] \Bigg\}. \end{aligned} \tag{4.9}$$

Here we have included the system-bath couplings as system-dependent shifts in the minima of the bath oscillators, which ensures translational invariance of the bath with respect to the system. The g coefficients in the above expressions are the bilinear coupling coefficients with the form,

$$g_{k,n} = \frac{\sqrt{2}c_{k,n}}{\hbar\omega_{k,n}}, \tag{4.10}$$

which comprise the spectral density function,

$$J_{m,k}(\omega) = \frac{\pi}{2} \sum_n \frac{c_{k,n}^2}{\hbar\omega_{k,n}} \delta(\omega - \omega_{k,n}). \tag{4.11}$$

Here $m =$ el,vib denotes whether the spectral density corresponds to an electronically- or vibrationally-coupled environment and k serves here as a composite index ($k = I$ for the electronic bath and $k = I, f/s$ for the vibrational bath) describing the environmental modes that are coupled to the different system DOF in Eqs. 4.7 and 4.9. The spectral densities are all assumed to have the Debye form,

$$J_{m,k}(\omega) = 2\lambda_m \gamma_m \omega \frac{1}{\gamma_m^2 + \omega^2}, \tag{4.12}$$

where λ_m is the reorganization energy and γ_m is the bath relaxation timescale and each m, k environment. These parameters are chosen such that the bath represents a weakly-coupled, Markovian bath so that the use of multilevel Redfield theory is justified in treating

the dynamics of the total system-bath Hamiltonian.[133, 134] We note here that while this form is consistent with much of the underlying physics of the total system, it is primarily phenomenologically included to induce weak dissipation and dephasing for ease of numerical simulations and a further study that considers the effects a more systematically imposed system-bath coupling is warranted. A detailed list of the model parameters used in this study can be found in Table 4.1.

Parameter	Value (cm^{-1})
$\hbar\omega_{A,g,f}$	1650
$\hbar\omega_{B,g,f}$	1660
$\hbar\omega_{A,e,f}$	1545
$\hbar\omega_{B,e,f}$	1540
$\hbar\omega_{A,s}$	200
ΔE	100
J_0	100
λ_{el}	35
λ_{vib}	17.5
$\hbar\gamma_{el}$, $\hbar\gamma_{vib}$	$\sim$106
$1/\beta$	$\sim$105
S_f	0.005 (dimensionless)
μ_{A0}/μ_{B0}	-4 (dimensionless)

Table 4.1: Fixed parameters used in the model heterodimer. All parameters are in units of cm^{-1} unless otherwise specified.

Linear Absorption and 2DEV Spectroscopy from Quantum Master Equations

To calculate spectroscopic observables we utilize the response function formalism, which has been described elsewhere[43], so we restrict our discussion to the key aspects of our simulation. In this formalism, linear and nonlinear spectra can be related via Fourier Transforms of correlation functions. Specifically, for a linear absorption spectrum in the impulsive limit, the relevant response function is

$$R(t) = \left(\frac{i}{\hbar}\right)\theta(t)\,\mathrm{tr}\,\mu_{el}G(t)\mu_{el}^{\times}\rho_{eq}, \tag{4.13}$$

where $\mu^{\times}\cdot = [\mu, \cdot]$, $\mathrm{tr}\cdot$ is the quantum mechanical trace over the full system plus bath Hilbert space, $\theta(t)$ is the Heaviside step function, and ρ_{eq} is the thermal equilibrium density matrix

given by

$$\rho_{eq} = \frac{e^{-\beta H}}{\mathrm{tr}\, e^{-\beta H}}, \tag{4.14}$$

where β is inverse thermal energy. This response function is a dipole-dipole autocorrelation function of the electronic dipole given by

$$\mu_{el} = \mu_A + \mu_B \tag{4.15}$$

where

$$\mu_I = \mu_{I0}\left(1 + \delta_{IA}\sqrt{2}\eta q_{A,s}\right)(IG + GI)\,. \tag{4.16}$$

The time-dependence is given by action of the propagator $G(t)\cdot = e^{-iHt/\hbar}\cdot e^{iHt/\hbar}$, which is the unitary evolution in the full Hilbert space. This unitary evolution is prohibitively expensive, so we utilize the quantum master equation (QME) technique whereby we take a partial trace over the bath DOF and compute the response function from the dynamics of the reduced density matrix[135],

$$G(t)\mu_{el}^{\times}\rho_{eq} = \mathcal{G}(t)\rho_{\mu} \tag{4.17}$$

where ρ_μ is the reduced density matrix of the system after action of the dipole operator and $\mathcal{G}(t)$ is the reduced propagator defined by our QME. The Redfield theory approach taken here uses a double perturbation theory in both the light-matter interaction and system-bath interaction, where the light-matter interaction is assumed to be even weaker than the weak system-bath coupling.[136, 137] In this representation the response function is,

$$R(t) = \left(\frac{i}{\hbar}\right)\theta(t)\mu_{el}\mathcal{G}(t)\rho_{\mu}. \tag{4.18}$$

Here we have assumed the pulses are in the parallel configuration and also invoked the rotating wave approximation (RWA), which reduces the terms allowed in the expansion of the commutators. Denoting the dipole operators as a sum of raising and lowering dipole operators, respectively,

$$\begin{aligned}\mu_{el}^{+} &= \mu_A^{+} + \mu_B^{+} \\ &= \mu_{A0}\left(1 + \sqrt{2}\eta q_{A,s}\right)AG + \mu_{B0}BG \qquad (4.19)\\ \mu_{el}^{-} &= \left(\mu_{el}^{+}\right)^{\dagger}, \qquad (4.20)\end{aligned}$$

and ignoring the negative frequency contribution, the response function then becomes

$$R(t) = \left(\frac{i}{\hbar}\right)\theta(t)\mu_{el}^{-}\mathcal{G}(t)\rho_{\mu^+}, \tag{4.21}$$

where $\mathcal{G}(t)\rho_{\mu^+} = G(t)\mu_{el}^+\rho_{eq}$. The corresponding linear absorption spectrum is given by the imaginary part of the Fourier transform

$$S(\omega_{\text{exc.}}) = \text{Im}\int dt\; e^{i\omega_{\text{exc.}}t}R(t), \tag{4.22}$$

where $\omega_{\text{exc.}}$ is the excitation frequency less the excitation energy ϵ.

2DEV spectroscopy is a cross-peak specific multidimensional spectroscopic technique where the signal arises from both visible and subsequent infrared light-matter interactions. Specifically, visible excitation pulses prepare an ensemble of electronic/vibronic states which evolve as a function of waiting time, T. The evolution of the ensemble is then tracked via an infrared detection pulse.

Within the same formalism, the response function for 2DEV spectroscopy can be written as

$$R_3(t_{\text{det.}}, T, t_{\text{exc.}}) = \left(\frac{i}{\hbar}\right)^3 \theta(t_{\text{det.}})\theta(T)\theta(t_{\text{exc.}}) \times \text{Tr}\left\{\mu_{vib}G(t_{\text{det.}})\mu_{vib}^{\times}G(T)\mu_{el}^{\times}G(t_{\text{exc.}})\mu_{el}^{\times}\rho_{eq}\right\}, \tag{4.23}$$

where $t_{\text{exc.}}$ denotes the time between the two visible pulses, $t_{\text{det.}}$ denotes the time between the infrared pulses, and the vibrational dipole operator acting on the high-frequency modes is given by

$$\mu_{vib} = \mu_{A,f} + \mu_{B,f} \tag{4.24}$$

where $\mu_{I,f} = \sqrt{2}q_{I,f}\langle I|I\rangle$ and we have ignored the vibrational TDM of the slow mode due to non-resonance with the infrared probe. We again utilize the QME technique to compute the response function, which in the weak-coupling ($\lambda_m \to 0$) and Markovian ($\gamma_m \to 0$) limits we have chosen here reduces to the expression obtained from the quantum regression theorem[135, 138],

$$R_3(t_{\text{det.}}, T, t_{\text{exc.}}) = \left(\frac{i}{\hbar}\right)^3 \theta(t_{\text{det.}})\theta(T)\theta(t_{\text{exc.}}) \times \mu_{vib}\mathcal{G}(t_{\text{det.}})\mu_{vib}^{\times}\mathcal{G}(T)\mu_{el}^{\times}\mathcal{G}(t_{\text{exc.}})\rho_{\mu}. \tag{4.25}$$

Working also with the RWA invokes further simplifications, specifically to the number of pathways[2], giving the response function as a sum of rephasing (RP) and non-rephasing (NR) pathways

$$R_3(t_{\text{det.}}, T, t_{\text{exc.}}) = R_3^{\text{RP}}(t_{\text{det.}}, T, t_{\text{exc.}}) + R_3^{\text{NR}}(t_{\text{det.}}, T, t_{\text{exc.}}), \tag{4.26}$$

where, denoting $K = \text{NR}, \text{RP}$,

$$R_3^K(t_{\text{det.}}, T, t_{\text{exc.}}) = R_{\text{GSB}}^K(t_{\text{det.}}, T, t_{\text{exc.}}) - R_{\text{ESA}}^K(t_{\text{det.}}, T, t_{\text{exc.}}) \tag{4.27}$$

where GSB denotes the ground-state bleach pathways given by

$$R^{\mathrm{RP}}_{\mathrm{GSB}}(t_{\mathrm{det.}},T,t_{\mathrm{exc.}}) = \left(\frac{i}{\hbar}\right)^3 \theta(t_{\mathrm{det.}})\theta(T)\theta(t_{\mathrm{exc.}}) \times \mu^-_{vib}\mathcal{G}(t_{\mathrm{det.}})\mu^+_{vib}\mathcal{G}(T)\mu^-_{el}\mathcal{G}(t_{\mathrm{exc.}})\rho_{\mu^+} \tag{4.28}$$

$$R^{\mathrm{NR}}_{\mathrm{GSB}}(t_{\mathrm{det.}},T,t_{\mathrm{exc.}}) = \left(\frac{i}{\hbar}\right)^3 \theta(t_{\mathrm{det.}})\theta(T)\theta(t_{\mathrm{exc.}}) \times \mu^-_{vib}\mathcal{G}(t_{\mathrm{det.}})\mu^+_{vib}\mathcal{G}(T)\left(\mathcal{G}(t_{\mathrm{exc.}})\rho^\dagger_{\mu^+}\right)\mu^+_{el} \tag{4.29}$$

and ESA denotes the excited state absorption pathways given by

$$R^{\mathrm{RP}}_{\mathrm{ESA}}(t_{\mathrm{det.}},T,t_{\mathrm{exc.}}) = \left(\frac{i}{\hbar}\right)^3 \theta(t_{\mathrm{det.}})\theta(T)\theta(t_{\mathrm{exc.}}) \times \mu^-_{vib}\mathcal{G}(t_{\mathrm{det.}})\mu^+_{vib}\mathcal{G}(T)\left(\mathcal{G}(t_{\mathrm{exc.}})\rho_{\mu^+}\right)\mu^-_{el} \tag{4.30}$$

$$R^{\mathrm{NR}}_{\mathrm{ESA}}(t_{\mathrm{det.}},T,t_{\mathrm{exc.}}) = \left(\frac{i}{\hbar}\right)^3 \theta(t_{\mathrm{det.}})\theta(T)\theta(t_{\mathrm{exc.}}) \times \mu^-_{vib}\mathcal{G}(t_{\mathrm{det.}})\mu^+_{vib}\mathcal{G}(T)\mu^+_{el}\mathcal{G}(t_{\mathrm{exc.}})\rho^\dagger_{\mu^+}. \tag{4.31}$$

We have used the raising and lowering operator representation of the vibrational dipole operator

$$\mu^+_{vib} = \mu_{A,f} + \mu_{B,f} = a^\dagger_{A,f}\langle A|A\rangle + a^\dagger_{B,f}\langle B|B\rangle, \tag{4.32}$$

$$\mu^-_{vib} = \left(\mu^+_{vib}\right)^\dagger \tag{4.33}$$

where $a^\dagger_{I,f}$ denotes the bosonic creation operator of the fast mode of chromophore I. The signal observed experimentally is then the double Fourier transform over the excitation and detection times,

$$\chi(\omega_{\mathrm{det.}},T,\omega_{\mathrm{exc.}}) = \mathrm{Re}\left\{\chi^{\mathrm{RP}}(\omega_{\mathrm{det.}},T,\omega_{\mathrm{exc.}}) + \chi^{\mathrm{NR}}(-\omega_{\mathrm{det.}},T,\omega_{\mathrm{exc.}})\right\}, \tag{4.34}$$

where,

$$\chi^{\mathrm{K}}(\omega_{\mathrm{det.}},T,\omega_{\mathrm{exc.}}) = \int dt_{\mathrm{det.}} \int dt_{\mathrm{exc.}} e^{i(\omega_{\mathrm{det.}}t_{\mathrm{det.}}+\omega_{\mathrm{exc.}}t_{\mathrm{exc.}})} \times R^K_3(t_{\mathrm{det.}},T,t_{\mathrm{exc.}}). \tag{4.35}$$

The visualization of the data is typically best presented in the form of excitation frequency ($\omega_{\mathrm{exc.}}$)-detection frequency ($\omega_{\mathrm{det.}}$) correlation plots of the total absorptive spectrum parameterized by T.

Eigenstate Structure of the Model Hamiltonian

As spectroscopic measurements probe the excitonic states of systems it is useful to illustrate the complex manner in which vibronic mixing qualitatively changes these states. The effects from the distinct vibronic coupling mecahnisms are displayed in the eigenenergy levels shown in Figure 4.1b for which we will first focus on the electronic/vibronic manifold. In the case

where there is no vibronic coupling ($S = 0$, $\eta = 0$) we see that the lowest energy eigenstates in the excited state manifold consist of two electronically mixed states with respect to the chromophore sites denoted by a square and circle. We note that, throughout this paper, we will colloquially refer to excitonic states of particular electronic or vibronic mixing character in accordance with their assigned shapes in Figure 4.1b. There is an additional state, denoted by a star, which is similar in its site character to the lowest-energy (square) eigenstate, but has a single quantum from the low-frequency mode on the A chromophore. This state is nearly degenerate with the higher-energy (circle) eigenstate, but is composed of sites that are virtually uncoupled to the aformentioned eigenstates due to the orthogonality of the vibrational states on different electronically excited states without any vibronic coupling.

When vibronic mixing is instigated through FC activity ($S = 0.1$, $\eta = 0$), the nearly degenerate energy eigenstates are strongly coupled and energetically split into the star state, which is a vibronically mixed state due to the additional character of multiple low-frequency vibrational states from a *single* electronically excited state, and the circle state, which is still primarily electronically coupled, but has additional character of multiple low-frequency vibrational states from *both* electronically excited states. We thus refer to the energy eigenstates denoted by a square and circle as electronically coupled states, while the state denoted by a star is referred to as a vibronically coupled state.

Although difficult to capture in the energy level diagram, the energetic splitting between the circle and star states increases in the HT active case (S=0.1, $\eta = -0.15$) versus FC active (S=0.1, $\eta = 0$). In either scenario, the vibronic coupling clearly serves to distribute site A character throughout the excited state manifold, therefore promoting additional possible relaxation pathways. HT activity, though, specifically results in the distribution of pure electronic character from site A to the vibronically coupled state (star) in contrast to FC activity which only distributes vibrational (low-frequency mode) character from site A. In this way, in the presence of HT activity, the circle state is nearly invariant, retaining its electronic-coupling character, but the star state gains pure electronic-coupling character, unlike in the FC active scenario. While not shown in Figure 4.1b, the next set of excitonic states in the electronic/vibronic manifold are electronic replicas of the star and circle states with an additional quantum in each vibrational state of the slow mode. These unpictured states thus contribute to the intensity borrowing effect of HT activity in the absorption lineshape.

Currently, the discussion has been restricted to the electronic/vibronic manifold, however, a comparison of the site character of the excitonic states in the vibrational manifold reveals striking differences. In fact, the high-frequency excited state vibrational modes are clearly influenced by changes in relative site contributions, which makes them sensitive reporters of vibronic mixing mechanisms. The eigenstates in the vibrational manifold are also labelled by shapes denoting the predominant transitions from the electronic/vibronic manifold due to the vibrational transition dipole moment. In this manner, we note that excitonic states in the vibrational manifold with the same shape as those in the electronic/vibronic manifold have the same electronic/vibronic character. When S is nonzero, transitions between these manifolds can change the electronic/vibronic character due to changes in the vibrational

transition dipole moment matrix elements. A focused discussion on the interpretation of vibronic coupling through a spectroscopic interrogation of the electronic/vibronic manifold versus both the electronic/vibronic and vibrational manifolds is reserved for Sec. 4.3.

4.3 Static Signatures of Vibronic Coupling

While 2DEV spectroscopy gives a time-dependent spectroscopic signal from which dynamical phenomena can be inferred, it is first useful to uncover the ways in which it can be utilized to unravel the detailed structure arising from the underlying system Hamiltonian. In particular, we compare the signal observed from electronic linear absorption spectroscopy and the signal observed from 2DEV spectroscopy at a waiting time of $T = 0$ fs. To show the specific effects arising from FC activity and HT activity we have computed both spectra with pair values of S and η at $(S, \eta) = (0, 0), (0.1, 0), (0.1, -0.15)$, which are shown in Figure 4.2. When both parameters are set to zero, that is, there is neither FC nor HT activity, we expect to see coupling between the two chromophores that is purely electronic in nature. Indeed the linear absorption spectra (Figure 4.2a) shows two peaks that are inhomogeneously broadened with respect to the stick spectra due to the weak coupling between the system and bath. These peaks are transitions to the two lowest excitonic states in the excited state manifold, with zero vibrational quanta in the low-frequency modes, which have an excitonic energy gap of $\hbar\Omega_R$. The 2DEV spectrum gives additional structural information in both the GSB (positive) or ESA (negative) signals from the quartet structure owing to the correlation of the excitonic states with the vibrational character of the fast modes for each chromophore in each electronic state populated. The two excitonic transitions are observable as bands along the excitation axis with splitting equal to $\hbar\Omega_R$, however, additional cross-correlation between these bands at various positions along the detection axis is observed (see Figure 4.2a in the region spanning 1570$\sim$1595 cm^{-1}) which shows that the excitonic states are comprised of sites that are electronically coupled. The peaks along each band report on the population of particular excitonic states in electronic/vibronic manifold. Since the high-frequency modes are local to each site, there are two vibrational peaks of the same electronic/vibronic character per band (denoted by the same shapes) that appear through coupling with excitonic states in the vibrational manifold (see Figure 4.1b). This locality also provides some information about the relative populations in each site rather than purely excitonic populations, despite working in the electronically coherent regime. The 2DEV signal, even in this very simple case, goes well beyond the observable description obtainable by linear absorption—particularly because both the electronic/vibronic and vibrational manifolds are directly interrogated spectroscopically in the former. In this way, it is understandable how vibronic mixing mechanisms could be heavily obscured—even in other multidimensional spectroscopies—that are limited only to interrogations of the electronic/vibronic manifold.

The stark contrast in detectable information between these spectroscopies arises in the presence of vibronic coupling activity. The linear absorption and 2DEV spectra for the FC active case (S=0.1, η=0) are shown in Figure 4.2b. Despite a significant change in the

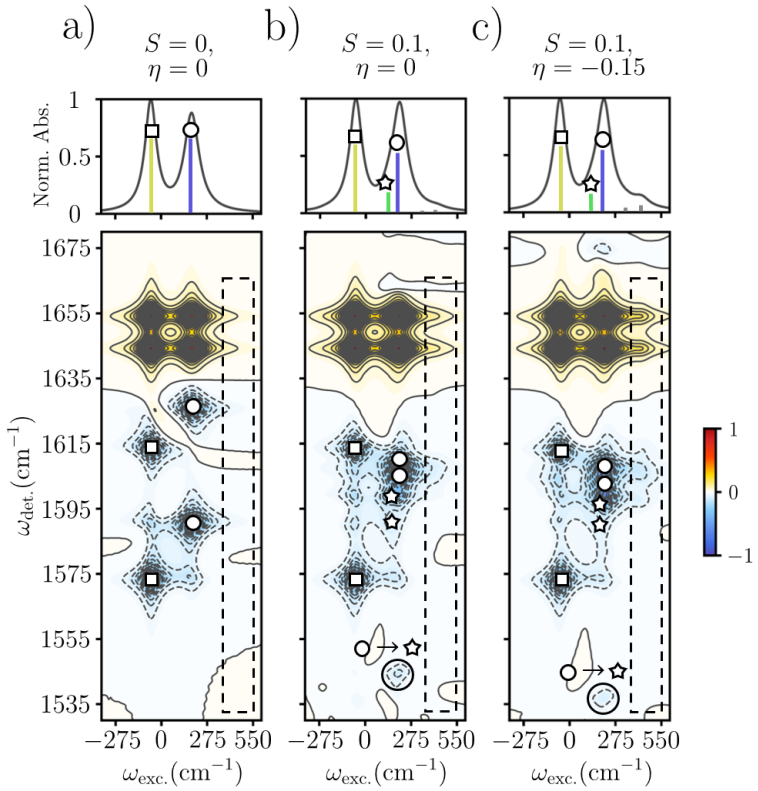

Figure 4.2: (Top row) Electronic linear absorption spectra for the three treatments of vibronic coupling—a) no coupling, b) FC activity, and c) HT activity. Stick spectra are also shown where yellow (square), green (star), and blue (circle) indicate the three lowest-energy excitonic transitions, explicitly described in Figure 4.1, while gray sticks indicate higher-lying vibronic transitions. (Bottom row) Corresponding 2DEV spectra at $T = 0$ fs. Positive, red/yellow features indicate GSBs and negative, blue features indicate ESAs. Contour levels are drawn in 2% intervals. All spectra have been normalized to the maximum in each data set. ESA peaks are labeled by shapes according to transitions to the electronic/vibronic manifold as indicated in Figure 4.1. The black, dashed box highlights the higher-excitation frequency portion of the spectra where vibronic transitions appear. In b) and c), the circled ESA transition at the bottom is assigned to a transition between states of different excitonic character through a vibrational pulse.

structure of the excitonic states, the linear absorption spectrum is virtually indistinguishable from the vibronically inactive spectrum when accounting for broadening. As is shown in the stick spectrum, the new vibronic excitonic state (star) is excited, however, due to the relative weakness of the transition and the comparable excitonic gap between the vibronic and the higher-energy electronic excitonic states (star and circle, respectively) this state is masked

under typical broadening. This excitonic state is, however, clearly shown in the 2DEV spectrum. As was expected from analysis of the excitonic states (see Sec. 4.2), the lowest-lying excitonic state remains largely unchanged in its excitation energy and vibrational structure, however, additional structure in the cross-coupling along the detection axis of this band is observed since this excitonic state now has site character that couples to the vibronic (star) state in addition to the higher-energy electronic (circle) state. In essence, detection via the vibrational manifold serves to disperse the spectroscopic signatures of the excitonic states along the detection axis where even slight changes due to various couplings can be readily observed.

The higher-energy excitation band retains this substructure from the additional vibronic excitonic state, however, it is notable that there is a small, but detectable, energy shift along this band corresponding to the different excitonic states—the vibronic (star) state is slightly lower in energy than the electronic (circle) state. An additional subtle feature arises along the higher-energy excitation band at a lower detection frequency. This feature is a unique consequence of FC activity and is a signature of the site mixing in both the vibronic/electronic (star/circle, respectively) states and newly allowed transitions in the vibrational TDM. Specifically, as a result of the mixing, vibrational transitions with lower energy difference (electronic circle to vibronic star transitions in Figure 4.2b) can emerge—a transition that is expressly disallowed without FC activity due to the orthogonality of the excitonic states with respect to the low-frequency vibrational states. We also note that additional broadening in the higher-energy band is exhibited in both the GSB and ESA signals, which we attribute to coupling between the higher-energy (circle) excitonic state and other vibronic states, however, this effect is likely not distinguishable in practice.

In the final case, $(S = 0.1, \eta = -0.15)$, we consider the simultaneous effect of both FC activity and HT activity on the structure of the spectra. While the vibronic state is still masked by broadening in the linear absorption spectrum, a new peak appears at an excitation energy nearly $\hbar\omega_{A,s}$ larger than the higher-energy excitonic (circle) state, which is due to the intensity borrowing effect of HT activity, i.e. there are even stronger dipole-allowed transitions to higher-lying excitonic states with additional vibrational quanta in the low-frequency mode. These additional transitions specifically build on the vibrational progression of the low-frequency mode in the circle and star states—rather than the square state—due to the near-resonance condition of the circle and star states in the FC inactive case and are unambiguously a consequence of HT activity as found in the matrix elements of the electronic TDM. The 2DEV spectra expectedly picks up this feature along the excitation axis in both the GSB and ESA signals, however, it is interestingly correlated with IR transitions similar to the circle state rather than the star state or a combination of the circle and star state. This correlation is due to the relative intensities that can be borrowed from the circle and star states, that is, the HT activity induces transitions that are like the circle state plus one vibrational quantum in the low-frequency mode with a stronger signal than the star state. This correlation also indicates that 2DEV spectroscopy directly reports on HT activity if the side-bands exactly replicate, with lower intensity, the lower-energy excitonic states along the detection axis and if no additional IR transitions emerge at lower detection

energies akin to the circle to star IR transition from FC activity described above.

A final point regarding the HT activity is that the observed signal here—the intensity borrowing from the dominant excitonic states along the excitation axis—is strictly due to the form of the non-Condon activity we have chosen, namely that the low-frequency mode changes the magnitude of the dipole moment and thus changes the electronic TDM directly. The same effect in the electronic coupling could arise, to first-order, from different modes that modulate the relative positions of the chromophores, but leave invariant the TDM. Since the structure of the excitonic states is apparently not influenced as much by HT activity as FC activity in the electronically coherent regime, this HT activity distinctly shows up as stronger side-band transitions along the excitation axis, which would not be present in other forms of mode-dependent electronic coupling terms.

4.4 Dynamical Signatures of Vibronic Coupling

With 2DEV spectroscopy established as a sensitive tool for witnessing vibronic effects, we turn to an analysis of how these effects manifest in the dynamics from the spectra. Rather than analyzing the complex dynamical signatures from the spectra in the time-domain, we convert to the frequency-domain to construct beat maps in the waiting time as a function of the excitation and detection frequencies. Specifically, these beat maps are formed by first filtering out the high-frequency oscillatory dynamics using a Savitzky-Golay filter[95], which produces a dynamical map of the excitonic population dynamics. These population dynamics are then subtracted from the total spectra yielding the remaining coherent dynamical components (denoted by $\tilde{\chi}$) from which the power spectrum is calculated as

$$S(\omega_{\text{det.}}, \omega_T, \omega_{\text{exc.}}) = |\Xi(\omega_{\text{det.}}, \omega_T, \omega_{\text{exc.}})|^2 \tag{4.36}$$

where

$$\Xi(\omega_{\text{det.}}, \omega_T, \omega_{\text{exc.}}) = \int dT e^{-i\omega_T T} \tilde{\chi}(\omega_{\text{det.}}, T, \omega_{\text{exc.}}). \tag{4.37}$$

In the following, we will show how these oscillatory components report directly on the interplay between excitonic states. Additionally, the conclusions drawn from this specific type of beat map analysis can be readily applied to more complex systems where the excitonic manifold, as well as the dynamics are often highly congested.

Population dynamics of the sites can also be inferred from these dynamical beat maps since 2DEV probes local intramolecular modes.[86] To illustrate this point, we compare the dynamical beat maps to the population dynamics starting from an initial vertical excitation to the B site given by,

$$\rho(0) = \mu_B \rho_{eq} \mu_B^\dagger. \tag{4.38}$$

This initial condition considers specifically the rapid population transfer from the higher-energy B site to the lower-energy A site to show the complex dynamical features observed

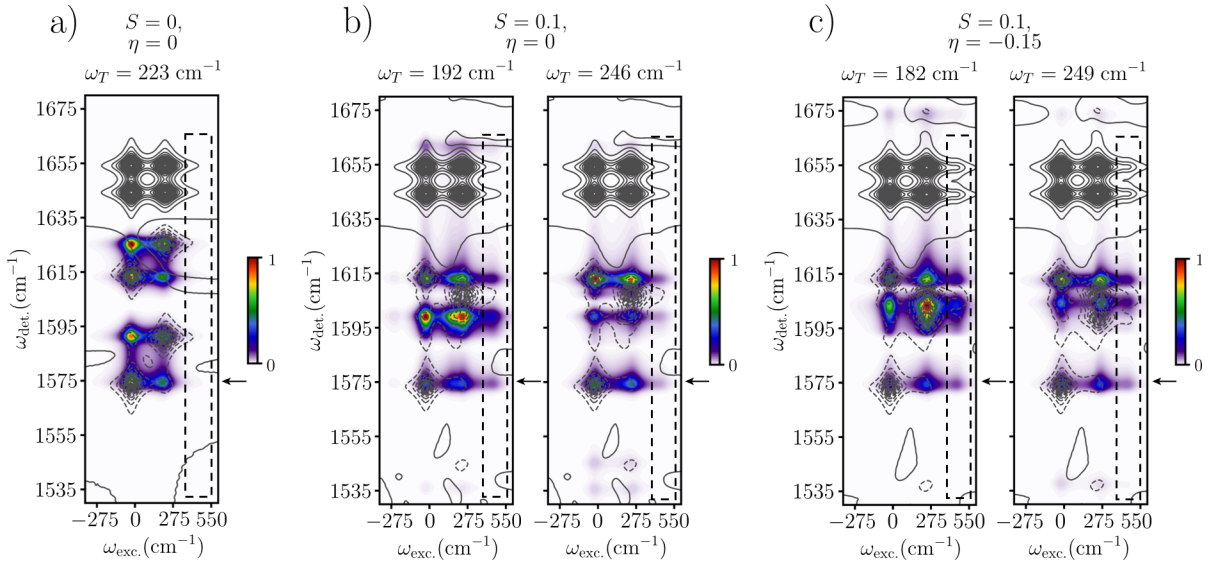

Figure 4.3: Beat maps at specific ω_T values corresponding to the excitonic energy gaps in the models where there is a) no vibronic coupling, b) FC activity, and c) HT activity. For each model, the plots are normalized to the maximum beat frequency amplitude. The colormap indicates spectral regions that oscillate at the given ω_T values with amplitudes ranging from zero (white) to one (red), the maximum value. Contour lines indicate the 2DEV spectra for each model at $T = 0$ fs. The black, dashed box highlights the higher-excitation frequency portion of the spectra where vibronic transitions appear. The black arrows indicate the spectral region of $\omega_{\text{det.}}$ that is further analyzed in Figure 4.5.

in this ultrafast process comparable to realistic systems such as LHCII. While this initial condition is not entirely physically realizable as the chromophores are intrinsically coupled and cannot be isolated in this way, it is useful to show how the dynamical signatures in 2DEV spectra are exhibited in more idealistic simulations for drawing connections between future atomistic simulations for which corresponding spectral simulations are beyond computational capabilities.

In the beat maps, we observe peaks in the dynamical frequency ω_T that correlate with the excitonic states at particular $\omega_{\text{exc.}}$ and $\omega_{\text{det.}}$. The correlations between the dynamical frequency and the excitonic states specifically show the contribution from certain states to a particular dynamical signature, that is, which states beat at which frequencies. We have analyzed these beat maps in each parameter set (S, η), which are shown in Figure 4.3 as overlayed with the $T = 0$ fs 2DEV spectra for clearer identification. In the case $(S = 0, \eta = 0)$ we observe a single dynamical frequency corresponding to the bare excitonic gap $\hbar\Omega_R$. This signature is to be expected as there is negligible contribution of FC activity from the high-frequency modes and no vibronic contribution from the low-frequency mode.

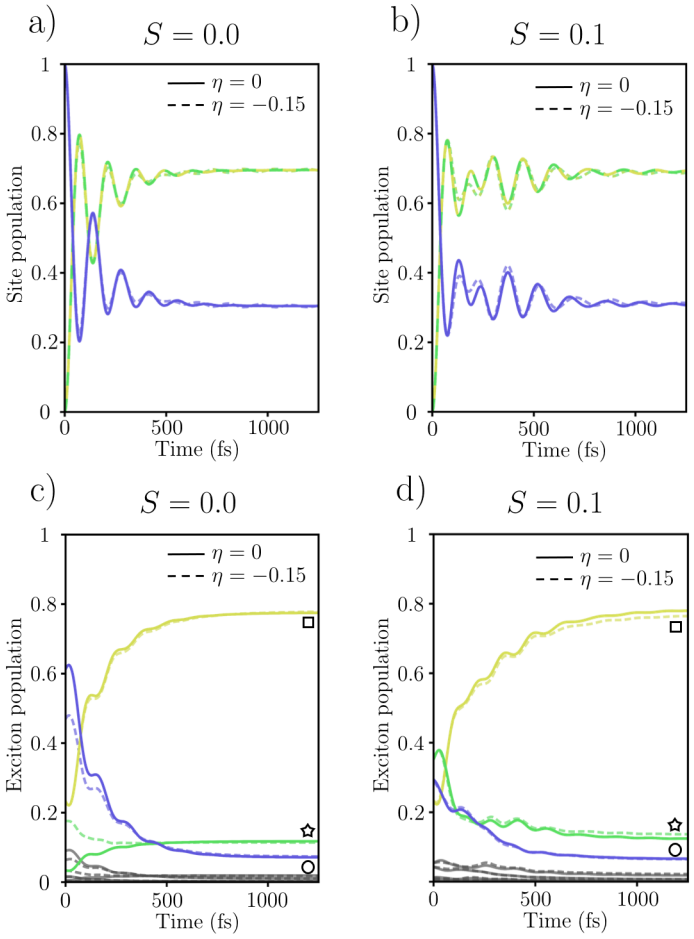

Figure 4.4: (Top row) Site populations for an initially, vertically excited wavepacket into the B site where a) $S = 0$ and b) $S = 0.1$. Yellow/green indicates the population of site A and blue indicates the population of site B. (Bottom row) Corresponding exciton populations where a) $S = 0$ and b) $S = 0.1$. Yellow (square), green (star), and blue (circle) indicate the populations of the three corresponding lowest-energy exciton levels, explicitly described in Figure 4.1, while gray indicates the populations of all higher-lying levels. Throughout, solid lines indicate $\eta = 0$ and dashed lines indicate $\eta = -0.15$ (i.e. no HT activity versus HT activity).

Thus, the state populations oscillate, at times shorter than the onset of thermalization, in accordance with the dynamics of a two-level system. This beat map is consistent with the population dynamics, shown in Figure 4.4a and 4.4c, which show the site and excitonic populations, respectively. In particular, the site populations exhibit beating only at the excitonic gap between the chromophoric states with subsequent thermal relaxation. This same beating appears in the excitonic populations where it is convoluted with population

transfer between the excitonic states. We have also computed the population dynamics considering only the HT activity, $(S = 0, \eta = -0.15)$, and found that there is little to no difference in the site population dynamics. Rather, the difference is in the initial excitation condition of the excitonic populations due to the aforementioned change in the structure of the excitonic states to which we are exciting.

With the addition of both cases of vibronic coupling comes an additional dynamical frequency associated with quantum beating at the excitonic gap between the square and star state, which is distinct from pure Rabi oscillations. While the Rabi frequency is slightly modified, this beating frequency is still associated predominantly with the excitonic state of mostly electronic character (circle), while the additional frequency is associated with the vibronic state (star). This distinction is emphasized when considering the correlation between the beat frequency and the excitonic state character as shown in Figure 4.3b and 4.3c, which show the beat maps for the $S = 0.1$ and $\eta = 0, -0.15$ cases. In both cases, the modified Rabi frequency is slightly higher due to the additional coupling but in the FC-only active case, this frequency is specifically correlated with the circle state with a small contribution from the star state. This correlation is most notable when considering the lower detection frequency circle to star transition (1530$\sim$1540 cm^{-1}) which has a weak signal at the modified Rabi frequency but no signal at the new vibronic frequency. The vibronic frequency has much more participation from the vibronic (star) state than does the modified Rabi frequency. At this new frequency, there is also notably more activity at higher-lying vibronic states along the excitation axis suggesting that these higher-lying vibronic states are relaxing mainly to the star state. These excitation side-band correlations become significantly more prevalent in the HT active case $(S = 0.1, \eta = -0.15)$. Noticeably, however, there is enhanced activity of these higher-lying vibronic states in *both* frequency components. The main difference is that HT activity leads to borrowing of pure electronic character from the circle to the star state (see Figure 4.1b). This activity, in turn, leads to more equal contributions from both states at the new vibronic frequency and the (further) modified Rabi frequency facilitating participation of the higher-lying vibronic states across all beat frequencies.

In both cases, $(S, \eta) = (0.1, 0), (0.1, -0.15)$, the population dynamics (shown in Figure 4.4b and 4.4d) are virtually identical and we will thus consider them in unison. The site populations show a seemingly polychromatic beating pattern with initial electronic oscillations corresponding to the modified Rabi frequency crossing over to beating on the vibronic frequency. This pattern is also exhibited in the excitonic populations with an initial beat between the electronic (square and circle) states followed by correlated oscillations in the square and star states. In this instance, it appears as though population transfer between the chromophores is assisted by vibronic coupling, specifically FC activity, by protecting the transfer from back-oscillations. In particular, the crossover from purely electronic oscillations at short times (about one period of the modified Rabi frequency) to oscillations at the excitonic gap coupling the star state prohibits further population from transferring back to the B site after transferring to the A site. We emphasize, however, that this is only a weakly drawn conclusion with respect to energy transfer in realistic systems and requires further

analysis in which we consider various regimes including the electronically incoherent regime. For example, the overall transfer between sites A and B in this case is largely dictated by the electronic coupling which distributes a reasonable amount of site B character in the lowest excitonic state—in direct competition with the vibronically-induced distribution of site A character among the higher-lying states. In the incoherent regime, the lowest excitonic state will almost completely resemble site A, however, vibronic mixing will still serve to distribute site A character throughout the higher-lying excitonic states in the same way as for the models considered here (see Figure 4.1b). Therefore, we expect that vibronic effects will manifest more strongly in the incoherent regime where they are the dominant means for the distribution of site A character—without the competing effects of electronic coupling distributing site B character in the opposite, undesirable direction. The treatment of this regime in regards to 2DEV spectral simulations, though, is beyond the perturbative limit of Redfield theory used in this study. Nevertheless, vibronic coupling has a clear impact on the population dynamics that emerges in the dynamical signatures of the 2DEV spectra from these models.

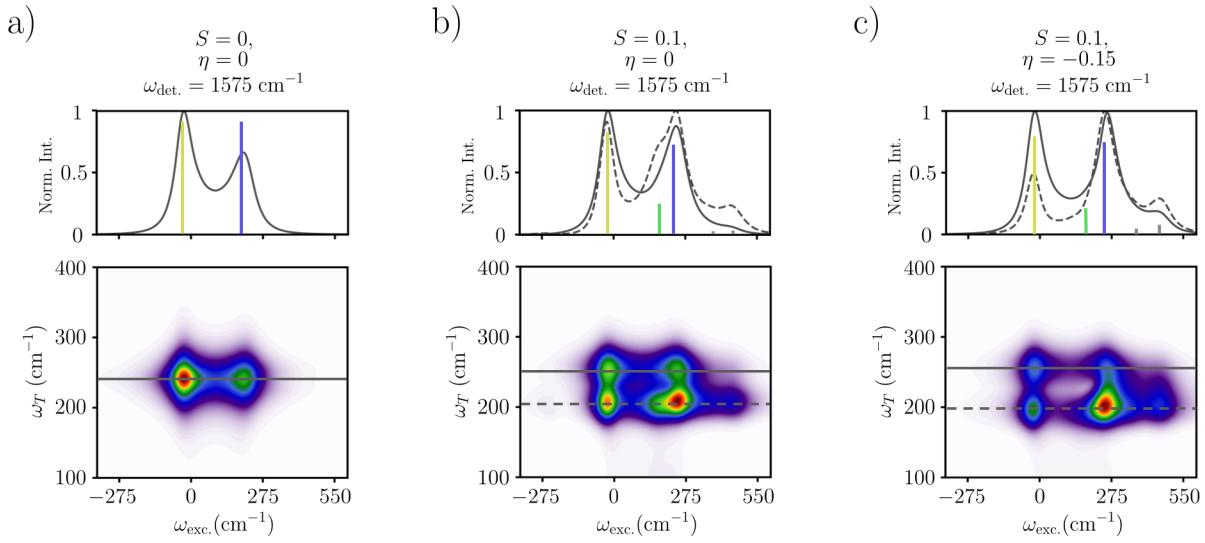

Figure 4.5: Beat maps at a fixed detection frequency, $\omega_{\text{det.}}$ (indicated by the black arrows in Figure 4.3), for the three models where there is a) no vibronic coupling, b) FC activity, and c) HT activity. The corresponding colormaps are identical to those in Figure 4.3. Slices along the excitation axis at specific beat frequencies, corresponding to the exciton energy gaps in the model, are shown above each beat map. Also shown in these plots for comparison are the electronic linear absorption stick spectra as described in Figure 4.2.

We further note that in both cases of vibronic mixing there are congested signals in the beat maps. It is thus useful to consider a particular slice of these beat maps along

the detection axis associate with the lowest-lying excitonic state. Since this state is mostly unchanged by vibronic coupling, it can serve as a sensitive reporter of the changes in the dynamical beat frequencies through which the effects from vibronic mixing emerge. These excitonic-state specific beat maps are shown in Figure 4.5. Along with these two-dimensional beat maps we consider slices along the observed dynamical frequencies shown relative to the linear absorption stick spectrum. In the vibronically inactive case, we again observe a single dynamical frequency associated with the Rabi frequency to which both excitonic states contribute. This signature clearly identifies the connectivity between these states.[3] In systems with more complex excited state manifolds, i.e. with vibronic mixing, the implications of these maps are striking. For example, in the FC active case ($S = 0.1, \eta = 0$) (Figure 4.5b) the additional peaks in the vibronic frequency band illustrate how energy flows within the excitonic manifold. By looking at slices along ω_T at the modified Rabi frequency, it is apparent that population primarily flows from the circle to square state. However, at ω_T specific to the vibronic frequency, there is an additional peak at the higher-lying vibronic side-band, as well as at the star state. This distinction reveals how FC activity promotes a "vibronic funnel" whereby excitation flows from the higher-lying states through the circle and star states down to the lowest excitonic state (square)—clearly demonstrating the additional relaxation channel. In the HT active case ($S = 0.1, \eta = -0.15$) (Figure 4.5c), we see similar features along the lower ω_T frequency, however, in the higher ω_T value, there is amplified contribution from the higher-lying vibronic states as compared to ($S = 0.1, \eta = 0$) (Figure 4.5b). This amplification is due to the borrowing of electronic character in the star state from the circle state, which promotes vibronic character in the circle state as is shown in Figure 4.1b. This feature is perhaps a clearer demonstration of how HT activity results in additional mixing, i.e. additional vibronically-promoted relaxation pathways through the modified electronic coupling.

4.5 Conclusion

In this chapter, we have introduced a minimal model for a vibronically coupled heterodimer for which two distinct mechanisms of vibronic coupling can be systematically tuned. This model adequately describes the coupling of a low-frequency nuclear mode to site-exciton states in a multichromophoric system and introduces a set of local high-frequency modes to report on the vibronic coupling in 2DEV spectroscopy. This low-frequency mode can induce vibronic coupling through Franck-Condon activity, which couples the nuclear mode to the site energies, or through Herzberg-Teller activity, which introduces nuclear dependence of the electronic coupling through the TDM of a single chromophore.

Through the development of these heterodimer models, we have shown how different mechanisms of vibronic coupling, or lack thereof, manifest in both the composition of the resulting excitonic states, as well as the 2DEV spectra through both static and dynamical contributions to the overall signal. In the absence of vibronic coupling, the system resembles that of a two-level model in which the dominant excitonic states are observable in the 2DEV

spectra through excitation bands with vibrational structure of the chromophores and cross-peaks characterizing the electronic coupling. When the low-frequency mode is coupled to the electronic manifold, vibronic structure emerges due to an additional vibronically mixed state in the case of FC activity and an increased signal in the electronic side-band arising specifically from HT activity rather than mode-dependent electronic coupling. 2DEV spectroscopy also reports on the population dynamics due to the locality of the vibrational probe and can thus reveal nature of quantum beating patterns during energy transfer. Without vibronic coupling, the system beats at a single frequency associated with the electronic coupling while vibronic coupling introduces a new quantum beat frequency due to additional vibronically mixed excitonic states. These beat frequencies directly characterize the population dynamics and show the additional relaxation pathways vibronic coupling affords the energy transfer dynamics. Ultimately, the insight gained from this chapter provides a general framework for the interpretation of the underlying Hamiltonian of vibronically coupled systems. In fact, connections between previous experimental work and the present models, addressed elsewhere, have uncovered details about the vibronic coupling mechanisms in LHCII.[12]

Various aspects do, however, require further investigation. For example, we have only considered here the electronically coherent and vibrationally resonant regimes where HT activity has little effect on the overall energy transfer, a feature which we do not expect to generically hold true across all regimes. With regard still to the nuclear dependence of the electronic coupling, our treatment is specific to that which arises from nuclear dependence of the dipole moment, however, a similar effect in the electronic coupling due to the spatial/orientational changes from short- or long-range nuclear fluctuations could be expected. Different signatures may arise from electronic states of different character or symmetry, such as charge transfer states. Further studies aimed at extracting vibronic parameters such as those showcased here and other mode couplings directly from 2DEV spectroscopy are needed. Simulating the polarization selectivity has recently been formulated in Refs. [139] and [140] and its application to heterodimer systems could prove fruitful. A more systematic understanding of the effect on the energy transfer and the signature in 2DEV spectroscopy from these separate coupling mechanisms warrants further study. While generalizations to the model presented here would be required, the way in which electron-nuclear coupling mechanistically mediates dynamics through conical intersections[20, 141] or assists in charge transfer[28, 109, 142] and singlet fission[143] are similarly deserving of explicit theoretical treatment with respect to 2DEV spectroscopy.

4.6 Vibronic Coupling in LHCII Revisited

A growing body of work has pointed to vibronic mixing as a crucial design principle for efficient energy and charge transfer in natural[3, 77, 78] and artificial systems[142, 144]. Notable among these studies was the recent observation of vibronically-promoted ultrafast energy flow in the major antenna complex of green plants and algae, LHCII—the most abundant membrane protein on earth[4]—via the emerging experimental technique 2DEV spectroscopy.[3]

This spectroscopy, which correlates electronic and nuclear DOF, shows promise for providing mechanistic insight into vibronic coupling, however, explicit theoretical input is necessary to extract such detail. In this chapter, we have developed a heterodimer model that describes various forms of vibronic coupling—which were speculated to be present in LHCII—resulting from diagonal electron-phonon coupling giving FC activity and nuclear dependence of the electronic transition dipole moment giving HT activity. In this section, we draw connections between this theoretical effort and recent experimental studies (covered in Chapters 2 and 3) in order to demonstrate how HT activity is leveraged in the function of LHCII.

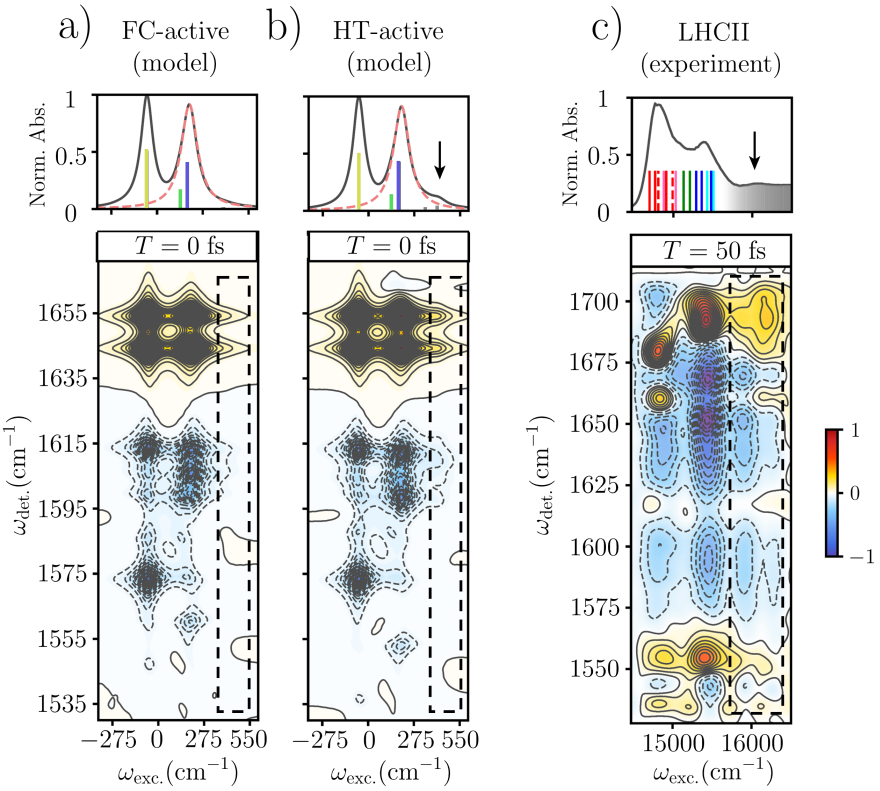

Figure 4.6: Electronic linear absorption spectra (Top row) and 2DEV spectra (Bottom row) for a heterodimer model without, a), and with, b), HT-activity and c) LHCII at 77 K. Vertical lines in the linear absorption spectra denote excitonic states (see Ref. [50] for LHCII). Dashed curves in the top row of a) and b) denote Lorentzian fits to the higher-energy peak. The dashed box highlights the higher-excitation frequency portion of the 2DEV spectra where HT-induced vibronic transitions appear. The black arrows indicate higher-energy vibronic states that are promoted by HT activity. Positive features indicate ground state bleaches and negative features indicate excited state absorptions.

We simulated the linear absorption and 2DEV spectra using the heterodimer model of

Ref. [11] (as described in this chapter) with similar parameters to LHCII for comparison. Specifically, all parameters have been kept the same as in Ref. [11] ($\eta = 0.0$ for FC-active case and $\eta = 0.15$ for HT-active case) except, here, $S = 0.05$. While the model heterodimer mimics the linear absorption spectrum of LHCII shown in Figure 4.6, exhibiting two dominant peaks arising from the excitonic states of the electronically coupled chromophores, the presence of the higher-energy side-band is the most significant similarity. By comparing the FC-active and HT-active models of Figure 4.6a and 4.6b, respectively, it is clear that this feature emerges specifically as a result of HT activity[11]—remaining hidden by the inhomogenous broadening when the system is only vibronically mixed by FC activity through a Huang-Rhys factor similar to those found in LHCII.[93] In the model, this side-band can only be observed when additional vibronic mixing through HT activity is included. This side-band also appeared in the heterodimer 2DEV spectra (highlighted by the dashed, black box in Figure 4.6b) where the vibrational structure specifically replicated the excitonic state with significant electronic character from the higher-energy chromophore (analogous to chlorophyll (Chl) *b* in LHCII).[11] Remarkably, not only does the experimental 2DEV spectrum of LHCII (Figure 4.6c) clearly display side-band features, but the vibrational structure along these bands replicates that of the higher-lying excitonic states composed of mainly Chl *b* (spanning 15200∼15600 cm^{-1}) as marked by the characteristic ground state bleach signature at 1690 cm^{-1} and predicted by the model. These observations, in agreement with the key features displayed by the model, highlight the potential presence of HT activity in LHCII.

The time evolution of 2DEV spectra also reports on the energy transfer dynamics. A frequency-domain characterization of the complex oscillatory signals is often performed and visualized with a beat map (as described previously in this chapter), which is shown in Figure 4.7. These beat maps are calculated at a fixed, local detection mode which serves as a sensitive reporter of the interplay between excitonic states. The beat map from the HT-active model simulations (Figure 4.7a) displays two distinct dynamical frequencies that report on the two relevant energy gaps and shows contributions from higher-lying excitonic states (shaded regions of Figure 4.7) at both dynamical frequencies. This manifests as an additional peak in the map that can be clearly seen at both beat frequencies (highlighted by black arrow in the top panel of Figure 4.7a), which is a feature specific to HT activity.[11] The experimental measurements (Figure 4.7b) are considerably more structured due to the many additional excitonic states relative to the model, but the beat map shows a similar distribution of higher-energy vibronic activity across the numerous beat frequencies. One example of the prevalence of the high-energy vibronic states in the observed beat frequencies corresponding to excitonic energy gaps is presented in Figure 4.7b (see top panel). Despite the complexity of the experimental beat maps, the observable features from our model analysis elucidates the role of vibronic mixing in promoting additional, ultrafast relaxation pathways in the energy transfer dynamics of LHCII.

More specifically, HT activity was found to be a potential mechanism of energy transfer in the model. Further 2DEV studies on LHCII, featuring excitation well into the green absorption region[6], have indicated that vibronically-induced ultrafast energy flow persists across nearly 3000 cm^{-1} of the electronic linear absorption spectrum of the complex, which

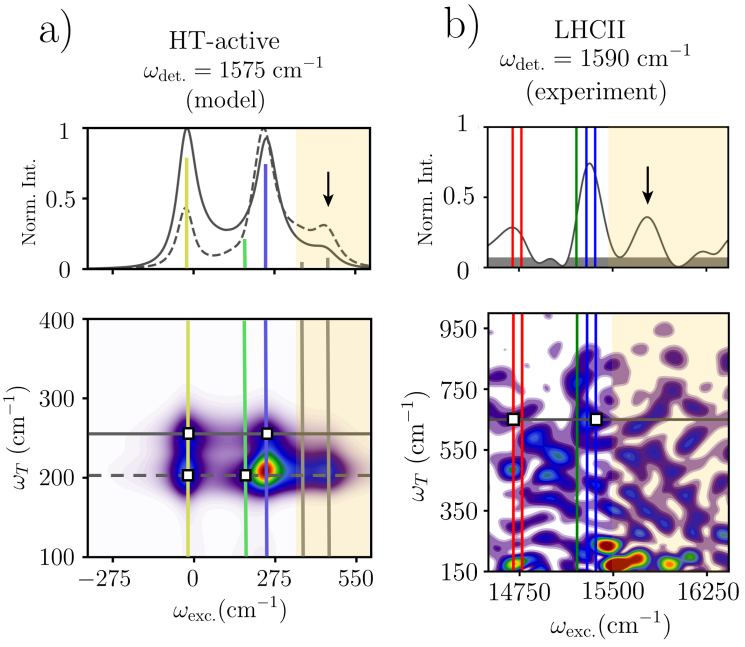

Figure 4.7: Beat maps at a fixed detection frequency (Bottom row), $\omega_{\text{det.}}$, for the a) model and b) experiment (only peaks that survive the noise floor are shown). Vertical lines denote excitonic states (for LHCII these are based on Ref. [50]) and horizontal lines are specific beat frequency slices which are shown in the top row (gray shading in b) represents the noise floor). In a), the activity of the two beat frequencies is distinguished with a solid versus dashed line. The yellow shaded region and black arrows indicate higher-energy vibronic states that are promoted by HT activity. At a given beat frequency, squares indicate the energetic gap between excitonic states corresponding to that frequency.

in conjunction with the model results, suggests that HT activity is also the mechanism responsible for the extension and enhancement of the light-harvesting capabilities of LHCII across the photosynthetically active region.

Chapter 5

The Initial Charge Separation Step in Oxygenic Photosynthesis

5.1 Introduction

Photosynthesis, the green engine of life on earth, produces molecular oxygen by using the light-driven water-plastoquinone oxidoreductase enzyme known as photosystem II.[1, 13, 14] The photosystem II-reaction center (PSII-RC) is one of the smallest photosynthetic components which can undergo charge separation (CS) and thus is an ideal model system to investigate the underlying mechanism of the initial light-energy conversion process of photosynthesis.[15–17] The PSII-RC consists of six pigments as central cofactors—two special pair chlorophylls (P_{D1} and P_{D2}), two accessory chlorophylls (Chl_{D1} and Chl_{D2}), and two pheophytins (Phe_{D1} and Phe_{D2})—arranged in a quasi-symmetric geometry (Figure 5.1a).[145, 146] These six molecules are generally referred to as RC pigments. In addition, there are two peripheral antenna Chls which are denoted as $Chlz_{D1}$ and $Chlz_{D2}$. Despite the similarity of the pigment arrangement in the D1 and D2 branches, electron transfer only proceeds along the D1 pigments. The specifics of how CS proceeds in the PSII-RC is, however, a matter of vivid debate. In particular, there remains a long-standing discussion concerned with whether the initial electron acceptor is P_{D1}[147, 148] or Phe_{D1}[149–151], i.e. whether the initial radical pair is $P_{D2}{}^{+}P_{D1}{}^{-}$ or $Chl_{D1}{}^{+}Phe_{D1}{}^{-}$. The uncertainty here is a consequence of the many closely spaced excitonic states arising from pigment-pigment interactions in the PSII-RC such that no observable structure is present even in the electronic linear absorption spectrum at cryogenic temperatures.[122, 152, 153]

To this end, the excited state dynamics of the PSII-RC has been the focus of extensive spectroscopic interest spanning over three decades. These works have included time-resolved fluorescence[155, 156], transient absorption[147, 148, 151, 157–159], optical photon-echo[150], visible pump-mid infrared (IR) probe[149], and two-dimensional electronic spectroscopy (2DES)[77, 122, 123, 160] studies. While electronic spectroscopies acutely suffer from a lack of spectral resolution in regards to the PSII-RC, the implementation of mid-IR

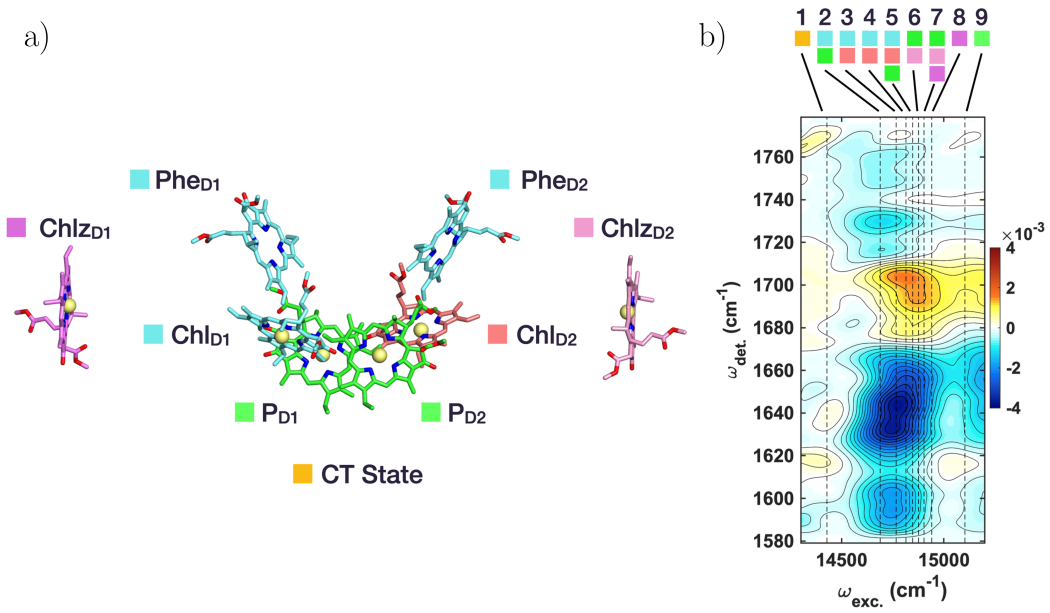

Figure 5.1: a) Pigment arrangement of the PSII-RC depicted based on the crystal structure (3WU2) reported by Umena et al.[146] b) 2DEV spectrum of the PSII-RC at 170 fs. Positive contours (red/yellow) indicate ground state bleach (GSB) features and negative contours (blue) indicate photoinduced absorption (PIA) features. The vertical dotted lines show the zero phonon exciton transition energies based on the model by Novoderezhkin et al.[154] Contour levels are drawn in 5% intervals. Colored squares on the top indicate the dominant pigments participating in each excitonic state as labeled in a).

spectroscopy has proven to be highly advantageous in addressing issues related to spectral congestion.[161–164] In particular, the keto and ester CO stretching modes of Chl and Phe show unique signatures in the mid-IR region depending on the local protein environment, electronic structure, and ionic states.[165–169] Additionally, the amide I modes of the backbone protein can be used as sensitive reporters for the electron transfer.[164, 165] These were notably demonstrated by Groot et al. in a visible pump-mid IR probe study of the PSII-RC where it was suggested that the initial electron acceptor was Phe based on its distinguishing vibrational structure.[149] However, the spectral resolution along the detection axis alone was not enough to disentangle the distinct excitonic contributions and dynamics or definitively assign the initial electron acceptor.

Many theoretical models have been developed in order to aid in experimental interpretation and to elucidate the nature of the electronic states at difference absorption wavelengths. Particularly, Stark spectroscopy suggests that the absorption spectrum of PSII is not characterized by purely excitonic states, rather it is composed of mixed exciton-charge transfer (CT) states possibly including contributions from $(Chl_{D1}{}^{\delta+}Phe_{D1}{}^{\delta-})^*$ and $(P_{D2}{}^{\delta+}P_{D1}{}^{\delta-})^*$.[170]

In an attempt to model this, one of the most sophisticated exciton models of the PSII-RC takes into account eight pigments—the six RC and two peripheral pigments—and one CS state.[154] Even in this model, there was uncertainty as to the character of the initial CS state because both $P_{D2}^{+}P_{D1}^{-}$ and $Chl_{D1}^{+}Phe_{D1}^{-}$ gave reasonable fits to the data with the former yielding slightly better agreement to experimental data considered. It is important to note here that the experimental data was, however, entirely from electronic spectroscopies.

While uncertainty surrounds the involvement and extent of exciton-CT mixing in the PSII-RC, studies have suggested that the mixed CT states are responsible for the far-red excitation of PSII.[171–173] Although the absorption of the PSII-RC and the required redox potential of water oxidation were believed to be located below 690 nm, it was demonstrated that PSII can be operated by far red light beyond 690 nm (exhibiting activities including oxygen evolution).[171, 174] Additionally, recent EPR experimental[172] and QM/MM theoretical[173] studies suggest that the far-red light excitation of PSII involves a lower lying CT state with a hole localized on Chl_{D1} rather than P_{D2}. However, just as spectral congestion obscures the assignment of the initial electron acceptor, the character of these mixed CT states remains undetermined.

Compared to the previously mentioned techniques, the emerging method of two-dimensional electronic-vibrational (2DEV) spectroscopy, which correlates electronic excitation and mid-IR detection[2, 3, 6, 53], has the potential to overcome the challenges associated with congested electronic spectra. In particular, the simultaneous spectral resolution along both the visible excitation and IR detection axis has been shown to enable the clear assignment of transient species.[3, 6, 28, 53] In this chapter, we investigated the excited state dynamics of the PSII-RC via 2DEV spectroscopy. Both highly excitation frequency-dependent spectral structure and dynamics were clearly resolved. This allowed for a broad analysis of the excitonic composition of the PSII-RC and direct insight into the involvement of mixed exciton-CT states—found to be directly prepared upon photoexcitation. Further, the spectra facilitated an assignment of the initial electron acceptor and enabled the excitation energy transfer (EET) and electron transfer pathways initiated by peripheral antenna excitation or RC pigments excitation to be disentangled.

5.2 Results and Discussion

General Insights From 2DEV Spectra and IR Band Assignments

Figure 5.1b shows the 2DEV spectrum of the PSII-RC 170 fs after photoexcitation. Of note is the significant excitation frequency ($\omega_{exc.}$)-dependence of the vibrationally resolved structure along the detection axis ($\omega_{det.}$) which, as we will demonstrate, allows for an excitonic state-specific analysis of the spectra with high frequency resolution (i.e. vibrationally resolved excitonic structure). For example, photoinduced absorptions (PIA) spanning ω_{det} = 1710-1760 cm^{-1} were seen to clearly favor the lower-lying excitonic states. Other strong indications of this $\omega_{exc.}$-dependent behavior were observed in the ground state bleach (GSB) region

spanning $\omega_{\text{det.}}$ = 1680-1710 cm^{-1} and the PIAs at $\omega_{\text{det.}}$ = 1620-1670 cm^{-1}. These three regions are of particular interest because, here, vibrational modes belonging to both the neutral and ionic forms of Chl and Phe can be clearly distinguished—thus serving as sensitive markers for the EET and CT steps leading to CS, as well as the character of the excitonic states.

The vibrational structure of the PSII-RC is not only highly $\omega_{\text{exc.}}$-dependent, but also shows a significant time-dependence. Therefore, our assignments will be based on the vibrational structure at specific $\omega_{\text{exc.}}$ corresponding to the energies of exciton 2 (14690 cm^{-1}) and exciton 8 (14940 cm^{-1}) in the model by Novoderezhkin et al.[154], which covers the relevant pigments along the D1 branch, and at either early or later waiting times (Figure 5.2).

Generally, the GSB observed at $\omega_{\text{det.}}$ = 1680-1710 cm^{-1} is assigned to the keto CO stretching mode of Chl/Phe.[165, 166, 168] On the electronic ground state, the frequency of this keto mode depends on the polarity of the environment and the presence of hydrogen bonding from surrounding media (the larger the polarity, or the stronger the hydrogen bond, the lower the frequency of the keto mode). Thus, the GSB can be used to broadly distinguish pigment contributions (further discussed in the next section). For example, in Figure 5.2, it is apparent at early waiting times that the GSB band of exciton 8 shows much more signal amplitude at 1680-1700 cm^{-1} compared to that of the exciton 2. This is in line with a light-induced Fourier transform IR difference spectroscopic study which reported that Chlz shows a GSB at 1684 cm^{-1}[165], whereas P and Phe exhibit higher and lower frequency GSBs at 1704 cm^{-1} and 1677 cm^{-1}, respectively.[165, 166, 168]

On the electronically excited state, the keto modes of Chl and Phe exhibit redshifted absorption.[149, 175] For example, in THF, the keto stretching mode in the previously measured Chl^*/Chl difference spectrum was seen to shift from 1695 cm^{-1} to 1660 cm^{-1}.[149] Correspondingly, the negative signal at $\omega_{\text{det.}}$ = 1620-1670 cm^{-1} in both exciton 2 and 8 is broadly assigned to the excited state absorption (ESA) of the keto modes of Chl and Phe. At later waiting times, however, there is a notable evolution in the vibrational structure of this region (Figure 5.2). Focusing on exciton 2, a clear dip at 1657 cm^{-1} appeared concomitantly with a new peak emerging at 1666 cm^{-1}. While both the P^+/P and Phe^-/Phe difference spectra exhibit features in this region at frequencies of 1653-1655 cm^{-1} and 1659 cm^{-1}[165, 166, 168], respectively, the signal for Phe^-/Phe agrees more closely with the observed feature at 1657 cm^{-1}. Resonance Raman spectroscopy of the PSII-RC shows no signal at 1640-1660 cm^{-1}, thus Groot et al. and Noguchi et al. suggested that the band at 1657 cm^{-1} is assigned to the amide CO mode reflecting the CS at the RC, rather than keto stretching mode of Chl or Phe.[149, 165] The band at 1666 cm^{-1} is similar to both Phe^-/Phe and P^+/P showing signal at 1662 cm^{-1} and 1663 cm^{-1}[165, 166, 168], respectively, which has been suggested as a counterpart of the previously mentioned band.[165] A more definitive assignment is reserved for later discussion.

This leaves the remaining PIA region spanning 1710-1760 cm^{-1}. While the ester modes Chl^* and Phe^* fall in this region[149], they are known to be very weak and would unlikely account for the full intensity of the observed features. Further, assuming that this region is only composed of Chl^* and Phe^* ester modes would not account for the significant $\omega_{\text{exc.}}$-

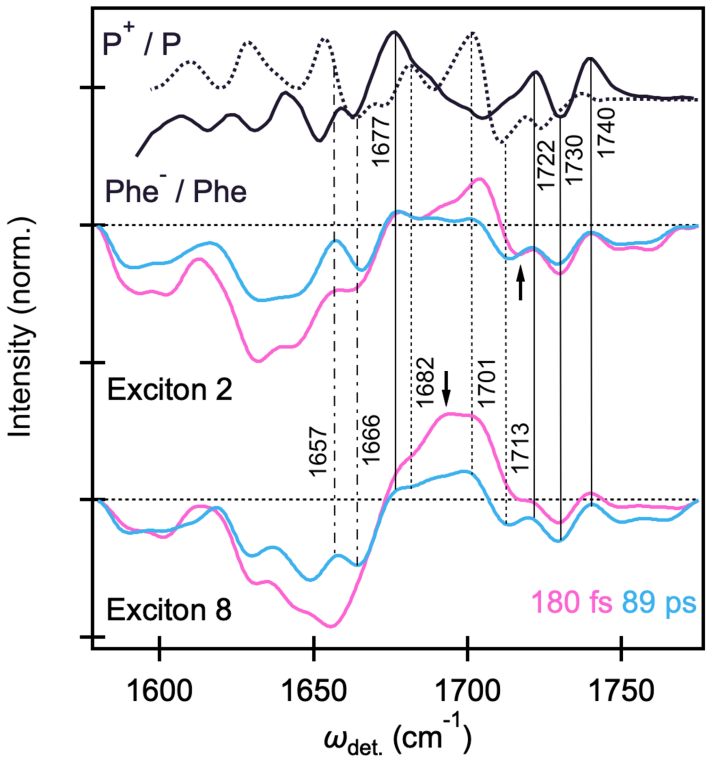

Figure 5.2: Slices of 2DEV spectrum at $\omega_{\text{exc.}} = 14690$ cm^{-1} and $\omega_{\text{exc.}} = 14940$ cm^{-1}, corresponding to the energies of exciton 2 and 8 at early (pink, 180 fs) and later (blue, 89 ps) waiting times. The difference absorption spectra of P^+/P (dotted line) and Phe^-/Phe (solid line) are shown above for comparison (where the signs have been reversed to match the convention of the 2DEV data). Vertical dotted (solid) lines indicate to band assignments corresponding P^+/P (Phe^-/Phe) while dash-dotted lines distinguish more ambiguous assignments. The black arrow in exciton 2 marks the $Chl_{D1}{}^+$ mode at 1716 cm^{-1} and in exciton 8 marks the $Chlz_{D1}$ ground state bleach. The P^+/P and Phe^-/Phe spectra are reproduced from Refs. [166] and [167].

dependence clearly present in Figure 5.1b. If this was the case, then this region should have a near uniform intensity across excitons 3 through 7 which have similar pigment contributions and exciton transition dipole strengths[154], but this is clearly not so (Figure 5.1b). As a result, contributions from Chl* and Phe* ester modes are likely small, which should leave this a relatively clear spectral window, yet, strong features are apparent in the 2DEV spectra. The Phe^-/Phe difference spectrum measured in PSII, however, shows characteristic signatures in this region, still related to the ester mode of chromophore itself or surrounding amino acid residue, with strong absorptions at 1722 cm^{-1}, 1730 cm^{-1}, and 1739 cm^{-1} (Figure

5.2).[166, 168] The corresponding peaks in the 2DEV spectrum (at 1722 cm^{-1}, 1730 cm^{-1}, and 1740 cm^{-1}), apparent at early waiting times for exciton 2 and emerging later for exciton 8, are therefore assigned to Phe^-. It should be noted that exciton 8 does show a slight negative signal around 1730 cm^{-1} immediately after photoexcitation, despite being near fully characterized by $Chlz_{D1}$. We attribute this signal to either slight contributions from the ester ESA, some degree of overlap between excitonic bands as these slices only represent the zero phonon transitions and the actual absorption has finite bandwidth, or a combination of the two. The ester mode of the Chl *a* cation (in THF), on the other hand, is known to blueshift from 1738 cm^{-1} (neutral) to 1750 cm^{-1}.[166] Yet, the P^+/P difference spectrum (Figure 5.2) does not exhibit any corresponding characteristic absorptions in this region (the ester mode of P^+ appears at 1743 cm^{-1}).[167] Thus, the bands in this region, 1750 cm^{-1} and 1764 cm^{-1}, are related to the intermediate Chl cation ($Chl_{D1}{}^+$) which are also clearly present in the structure of exciton 2 at early waiting times.

Further characteristic of the Chl *a* cation is a significantly blueshifted keto stretch, to 1718 cm^{-1}, (on the order of 25 cm^{-1}) versus neutral Chl *a* in THF.[169] At early waiting times in exciton 2, for example, a peak is observed at 1716 cm^{-1} which we assign to $Chl_{D1}{}^+$. However, at later waiting times, this peak noticeably redshifts to 1713 cm^{-1}, towards agreement with the characteristic P^+ absorption at 1711 cm^{-1}. This dynamical behavior will be the focus of later discussion.

To summarize, the significant markers tracking CS in this study are as follows: Phe^- (1722 cm^{-1}, 1730 cm^{-1}, and 1740 cm^{-1}), $Chl_{D1}{}^+$ (at early waiting times: 1716 cm^{-1}, 1750 cm^{-1}, and 1764 cm^{-1}), and P^+ (at later waiting times: 1713 cm^{-1}). The GSB of the amide CO bands at 1657 cm^{-1} and its up-shifted counterpart at 1666 cm^{-1} reflecting the CS at RC, where the former likely has predominant contributions from Phe^-, while the latter could potentially be a mixture of Phe^- and P^+.

Excitonic Composition and Charge Transfer Character

Following the vibrational assignments, we focus on a comparison of the vibrational structure at specific excitonic energies based on the model by Novoderezhkin et al.[154], in order to understand the character of the excitonic states and degree of CT mixing. Figure 5.3a shows the vibrational structure corresponding to excitons 1, 2, 5, and 8 at an early waiting time. We note again that the exciton energies discussed thus far are zero phonon lines (shown in Figure 5.1b). However, it has been reported that the actual absorption of the CT state shows a significant blue shift (∼5 nm) as a result of coupling to low-frequency phonons in the environment, compared to other excitonic bands (1∼2 nm).[154] Thus, to investigate the CT state specifically, the 2DEV signal corresponding exciton 1 as shown in Figure 5.3a was integrated in the range $\omega_{exc.}$ = 14500-14650 cm^{-1}.

At an early waiting time, the exciton 1 signal, formed directly upon photoexcitation, shows clear structure corresponding to Phe^- (1722 cm^{-1}, 1730 cm^{-1}, and 1740 cm^{-1}), and $Chl_{D1}{}^+$ (1716 cm^{-1}, 1750 cm^{-1}, and 1764 cm^{-1}). In addition, the amide CO bands reflecting CS at 1657 cm^{-1} and 1666 cm^{-1} show clear structure compared on the other excitonic states,

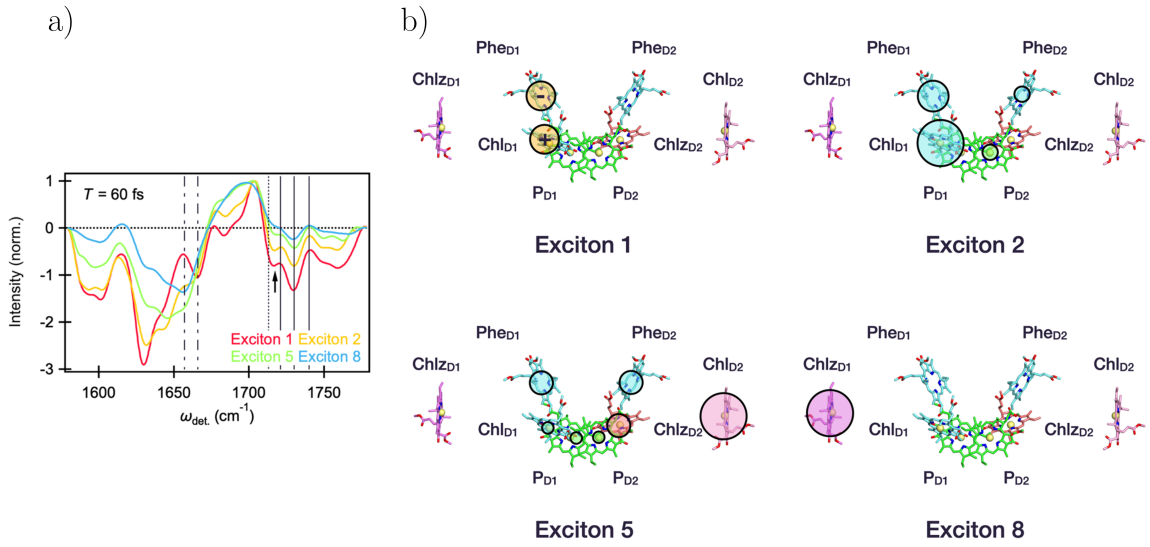

Figure 5.3: a) Slice along $\omega_{\text{det.}}$ of the 2DEV spectrum corresponding to exciton 1 (red, integrated at $\omega_{\text{exc.}}$ = 14500-14650 cm^{-1}), exciton 2 (yellow, exc. = 14690 cm^{-1}), exciton 5 (green, $\omega_{\text{exc.}}$ = 14850 cm^{-1}), and exciton 8 (blue, $\omega_{\text{exc.}}$ = 14940 cm^{-1}) at a waiting time of 60 fs. The vertical solid, dotted, and dash-dotted lines, as well as the black arrow follow the same convention as in Figure 5.2. b) Character of initial charge transfer state, exciton 1, along with the site contributions of excitons 2, 5, and 8 where the area of the shaded circles is proportional to the population of the corresponding sites based on the model of Novoderezhkin et al.[154] For clarity, the slight, additional contributions from D1 pigments, nearly identical to the relative contributions of exciton 2, were omitted from exciton 1. Likewise, the charge transfer character present in excitons 2 and 5 was precluded for simplicity.

highlighting the significant CT character of exciton 1 state. The characteristic P^+ signal (1713 cm^{-1}) only appears at later waiting times and is accompanied by evolution at both of the aforementioned band positions, as well as a decay in the 1750 cm^{-1} region assigned to Chl_{D1}^+ (Figure 5.4)—collectively indicating a conspicuous lack of initial contributions from P^+.

The lack of P^+ is in contrast to several previous spectroscopic studies that suggested there are two CS pathways in the PSII-RC.[123, 159, 160, 170] However, these experiments utilized spectroscopic methods solely in the visible region which are significantly disadvantaged when it comes to untangling the highly overlapping signals of the relevant states. In this case, the vibrational characterization of exciton 1 afforded by the application of 2DEV spectroscopy provides direct evidence that the initial CT state in the PSII-RC is characterized by $Chl_{D1}^+Phe_{D1}^-$ rather than $P_{D1}^+P_{D1}^-$ (Figure 5.3b). Such a result is consistent with a recent QM/MM calculation, utilizing range-separated TD-DFT theory and the coupled

cluster theory with single and double excitations (CCSD), which proposed that the lowest CT state was $Chl_{D1}{}^{+}Phe_{D1}{}^{-}$.[173] A previous transient IR study also suggested that the initial electron acceptor is Phe_{D1}[149], however, this study relied on an extrinsic deconvolution of the vibrational spectrum as opposed to the intrinsic ability of 2DEV spectroscopy to separate excitonic and CT contributions along the $\omega_{exc.}$ dimension. This advantage of 2DEV spectroscopy is particularly useful in the characterization of the CT state which is only weakly optically allowed and can therefore be easily obscured in other spectroscopic methods.

Considering the other states, an analysis of the GSB features of exciton 2 and 8 characterize these excitons as predominantly composed of RC pigments in the active (D1) branch and of the peripheral $Chlz_{D1}$, respectively, which is consistent with the model put forth by Novoderezhkin et al. (Figure 5.3b).[154] These assignments also substantiate that Chl and Phe at different binding position in the PSII-RC are indeed excited by different excitation frequencies—offering support for the importance of the protein environment in tuning the site energies of the embedded pigments.[173]

Exciton 2 also notably displays characteristic $Chl_{D1}{}^{+}$ and $Phe_{D1}{}^{-}$ signals at early waiting times (Figure 5.3a). In comparison to exciton 5, which is mainly composed of RC pigments in addition to $Chlz_{D2}$ (Figure 5.3b), these CT signatures in exciton 2 are markedly more pronounced. Here, we have chosen exciton 5 as a representative for the energetically intermediate excitonic states, where there is congestion even in the 2DEV spectra. However, the vibrational structure is still telling in that the additional $Chlz_{D2}$ contributions of exciton 5 should be similar to those of $Chlz_{D1}$, which is indeed reflected in the fact that exciton 5 resembles a mixture of exciton 2 (mainly RC pigments) and exciton 8 (mainly composed of a peripheral pigment). This comparison highlights the enhanced CT character in exciton 2 versus exciton 5 at early waiting times which confirms the suggestion put forth in the model by Novoderezhkin et al.[154] that exciton 2 is responsible for initiating primary charge separation. Further, in the model, exciton 1 was taken to be characterized by a CT state which borrowed intensity from the neighboring state, exciton 2. This is in agreement with the close resemblance between the GSB and ESA (particularly below 1650 cm^{-1} which is outside of the dominant window for the CS markers) structure of exciton 1 compared to that of exciton 2 (Figure 5.3a) and signifies similar overall pigment contributions. This point is made even clearer on comparison of exciton 1 versus exciton 5 or 8 where there is little similarity in these regions. Correspondingly, this indicates that exciton 2 is characterized by a mixed exciton-CT state, rather than a purely excitonic state that rapidly evolves to the CT state. The mixed character between exciton 1 and 2 also offers a mechanism through which rapid charge separation can be initiated in the RC.

Charge Separation Dynamics

To elucidate the dynamics, a global analysis of the data with sequential modeling was performed. We note that while the time constants represent a convolution of various processes, this method is able to holistically capture the spectral evolution along both frequency di-

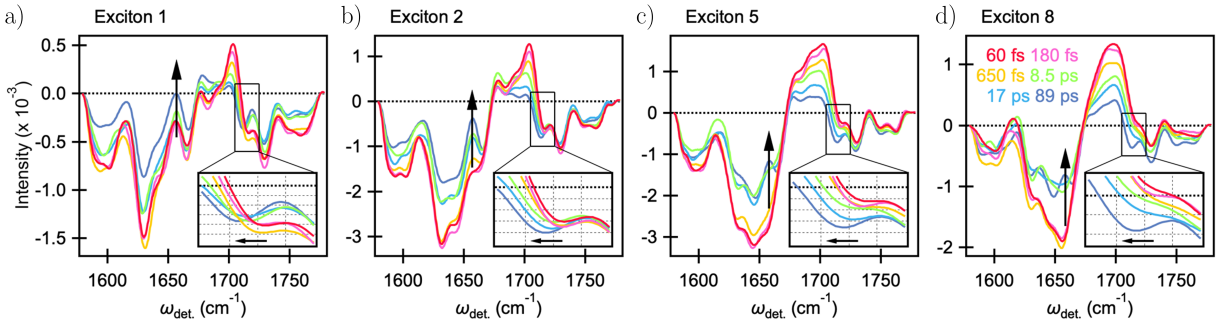

Figure 5.4: The time-dependent evolution of 2DEV spectra corresponding to excitons 1, 2, 5, and 8. Inset shows the range of $\omega_{\text{det.}}$ = 1705-1725 cm^{-1}, highlighting the red-shifting behavior of the Chl^{+} band.

mensions. Therefore, the analysis captures the $\omega_{\text{exc.}}$-dependent spectra and dynamics, the latter which can be largely disentangled via vibrational signatures as we will show. The two-dimensional-evolution associated difference spectra (2D-EADS) analysis (Figure C.1), which can be thought as the two-dimensional analogue of EADS[176], required five components for a reasonable fit (170 fs, 660 fs, 8.2 ps, 17 ps, and a non-decaying offset component beyond 100 ps, the duration of the experiment).

Figure 5.4 contains exciton-specific slices through the actual 2DEV spectra along $\omega_{\text{det.}}$ at the earliest resolvable waiting time and at subsequent waiting times corresponding to each of the above mentioned time constants. Throughout, we focus our attention on excitons 2, 5, and 8 as these states have substantially more oscillator strength than exciton 1 and therefore will have a larger influence on the obtained time constants. The evolution associated with these time constants can be interpreted such that each spectrum (or slice) evolves into the next one with the associated time constant. For example, in exciton 2 (Figure 5.4b), spectral evolution on the 170 fs timescale can be understood through a comparison of the pink and yellow slices. Noticeably, there is growth at 1657 cm^{-1}, a characteristic marker for CS. However, in exciton 5 and 8 (Figure 5.4c and 5.4d, respectively) there is no such growth indicative of CS, rather there are only slight changes in the keto GSB and ESA regions. On the 660 fs timescale (comparison of the yellow and green slices in Figure 5.4b), exciton 2 exhibits further growth at 1657 cm^{-1} and 1666 cm^{-1} while a slight shoulder begins to emerge in this region for exciton 5. This evolution is also accompanied by marked changes in the keto ESA structure. We assign both the 170 fs and 660 fs timescales to progressive completion of CS, i.e. $(\text{Chl}_{\text{D1}}{}^{\delta+}\text{Phe}_{\text{D1}}{}^{\delta-})^{*} \rightarrow \text{Chl}_{\text{D1}}{}^{+}\text{Phe}_{\text{D1}}{}^{-}$ (more pronounced for exciton 2), convoluted with EET within the excitonic manifold (more pronounced for exciton 5) and an environmental response. These timescales also agree with previous works which suggested that there is a fast component to the EET dynamics (100-200 fs time scale)[150] and that initial CS occurs within 600-800 fs[149], among others which have reported multiexponential

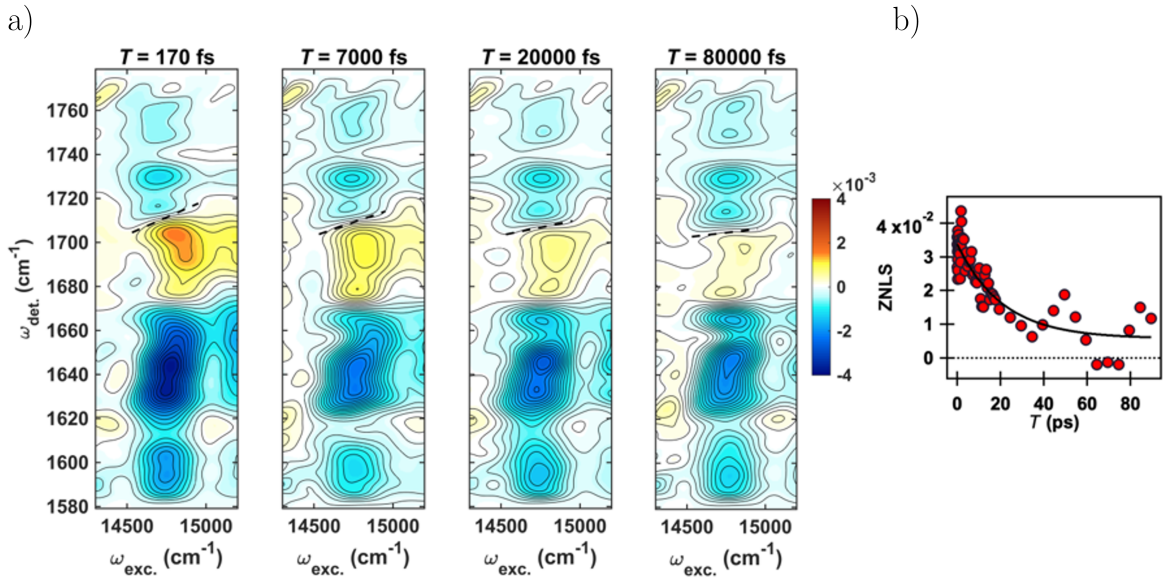

Figure 5.5: a) 2DEV spectra of the PSII-RC at different waiting times. Zero node line slope (ZNLS), obtained by a linear fit of the zero signal intensity distribution along the excitation axis, is depicted in the spectra as a dotted line. Contour levels are drawn in 5% intervals. b) ZNLS dynamics of the PSII-RC. Red dots indicate the ZNLS value at each waiting time and the black curve shows the fit result of a single exponential function (and an offset) with a time constant of 21±4 ps.

CS dynamics.[159, 160] The distinction here is that the vibrational structure allows for a targeted assessment of the dynamical components for each of the states.

On an 8.2 ps timescale, both the 1657 cm^{-1} and 1666 cm^{-1} CS markers exhibit further evolution along with a distinct, progressive redshift in the band at 1716 cm^{-1} to 1713 cm^{-1} for excitons 1, 2, and 5. This component is similar to the previously reported timescale for $Chl_{D1}{}^{+}Phe_{D1}{}^{-} \rightarrow P^{+}Phe_{D1}{}^{-}$ of 6 ps.[149] Additionally, in a previous light-induced FTIR difference spectroscopic study, it was proposed that the blue shift of the keto stretch of Chl cation is smaller for the charge delocalized dimeric Chl (∼10 cm^{-1} in the case of $P680^{+}$) compared to that of monomeric Chl (∼30 cm^{-1}).[177] Both experimental[177, 178] and theoretical[179, 180] efforts further support that the P680 cation is partially delocalized over the P_{D1} and P_{D2} pigments. Thus, we assign the slight red shift as the hole migration towards a more delocalized cationic state, i.e. $Chl_{D1}{}^{+}Phe_{D1}{}^{-} \rightarrow (P_{D1}P_{D2})^{+}Phe_{D1}{}^{-}$ (likely in addition to further environmental response to CS). Considering that the mode at 1713 cm^{-1}, the characteristic marker for P^{+}, only appears on an 8.2 ps timescale, it is very unlikely that P^{+} contributes appreciably to the features at 1657 cm^{-1} and 1666 cm^{-1} at earlier waiting times. The evolution observed around 1657 cm^{-1} and 1666 cm^{-1} at later waiting times can

therefore be understood as arising from both Phe^- and P^+.

The final 17 ps component can be understood as predominantly reflecting CS limited by EET from peripheral Chlz to RC pigments as only significant evolution at the CS markers is observed on this timescale for exciton 8 (Figure 5.4d). This timescale is also captured by the zero node line slope (ZNLS) present at $\omega_{\text{det.}} = 1710$ cm^{-1} (Figure 5.5a, dotted line) in the spectra which decays with a time constant of 21±4 ps (Figure 5.5b) and grossly indicates equilibration within the excitonic manifold. We note that while the ZNLS trends toward zero, a non-decaying component beyond the duration of the experiment (>100 ps) suggests the presence of the inhomogeneous CS due to the different conformational distributions of the proteins on the ground state.[159] This timescale also falls within the previously established range (14 ps to 37 ps determined at temperatures of 77 K and 277 K, respectively) for EET from peripheral Chlz to RC pigments.[151, 157]

5.3 Conclusion

Our results demonstrate that the CT state can be prepared directly upon photoexcitation, which is characterized by $Chl_{D1}{}^{\delta'+}Phe_{D1}{}^{\delta'-}$ ($\delta' > \delta$), and indicate that CS is facilitated by exciton-CT mixing with a contribution from $(Chl_{D1}{}^{\delta+}Phe_{D1}{}^{\delta-})^*$ throughout the excitonic manifold. The data further establishes that the initial electron acceptor in the PSII-RC is Phe_{D1} with no appreciable competition from P_{D1}—independent of excitation wavelength. These results are entirely in agreement with the recent theoretical work of Sirohiwal et al. where the $Chl_{D1}{}^{+}Phe_{D1}{}^{-}$ CT state was found to be the lowest energy excitation globally within the PSII-RC.[173] Further, no similarly low energy CT states involving $P_{D1}P_{D2}$ were found[173], thus theoretically excluding the special pair as a candidate for initial CS as our experimental data supports. This is notably distinct from the bacterial RC where CS is largely initiated at the special pair with the A branch bacteriochlorophyll acting as the primary acceptor. The distinct excitation asymmetry in the PSII-RC has been rationalized as a direct consequence of the electrostatic effect of the protein environment which likely arose as an evolutionary accommodation for water splitting in oxygenic photosynthetic systems (particularly its operation in the far-red).[171–173] However, this remains an open question as the initial CS step itself in the has long evaded clear characterization.

5.4 Experimental Methods

Sample Preparation

All procedures for sample preparation were performed in the dark to minimize exposure to light as much as possible. We first isolated PSII-enriched membranes according to the previous literature with some modifications as follows.[181, 182] We obtained spinach leaves (*Spinacia oleracea*) from a local store and kept in the dark overnight at 4 °C. The spinach leaves were briefly ground using a Waring blender in a buffer containing 50 mM MES-NaOH

(pH 6.0), 400 mM NaCl, and 2 mM $MgCl_2$ at 4 °C. The ground tissues were filtered through 4 layers of Miracloth (Millipore), and the filtered homogenate was centrifuged at 1400 × g for 10 min at 4 °C. The pellet was resuspended with a buffer containing 50 mM MES-NaOH (pH 6.0), 150 mM NaCl, and 5 mM $MgCl_2$, and resuspension was centrifuged at 4000 × g for 10 min at 4 °C. The pellet was then resuspended with a buffer containing 50 mM MES-NaOH (pH 6.0), 15 mM NaCl, and 5 mM $MgCl_2$, and resuspension was centrifuged at 6000 × g for 10 min at 4 °C. The pelleted thylakoid membranes were resuspended with the same buffer, and the concentration of Chls was quantified by using 80% (v/v) acetone as described previously.[183] The thylakoid membranes (2.1 mg Chl/mL) were solubilized with 3.75% (w/v) Triton X-100 for 20 min on ice. The solution was centrifuged at 3500 × g for 5 min at 4 °C. The supernatant was collected and further centrifuged at 40000 × g for 30 min at 4 °C. The pelleted PSII-enriched membranes were washed with the same buffer and centrifuged again at 40000 × g for 30 min at 4 °C. The PSII-enriched membranes were resuspended with a buffer containing 50 mM MES-NaOH (pH 6.0), 15 mM NaCl, 5 mM $MgCl_2$, and 400 mM sucrose, flash-frozen in liquid nitrogen, and stored at −80 °C until the following isolation procedures.

We isolated PSII-RC according to the previous literature with some modifications as follows.[184–186] The PSII-enriched membranes (1 mg Chl/mL) were solubilized with 4% (w/v) Triton X-100 in a buffer containing 50 mM Tris-HCl (pH 7.2) for 1 h on ice with gentle stirring. The solution was centrifuged at 33000 × g for 1 h at 4 °C. The supernatant was collected and loaded onto an anion exchange column (Toyopearl DEAE-650S resin) which was equilibrated with a buffer containing 50 mM Tris-HCl (pH 7.2), 30 mM NaCl, and 0.05% (w/v) Triton X-100 at 4 °C. The column was washed with the same buffer at a flow rate of 2.6 mL/min until the eluate showed the 417:435 nm ratio of about 1.16. Then, the column was subjected to a NaCl linear gradient from 30 to 200 mM at a flow rate of 1 mL/min. The green fraction eluted at 90-120 mM NaCl was collected. Then, polyethylene glycol 3350 was slowly added to the collected fraction at the final concentration of 0.325 g/mL, and the mixture was incubated for 30 min on ice with gentle stirring. The solution was centrifuged at 31300 × g for 15 min at 4 °C. The pelleted PSII RC was resuspended with the buffer containing 50 mM Tris-HCl (pH 7.2), 0.4 M sucrose, 0.1% (w/v) n-dodecyl-β-D-maltoside (Anatrace) prepared with D_2O. The PSII-RC was flash-frozen and stored at −80 °C until the 2DEV measurements were performed.

For the spectroscopic experiments, the PSII-RC sample was mixed with glycerol-d_8 in a 80:20 (v/v) glycerol:PSII-RC ratio. The sample cell was constructed from two CaF_2 plates held together with a Kapton tape spacer. The maximum optical density of the PSII-RC sample in the investigated visible range was set at ∼1.0 with a path length of 200 μm. The sample was placed in an optical cryostat (OptistatDN2, Oxford Instruments) at 77 K.

Spectroscopic Measurements

A detailed description for the 2DEV spectroscopic setup can be found elsewhere.[2] Briefly, the output of a Ti:Sapphire oscillator (Vitara-S, Coherent) was regeneratively amplified

with a 1 kHz repetition rate (Legend Elite, Coherent), an energy of 1 mJ/pulse and a pulse duration of 40 fs. The amplified pulse was divided into two and one was used to pump a home-built visible non-collinear optical parametric amplifier (NOPA). The other pulse was used to generate a mid-IR probe pulse (centered at 5.9 μm) by difference frequency generation with signal and idler pulses from a near-IR collinear OPA. The output of the NOPA (centered at 675 nm, 60 nm fwhm) was compressed to 20 fs at the sample position using a pair of prisms and an acousto-optic dispersive programmable filter (AODPF, Dazzler, Fastlite). The pulse pair was introduced to a retroreflector on a motorized translation stage to control the waiting time, T, between the pump and probe pulses. The total energy of the pump pulses was set at 80 nJ and the pulses were focused into the sample with spot size of 250 μm. The mid-IR pulse was divided by a 50:50 beam splitter to form probe and reference beams. The probe and reference beams were dispersed by a spectrometer (Triax 180, Horiba) and detected by a 64-pixel HgCdTe dual array (Infrared Systems Development). The cross-correlation between visible and mid-IR pulses was estimated to be ∼130 fs by a step-like transient IR response of a 50 μm Ge plate.

For each waiting time, a 2DEV spectrum was acquired by using the AODPF to scan the $t_{\text{exc.}}$ delay over 0-100 fs with 2.5 fs steps. For each $t_{\text{exc.}}$ delay, the signal was acquired with the relative phase between the pump pulses ϕ_{12} set by 0, $2\pi/3$, and $4\pi/3$, and the desired signal was isolated by a 3×1 phase cycling scheme.[45, 46] The excitation axis was obtained by a Fourier transformation over $t_{\text{exc.}}$. The signal was collected in the fully rotated frame with respect to $t_{\text{exc.}}$.

Chapter 6

Solvent Mediated Excited State Intramolecular Proton Transfer

6.1 Introduction

Excited state proton transfer (ESPT) plays a crucial role in the photoprotective mechanism of commercial organic photo-stabilizers and natural dyes, as well as biological molecules such as DNA and proteins.[187–193] Indigo is one such natural dye molecule, which is known for its exceptional photostability.[194, 195] Early studies proposed that this is due to intramolecular H-bonding in the excited state, which "locks" the structure in the *trans* configuration.[21] However, whether or not a proton-transfer reaction takes place to open up a rapid non-radiative pathway to the ground state has remained a subject of controversy.[21–26] Recently, experimental evidence of rapid (<1 ps) ESPT in Indigo Carmine (InC) has been reported.[25, 196] A solvent dependent transient spectroscopic study on InC refined this picture revealing that the dynamics are accelerated in polar protic solvents.[27] Nagasawa et al. proposed that intermolecular H-bonding with the solvent molecule is more effective than intramolecular H-bonding in accelerating the deactivation process. However, none of the studies to date clarify the intricate relationship between solvent-solute interaction and the ESPT.[27]

Two-dimensional electronic-vibrational (2DEV) spectroscopy has several capabilities that can clarify the excited state dynamics of the soluble form of Indigo, InC. Namely, the ability to simultaneously observe the electronic and nuclear evolution clarifies on which potential surfaces specific dynamics occur.[2, 3, 80–82] The center line slope (CLS) feature of the 2DEV spectra[37, 42] is also a unique quantity that is highly sensitive to changes in electronic structure.[47, 82] In this chapter, we employ transient infrared (IR) and 2DEV spectroscopy along with electronic structure calculations to make a comparison of the ultrafast excited state dynamics of InC in two different solvents, deuterated dimethyl sulfoxide (dDMSO) and D_2O, each having different polarities and H-bonding abilities and explore the mechanistic role of system-bath coupling in tuning the excited state deactivation. For InC in D_2O, the CLS provides a clear marker for the structural change accompanying the keto to enol transition,

corroborated by electronic structure calculations monitoring changes in the dipole moment.

6.2 Results and Discussion

The primary influence of differential solvent interactions is observed in the ground state Fourier transform IR (FTIR) spectra of InC (Figure 6.1a). In dDMSO, two peaks are observed at 1610 cm^{-1} and 1642 cm^{-1}. In D_2O, both peaks shift to a higher frequency (1616 cm^{-1} and 1645 cm^{-1}) and the vibrational line widths increase. For the steady state electronic spectra (Figure D.1), a similar spectral blue shift and broadening are observed in D_2O compared to dDMSO.

A set of transient IR measurements covering the spectral range from 1480-1660 cm^{-1} were carried out in both solvents. The transient IR spectra are shown in Figure 6.1b and 6.1c. In dDMSO, three major peaks are observed at all delay times (Figure 6.1b). In particular, there are two positive peaks at 1642 cm^{-1} and 1610 cm^{-1} corresponding to the ground state bleach (GSB) and one broad negative peak at 1530 cm^{-1} corresponding to the excited state absorption (ESA). The two GSB peaks have previously been assigned to the asymmetric stretching of two C=O groups and ring C=Cs of InC in the ground electronic state (S_0), whereas, the ESA peak was assigned to the C=O asymmetric stretching in the excited (S_1) electronic state.[21, 197] These assignments agree with our calculated IR spectra (Figure 6.1e), discussed later. In D_2O, both GSB (1645 cm^{-1} and 1616 cm^{-1}) and ESA (1525 cm^{-1}) peaks appear (Figure 6.1c) at a very similar spectral region as in dDMSO. However, three major differences are clearly observed between the evolution of the spectral bands in dDMSO and D_2O (Figure 6.1b versus 6.1c). First, a significant acceleration of the kinetics is observed in D_2O compared to dDMSO. It takes about 300 ps for the transient IR signal to decay to zero in dDMSO and less than 15 ps in D_2O. Second, an additional negative band is found around 1600 cm^{-1} in D_2O, which is completely absent in dDMSO. This 1600 cm^{-1} band is found to be distinct compared to the other three bands in two aspects: i) this band shows an initial rise (<0.5 ps) followed by an exponential decay, while the other bands show a monotonic decay (also see Figures D.3 and D.4) and ii) a continuous blue shift (1590 $cm^{-1} \rightarrow$ 1610 cm^{-1}) occurred from 0.2 ps until 1 ps for this particular band, while none of the other bands show any significant transient spectral shift. Third, all three transient bands in dDMSO show a monoexponential decay ($A_1 \exp(-t/\tau_1)$) with a time constant of about 130±20 ps whereas the corresponding bands in D_2O exhibit a biexponential decay ($A_1 \exp(-t/\tau_1) + A_2 \exp(-t/\tau_2)$) with time constants of 0.5±0.1 ps and 6±1 ps (Table 6.1). The band at 1600 cm^{-1}, however, shows triexponential kinetics with one fast rise time constant (0.44±0.05 ps) and two slower decay time constants (2.0±0.5 ps and 5.7±0.9 ps). The rise time constant of the 1600 cm^{-1} band is nearly the same as the first decay time constants of the other three bands (1645 cm^{-1}, 1616 cm^{-1}, and 1530 cm^{-1}) present in D_2O. The biexponential kinetics and the rise of the intermediate band with a rate almost identical to the decay of the other three bands, both indicate the formation of an intermediate species during the excited state decay in D_2O, which is absent in dDMSO. The assignment of the

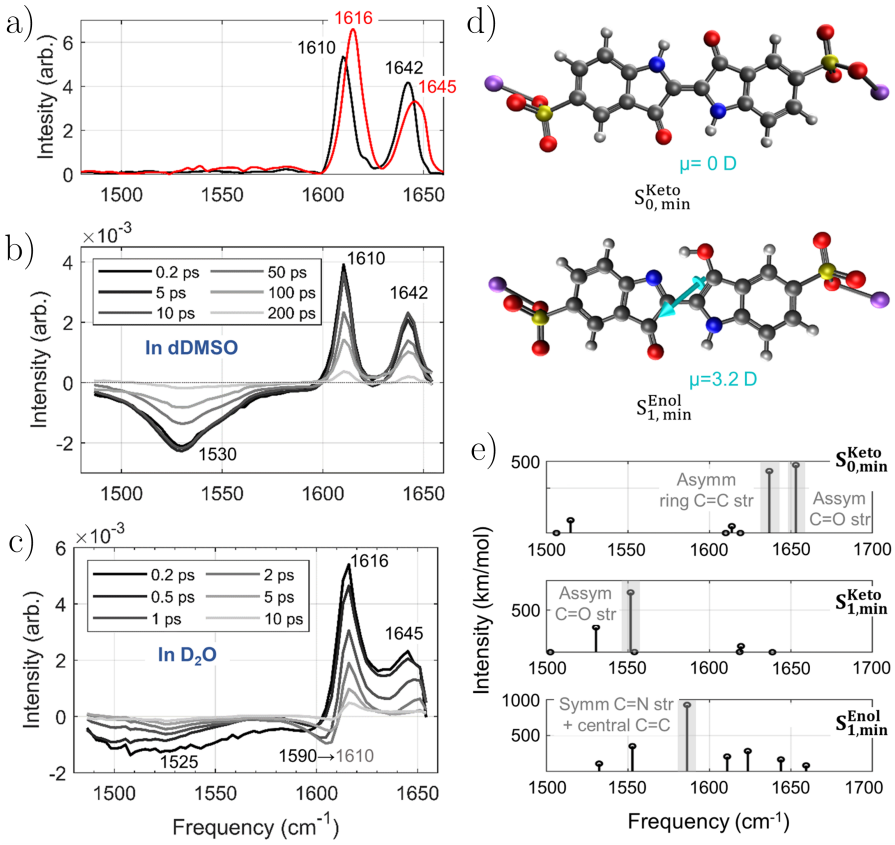

Figure 6.1: a) The solvent subtracted ground state FTIR spectra of InC in dDMSO (black) and D_2O (red). Time-resolved IR spectra of InC in b) dDMSO and c) D_2O at different time delays in the detection frequency range from 1480-1660 cm^{-1}, with $\omega_{exc.} = 16100$ cm^{-1}. d) The calculated the B3LYP/6-31+G* geometries of keto-S_0 and enol-S_1 forms of InC. The overlaid arrow represents the calculated permanent dipole. e) Calculated IR spectra for the optimized keto-S_0, keto-S_1, and enol-S_1 structures of InC. The major vibrational bands in each graph are highlighted in grey, which match the peaks in the experimental spectra a)-c).

intermediate species and the reason behind the blue shift of the 1600 cm^{-1} band will be discussed below.

The involvement of the ESPT has long been discussed in the context of excited state deactivation mechanism of InC.[23–27, 196] A gas phase ab initio calculation of Indigo showed that a low-lying conical intersection (CI) between the S_0 and S_1 potential energy surfaces exists for the mono-enol isomer.[24] More importantly, the transition from the photo-excited state to the mono-enol-S_1 minimum was found to correspond to a small energy barrier (∼0.2 eV). The barriers to the the di-enol and cis-isomer states appear to be significantly larger, at 1.06 eV and 1.36 eV, respectively. This suggests that a non-radiative route via the mono-

dDMSO	τ_1 (ps)	D_2O	τ_1 (ps)	τ_2 (ps)	τ_3 (ps)
1642 cm^{-1}	138±10	1645 cm^{-1}	0.62±0.02 (0.8)	5.7±0.7 (0.2)	-
1610 cm^{-1}	120±10	1616 cm^{-1}	0.56±0.02 (0.77)	5.0±0.2 (0.23)	-
1530 cm^{-1}	135±10	1525 cm^{-1}	0.42±0.05 (0.85)	6.0±0.8 (0.15)	-
		1600 cm^{-1}	0.44±0.05 (−0.68)	2.0±0.5 (0.15)	5.7±0.9 (0.17)

Table 6.1: Time constants from exponential fitting of the transients at different detection frequencies for InC in dDMSO and D_2O (see Figures D.2-D.4). The values in parenthesis give the amplitudes associated with each exponential. The negative and positive amplitudes represent exponential rise and decay, respectively.

enol intermediate is the most favorable pathway for the $S_1 \rightarrow S_0$ transition. With these findings in mind, we performed density functional theory (DFT) calculations to characterize the intermediate band found in our transient IR spectra. In particular, we utilized the B3LYP functional[198, 199] and 6-31+G* basis set[200] with the polarizable continuum model (PCM)[201] (using the Q-Chem 5.2 quantum chemistry package[202]) to compute the minimum energy geometries of keto and mono-enol forms on their ground ($S^{Keto}_{0,min}$) and excited ($S^{Keto}_{1,min}$, $S^{Enol}_{1,min}$) potential energy surfaces, and the corresponding IR vibrational frequencies (Figure 6.1d and 6.1e). Excited state optimizations and properties were computed via linear-response time-dependent (TD-) DFT.[203, 204]

The calculated IR spectra (Figure 6.1e) show good agreement with the experimental spectra (Figure 6.1a-c). Two major peaks (1635 cm^{-1} and 1653 cm^{-1}) appear for $S^{Keto}_{0,min}$ and match the ground state FTIR spectra. One major peak (1552 cm^{-1}) for $S^{Keto}_{1,min}$ matches the ESA peak in the transient IR spectra of InC in both dDMSO (1530 cm^{-1}) and D_2O (1525 cm^{-1}). Most significantly, a strong peak appears at 1585 cm^{-1} for $S^{Enol}_{1,min}$, which characterizes the intermediate band at 1600 cm^{-1} in the transient IR spectra of InC in D_2O, is assigned to the symmetric C−N stretch coupled with C=C stretch in the enol-S_1 state. This assignment explains the appearance of the intermediate band and subsequent spectral blue shift as follows. As the keto isomer is symmetric (C_{2h}), any symmetric vibrational mode should be Raman active (reported in Ref. [27]) and IR inactive. As soon as the proton transfer is initiated, the symmetry is broken as the keto is converted to the mono-enol form and the symmetric vibration becomes IR active. During the process of keto to enol conversion, the C−N bond begins to adopt increasingly double bond character, resulting in an increase in vibrational frequency. Furthermore, the survival of the asymmetric C=O stretch ESA band after the ESPT (∼0.5 ps) in D_2O (Figure 6.1c) is consistent with a single proton transfer mechanism, as suggested earlier[24] and, in fact, clearly rules out the double proton transfer mechanism.

The transient IR results in conjunction with the theoretical calculations, provide strong

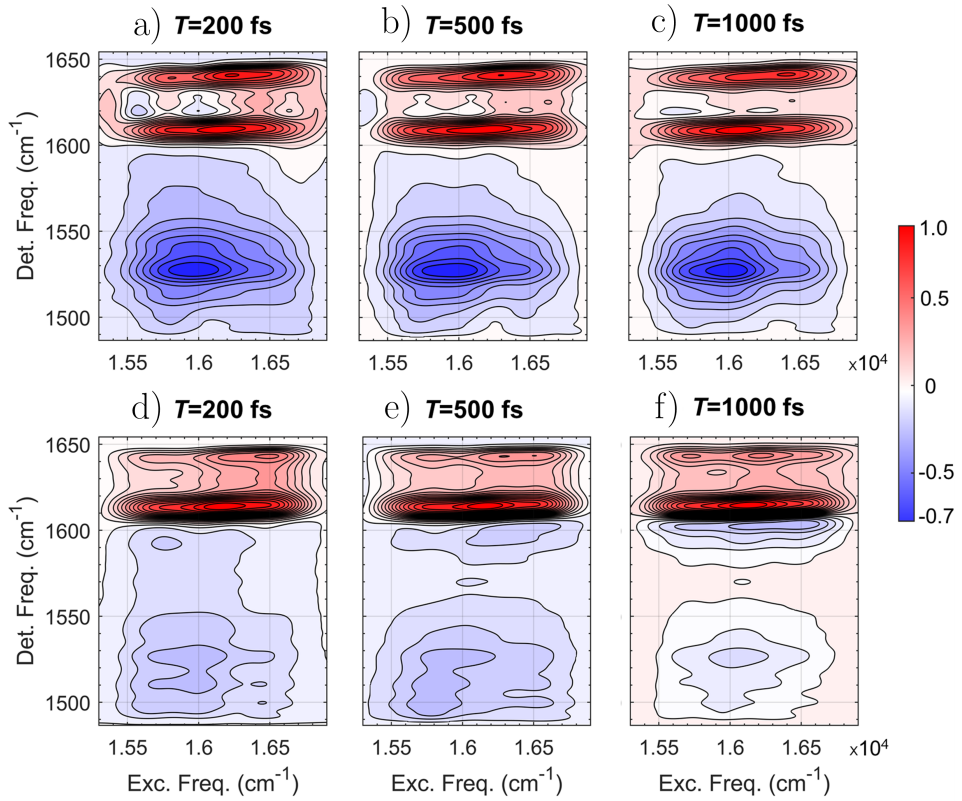

Figure 6.2: Two-dimensional electronic-vibrational (2DEV) spectra of Indigo Carmine in a)-c) dDMSO and d)-f) D_2O at different waiting times (T) in the detection frequency range from 1480-1660 cm^{-1}. Each waiting time has been normalized to unity.

evidence of the proton transferred mono-enol species in D_2O and of its absence in dDMSO. To elucidate the picture of the solvent dependent potential energy landscape, we utilized 2DEV spectroscopy. 2DEV spectra were recorded in dDMSO and D_2O with waiting times varying from 0-1 ps and 1-2.2 ps with time steps of 20 fs and 100 fs, respectively. Figure 2 illustrates typical 2DEV spectra at three different waiting times, T = 200, 500, and 1000 fs. The GSB (positive) and ESA (negative) bands are illustrated by red and blue colors, respectively. The appearance of the 2DEV spectral bands in both dDMSO and D_2O are the same as the transient IR spectra shown earlier (Figure 6.1b and 6.1c) because 2DEV spectroscopy is the two-dimensional analog of the former technique.

2DEV spectroscopy provides new information about the correlation of nuclear and electronic DOF in the form of center line slope (CLS).[42, 86] The dephasing of the vibrational modes and a change of the molecular electronic structure manifest as dynamical changes in the CLS of 2DEV spectral bands. Furthermore, the magnitude of the CLS gives a direct estimation of the relative strength of the vibrational coupling of the solvent bath with

electronic excited state versus the ground state. The CLSs are calculated by the method of conditional averaging described in detail in Ref. [47]. The slope has been calculated along the excitation frequency axis ($\omega_{\text{exc.}}$), which contains the same dynamical information that calculated along the detection frequency axis ($\omega_{\text{det.}}$).[37] The spectral region with an amplitude within 25-50% of the peak maximum (to exclude any noise/peak overlap effects) was chosen when calculating the CLS. For each spectral band, the CLS is plotted as a function of waiting time (Figure 6.3). Both in dDMSO and D_2O, the GSB bands (1642 cm^{-1} and 1610 cm^{-1} in dDMSO and 1645 cm^{-1} and 1616 cm^{-1} in D_2O) show no significant change through the waiting time (Figure 6.3a and 6.3c), whereas the ESA bands (1530 cm^{-1} in dDMSO and 1525 cm^{-1} and 1600 cm^{-1} in D_2O) start with a large negative slope and show a substantial change with increased waiting time (Figure 6.3b and 6.3d). This indicates a stronger coupling of the solvent environment with the electronic excited state (S_1) of InC compared to its electronic ground state, which agrees with the work of Nagasawa et al.[27] More significantly, a striking difference between the CLS dynamics of these ESA bands in dDMSO and D_2O is observed. The CLS of the 1530 cm^{-1} band in dDMSO shows only a rapid ($\tau = 90\pm20$ fs) exponential decay (Figure 6.3b), consistent with a simple vibrational dephasing model.[37] In D_2O, the CLS of the 1525 cm^{-1} band also shows a sharp decay initially but later ($\sim$200 fs) flips sign from negative to positive, which is followed by a decay to zero within 2 ps (Figure 6.3d). The 1600 cm^{-1} band follows the same trend following its appearance around $T = 200$ fs.

The stark contrast in the CLS plots of the ESA bands in dDMSO and D_2O clearly demonstrates different evolution of the electronic and nuclear degrees of freedom (DOF) of InC in these two solvents. The sign flip of the CLS corresponds to switching of the correlation between ($\omega_{\text{exc.}}$) and ($\omega_{\text{det.}}$). The change in correlation is directly linked to the change in permanent dipole of the molecule and its consequent effect on solvent.[47] When the system has zero dipole moment, the surrounding polar solvent molecules are arranged with no specific orientation. As soon as the system adopts a non-zero dipole, the libration of the solvent molecules will stabilize the system and create a correlation between ($\omega_{\text{exc.}}$) and ($\omega_{\text{det.}}$). When the direction of dipole moment flips by $>90°$, the stabilizing solvent environment becomes destabilizing and the correlation between ($\omega_{\text{exc.}}$) and ($\omega_{\text{det.}}$) switches its sign. We tracked the change in molecular dipole moment from $S^{\text{Keto}}_{1,\text{FC}}$ (Frank-Condon region) $\rightarrow$ $S^{\text{Keto}}_{1,\text{min}}$ $\rightarrow$ $S^{\text{Enol}}_{1,\text{min}}$ $\rightarrow$ enol S_0/S_1 minimum energy crossing point (MECP) to explain the corresponding change in the CLS. For the first three states we utilize the same level of theory used for the vibrational frequency calculations, i.e. B3LYP/6-31+G* with the PCM solvation treatment. We believe this level of theory provides an accurate description, in light of the good agreement of the calculated vertical excitation energy (2.11 eV) with the experimental value (1.99 eV), however, the lack of explicit solvent cannot properly describe the effects of solute-solvent intermolecular H-bonding. Optimization of the geometry at the MECP between enol S_0 and S_1 potential energy surfaces was performed via the branching plane algorithm[205, 206], and required use of the spin–flip variant of time-dependent density functional theory (SF-TDDFT)[207], which describes the S_0 and S_1 states on an equal footing, i.e. as excitations from a shared triplet reference state (a crucial property

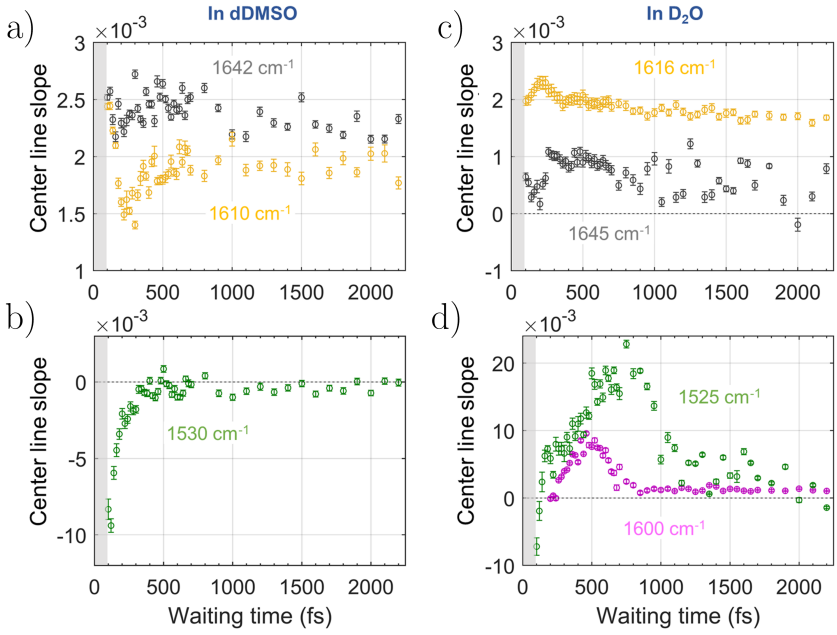

Figure 6.3: Center line slope (CLS) of different vibrational bands along the excitation axis as function of waiting time (T) for InC in a), b) dDMSO and c), d) D_2O. In a) and c), the black and yellow points represent the CLS dynamics for the specified GSB bands, whereas, in b) and d), the green and magenta points represent the CLS dynamics for the specified ESA bands. In each graph, the circles represent the experimental data points and the vertical bar represent the corresponding standard error. The grey shaded area covers the region that falls within the time resolution of the experiment.

as their energies approach degeneracy). All SF-TDDFT calculations utilize the BHHLYP functional.[208, 209] While conformations defined by rotation of the SO_3Na end groups were found to be nearly energetically degenerate (we found a range of merely 0.06 kcal/mol), the associated permanent dipole moments varied substantially (from 0 to ∼18 D). However, as the end groups are not expected to significantly affect the photophysical properties of InC (indeed, the calculated relative energetics of the relevant states along the reaction pathway are indistinguishable with and without end groups, as shown in Tables D.1 and D.2), in what follows we analyze the evolution of the dipole moments of the Indigo molecule, i.e. InC with end groups removed.

The calculated geometry of the keto-S_1 minimum (Figure D.5) is planar and the dipole moments of both InC and Indigo are zero. This is inconsistent with the initial (∼100 fs) large negative amplitude of the CLS for the ESA band in both solvents (Figure 6.3b and 6.3d). However, in a previous theoretical study of the non-adiabatic dynamics of a truncated version of the Indigo molecule, typical trajectories showed a twist of up to 25-30° around the

central C=C bond.[23] This twist breaks the symmetry and can induce a permanent dipole in InC, as is known to occur, for example, in ethylene upon photoexcitation to the S_1 state.[210] To investigate this further, we computed the energy and dipole moment of the $S_{1,\min}^{\text{Keto}}$ state as a function of dihedral angle around the central C=C bond, again using Indigo as a proxy for InC (Figure D.6), which shows that a twist up to $\sim$15° is easily accessible at room temperature ($\sim$0.6 kcal mol^{-1} / $\sim$0.026 eV) without any other external force. This would give rise to a non-zero permanent dipole (Figure D.7), supported by the large initial CLS magnitude and it is likely that inclusion of explicit intermolecular H-bonding interactions should further stabilize configurations with non-zero dihedral angles.

The optimized geometry and corresponding dipole moment of the mono-enol-S_1 minimum for InC are shown in Figure 6.1e. The enol excited state minimum is slightly uphill by $\sim$0.04 eV from the Franck-Condon keto-S_1 state. This is consistent with a temperature dependent fluorescence study which found that the activation energy for the non-radiative deactivation was higher in DMSO (8.8 kJ mol^{-1} / 0.091 eV) than in water (3.5 kJ mol^{-1} / 0.037 eV).[27] The single proton transfer process involves a change in the dipole moment shown explicitly for Indigo in Figure D.7, which correlates with the change in sign of the CLS in Figure 6.3d. The computed geometry at the S_0/S_1 MECP is very similar to that of the enol-S_1 minimum, in agreement with calculations from Ref. [24]. Our calculations also show that this MECP is $\sim$0.5 eV above the enol-S_1 minimum state, using SF-TDDFT for both states, and corresponds to a decrease in magnitude of the dipole moment, while its direction remains nearly unchanged (Figure D.7). This suggests that back proton transfer occurs after the conical intersection on the ground state potential energy surface, which can be observed in the decay of the CLS of the 1525 cm^{-1} and 1600 cm^{-1} modes back to zero after reaching a maximum (Figure 6.3d).

6.3 Conclusion

In summary, both transient IR and 2DEV spectroscopic results show that the excited state deactivation dynamics of InC is strongly solvent dependent. In dDMSO, the decay is mono-exponential with a time constant of 130 ps matching the excited lifetime ($\sim$110 ps) reported for InC in a similar protic solvent, like dimethyl formamide.[26] On the other hand, InC in D_2O shows accelerated bi-exponential kinetics via a rapid ($\sim$0.5 ps) ESPT process, supported by our ab initio calculations. The proton transfer from N−H to the C=O group can be either intramolecular or intermolecular (i.e. "indirectly" via the solvent though the formation of anionic intermediate). However, the lack of evidence of an anionic intermediate species before the S_1-enol formation excludes the latter mechanism. A similar time scale for the intramolecular ESPT (<0.5 ps) in Indigo has been suggested by Iwakura et al.[25, 196], although they suggested concluded that the enol to keto back proton transfer occurs in the S_1 state (<1 ps) inconsistent with our interpretation. In this chapter, we find that enol to keto back transfer ($\sim$6 ps) is likely to take place in the S_0 state after passing the conical intersection, in agreement with previous studies by Yamazaki[24] and Cui et al.[23]

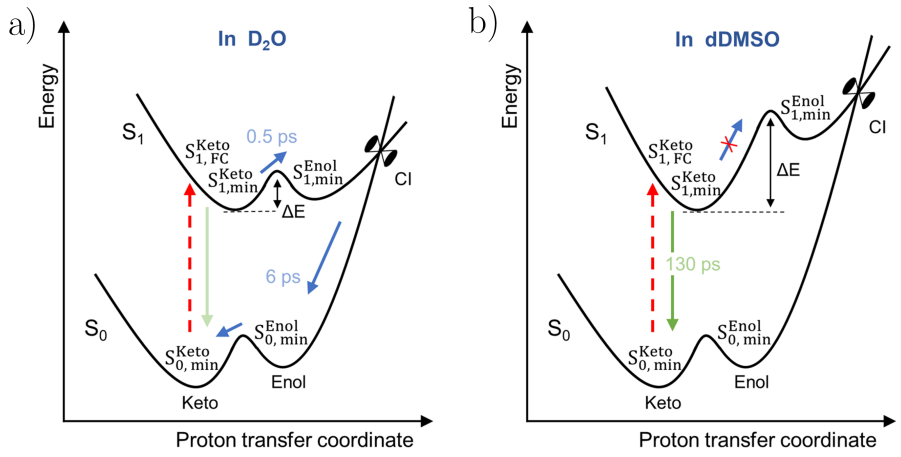

Figure 6.4: Schematic potential surfaces as a function of proton transfer reaction coordinate pathways proposed for InC in a) D_2O and b) dDMSO, respectively. In each graph, the red dotted arrow represents the photoexcitation and ΔE represents the energy barrier between keto and enol forms in the S_1 state of InC.

The combination of 2DEV experimental CLSs and electronic structure calculations provides a powerful probe of the excited state dynamics via tracking changes in electronic structure and accompanying nuclear rearrangements. Specifically for InC, two distinct excited state deactivation pathways in dDMSO and D_2O are apparent (Figure 6.4). In a non-protic solvent such as dDMSO, the barrier to enol formation is high and the conical intersection region is not reached. However, in D_2O, we find that facile excited state proton transfer makes deactivation through the conical intersection the dominant pathway.

6.4 Experimental Methods

The transient IR and 2DEV experimental apparatus with a partially collinear pump-probe geometry used for this study has been explained in detail previously.[2] In brief, the visible excitation spectrum (pulse duration: 10 fs, energy: 200 nJ) was centered around the $S_0 \rightarrow S_1$ absorption maximum of InC. The pulse duration was measured by autocorrelation based on two photon absorption in a SiC photodiode. To determine the instrument response function (and from this estimate the IR pulse duration), a cross-correlation between the IR and visible pulses in a 50 μm Ge plate was performed. The IR probe spectrum with a pulse duration of ∼70 fs covered the fingerprint frequency region from 1498-1660 cm^{-1}. For the 2DEV experiments, a pulse shaper (Dazzler, Fastlite) was utilized to derive an excitation pulse pair and to control the phase and delay between them. For each waiting time, a 2D spectrum was collected as a function of coherence time (scanned for 100 fs with 2.5 fs time step) and detected via a spectrometer (Triax 180, Horiba) coupled with a dual-array 64

element HgCdTe detector (Infrared Systems Development). At each $t_{\text{exc.}}$ delay (coherence time), the signal was measured with the relative phase, ϕ_{12}, set to 0, $2\pi/3$, $4\pi/3$ and a 3×1 phase cycling scheme was employed to remove the pump-probe background signal.[45, 46] The signal was collected in the fully rotated frame with respect to $t_{\text{exc.}}$ in order to remove the optical frequency of the pump laser. The waiting time (T) was scanned by a motor-controlled delay stage. The coherence time axis was Fourier transformed to obtain the 2DEV frequency-frequency correlation maps (Figure 6.3). All the measurements were carried out with the sample concentration of 0.7 OD at λ_{max} in a flow cell with 0.25 and 0.1 mm optical path lengths for InC in dDMSO and D_2O, respectively. A shorter path length was used to measure in D_2O to minimize absorption of the IR probe by the solvent.

Chapter 7

Electron-Nuclear Dynamics Accompanying Proton-Coupled Electron Transfer

7.1 Introduction

Proton-coupled electron transfer (PCET) is ubiquitous in chemistry and biology.[211–218] In the energy transducing membranes of all cells PCET serves to reversibly couple energy linked redox processes to the generation and use of proton-motive force. PCET is crucial to the favorable energetics of water splitting by the photosystem II reaction center (PSII-RC) of green plants and algae where it is one of the iconic processes in biology. Following excitation and charge separation (CS) in the PSII-RC, the highly oxidizing chlorophyll (P_{680}^+) oxidizes the water splitting CaO_5Mn_4 catalytic cluster via an electron transfer relay comprising a tyrosine (Tyr_z) histidine (His190) pair.[18, 19] This relay functions by using PCET associated with the reversible transfer of the phenolic proton of Tyr_z to the imidazole of His190 during the redox cycle to control both the thermodynamics and kinetics of water oxidation by P_{680}^+.[212, 217] Inspired by natural biological systems, many artificial photosynthetic systems have been developed to achieve highly efficient light-energy conversion and to understand the underlying mechanism of PCET.[218–226] Our model for P_{680} and the H-bonded Tyr_z-His190 pair is benzimidazole-phenol-pentafluorophenylporphyrin ($BIPPF_{15}$)[218–223, 225] (Figure 7.1a), where the porphyrin mimics P_{680} and benzimidazole-phenol mimics His190 and Tyr_z, respectively.

PCET reactions can be described as non-adiabatic transitions between diabatic charge-localized vibronic states because the motions of electrons, protons, and surrounding media are often strongly coupled.[213, 215] The high degree of dimensionality and mixing especially complicate photoinduced PCET dynamics, thus making the study of such phenomena challenging. Despite these complexities, recent work has begun to advance our understanding of photoinduced PCET reactions. For example, the relation between free energy gaps and elec-

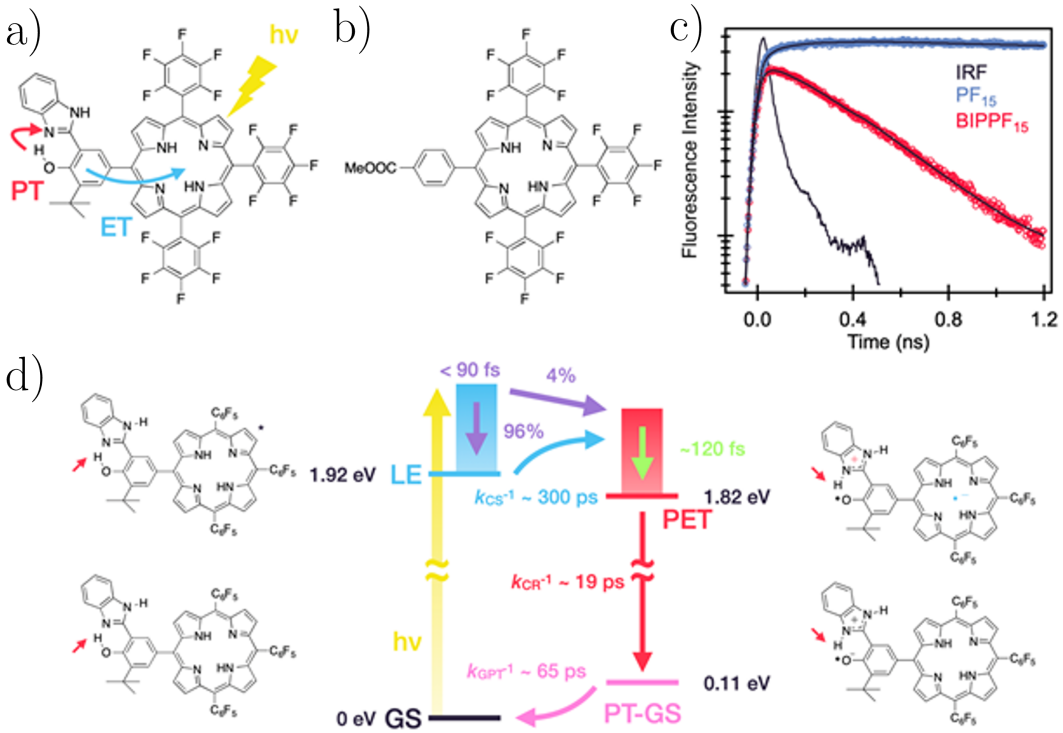

Figure 7.1: a) Molecular structure of the biomimetic photoinduced PCET system ($BIPPF_{15}$) and b) reference system (PF_{15}). c) Time-resolved fluorescence of PF_{15} and $BIPPF_{15}$ in acetonitrile with excitation at 583 nm and emission detection at 710 nm. Open circles: raw data. Solid lines: fit with 9.8 ns and 272 ps (292 ps in deuterated acetonitrile) lifetimes for PF_{15} and $BIPPF_{15}$, respectively. Both compounds had the same optical density at excitation wavelength and kinetics were collected for the same amount of time. The data at longer time is provided in Figure E.13. d) Schematic of photoinduced PCET dynamics in deuterated acetonitrile. On photoexcitation, the initial Franck-Condon population branches into two pathways (purple arrows) towards: i) a relaxed locally excited (LE) state which is followed by a slow, activated PCET pathway (blue arrow) with k_{CS}^{-1} ~300 ps (calculated from fluorescence decay lifetimes in deuterated acetonitrile) to the unrelaxed proton and electron transferred (PET) state (vide infra), and ii) an unrelaxed PET state within 90 fs. From there, the unrelaxed PET state rapidly evolves towards the relaxed product with concomitant charge transfer on a time scale of 120 fs (green arrow). The PET state relaxes to a proton transferred-ground state (PT-GS) with k_{CR}^{-1} ~19 ps through charge recombination (CR) (red arrow), and subsequently returns to the original GS with k_{GPT}^{-1} ~65 ps (pink arrow). The energy levels of LE (1.92 eV), PET (1.82 eV), and PT-GS (0.11 eV) states were estimated by absorption and fluorescence spectra, the Rehm-Weller equation and quantum chemical calculation, respectively.

tron transfer (ET) kinetics was successfully described by non-adiabatic PCET theory.[224] Another study revealed that optical excitation can directly prepare the electron-proton transfer photoproduct.[227]

However, it is important to note that all of these previous time-resolved spectroscopic studies have regarded the photoinduced PCET reaction as a state-to-state transition.[224, 227–229] Yet, contrary to this treatment, electronically excited states are typically best described via mixing of different electronic configurations, and the degree of mixing can change throughout the course of the movement of electrons and protons.[129, 230] Moreover, photoexcitation leads a system into a non-equilibrium distribution of many vibronic energy levels.[231] For the above reasons, the mechanism of ultrafast photoinduced PCET remains essentially unexplored. If the process has a free energy barrier, dynamical studies of the system are incapable of following the evolution of the electronic/vibrational distribution as the fractional population of states other than the initial and final states is very small at all times. In contrast, ultrafast relaxation proceeding without a barrier has the potential to enable tracking of the continuous evolution of the electronic and vibrational distribution. Such measurements, then, can provide a significantly more nuanced view of PCET. As we show below the molecule $BIPPF_{15}$ (Figure 7.1a) undergoes excited state PCET on two timescales—ultrafast (<fs) (4%) and a few hundred ps (270-290 ps) (96%), with the latter, relaxed PCET likely having to overcome a free energy barrier. For the reasons just outlined, we focus on the ultrafast PCET, as this process reveals details that must underlie many PCET reactions on all timescales, but are simply not discernable in these systems. For completeness, we give a thorough analysis of the longer timescale kinetics and spectroscopy in Appendix E. The recently developed spectroscopic technique, two-dimensional electronic-vibrational (2DEV) spectroscopy, which correlates electronic and nuclear evolution, is particularly suited for studies of PCET.[2, 3, 37, 47, 109] Unlike degenerate multidimensional Fourier transform spectroscopies, such as two-dimensional electronic or infrared (IR) spectroscopy, 2DEV spectroscopy has a number of advantages for elucidating the non-equilibrium dynamics of vibronic states. These include: i) simultaneous spectral resolution along both visible excitation axis and IR detection axis, which enables the clear assignment of transient species as the IR frequencies are now dispersed along the excitation axis, ii) high spectral sensitivity to the mixing of electronic/vibronic states, which significantly alters vibrational transition moments, and iii) identification of the center line slope (CLS) of the spectral features, which is related to a cross-correlation of vibrational and electronic dipoles and is very sensitive to significant changes in electronic structure.

Previously, the excited state dynamics of a high-potential porphyrin bearing two pentafluorophenyl groups (PF_{10}), $BIPPF_{10}$, were investigated by means of transient absorption spectroscopy.[219, 221] In acetonitrile, upon photoexcitation of the porphyrin moiety, the lifetime of $BIPPF_{10}$ was determined to be 430 ps—significantly shorter than that of PF_{10} ($\sim$10 ns)—suggesting that the excited state is quenched by ET. However, the spectrum of the CS state was not observed. Thus, it was concluded that the system undergoes inverted kinetics, wherein CS is slower than CR. The slower CS reaction was rationalized by the small driving force.[219, 221] In the above study, the broad and featureless transient spectra of the PF_{10}

ion in the visible range made it difficult to detect the PCET product during the course of the reaction and therefore even harder to potentially resolve additional fast PCET pathways. Furthermore, the relatively large molecules involved rendered the CS states challenging to accurately and tractably describe with traditional quantum chemical calculations.

In this study, we investigated the excited state dynamics of 5-[4-hydroxy-3-(benzimidazole-2-yl)-5-*tert*-butylphenyl]-10,15,20-*tris*(pentafluorophenyl)porphyrin[232], ($BIPPF_{15}$, Figure 7.1a) by means of transient IR and 2DEV spectroscopies and specialized density functional theory (DFT) calculations. Compared to $BIPPF_{10}$, $BIPPF_{15}$ contains an additional pentafluorophenyl group, resulting in a less negative $E_{1/2}$ value for the porphyrin/porphyrin$^-$ redox couple, thus, a larger driving force and a faster rate of photoinduced ET can be expected. By combining IR spectroelectrochemical (IRSEC) measurements with electronic-vibrational spectroscopies, we can clearly track the PT and ET dynamics associated with the BIP radical cation and porphyrin radical anion, respectively.[218, 222, 223] The spectroscopic data was complemented by ab initio electronic structure calculations using a long-range-corrected (LRC) hybrid functional[233, 234], which can be optimally and nonempirically tuned to provide a robust and efficient characterization of the CS state, even for large molecules.[235–237] As a control, we also investigated the dynamics of the reference porphyrin system, 5-(4-carbomethoxyphenyl)-10,15,20-*tris*(pentafluorophenyl)porphyrin (PF_{15}, Figure 7.1b).[232]

7.2 Results and Discussion

Fluorescence Lifetime Measurement

Figure 7.1c shows time-resolved fluorescence decays of PF_{15} and $BIPPF_{15}$ in acetonitrile. The lifetime of $BIPPF_{15}$ was 272 ps (292 ps in deuterated acetonitrile), which is much shorter than that of PF_{15} (9.8 ns), indicating that ET takes place within this time scale. Fluorescence kinetics were collected for the same amount of time with the same experimental setup, and the excitation was set at 583 nm where PF_{15} and $BIPPF_{15}$ have the same extinction coefficient, and at identical concentrations. Exponential fits with instrument response function (IRF) deconvolution give normalized pre-exponential factors of 1.00 versus 0.75 for PF_{15} and $BIPPF_{15}$, respectively. This indicates that some fraction of the fluorescence intensity of $BIPPF_{15}$ is lost at short times (within the IRF of the time-resolved fluorescence measurement), in agreement with ultrafast PCET occurring from unrelaxed levels as will be discussed in detail below.

Electrochemistry

IRSEC measurements were performed to examine the change in the IR spectra following the oxidation or reduction of $BIPPF_{15}$. Upon oxidation of $BIPPF_{15}$ (Figure 7.2a), a new band at 1552 cm^{-1} appeared. This band is indicative of the benzimidazolium cation (NH in-plane bending vibration) generated following a PT from the phenol moiety, as observed in

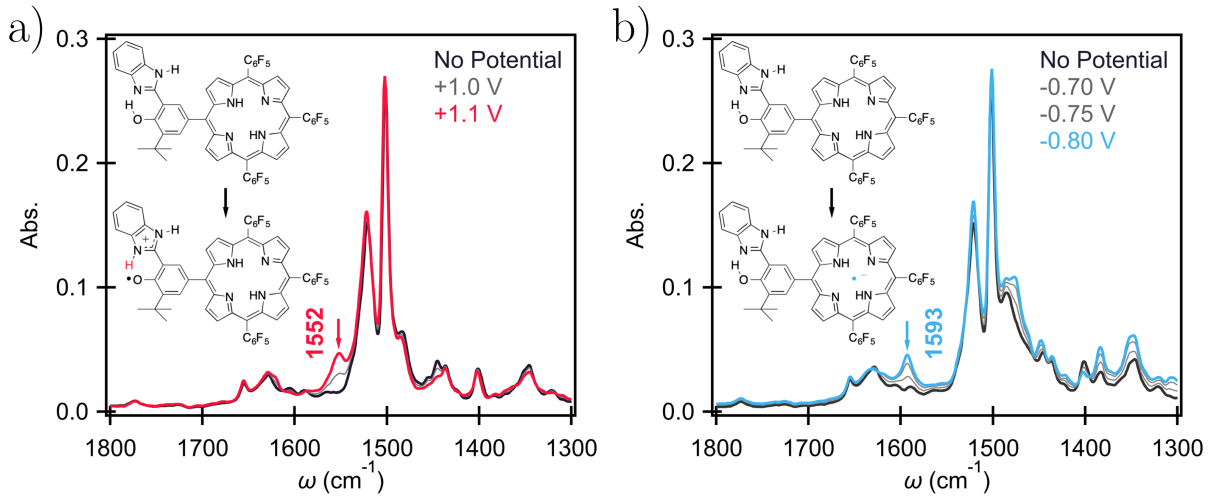

Figure 7.2: a) Upon oxidation of $BIPPF_{15}$, a band at 1552 cm^{-1} appeared, and is assigned to benzimidazolium cation formation following a PT from the phenol moiety. b) Upon reduction of $BIPPF_{15}$, a band at 1593 cm^{-1} appeared, which is indicative of porphyrin radical anion formation. Spectra were recorded in dry deuterated acetonitrile solution with 0.1 M $TBAPF_6$. The colored curves show oxidized (red) or reduced (blue) species. In a) and b), the black curve indicates the neutral species. The applied potentials indicated in the figure legend are versus a silver wire reference electrode (see Section 7.4 for further details).

earlier studies.[218, 222, 223] Upon reduction of $BIPPF_{15}$ (Figure 7.2b), a new band that is characteristic of porphyrin radical anion formation was observed at 1593 cm^{-1}.[225] Quantum chemical calculations at the B3LYP/6-31G** level find a mode with similar frequency for the anion which involves only atoms of the porphyrin. Therefore, the bands at 1593 cm^{-1} and 1552 cm^{-1} are used as evidence for ET and PT, respectively.

The midpoint potentials ($E_{1/2}$) for the $BIPPF_{15}^{+}/BIPPF_{15}$ and $BIPPF_{15}/BIPPF_{15}^{-}$ redox couples were estimated to be +1.05 and −0.83 V versus SCE, respectively, by cyclic voltammetry measurements (Figure E.1). By assuming the center-to-center distance between the phenol and porphyrin moieties to be $l = 6.4$ Å and excited state (S_1) energy to be $E_{00} = 1.92$ eV, the driving force can be estimated from the Rehm-Weller equation to be $\Delta G = -100$ meV (other parameters and details are provided in Appendix E). The excited state characterized by electron transfer from the phenol moiety of $BIPPF_{15}$ to the porphyrin, but without proton transfer, is designated as the CSS species in Figure 7.6 and is calculated to be 3.35 eV above the GS, resulting in an endergonic pathway following photoexcitation.

Transient IR Spectroscopy

Transient IR spectroscopy was applied to $BIPPF_{15}$ and PF_{15} to elucidate the excited state kinetics. For PF_{15} (Figure 7.3a), the reference system, photoinduced increase in transmission were observed at 1481 cm^{-1}, 1503 cm^{-1}, and 1515 cm^{-1}, and are assigned to ground state bleach (GSB) signals. Excited state absorption (ESA) bands were observed at 1495 cm^{-1}, 1522 cm^{-1}, 1546 cm^{-1}, and 1606 cm^{-1}. The lifetime of PF_{15} was longer than the detection limit of our experimental setup of 500 ps.

The spectral features of $BIPPF_{15}$ (Figure 7.3b) were similar to those of PF_{15} at frequencies

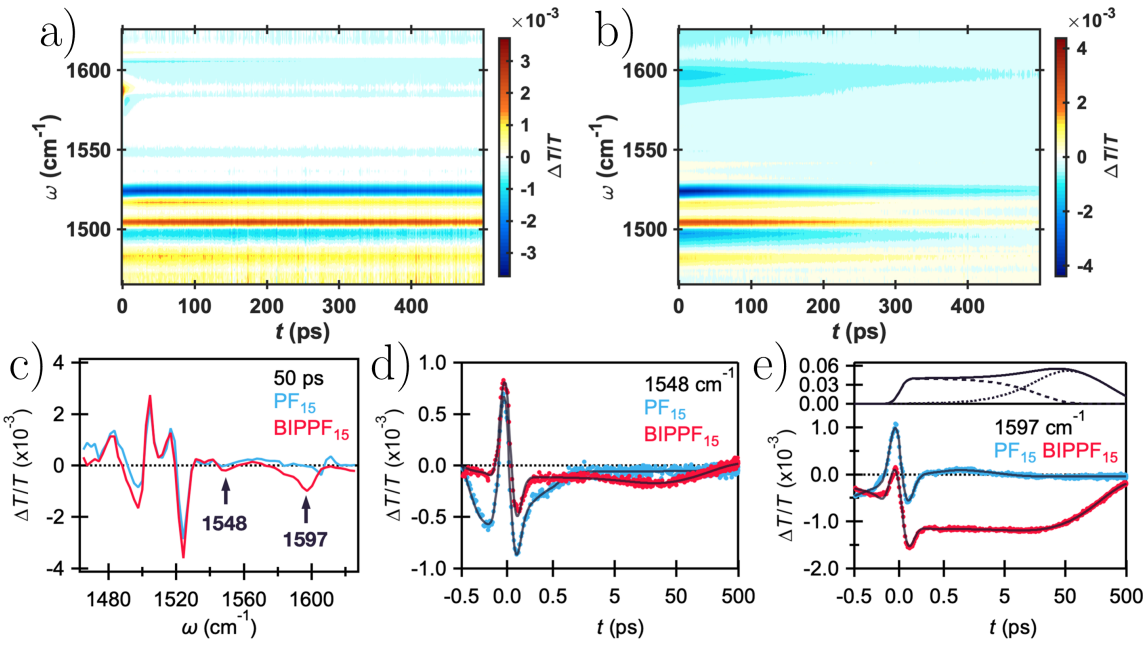

Figure 7.3: Contour plot of transient IR spectra of a) PF_{15} and b) $BIPPF_{15}$ in dry deuterated acetonitrile. Positive signal (red contours) represents ground state bleach and negative signal (blue contours) represents excited state absorption. c) Transient IR spectra of PF_{15} (blue) and $BIPPF_{15}$ (red) at 50 ps. This delay time was chosen to avoid the interference from vibrational relaxation (within 10 ps) observed in PF_{15}. Time traces of the transient IR signals of PF_{15} (blue) and $BIPPF_{15}$ (red) probed at d) 1548 cm^{-1} and e) 1597 cm^{-1}. The time axis is linear from -0.5 ps to 0.5 ps and logarithmic at later delay times. The black curves show the fit results using the fitting parameters summarized in Table E.2. Population dynamics of the PET state for ultrafast unrelaxed (dashed curve) and slower relaxed (dotted line curve) pathways, along with the sum total (solid curve), as obtained by the model (Figure E.10) are also plotted at the top of e). The center wavelength of excitation was 580 nm (Figure E.2).

below 1540 cm^{-1}. However, the lifetime of $BIPPF_{15}$ (290 ps) was significantly shorter than that of PF_{15}, indicating that the excited state is quenched by ET. By comparing the spectra at frequencies above 1540 cm^{-1} (Figure 7.3c), three additional negative bands were observed at 1548 cm^{-1}, 1580 cm^{-1}, and 1597 cm^{-1} for $BIPPF_{15}$. The bands at 1548 cm^{-1} and 1597 cm^{-1} were similar to those observed in the IRSEC measurements (Figure 7.2), indicating that both PT and ET, respectively, take place in $BIPPF_{15}$ following photoexcitation of the porphyrin moiety. Small frequency differences between the transient IR and IRSEC measurements are ascribed to the IR Stark effect. The band at 1580 cm^{-1} is likely due to a byproduct or a photodegraded sample as the relative intensity of this band changes in different measurements. It should be noted that $BIPPF_{15}$ shows larger ESA signals at 1495 cm^{-1} and 1522 cm^{-1}, however, to avoid the influence of overlapping bands from the signal of the LE state, we focus on the dynamics of the 1548 cm^{-1} and 1597 cm^{-1} bands in the following. As noted above, both the 1548 cm^{-1} and the 1597 cm^{-1} modes are quite delocalized on BIP and PF_{15} moieties, and act as reporters of the proton and electron moving, respectively, rather than as key components of the reaction coordinate.

The time traces at 1548 cm^{-1} and 1597 cm^{-1} were analyzed to elucidate the kinetics (Figure 7.3d and 7.3e). Compared on a picosecond time scale, the ESAs of $BIPPF_{15}$ showed an increase in the signal intensity with a few tens of picoseconds, while such a change was absent in PF_{15}. Here, the dynamics suggest that the PCET reaction can be viewed simply as a kinetic phenomenon where the rise of the signal reflects the CR rate in the previously proposed inverted kinetics scheme (Figure 7.1c where $k_{CS} \ll k_{CR}$)[221] and the small signal change can be rationalized by the relation between the rate constants for the k_{CS}^{-1} ~300 ps (calculated from fluorescence lifetime of $BIPPF_{15}$ and PF_{15}) and the k_{CR}^{-1} ~19 ps (see Appendix E.5 for more detail). However, the remainder of the discussion will focus on 2DEV experiments and analysis which reveals an additional ultrafast PCET pathway.

Initial evidence for such pathway is that, notably, the ESAs of $BIPPF_{15}$ at 1548 cm^{-1} and 1597 cm^{-1} appeared immediately after the photoexcitation. The immediate appearance of these bands suggests that a PET state is either: i) prepared directly by photoexcitation or ii) formed via an additional non-equilibrium pathway which proceeds within our instrument response time of ~90 fs. However, the small negative signal at 1546 cm^{-1} also appeared instantaneously for PF_{15}, suggesting the need for further data before the 1548 cm^{-1} band is assigned to PT at short times.

2DEV Spectroscopy

In order to make definitive assignments and probe further into the dynamics and mechanism of a potential additional unrelaxed PCET pathway in $BIPPF_{15}$, we recorded 2DEV spectra of PF_{15} and $BIPPF_{15}$ (Figure 7.4a and 7.4b). The spectral features of the 2DEV spectra along the excitation axis at 17000 cm^{-1}, which corresponds to the peak of the optical absorption spectra, were the same as in the transient IR spectra, as expected. The ESA bands at 1597 cm^{-1} and 1548 cm^{-1} of $BIPPF_{15}$ become weaker at shorter excitation frequenices, implying that the ultrafast PCET may not depend only on the amount of excess energy. It can also be

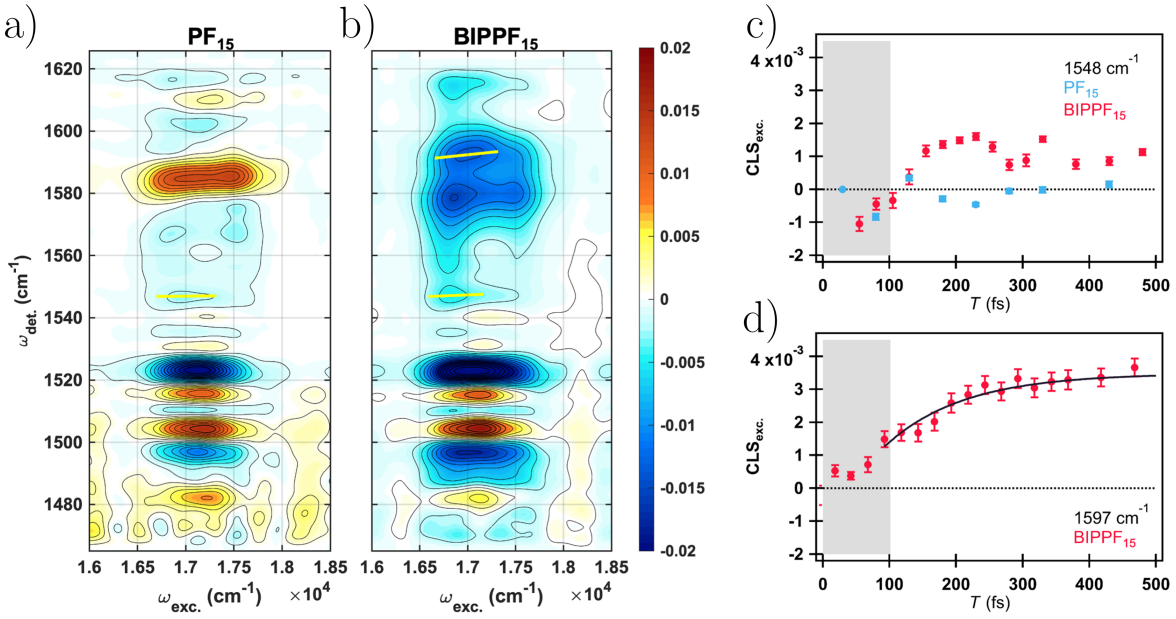

Figure 7.4: 2DEV spectra of a) PF_{15} and b) $BIPPF_{15}$ at 500 fs. Positive signals (red contours) indicate ground state bleaches and negative signals (blue contours) represent excited state absorptions. Contour levels are drawn in 5% intervals. Yellow lines indicate the CLS (with respect to the excitation axis) obtained by a linear fit of the conditional average.[47] CLS dynamics of PF_{15} (blue) and $BIPPF_{15}$ (red) at c) 1548 cm^{-1} and d) 1597 cm^{-1}. The time range where visible and IR pulses overlap, <100 fs, is indicated by the shaded area. The error bars show standard error of the CLS, obtained by a linear fit of the conditional average.[47] The black curve indicates the fit result of the CLS dynamics with a single exponential function. The CLS dynamics of the other observed bands and corresponding fit results are shown in Figures E.3-E.6.

seen that negative bands at 1546 cm^{-1} and 1548 cm^{-1} were observed for PF_{15} and $BIPPF_{15}$, respectively.

The CLS dynamics of these two bands showed significant differences between the two species (Figure 7.4c). We note that the proton and partial charge have transferred before the temporal range over which we discuss the CLS. In a previous study, we showed that the CLS is directly related to the solvation correlation function for the vibrational degrees of freedom and the time constant of its decay is close to the vibrational dephasing time[37] and more recently provided a detailed derivation for the 2DEV lineshape and its evolution.[38] Here, we provide a general, approximate form of the center line slope (CLS) in a 2DEV experiment where we take it to be proportional to the frequency-frequency correlation function[38]

$$\mathrm{CLS} \propto \langle \delta\omega_{\mathrm{elec.}}(T)\delta\omega_{\mathrm{vib.}}(0)\rangle \tag{7.1}$$

where $\delta\omega(T)$ is the fluctuating frequency for a given electronic or vibrational transition. We note that while such a direct proportionality may not hold in every case[238, 239], this approximate form is nonetheless useful to gain intuition for the behavior of the CLS and the governing system dynamics. Particularly, it is straightforward to demonstrate how the CLS in a 2DEV experiment is a cross-correlation between electronic and vibrational dipoles if we simply approximate the fluctuating transition frequency as

$$\delta\omega_{\text{elec.}} \propto \Delta\mu_{\text{elec.}} E_{\text{sol.}} \tag{7.2}$$

$$\delta\omega_{\text{vib.}} \propto \delta\mu_{\text{vib.}} E_{\text{sol.}} \tag{7.3}$$

where $\Delta\mu_{\text{elec.}}$ is the difference in the dipole moment between the ground and excited states of the given transition, $\delta\mu_{\text{vib.}}$ is vibrational Stark tuning rate, and $E_{\text{sol.}}$ is the solvent electric field. The resulting form of the CLS can then be written

$$\text{CLS} \propto \langle E_{\text{sol.}}(T) \cdot [\Delta\mu_{\text{elec.}}(T)\delta\mu_{\text{vib.}}(0)] \cdot E_{\text{sol.}}(0) \rangle \tag{7.4}$$

which makes it clear that dynamical changes in the direction and magnitude of the electronic dipoles, in addition to solvent rearrangement, are key drivers of the CLS. For PF_{15}, the CLS of the 1548 cm^{-1} band remained near zero after photoexcitation (Figure 7.4c, blue), indicating a very similar solvent environment for the mode in both electronic states. On the other hand, for $BIPPF_{15}$, the CLS of the band at 1548 cm^{-1} was positive and essentially constant over 200-500 fs (Figure 7.4c, red). In this case, the solvent configuration is clearly different after 150 fs and we ascribe the positive CLS to the product of the PCET reaction, which has a large electric dipole moment. This also suggests the presence of an additional, very rapid, unrelaxed pathway for the PCET reaction, with a time scale similar to or less than the current experimental time resolution of $\sim$90 fs. Notably, the CLS of the 1548 cm^{-1} band shows a rise over approximately the initial 200 fs (Figure 7.4c). However, this band has quite low intensity and so we turn to a more quantitative discussion of the CLS behavior of the ET band at 1597 cm^{-1} (Figure 7.4d). The CLS of the 1597 cm^{-1} band is positive and observed to rise to a plateau with a time constant of 120$\pm$20 fs. Such a rapid rise was not observed in the transient IR signal of the band at 1597 cm^{-1} (Table E.2), which suggests that the underlying physical process is distinct from population dynamics. The CLS is uniquely sensitive to the correlation between electronic and nuclear degrees of freedom and correspondingly contains crucial information on this unrelaxed pathway. To further interpret the rapid changes in the CLS, we turn to electronic structure calculations.

Quantum Chemical Calculations

Quantum chemical calculations were performed within the Born-Oppenheimer approximation, which neglects the quantum-mechanical nature of nuclear motions in utilizing fixed nuclei to parameterize the electronic structure problem. Nevertheless, these calculations provide important insight into the CLS dynamics. The natural transition orbital (NTO)[240]

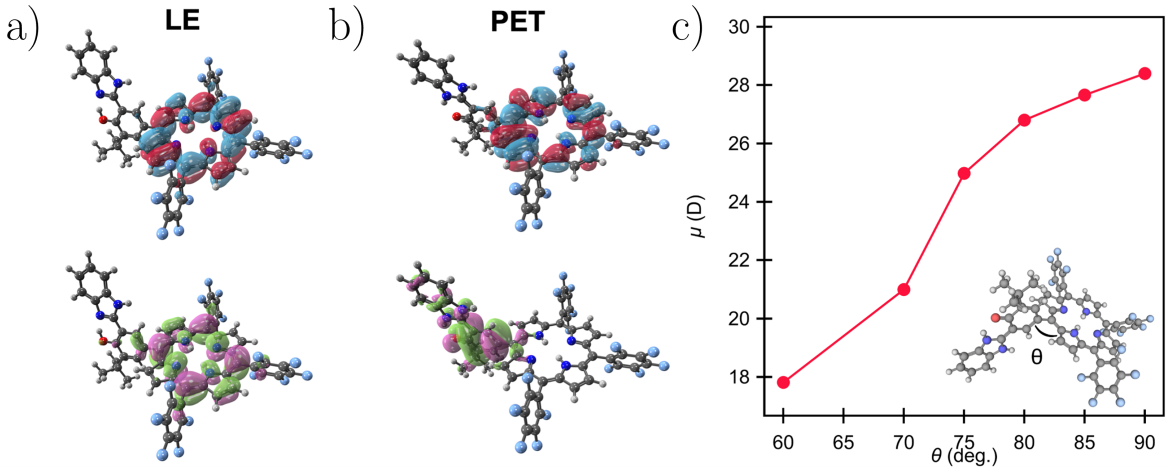

Figure 7.5: The dominant NTO pairs for a) locally excited (LE) and b) proton and electron transferred (PET) states of $BIPPF_{15}$. For each state, the HONTO is on the bottom and LUNTO is on the top. c) Calculated dipole moment of $BIPPF_{15}$ as a function of dihedral angle between BIP and porphyrin moieties. The optimized structure of the PET state of $BIPPF_{15}$ is also shown in the inset.

pairs of $BIPPF_{15}$ for the locally excited (LE) and proton and electron transferred (PET) states are shown in Figure 7.5a and 7.5b. For the LE state, both the highest occupied NTO (HONTO) and lowest unoccupied NTO (LUNTO) are localized on the porphyrin moiety, indicating that the permanent electric dipole moments are very similar in both the electronic ground and excited states, resulting in minimal solvent rearrangement upon photoexcitation. As the $BIPPF_{15}$ molecule evolves from the LE state to the PET geometry, the hole (HONTO) localized on the porphyrin moiety moves to the phenol moiety, while the LUNTO essentially remains at the same distribution. This confirms that the PET state is characterized by the transfer of an electron from the BIP to the porphyrin. As the electron density distribution of the PET state is significantly different from that on the ground state potential energy surface and also from that of the LE state, the emergence of a large electric dipole moment in the PET state can be expected to cause a dramatic change in the solvent configuration, which in turn is reflected in the CLS as observed.

In addition, calculations revealed a reaction pathway for the photoinduced PCET, which lays the groundwork for an interpretation of the rise of the CLS. The optimized structures of $BIPPF_{15}$ in the ground state (GS), LE, and PET states are shown in Figure E.14. The calculated values of the dihedral angle between BIP and porphyrin subunits are 67.4°, 62.6°, and 93.1° for the GS, LE (minimum), and PET states, respectively. The orthogonal dihedral angle for the PET state is indicative of twisted intramolecular charge transfer (TICT) where the twisting angle plays a significant role in the reaction coordinate, serving to stabilize the CS states.[241] While optimally tuning (OT) the LRC-ωPBEh functional lowers the calcu-

lated energy of the PET state by ∼0.42 eV such that it becomes the lowest singlet excited state in the 93.1° geometry, this PET state is predicted to lie above the Franck-Condon LE state (67.4°) by ∼0.27 eV. However, approximating the strong electrostatic interactions between the dipole moment of a TICT state and polar acetonitrile solvent molecules with a polarizable continuum model has been shown to lead to systematically overestimated excitation energies (by as much as ∼0.39 eV) versus experiment even with the OT-LRC-ωPBEh functional.[242] In light of this, our calculation still serves to corroborate our experimental result that this pathway is slightly exergonic ($\Delta G = -0.10$ eV as determined via electrochemical measurements).

Moreover, to interpret the evolution of the CLS dynamics, the dipole moment of the PET state was calculated as a function of dihedral angle over the range 60° to 90°, corresponding to the evolution from the minimum of the LE state to the minimum of the PET state (Figure 7.5c). We note that calculated densities (and therefore, dipole moments) are much less sensitive to the choice of functional than excitation energies, and that the LRC-ωPBEh functional employed presently has shown high accuracy in computed dipole moments.[243] It can be seen that the dipole moment increases significantly, from 18 D to 28 D, with the increase in the dihedral angle. This is consistent with the following estimate: assuming the center-to-center distance between phenol and porphyrin to be 6.4 Å, the dipole of the system increases by 30.7 D with a complete ET. As the dipole moment of the GS was calculated to be 3.93 D, it can be seen that the degree of the ET in the Franck-Condon region ($\theta \sim 67°$) is one half and it reaches unity as the angle increases.

The above and Equation 7.4 strongly suggest that the 120 fs time scale in the CLS of the 1597 cm^{-1} mode be assigned to the twisting of the dihedral angle with the concomitant charge redistribution leading to a large dipole moment approaching ∼30 D (Figure 7.6). We note that fast inertial rotations in TICT systems have also been observed in earlier work by means of visible transient absorption or transient IR spectroscopies.[244, 245] In the case of an aniline-triazine donor-acceptor dyad with an alkyne spacer, for example, twisting isomerization dynamics was monitored by the evolution from a vibrational band associated with an alkyne (C≡C−C) to that with an allene (C=C=C) on the time scale of 0.3-2.5 ps, depending on the solvent molecule.[245] However, in 2DEV spectroscopy, the CLS dynamics are free from population dynamics[3] and the current calculation revealed that twisting occurs without significant bond rearrangements. Thus, the rising CLS dynamics reflects the change of the electron density distribution which leads the unrelaxed PET state into the relaxed product, rather than a simple kinetic evolution from LE to PET states.

7.3 Conclusion

Proton-coupled electron transfer in $BIPPF_{15}$ takes place on two timescales, an ultrafast unrelaxed process from the initial excited levels and a slower relaxed process on a few hundred picoseconds timescale. The ultrafast process, though not the dominant pathway, enables us to observe the evolution of the initial, partly charge-transferred, state to full charge

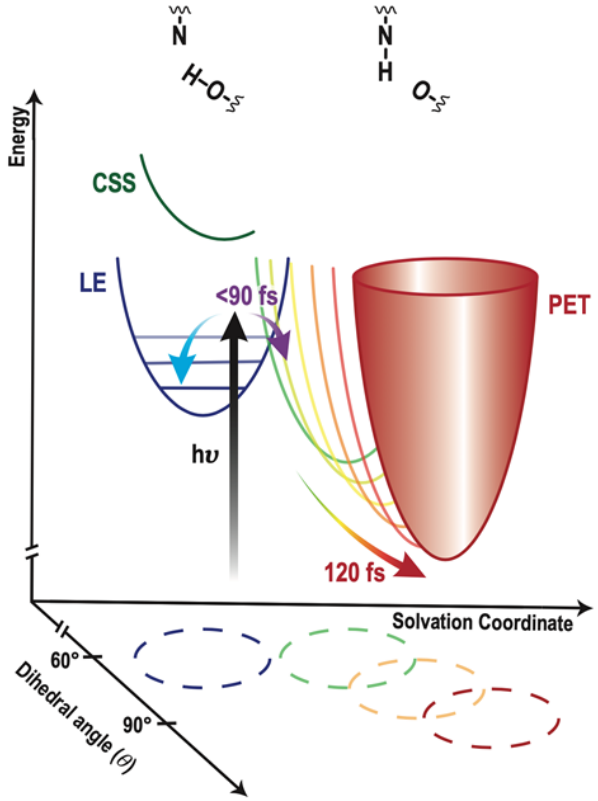

Figure 7.6: Upon the photoexcitation, the system is led to the unrelaxed Franck-Condon region and branches into two pathways towards: i) a relaxed locally excited (LE) state (blue arrow), which is followed by a slow PCET pathway (not shown) and can be described as a kinetic phenomenon (Figure 7.1c where $k_{CS} \ll k_{CR}$) and ii) an unrelaxed proton and electron transferred (PET) state (purple arrow) within 90 fs. From there, the unrelaxed PET state further rapidly evolves towards the twisted product with concomitant charge localization on a time scale of 120 fs (rainbow arrow). Additionally, it should be noted that the collective solvent response contributes to the reaction coordinate over the course of the ultrafast PCET reaction as the solvation timescale in acetonitrile[246] is similar to the timescale of twisting. The higher energy charge separated state (CSS) where the proton has not been transferred is not populated.

separation as molecular rearrangement and solvation proceed. The clear rise in the CLS in 120 fs demonstrates that the ET component of the PCET cannot be described as a single kinetic step and the degree of charge transfer begins around 50% and only reaches near unity when a ∼90° dihedral angle between BIP and porphyrin components is reached. While such a clearly identifiable nuclear rearrangement is hardly observable in slower PCET system, it seems highly likely that all PCET systems will require substantial rearrangement to complete

the transfers, as they all involve large changes in electronic structure. Thus, the detailed picture of synergistic motions accompanying PCET elucidated by the present combination of experimental and computational techniques provides general insights relevant to PCET and beyond.

7.4 Experimental and Theoretical Methods

Electronic-Vibrational Spectroscopy

A detailed description for the experimental setup of one- and two- dimensional electronic-vibrational spectroscopy can be found elsewhere.[2] Briefly, the output of a Ti:sapphire oscillator (Vitara-S, Coherent) was regeneratively amplified with a 1 kHz repetition rate (Legend Elite, Coherent), an energy of 1 mJ/pulse and a pulse duration of 40 fs. The amplified pulse was divided into two and one was used to pump a home-built visible non-collinear optical parametric amplifier (NOPA). The other pulse was used to generate a mid-IR probe pulse (centered at 6.4 μm) by difference frequency generation with signal and idler pulses from a near-IR collinear OPA. The output of the NOPA (centered at 580 nm, 60 nm fwhm, Figure E.2) was compressed to 10 fs at the sample position using a pair of prisms and an acousto-optic dispersive programmable filter (AODPF, Dazzler, Fastlite). The pulse pair was introduced to a retroreflector on a motorized translation stage to control the waiting time, T, between the pump and probe pulses. The total energy of the pump pulses was 200 nJ and the pulses were focused into the sample with spot size of 250 μm. The mid-IR pulse was divided by a 50:50 beam splitter to form probe and reference beams. The probe and reference beams were dispersed by a spectrometer (Triax 180, Horiba) and detected by a 64-pixel HgCdTe dual array (Infrared Systems Development). The cross-correlation between visible and mid-IR pulses was estimated to be 90 fs by a step-like transient IR response of a 50 μm Ge plate and by a solvent only measurement.

The group velocity dispersion of mid-IR probe pulse was calibrated by a dispersion curve estimated by a solvent only measurement. The transient IR signal at negative delay (perturbed free induction decay) was analyzed by a model function according to the literature.[247] The signal at positive delay was analyzed by a sum of exponential functions convoluted with the system response function.

For each waiting time, a 2DEV spectrum was acquired by using the AODPF to scan the $t_{\text{exc.}}$ delay over 0-100 fs with 2.5 fs steps. For each $t_{\text{exc.}}$ delay, the signal was acquired with the relative phase between the pump pulses ϕ_{12} set by 0, $2\pi/3$, and $4\pi/3$, and the desired signal was isolated by a 3×1 phase cycling scheme.[45, 46] The excitation axis was obtained by a Fourier transformation over $t_{\text{exc.}}$. The signal was collected in the fully rotated frame with respect to $t_{\text{exc.}}$. The CLS is calculated by linear fitting of the conditional averages along visible axis[47] as the CLS along the IR axis contains the same information.[37]

Synthesis

The required porphyrin was prepared by the Lindsey's method[248] and the aldehyde group of the salicylaldehyde moiety at the meso position of the porphyrin was condensed with phenylenediamine by the Philipps–Ladenburg reaction to yield $BIPPF_{15}$.[232, 249] The reference compound PF_{15} was synthesized as previously described.[250]

IR Spectroelectrochemistry

IRSEC measurements were conducted using a Biologic SP200 potentiostat connected to an optically transparent thin-layer electrochemical cell (Spectroelectrochemistry Reading RT OTTLE cell) equipped with CaF_2 optical windows. The cell (pathlength 0.2 mm) contained a Pt mesh counter electrode, a Ag wire pseudoreference electrode, and a Pt mesh working electrode, which was positioned in the light path of the IR spectrophotometer (Bruker Vertex 70 spectrometer, GloBar MIR source, broadband KBr beamsplitter, and liquid nitrogen cooled MCT detector). For all IRSEC measurements, the compounds were used at a concentration of ∼5 mM, with 0.1 M tetrabutylammonium hexafluorophosphate ($TBAPF_6$) as the supporting electrolyte in deuterated acetonitrile, and the cell was sealed under an argon atmosphere. Thin-layer constant potential electrolysis was monitored via FTIR as the working electrode was polarized in 100 and 50 mV increments versus the silver wire reference. Absorption spectra (64 scans, 2 cm^{-1} resolution) were continuously collected at each applied potential until there were no further significant changes. This procedure was repeated until increasing the polarization no longer resulted in significant changes of the spectra.[251]

Cyclic Voltammetry

Cyclic voltammetry measurements were performed with a Biologic SP200 potentiostat using a glassy carbon (3 mm diameter) working electrode, a Pt wire counter electrode, and a Ag wire pseudo-reference electrode in a conventional three-electrode cell. These measurements were collected at room temperature in anhydrous acetonitrile containing the compound of interest at a concentration of 1 mM and under an argon atmosphere. Tetrabutylammonium hexafluorophosphate ($TBAPF_6$, 0.5 M in acetonitrile) was used as the supporting electrolyte, and the scan rate was 100 mV s^{-1}. The working electrode was cleaned between experiments by polishing with a 0.05 μm alumina slurry on a microcloth pad, followed by solvent rinses and drying under a stream of nitrogen. The potential of the pseudoreference electrode was determined using the ferrocenium/ferrocene redox couple as an internal standard and adjusting to the saturated calomel electrode (SCE) scale (with $E_{1/2}$ taken to be 0.40 V versus SCE in acetonitrile).[252]

Fluorescence Lifetime Measurement

Fluorescence decay measurements were performed on optically dilute ($\sim 1 \times 10^{-5}$ M) samples by the time-correlated single-photon-counting method. The excitation source was a fiber supercontinuum laser based on a passive mode locked fiber laser and a high-nonlinearity photonic crystal fiber supercontinuum generator (Fianium SC450). The laser provides 6 ps pulses at a repetition rate variable between 0.1-40 MHz. The laser output was sent through an acousto-optical tunable filter (Fianium AOTF) and the relevant 10 nm interference filter to obtain excitation pulses at a desired wavelength. Fluorescence emission was detected at the magic angle using a double-grating monochromator (Jobin Yvon Gemini-180) and a microchannel plate photomultiplier tube (Hamamatsu R3809U-50). The instrument response function was 35-65 ps. The spectrometer was controlled by software based on the LabView programming language and data acquisition was done using a single photon counting card (Becker-Hickl, SPC-830). Data analysis was carried out using locally written software (ASU-FIT) developed under a MATLAB environment (Mathworks Inc.). Random errors associated with the reported lifetimes obtained from fluorescence measurements were typically $\leq 5\%$.

Details of the Computational Method for Charge Transfer States

All calculations were performed with Q-Chem 5.2.[202] The def2-SV(P) basis set[253] and PCM solvation model were used for all DFT calculations. Optimized geometries and dipole moments were calculated with the LRC-ωPBEh functional.[254] Excited state geometries and properties were computed using linear-response time-dependent density functional theory (TD-DFT).[203, 255] While the LRC-ωPBEh functional yielded an excitation energy for the LE state consistent with the absorption spectrum, the theoretical description of the PET state required careful attention given the well-known systematic underestimation of excitation energies via semi-local and hybrid functionals[203], and the overestimation that has been found to result when common range-separated functionals are applied to molecules relevant to thermally activated delayed fluoresence.[256] We use a non-empirical procedure, which largely mitigates delocalization error[257] by ensuring minimal deviations from Koopman's theorem for the N and $N+1$ electron systems, to generate an optimally tuned range-separated hybrid density functional.[235–237] The resulting functional, OT-LRC-ωPBEh (with $\omega = 0.115$), is used to compute the NTOs and relevant energetics of the PET state, as further detailed in the following.

Our computational protocol for the PET state consists of the following steps:

1) Signatures of an excited state exhibiting directional charge transfer include a large dipole moment (and a large *change* in dipole moment, as compared with the ground-state), and a HONTO (LUNTO) which exhibits electron density localized on the D (A) subunit. Once identified, the minimum energy structure on the potential energy surface is obtained by performing an excited state geometry optimization with respect to the target state with the LRC-ωPBEh functional and the equilibrium PCM model. This target state may not

be the energetically lowest excited state, e.g. the PET state is S_3 with the LRC-ωPBE functional.

2) At this geometry, the optimal value of the range-separation parameter is obtained by minimizing:

$$J^2 = \sum_{N}^{N+1} [\varepsilon_{\mathrm{HOMO}}(i) + IP(i)]^2.$$

This ensures minimal deviations from a property of the exact density functional, which states that the negative of the highest-occupied molecular orbital energy should equal to the ionization potential, for both the N and $N+1$ electron systems. These quantities are calculated via Kohn-Sham DFT in the gas phase.

3) The resulting OT-LRC-ωPBEh functional is employed in a single-point TD-DFT/PCM calculation to obtain the excited state total (and excitation) energy and NTOs.

4) Having computed the PET total energy in Step 3 of the protocol outlined above, we additionally compute the total energy of the phenolic ground-state with the same OT-LRC-ωPBEh functional. Although the ω value is not optimal for the ground-state, we expect this to afford a high level of accuracy, as it is known that ground-state energies are less sensitive to the range-separation parameter compared to CS excited states. Besides, it is our view that relative energetics should, in principle, be compared using the same density functional.

Chapter 8

Outlook

8.1 Introduction

While the method of two-dimensional electronic-vibrational (2DEV) spectroscopy has shown great promise in untangling the complex interplay between electronic and vibrational degrees of freedom in many photoactive species, there remains a wide-open frontier yet to be explored in a variety of other systems. Here, we will illustrate various ongoing efforts in the application and improvement of 2DEV spectroscopy, as well as future pursuits of great potential.

8.2 Photosystem II Core Complex

In regards to the natural system, up to this point, our spectroscopic investigations have focused on either isolated light-harvesting complexes (Chapters 2 and 3) or isolated photosystem II reaction centers (PSII-RCs) (Chapter 5). The ultimate next step would be to bridge this gap and study a photosynthetic unit composed of a RC connected to a peripheral antenna system. In this way, we can begin to understand the way in which excitation energy transfer (EET) from the antennas populates the RC and initiates the charge separation process. However, the gap in complexity between these two worlds is significant. The simplest system towards this goal is the PSII core complex (PSII-CC) which is composed of a RC and two peripheral antennas, CP43 and CP47 (Figure 8.1a).[146] The difficulty is that the PSII-CC is often dimeric in form, giving rise to a system of 70 chlorophylls (Chls) of nearly identical spectral characteristics. For this reason, the dynamics of the PSII-CC have been little studied via time-resolved spectroscopic methods to date.[76, 151, 258–260] Understanding such a system, and even more complex ones, requires an experimental method capable of providing simultaneously high temporal and spectral resolution—such as 2DEV spectroscopy. Indeed, preliminary 2DEV experimental results on the PSII-CC yield astoundingly resolved spectra, where clear and significant excitation frequency-dependent vibrational structure and dynamical evolution can be observed (Figure 8.1b). Through this application,

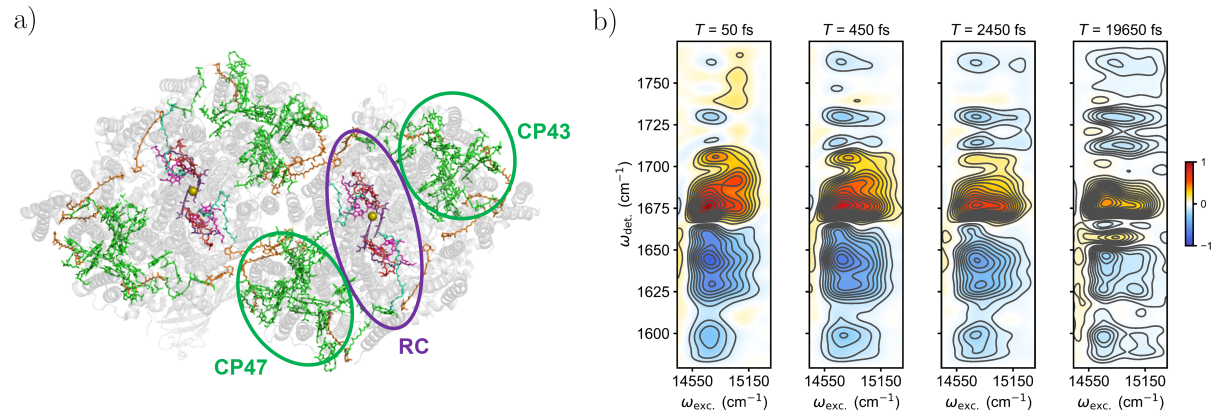

Figure 8.1: a) Pigment arrangement of the PSII-CC (in dimeric form) depicted based on the crystal structure (3WU2) reported by Umena et al.[146] In one of the monomeric units, the groupings of pigments giving rise to the antenna proteins, CP43 and CP47, are circled in green, while the pigments forming the reaction center (RC) are circled in purple. b) 2DEV spectra at 77 K of the PSII-RC at $T = 50$ fs, 450 fs, 2450 fs, and 19650 fs. Positive contours (red/yellow) indicate ground state bleach features and negative contours (blue) indicate photoinduced absorption features. Contour levels are drawn in 5% intervals.

it will be possible to directly study the mechanisms of EET connecting antenna and reaction center proteins leading to charge separation—a critial step in the photosynthetic engine.

With the observation of the surprisingly well-resolved 2DEV spectra of the PSII-CC, it is interesting (and probably beneficial) to consider the limit of how large a system can be usefully studied before spectral congestion overwhelms the enhanced capabilities of the method. Of course, while the specific limitations will be system-dependent, it is interesting to speculate whether the yet larger photosystem I core complex (∼96 Chls)[261] would yield any resolvable features in a 2DEV spectrum, for example. With additional considerations (e.g. mutants) it may even be possible to further enhance the ability of this spectroscopic method to untangle complex, congested spectra and to target specific molecular actors in the photosynthetic apparatus. However, this remains unexplored to date.

8.3 Photodriven One-Electron Two-Proton Transfer

As described in Chapter 7, proton-coupled electron transfer (PCET) is critical to the photosynthetic process, as it provides a low activation energy reaction coordinate for water oxidation at the oxygen evolving complex[262], where four protons are extracted from coordinated waters during the Kok-cycle. These protons are then transferred to the luminal side of the photosynthetic membrane presumably by a Grotthus-type proton relay mechanism.[263] On

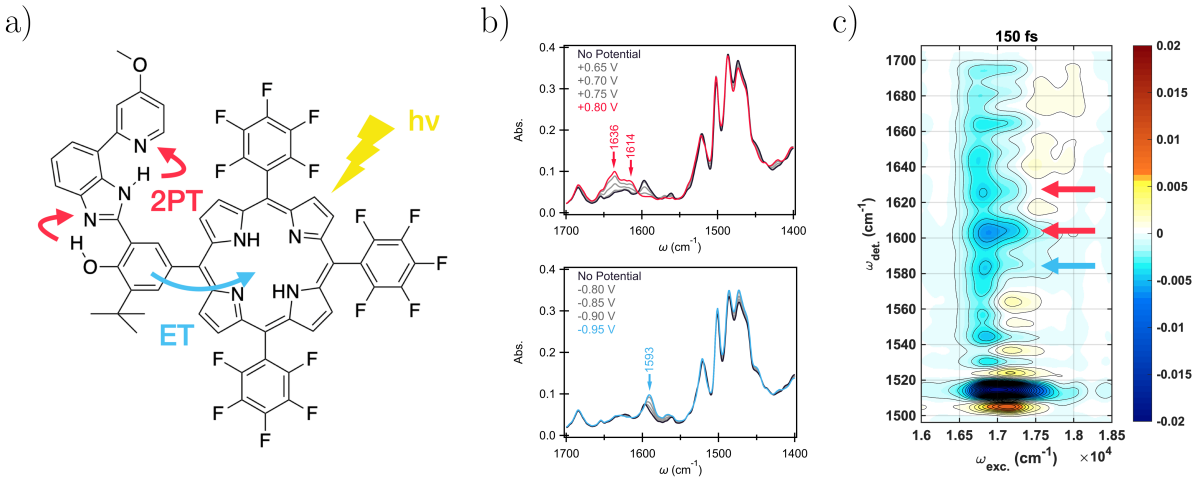

Figure 8.2: a) Molecular structure of the biomimetic photoinduced E2PT system (PF_{15}-BIP-Pyr). b) IRSEC spectra of PF_{15}-BIP-Pyr upon oxidation (red) and reduction (blue). The black curves show the neutral species and colored curves show oxidized (red) and reduced species (blue). The applied potentials indicated in the figure legend are versus a silver wire reference electrode. c) 2DEV spectra of PF_{15}-BIP-Pyr in deuterated acetonitrile at 150 fs. Positive signals (red/yellow contours) indicate ground state bleaches and negative signals (blue contours) represent excited state absorptions. Contour levels are drawn in 5% intervals. In b) and c), red arrows indicate the IR bands that track the double proton transfer and the blue arrow indicates the IR band that tracks the electron transfer process.

the stromal side of the membrane, proton uptake by the reduced quinone and subsequent transfer of the electron through the $Cytb_6f$ complex to photosystem I almost certainly involves PCET at multiple points and conducts a proton uptake reaction, which eventually creates a proton-motive force across the thylakoid membrane to drive ATP synthase and myriad bioenergic processes.[1] To elucidate the mechanism underlying proton management in natural photosynthesis and develop highly efficient artificial photosynthetic species, it is often beneficial to turn to bioinspired systems. In particular, benzimidazole-phenol (BIP) constructs which mimic the Tyr_z and His190 in the PSII-RC is an ideal model system, as we have seen in Chapter 7. Through appropriate chemical substitution, it is also possible to achieve multiple proton transfers upon oxidation of the phenol moiety since one or multiple proton transfers can be achieved upon oxidation of the phenol moiety.[218, 220–223, 225, 232, 264, 265] In future pursuits, the application of 2DEV spectroscopy to the model system composed of a porphyrin-benzimidazole-phenol-pyridine (PF_{15}-BIP-Pyr, Figure 8.3a) triad—which undergoes one-electron two-proton transfer (E2PT)—is of significant promise. Indeed, preliminary results (Figure 8.3) reveal the ability of 2DEV spectroscopy to track the formation of the E2PT product, again, with input from infrared spectroelectrochemical

(IRSEC) measurements. These studies will be critical in examining the coupled dynamics of the protons and electron following photoexcitation.

8.4 Experimental Improvements

Adaptations to the Current IR Source

In the previous chapters, the time resolution of the 2DEV spectroscopic method was often challenged by some of the most rapid dynamical processes under investigation. For example, the timescales of ultrafast energy flow within the Chl Q_y vibronic manifold in LHCII (Chapter 3) and the initial formation of the non-equilibrium proton-coupled electron transfer state (Chapter 7) fell within the instrument response function (IRF) of the 2DEV spectrometer. In the current experimental setup, the infrared (IR) probe is generated via a home-built near-IR collinear optical parametric amplifier (OPA)-pumped difference frequency generation (DFG) source. This design, first put forth by Hamm et al.[266], is continuously tunable from 1250∼3350 cm^{-1} and produces pulses with a bandwidth of a few hundred wavenumbers and temporal duration of 50∼100 fs depending on the set center frequency. In practice, the IR pulses out of the OPA-DFG source are temporally broadened by a 50:50 ZnSe beam splitter (used to generate the probe and reference arms) and by the sample windows (typically a few millimeters of CaF_2). This translates to an IRF of 80∼150 fs, depending on the adequacy of dispersion compensation by germanium plates.

One relatively straightforward way to address the temporal limitations of the IR source is to implement a supercontinuum generation step following DFG in the existing infrastructure. Particularly, Lanin et al.[267, 268] and Stepanov et al.[269] have demonstrated that in anomalously dispersive, highly nonlinear bulk media, mid-IR pulses undergo self-focusing concomitant with soliton self-compression. Depending on the chosen center frequency, under these conditions, mid-IR pulses from an OPA-DFG source with few microjoule pulse energies can generate few-cycle or even subcycle pulse widths when focused tightly into a few millimeter GaAs plate (typically either 5 mm or 7 mm) followed by dispersion compensation with few millimeter BaF_2 and/or CaF_2 plates.[267–269] Correspondingly, bandwithds ranging form 900∼2800 cm^{-1} are achievable—in comparison to the 100∼200 cm^{-1} bandwidths of the incident pulses.

Currently, we have implemented such a supercontinuum generation source following our DFG source based on Ref. [268]. Following the OPA-DFG, a $f = 10$ cm off axis parabolic (OAP) mirror was used to focus the mid-IR beam (centered at ∼1600 cm^{-1}) into the back of a 5 mm GaAs plate after which the supercontinuum IR output was collimated with a second $f = 10$ cm OAP mirror. In practice, the GaAs plate is on a magnetic optical mount, so that it can be removed or incorporated on-demand. In Figure 8.3, we demonstrate that it is possible to improve our IRF by nearly a factor of two with this design. These preliminary results demonstrate how simultaneous self-compression and spectral broadening in bulk media works well in practice to improve the temporal duration of our IR pulses. However, various aspects

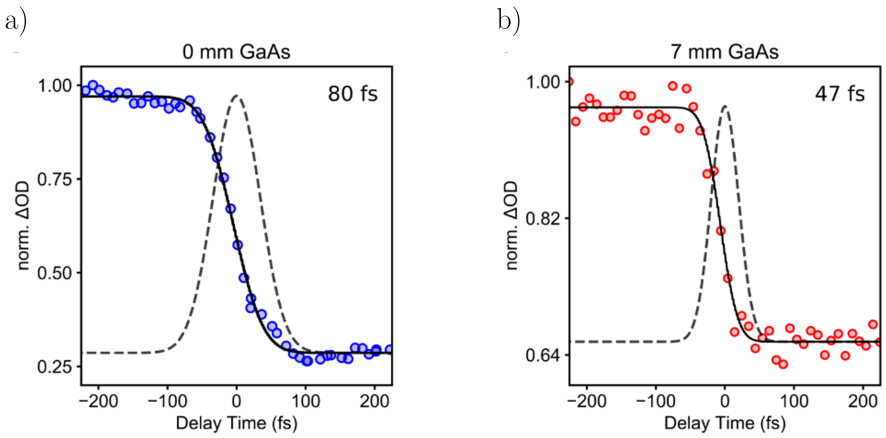

Figure 8.3: a) and b) Cross-correlation of visible pump pulse (10 fs, centered at 620 nm) and IR probe pulse (centered at 1600 cm^{-1}) in a Ge plate. The instrument response function is shown with the dashed line. In b), the output of the OPA-DFG source is focused into a 7 mm GaAs plate such that the IR pulse is spectrally broadened and self-compressed, whereas no GaAs plate was employed in a). We note that in this case, no CaF_2 plates were incorporated to mimic the sample holder and 9 mm Ge was used for dispersion compensation.

remain to be considered. Firstly, the supercontinuum process can be fine-tuned by changing: i) the thickness of the GaAs plate and ii) the position within the GaAs plate that the incident IR beam is focused. Particularly, it has been demonstrated that the resulting supercontinuum is highly sensitive to the latter.[267–269] With further optimization, it is possible in principle to achieve an IRF approaching 30 fs. In the supercontinuum generation process, however, energy losses are sustained which can lead to insufficient mid-IR pulse energies for experimental implementation. Therefore, improving the energy output of the OPA-DFG source is the critical step in realizing this adaptation to our current IR source.

As a final comment, accessing higher IR frequencies with similar temporal profiles is possible if the nonlinear crystal in the DFG stage was change from from $AgGaS_2$ to $KNbO_3$[270] and either bulk YAG, CaF_2, or BaF_2 rather than GaAs was used for supercontinuum generation.[271] In principle, this should allow us to to achieve a sub-30 fs IRF with IR pulses centered at ∼3300 cm^{-1}.

Implementation of a New IR Source

Entirely new IR sources, also based on supercontinuum generation, are likely to be promising alternatives to the OPA-DFG-based method. Since the inception of the previously introduced design by Hamm et al.[266] nearly 20 years ago, significant research effort has been

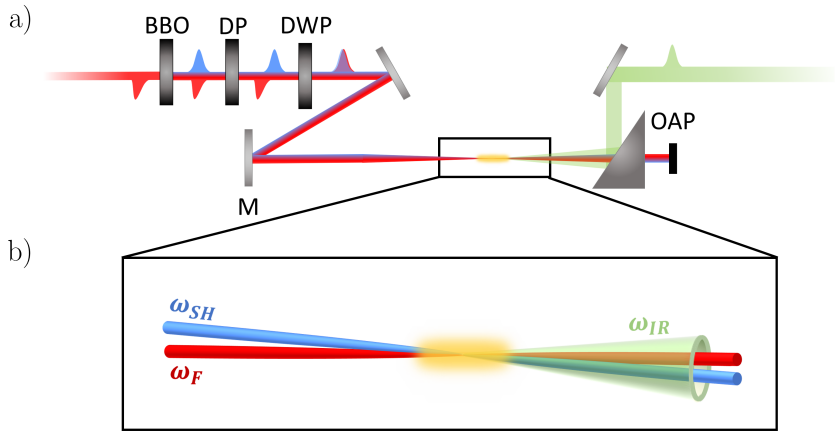

Figure 8.4: a) Four-wave mixing process of the fundamental (ω_{F}) and second harmonic (ω_{SH}) of a Ti:sapphire laser to generate a supercontinuum IR (ω_{IR}) source from filamentation (shown in yellow) in a gaseous medium. b) Experimental layout of the supercontinuum IR source.[277] The red, blue, and green lines indicate the fundamental, second harmonic, and IR supercontinuum, respectively. The optics are labeled as follows: BBO - β-BaB_2O_4 crystal (Type I, $\theta = 29.2°$, thickness = 100 μm), DP - calcite delay plate (thickness = 1.7 mm), DWP - dual wave plate ($\lambda/2$ @ 800 nm, λ @ 400 nm), M - focusing mirror ($f = 1$ m), and OAP - off axis parabolic mirror (with hole to let residual fundamental and second harmonic through).

focused towards improving the duration (and therefore inherently the bandwidth) of ultrafast IR sources. To that end, the development of stable (shot-to-shot noise <4% rms) IR supercontinuum sources possessing durations <50 fs and bandwidths >1500 cm^{-1} with sufficient pulse energies (>100 nJ) reveals a promising new direction for ultrafast spectroscopies employing IR pulses.[272–279] The supercontinuum sources with the most favorable pulse characteristics for spectroscopic experiments utilize four-wave mixing in gaseous media (such as dry air) of the fundamental, ω_{F}, and second harmonic, ω_{SH}, of Ti:Sapphire pump lasers in the parametric processes $\pm\omega_{\mathrm{F}} \pm \omega_{\mathrm{F}} \mp \omega_{\mathrm{SH}} \rightarrow \omega_{\mathrm{IR}}$ to generate supercontinuum IR pulses, ω_{IR}.[274, 277–279] In this process, filamentation effects are exploited in order to overcome the low nonlinearities intrinsic to gasses.[280–282] A cartoon of this third-order nonlinear process is presented in Figure 8.4.

Recently, Gaynor et al. showed the applicability of such a such source in 2DEV spectroscopy, however, the instability (>3% rms) and low pulse energy (∼100 nJ after the pulse has been split into probe and reference) of the IR supercontinuum in this work might limit the applicability of this particular source.[283] In comparison, the supercontinuum source based on the design of Fuji et al.[274, 277] and Nomura et al.[278, 279] features better energy stability (<1.6% rms) and pulse energy (∼250 nJ after the pulse has been split into

probe and reference) making it an ideal candidate for implementation in 2DEV spectroscopy. Figure 8.4 shows a schematic of this IR source.[274, 277–279]

The pursuit and employment of such supercontinuum IR sources is likely to open up a promising new realm for 2DEV spectroscopy—allowing access to dynamical processes occurring on a sub-100 fs timescale.

8.5 Beyond

Throughout the preceding chapters, we have illustrated applications of the 2DEV spectroscopic method to natural photosynthetic and biomimetic model systems. We have emphasized how aspects such as the improved spectral resolution and the apparently unique information contained in the center line slope of the spectral features in 2DEV spectroscopy make this a powerful tool for investigating the dynamics of these complex, condensed phase systems. In the following, we briefly a new potential future direction that can be pursued with 2DEV spectroscopy—beyond the several actively pursued paths already described above.

This dissertation has largely focused on photosythetically-related systems, this represents only one avenue for the applicability of this technique. For example, Khalil and coworkers have elegantly demonstrated how 2DEV spectroscopy can also be a powerful tool to understand synthetic components utilized for solar conversion.[84, 109] Perhaps a fitting future challenge—incorporating much of what was learned based on all of the applications described here—would be the application of 2DEV spectroscopy to understand solar conversion systems complete with light absorbers, catalysts, and membranes.[284] In particular, 2DEV spectroscopy should be useful for characterizing the new generation of solid-molecule hybrid systems for solar to fuel conversion based on water splitting. In these systems, charge transfer and proton motion must be managed and optimized for maximum efficiency[217, 285, 286] and, as shown, 2DEV spectroscopy has the unique ability to report on dynamic alterations to the molecular framework (and more) accompanying such processes.

While far from mature, 2DEV spectroscopy has already proved to be a particularly useful method capable of producing detailed and often nuanced insight into the way in which electron-nuclear interactions exert influence over the function of natural and artificial photosynthetic systems and beyond.

Bibliography

[1] Robert E Blankenship. *Molecular Mechanisms of Photosynthesis*. John Wiley & Sons, 2014.

[2] Thomas AA Oliver, Nicholas HC Lewis, and Graham R Fleming. "Correlating the motion of electrons and nuclei with two-dimensional electronic–vibrational spectroscopy". In: *Proceedings of the National Academy of Sciences* 111.28 (2014), pp. 10061–10066.

[3] Eric A Arsenault et al. "Vibronic mixing enables ultrafast energy flow in light-harvesting complex II". In: *Nature Communications* 11.1 (2020), p. 1460.

[4] Jörg Standfuss et al. "Mechanisms of photoprotection and nonphotochemical quenching in pea light-harvesting complex at 2.5 Å resolution". In: *The EMBO Journal* 24.5 (2005), pp. 919–928.

[5] Tessa R Calhoun et al. "Quantum coherence enabled determination of the energy landscape in light-harvesting complex II". In: *The Journal of Physical Chemistry B* 113.51 (2009), pp. 16291–16295.

[6] Eric A Arsenault et al. "The role of mixed vibronic Q_y-Q_x states in green light absorption of light-harvesting complex II". In: *Nature Communications* 11.1 (2020), p. 6011.

[7] Ichiro Terashima et al. "Green light drives leaf photosynthesis more efficiently than red light in strong white light: revisiting the enigmatic question of why leaves are green". In: *Plant and Cell Physiology* 50.4 (2009), pp. 684–697.

[8] Andrea Rivadossi et al. "Light Absorption by the Chlorophyll a–b Complexes of Photosystem II in a Leaf with Special Reference to LHCII". In: *Photochemistry and Photobiology* 80.3 (2004), pp. 492–498.

[9] Flavio Massimo Garlaschi, Giuseppe Zucchelli, and Robert Charles Jennings. "Studies on light absorption and photochemical activity changes in chloroplast suspensions and leaves due to light scattering and light filtration across chloroplast and vegetation layers". In: *Photosynthesis Research* 20.3 (1989), pp. 207–220.

[10] Atsushi Kume. "Importance of the green color, absorption gradient, and spectral absorption of chloroplasts for the radiative energy balance of leaves". In: *Journal of Plant Research* 130.3 (2017), pp. 501–514.

[11] Eric A Arsenault et al. "Vibronic coupling in energy transfer dynamics and two-dimensional electronic-vibrational spectra". In: *The Journal of Chemical Physics* 155.5 (2021), p. 054201.

[12] Eric A Arsenault et al. "Vibronic coupling in light-harvesting complex II revisited". In: *The Journal of Chemical Physics* 155.9 (2021), p. 096101.

[13] Joel A Freeman. *Photosystem II: The Light-Driven Water: Plastoquinone Oxidoreductase*. Vol. 22. Springer Science & Business Media, 2006.

[14] Jian-Ren Shen. "The structure of photosystem II and the mechanism of water oxidation in photosynthesis". In: *Annual Review of Plant Biology* 66 (2015), pp. 23–48.

[15] Gernot Renger and Thomas Renger. "Photosystem II: The machinery of photosynthetic water splitting". In: *Photosynthesis Research* 98.1 (2008), pp. 53–80.

[16] Roberta Croce and Herbert van Amerongen. "Light-harvesting and structural organization of photosystem II: from individual complexes to thylakoid membrane". In: *Journal of Photochemistry and Photobiology B: Biology* 104.1-2 (2011), pp. 142–153.

[17] Elisabet Romero, Vladimir I Novoderezhkin, and Rienk van Grondelle. "Quantum design of photosynthesis for bio-inspired solar-energy conversion". In: *Nature* 543.7645 (2017), pp. 355–365.

[18] Bridgette A Barry and Gerald T Babcock. "Tyrosine radicals are involved in the photosynthetic oxygen-evolving system". In: *Proceedings of the National Academy of Sciences* 84.20 (1987), pp. 7099–7103.

[19] Bridgette A Barry. "Reaction dynamics and proton coupled electron transfer: Studies of tyrosine-based charge transfer in natural and biomimetic systems". In: *Biochimica et Biophysica Acta (BBA)-Bioenergetics* 1847.1 (2015), pp. 46–54.

[20] Partha Pratim Roy et al. "Solvent mediated excited state proton transfer in Indigo Carmine". In: *The Journal of Physical Chemistry Letters* 11.10 (2020), pp. 4156–4162.

[21] T Elsaesser, W Kaiser, and W Lüttke. "Picosecond spectroscopy of intramolecular hydrogen bonds in 4, 4′, 7, 7′-tetramethylindigo". In: *The Journal of Physical Chemistry* 90.13 (1986), pp. 2901–2905.

[22] Nathália D Bernardino et al. "Time-resolved spectroscopy of indigo and of a Maya blue simulant". In: *The Journal of Physical Chemistry C* 120.38 (2016), pp. 21905–21914.

[23] Ganglong Cui and Walter Thiel. "Nonadiabatic dynamics of a truncated indigo model". In: *Physical Chemistry Chemical Physics* 14.35 (2012), pp. 12378–12384.

[24] Shohei Yamazaki, Andrzej L Sobolewski, and Wolfgang Domcke. "Molecular mechanisms of the photostability of indigo". In: *Physical Chemistry Chemical Physics* 13.4 (2011), pp. 1618–1628.

[25] Izumi Iwakura, Atushi Yabushita, and Takayoshi Kobayashi. "Why is indigo photostable over extremely long periods?" In: *Chemistry Letters* 38.11 (2009), pp. 1020–1021.

[26] J Seixas de Melo, AP Moura, and MJ Melo. "Photophysical and spectroscopic studies of indigo derivatives in their keto and leuco forms". In: *The Journal of Physical Chemistry A* 108.34 (2004), pp. 6975–6981.

[27] Yutaka Nagasawa et al. "The effect of hydrogen-bonding on the ultrafast electronic deactivation dynamics of indigo carmine". In: *Physical Chemistry Chemical Physics* 6.23 (2004), pp. 5370–5378.

[28] Yusuke Yoneda et al. "Electron–Nuclear Dynamics Accompanying Proton-Coupled Electron Transfer". In: *Journal of the American Chemical Society* 143.8 (2021), pp. 3104–3112.

[29] Eric A Arsenault et al. "Two-dimensional electronic–vibrational spectroscopy: Exploring the interplay of electrons and nuclei in excited state molecular dynamics". In: *The Journal of Chemical Physics* 155.2 (2021), p. 020901.

[30] Peter Hamm, Manho Lim, and Robin M Hochstrasser. "Structure of the amide I band of peptides measured by femtosecond nonlinear-infrared spectroscopy". In: *The Journal of Physical Chemistry B* 102.31 (1998), pp. 6123–6138.

[31] Peter Hamm et al. "The two-dimensional IR nonlinear spectroscopy of a cyclic pentapeptide in relation to its three-dimensional structure". In: *Proceedings of the National Academy of Sciences* 96.5 (1999), pp. 2036–2041.

[32] O Golonzka et al. "Vibrational anharmonicities revealed by coherent two-dimensional infrared spectroscopy". In: *Physical Review Letters* 86.10 (2001), p. 2154.

[33] John B Asbury et al. "Hydrogen bond breaking probed with multidimensional stimulated vibrational echo correlation spectroscopy". In: *The Journal of Chemical Physics* 119.24 (2003), pp. 12981–12997.

[34] Tobias Brixner et al. "Phase-stabilized two-dimensional electronic spectroscopy". In: *The Journal of Chemical Physics* 121.9 (2004), pp. 4221–4236.

[35] John D Hybl, Allison Albrecht Ferro, and David M Jonas. "Two-dimensional Fourier transform electronic spectroscopy". In: *The Journal of Chemical Physics* 115.14 (2001), pp. 6606–6622.

[36] ML Cowan, JP Ogilvie, and RJD Miller. "Two-dimensional spectroscopy using diffractive optics based phased-locked photon echoes". In: *Chemical Physics Letters* 386.1-3 (2004), pp. 184–189.

[37] Nicholas HC Lewis et al. "Measuring correlated electronic and vibrational spectral dynamics using line shapes in two-dimensional electronic-vibrational spectroscopy". In: *The Journal of Chemical Physics* 142.17 (2015), p. 174202.

[38] Minhaeng Cho and Graham R Fleming. "Two-Dimensional Electronic–Vibrational Spectroscopy Reveals Cross-Correlation between Solvation Dynamics and Vibrational Spectral Diffusion". In: *The Journal of Physical Chemistry B* 124.49 (2020), pp. 11222–11235.

[39] Minhaeng Cho. "Coherent two-dimensional optical spectroscopy". In: *Chemical Reviews* 108.4 (2008), pp. 1331–1418.

[40] Peter Hamm and Martin Zanni. *Concepts and Methods of 2D Infrared Spectroscopy*. Cambridge University Press, 2011.

[41] Minhaeng Cho. *Two-Dimensional Optical Spectroscopy*. CRC Press, 2009.

[42] Hui Dong et al. "Determining the static electronic and vibrational energy correlations via two-dimensional electronic-vibrational spectroscopy". In: *The Journal of Chemical Physics* 142.17 (2015), p. 174201.

[43] Shaul Mukamel. *Principles of Nonlinear Optical Spectroscopy*. Oxford University Press on Demand, 1999.

[44] Paul M Donaldson, Halina Strzalka, and Peter Hamm. "High sensitivity transient infrared spectroscopy: a UV/Visible transient grating spectrometer with a heterodyne detected infrared probe". In: *Optics Express* 20.12 (2012), pp. 12761–12770.

[45] Jeffrey A Myers et al. "Two-color two-dimensional Fourier transform electronic spectroscopy with a pulse-shaper". In: *Optics Express* 16.22 (2008), pp. 17420–17428.

[46] Zhengyang Zhang et al. "Phase-cycling schemes for pump–probe beam geometry two-dimensional electronic spectroscopy". In: *Chemical Physics Letters* 550 (2012), pp. 156–161.

[47] Eric C Wu et al. "Two-dimensional electronic-vibrational spectroscopic study of conical intersection dynamics: an experimental and electronic structure study". In: *Physical Chemistry Chemical Physics* 21.26 (2019), pp. 14153–14163.

[48] Denis J Murphy. "The molecular organisation of the photosynthetic membranes of higher plants". In: *Biochimica et Biophysica Acta (BBA)-Reviews on Biomembranes* 864.1 (1986), pp. 33–94.

[49] Zhenfeng Liu et al. "Crystal structure of spinach major light-harvesting complex at 2.72 Å resolution". In: *Nature* 428.6980 (2004), pp. 287–292.

[50] Vladimir I Novoderezhkin et al. "Excitation dynamics in the LHCII complex of higher plants: modeling based on the 2.72 Å crystal structure". In: *The Journal of Physical Chemistry B* 109.20 (2005), pp. 10493–10504.

[51] Daniel D Eads et al. "Direct observation of energy transfer in a photosynthetic membrane: chlorophyll b to chlorophyll a transfer in LHC". In: *The Journal of Physical Chemistry* 93.26 (1989), pp. 8271–8275.

[52] Vladimir I Novoderezhkin et al. "Energy-transfer dynamics in the LHCII complex of higher plants: modified Redfield approach". In: *The Journal of Physical Chemistry B* 108.29 (2004), pp. 10363–10375.

[53] Nicholas HC Lewis et al. "Observation of electronic excitation transfer through light harvesting complex II using two-dimensional electronic–vibrational spectroscopy". In: *The Journal of Physical Chemistry Letters* 7.20 (2016), pp. 4197–4206.

[54] Gabriela S Schlau-Cohen et al. "Pathways of energy flow in LHCII from two-dimensional electronic spectroscopy". In: *The Journal of Physical Chemistry B* 113.46 (2009), pp. 15352–15363.

[55] Gabriela S Schlau-Cohen et al. "Spectroscopic elucidation of uncoupled transition energies in the major photosynthetic light-harvesting complex, LHCII". In: *Proceedings of the National Academy of Sciences* 107.30 (2010), pp. 13276–13281.

[56] Gabriela S Schlau-Cohen et al. "Elucidation of the timescales and origins of quantum electronic coherence in LHCII". In: *Nature Chemistry* 4.5 (2012), pp. 389–395.

[57] Hong-Guang Duan et al. "Two-dimensional electronic spectroscopy of light-harvesting complex II at ambient temperature: a joint experimental and theoretical study". In: *The Journal of Physical Chemistry B* 119.36 (2015), pp. 12017–12027.

[58] Gregory S Engel et al. "Evidence for wavelike energy transfer through quantum coherence in photosynthetic systems". In: *Nature* 446.7137 (2007), pp. 782–786.

[59] Elisabetta Collini et al. "Coherently wired light-harvesting in photosynthetic marine algae at ambient temperature". In: *Nature* 463.7281 (2010), pp. 644–647.

[60] Darius Abramavicius and Shaul Mukamel. "Quantum oscillatory exciton migration in photosynthetic reaction centers". In: *The Journal of Chemical Physics* 133.6 (2010), 08B603.

[61] Gitt Panitchayangkoon et al. "Direct evidence of quantum transport in photosynthetic light-harvesting complexes". In: *Proceedings of the National Academy of Sciences* 108.52 (2011), pp. 20908–20912.

[62] Roel Tempelaar, Thomas LC Jansen, and Jasper Knoester. "Vibrational beatings conceal evidence of electronic coherence in the FMO light-harvesting complex". In: *The Journal of Physical Chemistry B* 118.45 (2014), pp. 12865–12872.

[63] Brian S Rolczynski et al. "Correlated protein environments drive quantum coherence lifetimes in photosynthetic pigment-protein complexes". In: *Chem* 4.1 (2018), pp. 138–149.

[64] Hou-Dao Zhang et al. "Effects of Herzberg–Teller vibronic coupling on coherent excitation energy transfer". In: *The Journal of Chemical Physics* 145.20 (2016), p. 204109.

[65] Martin B Plenio, J Almeida, and Susana F Huelga. "Origin of long-lived oscillations in 2D-spectra of a quantum vibronic model: electronic versus vibrational coherence". In: *The Journal of Chemical Physics* 139.23 (2013), 12B614_1.

[66] Vytautas Butkus, Leonas Valkunas, and Darius Abramavicius. "Vibronic phenomena and exciton–vibrational interference in two-dimensional spectra of molecular aggregates". In: *The Journal of Chemical Physics* 140.3 (2014), p. 034306.

[67] Shu-Hao Yeh et al. "Elucidation of near-resonance vibronic coherence lifetimes by nonadiabatic electronic-vibrational state character mixing". In: *Proceedings of the National Academy of Sciences* 116.37 (2019), pp. 18263–18268.

[68] Niklas Christensson et al. "Origin of long-lived coherences in light-harvesting complexes". In: *The Journal of Physical Chemistry B* 116.25 (2012), pp. 7449–7454.

[69] Sergey Polyutov, Oliver Kühn, and Tõnu Pullerits. "Exciton-vibrational coupling in molecular aggregates: Electronic versus vibronic dimer". In: *Chemical Physics* 394.1 (2012), pp. 21–28.

[70] David M Jonas. "Vibrational and nonadiabatic coherence in 2D electronic spectroscopy, the Jahn–Teller effect, and energy transfer". In: *Annual Review of Physical Chemistry* 69 (2018), pp. 327–352.

[71] Jeffrey A Cina and Graham R Fleming. "Vibrational coherence transfer and trapping as sources for long-lived quantum beats in polarized emission from energy transfer complexes". In: *The Journal of Physical Chemistry A* 108.51 (2004), pp. 11196–11208.

[72] Joachim Seibt and Tomáš Mančal. "Treatment of Herzberg-Teller and non-Condon effects in optical spectra with Hierarchical Equations of Motion". In: *Chemical Physics* 515 (2018), pp. 129–140.

[73] James Lim et al. "Vibronic origin of long-lived coherence in an artificial molecular light harvester". In: *Nature Communications* 6.1 (2015), pp. 1–7.

[74] Fei Ma et al. "Vibronic coherence in the charge separation process of the Rhodobacter sphaeroides reaction center". In: *The Journal of Physical Chemistry Letters* 9.8 (2018), pp. 1827–1832.

[75] Erling Thyrhaug et al. "Identification and characterization of diverse coherences in the Fenna–Matthews–Olson complex". In: *Nature Chemistry* 10.7 (2018), pp. 780–786.

[76] Jie Pan et al. "Ultrafast energy transfer within the photosystem II core complex". In: *Physical Chemistry Chemical Physics* 19.23 (2017), pp. 15356–15367.

[77] Franklin D Fuller et al. "Vibronic coherence in oxygenic photosynthesis". In: *Nature Chemistry* 6.8 (2014), pp. 706–711.

[78] Jacob C Dean et al. "Vibronic enhancement of algae light harvesting". In: *Chem* 1.6 (2016), pp. 858–872.

[79] Vladimir I Novoderezhkin et al. "Exciton-vibrational resonance and dynamics of charge separation in the photosystem II reaction center". In: *Physical Chemistry Chemical Physics* 19.7 (2017), pp. 5195–5208.

[80] Eric C Wu et al. "Two-dimensional electronic vibrational spectroscopy and ultrafast excitonic and vibronic photosynthetic energy transfer". In: *Faraday Discussions* 216 (2019), pp. 116–132.

[81] Nicholas HC Lewis and Graham R Fleming. "Two-dimensional electronic-vibrational spectroscopy of chlorophyll *a* and *b*". In: *The Journal of Physical Chemistry Letters* 7.5 (2016), pp. 831–837.

[82] Thomas AA Oliver and Graham R Fleming. "Following coupled electronic-nuclear motion through conical intersections in the ultrafast relaxation of β-Apo-8′-carotenal". In: *The Journal of Physical Chemistry B* 119.34 (2015), pp. 11428–11441.

[83] Pallavi Bhattacharyya and Graham R Fleming. "Two-dimensional electronic–vibrational spectroscopy of coupled molecular complexes: A near-analytical approach". In: *The Journal of Physical Chemistry Letters* 10.9 (2019), pp. 2081–2089.

[84] James D Gaynor et al. "Mapping vibronic couplings in a solar cell dye with polarization-selective two-dimensional electronic–vibrational spectroscopy". In: *The Journal of Physical Chemistry Letters* 9.21 (2018), pp. 6289–6295.

[85] James D Gaynor and Munira Khalil. "Signatures of vibronic coupling in two-dimensional electronic-vibrational and vibrational-electronic spectroscopies". In: *The Journal of Chemical Physics* 147.9 (2017), p. 094202.

[86] Nicholas HC Lewis et al. "A method for the direct measurement of electronic site populations in a molecular aggregate using two-dimensional electronic-vibrational spectroscopy". In: *The Journal of Chemical Physics* 143.12 (2015), p. 124203.

[87] Sebastian Westenhoff et al. "Coherent picosecond exciton dynamics in a photosynthetic reaction center". In: *Journal of the American Chemical Society* 134.40 (2012), pp. 16484–16487.

[88] Vincenzo Barone et al. "Toward anharmonic computations of vibrational spectra for large molecular systems". In: *International Journal of Quantum Chemistry* 112.9 (2012), pp. 2185–2200.

[89] Daniel B Turner et al. "Comparison of electronic and vibrational coherence measured by two-dimensional electronic spectroscopy". In: *The Journal of Physical Chemistry Letters* 2.15 (2011), pp. 1904–1911.

[90] Laurie A Bizimana et al. "Resolving molecular vibronic structure using high-sensitivity two-dimensional electronic spectroscopy". In: *The Journal of Chemical Physics* 143.16 (2015), p. 164203.

[91] Vladimir Novoderezhkin, Alessandro Marin, and Rienk van Grondelle. "Intra-and inter-monomeric transfers in the light harvesting LHCII complex: the Redfield–Förster picture". In: *Physical Chemistry Chemical Physics* 13.38 (2011), pp. 17093–17103.

[92] Bradley S Prall et al. "Anti-correlated spectral motion in bisphthalocyanines: Evidence for vibrational modulation of electronic mixing". In: *The Journal of Physical Chemistry A* 109.48 (2005), pp. 10870–10879.

[93] Yiwei Jia et al. "Simulations of the temperature dependence of energy transfer in the PSI core antenna". In: *Biophysical Journal* 63.1 (1992), pp. 259–273.

[94] Masakazu Iwai et al. "Light-harvesting complex Lhcb9 confers a green alga-type photosystem I supercomplex to the moss Physcomitrella patens". In: *Nature Plants* 1.2 (2015), pp. 1–7.

[95] Abraham Savitzky and Marcel JE Golay. "Smoothing and differentiation of data by simplified least squares procedures." In: *Analytical Chemistry* 36.8 (1964), pp. 1627–1639.

[96] Robert E Blankenship. "Early evolution of photosynthesis". In: *Plant Physiology* 154.2 (2010), pp. 434–438.

[97] Roger Buick. "When did oxygenic photosynthesis evolve?" In: *Philosophical Transactions of the Royal Society B: Biological Sciences* 363.1504 (2008), pp. 2731–2743.

[98] JP Connelly et al. "Ultrafast spectroscopy of trimeric light-harvesting complex II from higher plants". In: *The Journal of Physical Chemistry B* 101.10 (1997), pp. 1902–1909.

[99] Kym L Wells et al. "Pathways of energy transfer in LHCII revealed by room-temperature 2D electronic spectroscopy". In: *Physical Chemistry Chemical Physics* 16.23 (2014), pp. 11640–11646.

[100] Ritesh Agarwal et al. "Ultrafast energy transfer in LHC-II revealed by three-pulse photon echo peak shift measurements". In: *The Journal of Physical Chemistry B* 104.13 (2000), pp. 2908–2918.

[101] Minjung Son et al. "The electronic structure of lutein 2 is optimized for light harvesting in plants". In: *Chem* 5.3 (2019), pp. 575–584.

[102] Minjung Son et al. "Observation of dissipative chlorophyll-to-carotenoid energy transfer in light-harvesting complex II in membrane nanodiscs". In: *Nature Communications* 11.1 (2020), pp. 1–8.

[103] Mei Du et al. "Direct observation of ultrafast energy-transfer processes in light harvesting complex II". In: *The Journal of Physical Chemistry* 98.17 (1994), pp. 4736–4741.

[104] Zhengyang Zhang et al. "Direct observation of multistep energy transfer in LHCII with fifth-order 3D electronic spectroscopy". In: *Nature Communications* 6.1 (2015), pp. 1–7.

[105] Tomáš Polıvka et al. "Carotenoid S_1 state in a recombinant light-harvesting complex of photosystem II". In: *Biochemistry* 41.2 (2002), pp. 439–450.

[106] Hayley L Smith, Lorna McAusland, and Erik H Murchie. "Don't ignore the green light: exploring diverse roles in plant processes". In: *Journal of Experimental Botany* 68.9 (2017), pp. 2099–2110.

[107] Robert E Blankenship et al. "Comparing photosynthetic and photovoltaic efficiencies and recognizing the potential for improvement". In: *Science* 332.6031 (2011), pp. 805–809.

[108] Xin-Guang Zhu, Stephen P Long, and Donald R Ort. "What is the maximum efficiency with which photosynthesis can convert solar energy into biomass?" In: *Current Opinion in Biotechnology* 19.2 (2008), pp. 153–159.

[109] James D Gaynor, Jason Sandwisch, and Munira Khalil. "Vibronic coherence evolution in multidimensional ultrafast photochemical processes". In: *Nature Communications* 10.1 (2019), p. 5621.

[110] William P Bricker et al. "Non-radiative relaxation of photoexcited chlorophylls: theoretical and experimental study". In: *Scientific Reports* 5.1 (2015), pp. 1–16.

[111] Erling Thyrhaug et al. "Exciton structure and energy transfer in the Fenna–Matthews–Olson complex". In: *The Journal of Physical Chemistry Letters* 7.9 (2016), pp. 1653–1660.

[112] Elizabeth L Read et al. "Cross-peak-specific two-dimensional electronic spectroscopy". In: *Proceedings of the National Academy of Sciences* 104.36 (2007), pp. 14203–14208.

[113] Iwao Yamazaki et al. "Observation of quantum coherence for recurrence motion of exciton in anthracene dimers in solution". In: *Journal of the American Chemical Society* 125.24 (2003), pp. 7192–7193.

[114] Martin Gouterman. "Spectra of porphyrins". In: *Journal of Molecular Spectroscopy* 6 (1961), pp. 138–163.

[115] Claude Houssier and Kenneth Sauer. "Circular dichroism and magnetic circular dichroism of the chlorophyll and protochlorophyll pigments". In: *Journal of the American Chemical Society* 92.4 (1970), pp. 779–791.

[116] Juha Linnanto and Jouko Korppi-Tommola. "Spectroscopic properties of Mg-chlorin, Mg-porphin and chlorophylls a, b, c_1, c_2, c_3 and d studied by semi-empirical and ab initio MO/CI methods". In: *Physical Chemistry Chemical Physics* 2.21 (2000), pp. 4962–4970.

[117] James R Diers et al. "Q_y-excitation resonance Raman spectra of chlorophyll a and bacteriochlorophyll c/d aggregates. Effects of peripheral substituents on the low-frequency vibrational characteristics". In: *The Journal of Physical Chemistry* 100.20 (1996), pp. 8573–8579.

[118] Chengli Zhou, James R Diers, and David F Bocian. "Q_y-excitation resonance Raman spectra of chlorophyll a and related complexes. Normal mode characteristics of the low-frequency vibrations". In: *The Journal of Physical Chemistry B* 101.46 (1997), pp. 9635–9644.

[119] Philipp Kukura, Renee Frontiera, and Richard A Mathies. "Direct observation of anharmonic coupling in the time domain with femtosecond stimulated Raman scattering". In: *Physical Review Letters* 96.23 (2006), p. 238303.

[120] Hideaki Kano, Takashi Saito, and Takayoshi Kobayashi. "Observation of Herzberg-Teller-type Wave Packet Motion in Porphyrin J-Aggregates Studied by Sub-5-fs Spectroscopy". In: *The Journal of Physical Chemistry A* 106.14 (2002), pp. 3445–3453.

[121] Gregory D Scholes et al. "Lessons from nature about solar light harvesting". In: *Nature Chemistry* 3.10 (2011), pp. 763–774.

[122] Jeffrey A Myers et al. "Two-dimensional electronic spectroscopy of the D1-D2-cyt b559 photosystem II reaction center complex". In: *The Journal of Physical Chemistry Letters* 1.19 (2010), pp. 2774–2780.

[123] Elisabet Romero et al. "Quantum coherence in photosynthesis for efficient solar-energy conversion". In: *Nature Physics* 10.9 (2014), pp. 676–682.

[124] Jacob S Higgins et al. "Photosynthesis tunes quantum-mechanical mixing of electronic and vibrational states to steer exciton energy transfer". In: *Proceedings of the National Academy of Sciences* 118.11 (2021).

[125] Yuta Fujihashi, Graham R Fleming, and Akihito Ishizaki. "Impact of environmentally induced fluctuations on quantum mechanically mixed electronic and vibrational pigment states in photosynthetic energy transfer and 2D electronic spectra". In: *The Journal of Chemical Physics* 142.21 (2015), p. 212403.

[126] Jianshu Cao et al. "Quantum biology revisited". In: *Science Advances* 6.14 (2020), eaaz4888.

[127] Hong-Guang Duan et al. "Ultrafast energy transfer in excitonically coupled molecules induced by a nonlocal Peierls phonon". In: *The Journal of Physical Chemistry Letters* 10.6 (2019), pp. 1206–1211.

[128] Hong-Guang Duan et al. "Intramolecular vibrations enhance the quantum efficiency of excitonic energy transfer". In: *Photosynthesis Research* 144.2 (2020), pp. 137–145.

[129] Yusuke Yoneda et al. "Non-condon effect on ultrafast excited-state intramolecular proton transfer". In: *The Journal of Physical Chemistry A* 124.2 (2019), pp. 265–271.

[130] Marek Z Zgierski. "Herzberg-Teller interactions and spectra of dimers: Stable anthracene dimer". In: *The Journal of Chemical Physics* 59.6 (1973), pp. 3319–3322.

[131] M Wykes et al. "Vibronic coupling in molecular crystals: A Franck-Condon Herzberg-Teller model of H-aggregate fluorescence based on quantum chemical cluster calculations". In: *The Journal of Chemical Physics* 143.11 (2015), p. 114116.

[132] Andreas C Albrecht. ""Forbidden" Character in Allowed Electronic Transitions". In: *The Journal of Chemical Physics* 33.1 (1960), pp. 156–169.

[133] Andrés Montoya-Castillo, Timothy C Berkelbach, and David R Reichman. "Extending the applicability of Redfield theories into highly non-Markovian regimes". In: *The Journal of Chemical Physics* 143.19 (2015), p. 194108.

[134] Addison J Schile and David T Limmer. "Simulating conical intersection dynamics in the condensed phase with hybrid quantum master equations". In: *The Journal of Chemical Physics* 151.1 (2019), p. 014106.

[135] Jonathan H Fetherolf and Timothy C Berkelbach. "Linear and nonlinear spectroscopy from quantum master equations". In: *The Journal of Chemical Physics* 147.24 (2017), p. 244109.

[136] Victor V Albert et al. "Geometry and response of Lindbladians". In: *Physical Review X* 6.4 (2016), p. 041031.

[137] Amikam Levy, Eran Rabani, and David T Limmer. "Response theory for nonequilibrium steady states of open quantum systems". In: *Physical Review Research* 3.2 (2021), p. 023252.

[138] Daniel Alonso and Inés de Vega. "Multiple-time correlation functions for non-Markovian interaction: beyond the quantum regression theorem". In: *Physical Review Letters* 94.20 (2005), p. 200403.

[139] James D Gaynor, Robert B Weakly, and Munira Khalil. "Multimode two-dimensional vibronic spectroscopy. I. Orientational response and polarization-selectivity". In: *The Journal of Chemical Physics* 154.18 (2021), p. 184201.

[140] Robert B Weakly, James D Gaynor, and Munira Khalil. "Multimode two-dimensional vibronic spectroscopy. II. Simulating and extracting vibronic coupling parameters from polarization-selective spectra". In: *The Journal of Chemical Physics* 154.18 (2021), p. 184202.

[141] Stephanie M Hart et al. "Identification of nonradiative decay pathways in Cy3". In: *The Journal of Physical Chemistry Letters* 11.13 (2020), pp. 5000–5007.

[142] Sarah Maria Falke et al. "Coherent ultrafast charge transfer in an organic photovoltaic blend". In: *Science* 344.6187 (2014), pp. 1001–1005.

[143] Jonathan D Schultz et al. "Influence of Vibronic Coupling on Ultrafast Singlet Fission in a Linear Terrylenediimide Dimer". In: *Journal of the American Chemical Society* 143.4 (2021), pp. 2049–2058.

[144] Carlo Andrea Rozzi et al. "Quantum coherence controls the charge separation in a prototypical artificial light-harvesting system". In: *Nature Communications* 4.1 (2013), p. 1602.

[145] Bernhard Loll et al. "Towards complete cofactor arrangement in the 3.0 Å resolution structure of photosystem II". In: *Nature* 438.7070 (2005), pp. 1040–1044.

[146] Yasufumi Umena et al. "Crystal structure of oxygen-evolving photosystem II at a resolution of 1.9 Å". In: *Nature* 473.7345 (2011), pp. 55–60.

[147] IV Shelaev et al. "Primary light-energy conversion in tetrameric chlorophyll structure of photosystem II and bacterial reaction centers: II. Femto-and picosecond charge separation in PSII D1/D2/Cyt b559 complex". In: *Photosynthesis Research* 98.1 (2008), pp. 95–103.

[148] VA Nadtochenko, A Yu Semenov, and VA Shuvalov. "Formation and decay of P680 $(P_{D1}\text{-}P_{D2})^{+}Pheo_{D1}^{-}$ radical ion pair in photosystem II core complexes". In: *Biochimica et Biophysica Acta (BBA)-Bioenergetics* 1837.9 (2014), pp. 1384–1388.

[149] Marie Louise Groot et al. "Initial electron donor and acceptor in isolated photosystem II reaction centers identified with femtosecond mid-IR spectroscopy". In: *Proceedings of the National Academy of Sciences* 102.37 (2005), pp. 13087–13092.

[150] Valentin I Prokhorenko and Alfred R Holzwarth. "Primary processes and structure of the photosystem II reaction center: a photon echo study". In: *The Journal of Physical Chemistry B* 104.48 (2000), pp. 11563–11578.

[151] Alfred R Holzwarth et al. "Kinetics and mechanism of electron transfer in intact photosystem II and in the isolated reaction center: pheophytin is the primary electron acceptor". In: *Proceedings of the National Academy of Sciences* 103.18 (2006), pp. 6895–6900.

[152] James R Durrant et al. "A multimer model for P680, the primary electron donor of photosystem II". In: *Proceedings of the National Academy of Sciences* 92.11 (1995), pp. 4798–4802.

[153] Grzegorz Raszewski et al. "Spectroscopic properties of reaction center pigments in photosystem II core complexes: revision of the multimer model". In: *Biophysical Journal* 95.1 (2008), pp. 105–119.

[154] Vladimir I Novoderezhkin, Jan P Dekker, and Rienk Van Grondelle. "Mixing of exciton and charge-transfer states in photosystem II reaction centers: modeling of stark spectra with modified Redfield theory". In: *Biophysical Journal* 93.4 (2007), pp. 1293–1311.

[155] Paula J Booth et al. "Observation of multiple radical pair states in photosystem 2 reaction centers". In: *Biochemistry* 30.30 (1991), pp. 7573–7586.

[156] Lars Konermann, Guido Gatzen, and Alfred R Holzwarth. "Primary Processes and Structure of the Photosystem II Reaction Center. 5. Modeling of the Fluorescence Kinetics of the D1-D2-cyt-b 559 Complex at 77 K". In: *The Journal of Physical Chemistry B* 101.15 (1997), pp. 2933–2944.

[157] H Matthieu Visser et al. "Subpicosecond transient absorption difference spectroscopy on the reaction center of photosystem II: radical pair formation at 77 K". In: *The Journal of Physical Chemistry* 99.41 (1995), pp. 15304–15309.

[158] Marie-Louise Groot et al. "Charge separation in the reaction center of photosystem II studied as a function of temperature". In: *Proceedings of the National Academy of Sciences* 94.9 (1997), pp. 4389–4394.

[159] Elisabet Romero et al. "Two different charge separation pathways in photosystem II". In: *Biochemistry* 49.20 (2010), pp. 4300–4307.

[160] Hong-Guang Duan et al. "Primary charge separation in the Photosystem II reaction center revealed by a Global Analysis of the two-dimensional electronic spectra". In: *Scientific Reports* 7.1 (2017), pp. 1–9.

[161] Marie Louise Groot, Luuk JGW van Wilderen, and Mariangela Di Donato. "Time-resolved methods in biophysics. 5. Femtosecond time-resolved and dispersed infrared spectroscopy on proteins". In: *Photochemical & Photobiological Sciences* 6.5 (2007), pp. 501–507.

[162] Mariangela Di Donato and Marie Louise Groot. "Ultrafast infrared spectroscopy in photosynthesis". In: *Biochimica et Biophysica Acta (BBA)-Bioenergetics* 1847.1 (2015), pp. 2–11.

[163] Jacques Breton. "Fourier transform infrared spectroscopy of primary electron donors in type I photosynthetic reaction centers". In: *Biochimica et Biophysica Acta (BBA)-Bioenergetics* 1507.1-3 (2001), pp. 180–193.

[164] Takumi Noguchi and Catherine Berthomieu. "Molecular analysis by vibrational spectroscopy". In: *Photosystem II* (2005), pp. 367–387.

[165] Takumi Noguchi, Tatsuya Tomo, and Yorinao Inoue. "Fourier transform infrared study of the cation radical of P680 in the photosystem II reaction center: evidence for charge delocalization on the chlorophyll dimer". In: *Biochemistry* 37.39 (1998), pp. 13614–13625.

[166] E Nabedryk et al. "Characterization of bonding interactions of the intermediary electron acceptor in the reaction center of photosystem II by FTIR spectroscopy". In: *Biochimica et Biophysica Acta (BBA)-Bioenergetics* 1016.1 (1990), pp. 49–54.

[167] J Breton, R Hienerwadel, and E Nabedryk. "FTIR difference spectrum of the photooxidation of the primary electron donor of photosystem II". In: *Spectroscopy of Biological Molecules: Modern Trends*. Springer, 1997, pp. 101–102.

[168] Takumi Noguchi, Tatsuya Tomo, and Chihiro Kato. "Triplet formation on a monomeric chlorophyll in the photosystem II reaction center as studied by time-resolved infrared spectroscopy". In: *Biochemistry* 40.7 (2001), pp. 2176–2185.

[169] E Nabedryk et al. "Fourier transform infrared difference spectroscopy shows no evidence for an enolization of chlorophyll a upon cation formation either in vitro or during P700 photooxidation". In: *Biochemistry* 29.13 (1990), pp. 3242–3247.

[170] Elisabet Romero et al. "Mixed exciton–charge-transfer states in photosystem II: stark spectroscopy on site-directed mutants". In: *Biophysical Journal* 103.2 (2012), pp. 185–194.

[171] Anders Thapper et al. "Defining the far-red limit of photosystem II in spinach". In: *The Plant Cell* 21.8 (2009), pp. 2391–2401.

[172] Andrea Pavlou et al. "The wavelength of the incident light determines the primary charge separation pathway in Photosystem II". In: *Scientific Reports* 8.1 (2018), pp. 1–11.

[173] Abhishek Sirohiwal, Frank Neese, and Dimitrios A Pantazis. "Protein matrix control of reaction center excitation in photosystem II". In: *Journal of the American Chemical Society* 142.42 (2020), pp. 18174–18190.

[174] Hugo Pettai et al. "Photosynthetic activity of far-red light in green plants". In: *Biochimica et Biophysica Acta (BBA)-Bioenergetics* 1708.3 (2005), pp. 311–321.

[175] Marie Louise Groot et al. "Femtosecond visible/visible and visible/mid-IR pump-probe study of the photosystem II core antenna complex CP47". In: *The Journal of Physical Chemistry B* 108.23 (2004), pp. 8001–8006.

[176] Ivo HM van Stokkum, Delmar S Larsen, and Rienk Van Grondelle. "Global and target analysis of time-resolved spectra". In: *Biochimica et Biophysica Acta (BBA)-Bioenergetics* 1657.2-3 (2004), pp. 82–104.

[177] Tatsunori Okubo et al. "Perturbation of the structure of P680 and the charge distribution on its radical cation in isolated reaction center complexes of photosystem II as revealed by Fourier transform infrared spectroscopy". In: *Biochemistry* 46.14 (2007), pp. 4390–4397.

[178] Bruce A Diner et al. "Site-directed mutations at D1-His198 and D2-His197 of photosystem II in Synechocystis PCC 6803: sites of primary charge separation and cation and triplet stabilization". In: *Biochemistry* 40.31 (2001), pp. 9265–9281.

[179] Keisuke Saito et al. "Distribution of the cationic state over the chlorophyll pair of the photosystem II reaction center". In: *Journal of the American Chemical Society* 133.36 (2011), pp. 14379–14388.

[180] Daniele Narzi et al. "Dynamics of the special pair of chlorophylls of photosystem II". In: *Journal of the American Chemical Society* 138.1 (2016), pp. 257–264.

[181] Deborah A Berthold, Gerald T Babcock, and Charles F Yocum. "A highly resolved, oxygen-evolving photosystem II preparation from spinach thylakoid membranes: EPR and electron-transport properties". In: *FEBS Letters* 134.2 (1981), pp. 231–234.

[182] Stefano Caffarri et al. "Functional architecture of higher plant photosystem II supercomplexes". In: *The EMBO Journal* 28.19 (2009), pp. 3052–3063.

[183] RJ Porra, WA Thompson, and PE Kriedemann. "Determination of accurate extinction coefficients and simultaneous equations for assaying chlorophylls *a* and *b* extracted with four different solvents: verification of the concentration of chlorophyll standards by atomic absorption spectroscopy". In: *Biochimica et Biophysica Acta (BBA)-Bioenergetics* 975.3 (1989), pp. 384–394.

[184] Osamu Nanba and Kimiyuki Satoh. "Isolation of a photosystem II reaction center consisting of D-1 and D-2 polypeptides and cytochrome b-559". In: *Proceedings of the National Academy of Sciences* 84.1 (1987), pp. 109–112.

[185] Hugh McTavish, Rafael Picorel, and Michael Seibert. "Stabilization of isolated photosystem II reaction center complex in the dark and in the light using polyethylene glycol and an oxygen-scrubbing system". In: *Plant Physiology* 89.2 (1989), pp. 452–456.

[186] Michael Seibert, Inmaculada Yruela, and Rafael Picorel. "Isolation of photosystem II reaction center complexes from plants". In: *Photosynthesis Research Protocols*. Springer, 2004, pp. 53–62.

[187] Deniz Tuna et al. "Mechanisms of Photostability in Kynurenines: A Joint Electronic-Structure and Dynamics Study". In: *The Journal of Physical Chemistry B* 119.6 (2015), pp. 2112–2124.

[188] Serhiy Perun, Andrzej L Sobolewski, and Wolfgang Domcke. "Ab initio studies on the radiationless decay mechanisms of the lowest excited singlet states of 9H-adenine". In: *Journal of the American Chemical Society* 127.17 (2005), pp. 6257–6265.

[189] Andrzej L Sobolewski and Wolfgang Domcke. "The chemical physics of the photostability of life". In: *Europhysics News* 37.4 (2006), pp. 20–23.

[190] Andrzej L Sobolewski and Wolfgang Domcke. "Relevance of Electron-Driven Proton-Transfer Processes for the Photostability of Proteins". In: *ChemPhysChem* 7.3 (2006), pp. 561–564.

[191] Andrzej L Sobolewski and Wolfgang Domcke. "Computational studies of the photophysics of hydrogen-bonded molecular systems". In: *The Journal of Physical Chemistry A* 111.46 (2007), pp. 11725–11735.

[192] Annapaola Migani et al. "An extended conical intersection seam associated with a manifold of decay paths: excited-state intramolecular proton transfer in O-hydroxybenzaldehyde". In: *Journal of the American Chemical Society* 130.22 (2008), pp. 6932–6933.

[193] Mario Barbatti et al. "Ultrafast internal conversion pathway and mechanism in 2-(2-hydroxyphenyl) benzothiazole: a case study for excited-state intramolecular proton transfer systems". In: *Physical Chemistry Chemical Physics* 11.9 (2009), pp. 1406–1415.

[194] Maria J Melo and Ana Claro. "Bright light: microspectrofluorimetry for the characterization of lake pigments and dyes in works of art". In: *Accounts of Chemical Research* 43.6 (2010), pp. 857–866.

[195] Jeffrey C Splitstoser et al. "Early pre-Hispanic use of indigo blue in Peru". In: *Science Advances* 2.9 (2016), e1501623.

[196] Izumi Iwakura, Atsushi Yabushita, and Takayoshi Kobayashi. "Kinetic isotope effect on the proton-transfer in indigo carmine". In: *Chemical Physics Letters* 484.4-6 (2010), pp. 354–357.

[197] Xuemei He et al. "Efficient vibrational energy transfer through covalent bond in indigo carmine revealed by nonlinear IR spectroscopy". In: *The Journal of Physical Chemistry B* 121.40 (2017), pp. 9411–9421.

[198] Philip J Stephens et al. "Ab initio calculation of vibrational absorption and circular dichroism spectra using density functional force fields". In: *The Journal of Physical Chemistry* 98.45 (1994), pp. 11623–11627.

[199] Axel D Beck. "Density-functional thermochemistry. III. The role of exact exchange". In: *The Journal of Chemical Physics* 98.7 (1993), pp. 5648–5652.

[200] Michael J Frisch, John A Pople, and J Stephen Binkley. "Self-consistent molecular orbital methods 25. Supplementary functions for Gaussian basis sets". In: *The Journal of Chemical Physics* 80.7 (1984), pp. 3265–3269.

[201] Maurizio Cossi et al. "Energies, structures, and electronic properties of molecules in solution with the C-PCM solvation model". In: *Journal of Computational Chemistry* 24.6 (2003), pp. 669–681.

[202] Yihan Shao et al. "Advances in molecular quantum chemistry contained in the Q-Chem 4 program package". In: *Molecular Physics* 113.2 (2015), pp. 184–215.

[203] Andreas Dreuw and Martin Head-Gordon. "Single-reference ab initio methods for the calculation of excited states of large molecules". In: *Chemical Reviews* 105.11 (2005), pp. 4009–4037.

[204] Tie-Cheng Li and Pei-qing Tong. "Time-dependent density-functional theory for multicomponent systems". In: *Physical Review A* 34 (1986), pp. 529–532.

[205] Xing Zhang and John M Herbert. "Excited-State Deactivation Pathways in Uracil versus Hydrated Uracil: Solvatochromatic Shift in the $^1n\pi^*$ State is the Key". In: *The Journal of Physical Chemistry B* 118.28 (2014), pp. 7806–7817.

[206] Satoshi Maeda, Koichi Ohno, and Keiji Morokuma. "Updated branching plane for finding conical intersections without coupling derivative vectors". In: *Journal of Chemical Theory and Computation* 6.5 (2010), pp. 1538–1545.

[207] Xing Zhang and John M Herbert. "Analytic derivative couplings for spin-flip configuration interaction singles and spin-flip time-dependent density functional theory". In: *The Journal of Chemical Physics* 141.6 (2014), p. 064104.

[208] Axel D Becke. "A new mixing of Hartree–Fock and local density-functional theories". In: *The Journal of Chemical Physics* 98.2 (1993), pp. 1372–1377.

[209] Yihan Shao, Martin Head-Gordon, and Anna I Krylov. "The spin–flip approach within time-dependent density functional theory: Theory and applications to diradicals". In: *The Journal of Chemical Physics* 118.11 (2003), pp. 4807–4818.

[210] Robert J Buenker, Vlasta Bonačić-Kouteck, and Lionello Pogliani. "Potential energy and dipole moment surfaces for simultaneous torsion and pyramidalization of ethylene in its lowest-lying singlet excited states: A CI study of the sudden polarization effect". In: *The Journal of Chemical Physics* 73.4 (1980), pp. 1836–1849.

[211] My Hang V Huynh and Thomas J Meyer. "Proton-coupled electron transfer". In: *Chemical Reviews* 107.11 (2007), pp. 5004–5064.

[212] Thomas J Meyer, My Hang V Huynh, and H Holden Thorp. "The possible role of proton-coupled electron transfer (PCET) in water oxidation by photosystem II". In: *Angewandte Chemie International Edition* 46.28 (2007), pp. 5284–5304.

[213] Sharon Hammes-Schiffer and Alexander V Soudackov. "Proton-coupled electron transfer in solution, proteins, and electrochemistry". In: *The Journal of Physical Chemistry B* 112.45 (2008), pp. 14108–14123.

[214] Steven Y Reece and Daniel G Nocera. "Proton-coupled electron transfer in biology: results from synergistic studies in natural and model systems". In: *Annual Review of Biochemistry* 78 (2009), pp. 673–699.

[215] Sharon Hammes-Schiffer and Alexei A Stuchebrukhov. "Theory of coupled electron and proton transfer reactions". In: *Chemical Reviews* 110.12 (2010), pp. 6939–6960.

[216] Leif Hammarström and Stenbjörn Styring. "Proton-coupled electron transfer of tyrosines in Photosystem II and model systems for artificial photosynthesis: the role of a redox-active link between catalyst and photosensitizer". In: *Energy & Environmental Science* 4.7 (2011), pp. 2379–2388.

[217] David R Weinberg et al. "Proton-coupled electron transfer". In: *Chemical Reviews* 112.7 (2012), pp. 4016–4093.

[218] S Jimena Mora et al. "Proton-coupled electron transfer in artificial photosynthetic systems". In: *Accounts of Chemical Research* 51.2 (2018), pp. 445–453.

[219] Jackson D Megiatto et al. "Mimicking the electron transfer chain in photosystem II with a molecular triad thermodynamically capable of water oxidation". In: *Proceedings of the National Academy of Sciences* 109.39 (2012), pp. 15578–15583.

[220] Jackson D Megiatto Jr et al. "A bioinspired redox relay that mimics radical interactions of the Tyr–His pairs of photosystem II". In: *Nature Chemistry* 6.5 (2014), pp. 423–428.

[221] Janneke Ravensbergen et al. "Spectroscopic analysis of a biomimetic model of TyrZ function in PSII". In: *The Journal of Physical Chemistry B* 119.37 (2015), pp. 12156–12163.

[222] Emmanuel Odella et al. "Proton-coupled electron transfer drives long-range proton translocation in bioinspired systems". In: *Journal of the American Chemical Society* 141.36 (2019), pp. 14057–14061.

[223] Mioy T Huynh et al. "Concerted one-electron two-proton transfer processes in models inspired by the Tyr-His couple of photosystem II". In: *ACS Central Science* 3.5 (2017), pp. 372–380.

[224] Giovanny A Parada et al. "Concerted proton-electron transfer reactions in the Marcus inverted region". In: *Science* 364.6439 (2019), pp. 471–475.

[225] Gary F Moore et al. "A bioinspired construct that mimics the proton coupled electron transfer between $P680^{\bullet+}$ and the Tyr_Z-His190 pair of photosystem II". In: *Journal of the American Chemical Society* 130.32 (2008), pp. 10466–10467.

[226] Degao Wang et al. "Molecular photoelectrode for water oxidation inspired by photosystem II". In: *Journal of the American Chemical Society* 141.19 (2019), pp. 7926–7933.

[227] Brittany C Westlake et al. "Concerted electron-proton transfer in the optical excitation of hydrogen-bonded dyes". In: *Proceedings of the National Academy of Sciences* 108.21 (2011), pp. 8554–8558.

[228] Thomas T Eisenhart and Jillian L Dempsey. "Photo-induced proton-coupled electron transfer reactions of acridine orange: comprehensive spectral and kinetics analysis". In: *Journal of the American Chemical Society* 136.35 (2014), pp. 12221–12224.

[229] Christopher J Gagliardi et al. "Direct observation of light-driven, concerted electron–proton transfer". In: *Proceedings of the National Academy of Sciences* 113.40 (2016), pp. 11106–11109.

[230] Eisuke Takeuchi et al. "Sub-100 fs charge separation and subsequent diffusive solvation observed for asymmetric bianthryl derivative in ionic liquid". In: *The Journal of Physical Chemistry C* 120.27 (2016), pp. 14502–14512.

[231] Anirban Hazra, Alexander V Soudackov, and Sharon Hammes-Schiffer. "Isotope effects on the nonequilibrium dynamics of ultrafast photoinduced proton-coupled electron transfer reactions in solution". In: *The Journal of Physical Chemistry Letters* 2.1 (2011), pp. 36–40.

[232] S Jimena Mora et al. "Design and synthesis of benzimidazole phenol-porphyrin dyads for the study of bioinspired photoinduced proton-coupled electron transfer". In: *Journal of Porphyrins and Phthalocyanines* 23.11n12 (2019), pp. 1336–1345.

[233] Hisayoshi Iikura et al. "A long-range correction scheme for generalized-gradient-approximation exchange functionals". In: *The Journal of Chemical Physics* 115.8 (2001), pp. 3540–3544.

[234] Yoshihiro Tawada et al. "A long-range-corrected time-dependent density functional theory". In: *The Journal of Chemical Physics* 120.18 (2004), pp. 8425–8433.

[235] Tamar Stein et al. "Fundamental gaps in finite systems from eigenvalues of a generalized Kohn-Sham method". In: *Physical Review Letters* 105.26 (2010), p. 266802.

[236] Thomas Körzdörfer and Jean-Luc Bredas. "Organic electronic materials: recent advances in the DFT description of the ground and excited states using tuned range-separated hybrid functionals". In: *Accounts of Chemical Research* 47.11 (2014), pp. 3284–3291.

[237] Tamar Stein, Leeor Kronik, and Roi Baer. "Reliable prediction of charge transfer excitations in molecular complexes using time-dependent density functional theory". In: *Journal of the American Chemical Society* 131.8 (2009), pp. 2818–2820.

[238] Kyungwon Kwak et al. "Frequency-frequency correlation functions and apodization in two-dimensional infrared vibrational echo spectroscopy: A new approach". In: *The Journal of Chemical Physics* 127.12 (2007), p. 124503.

[239] Kyungwon Kwak, Daniel E Rosenfeld, and MD Fayer. "Taking apart the two-dimensional infrared vibrational echo spectra: More information and elimination of distortions". In: *The Journal of Chemical Physics* 128.20 (2008), p. 204505.

[240] Richard L Martin. "Natural transition orbitals". In: *The Journal of Chemical Physics* 118.11 (2003), pp. 4775–4777.

[241] Zbigniew R Grabowski, Krystyna Rotkiewicz, and Wolfgang Rettig. "Structural changes accompanying intramolecular electron transfer: focus on twisted intramolecular charge-transfer states and structures". In: *Chemical Reviews* 103.10 (2003), pp. 3899–4032.

[242] James Shee and Martin Head-Gordon. "Predicting excitation energies of twisted intramolecular charge-transfer states with the time-dependent density functional theory: Comparison with experimental measurements in the gas phase and solvents ranging from hexanes to acetonitrile". In: *Journal of Chemical Theory and Computation* 16.10 (2020), pp. 6244–6255.

[243] Diptarka Hait and Martin Head-Gordon. "How accurate is density functional theory at predicting dipole moments? An assessment using a new database of 200 benchmark values". In: *Journal of Chemical Theory and Computation* 14.4 (2018), pp. 1969–1981.

[244] Monique M Martin et al. "UV-vis Subpicosecond Spectroscopy of 4-(9-Anthryl)-N,N′-dimethylaniline in Polar and Nonpolar Solvents: A Two-Dimensional View of the Photodynamics". In: *The Journal of Physical Chemistry A* 106.10 (2002), pp. 2351–2358.

[245] Bogdan Dereka et al. "Direct observation of a photochemical alkyne–allene reaction and of a twisted and rehybridized intramolecular charge-transfer state in a donor–acceptor dyad". In: *Journal of the American Chemical Society* 139.46 (2017), pp. 16885–16893.

[246] Sandra J Rosenthal et al. "Femtosecond solvation dynamics in acetonitrile: Observation of the inertial contribution to the solvent response". In: *The Journal of Chemical Physics* 95.6 (1991), pp. 4715–4718.

[247] Peter Hamm. "Coherent effects in femtosecond infrared spectroscopy". In: *Chemical Physics* 200.3 (1995), pp. 415–429.

[248] Jonathan S Lindsey. "Synthetic routes to meso-patterned porphyrins". In: *Accounts of Chemical Research* 43.2 (2010), pp. 300–311.

[249] Jackson D Megiatto et al. "Intramolecular hydrogen bonding as a synthetic tool to induce chemical selectivity in acid catalyzed porphyrin synthesis". In: *Chemical Communications* 48.38 (2012), pp. 4558–4560.

[250] Devens Gust et al. "Long-lived photoinitiated charge separation in carotene-diporphyrin triad molecules". In: *Journal of the American Chemical Society* 113.10 (1991), pp. 3638–3649.

[251] Charles W Machan et al. "Developing a mechanistic understanding of molecular electrocatalysts for CO_2 reduction using infrared spectroelectrochemistry". In: *Organometallics* 33.18 (2014), pp. 4550–4559.

[252] Neil G Connelly and William E Geiger. "Chemical redox agents for organometallic chemistry". In: *Chemical Reviews* 96.2 (1996), pp. 877–910.

[253] Florian Weigend and Reinhart Ahlrichs. "Balanced basis sets of split valence, triple zeta valence and quadruple zeta valence quality for H to Rn: Design and assessment of accuracy". In: *Physical Chemistry Chemical Physics* 7.18 (2005), pp. 3297–3305.

[254] Mary A Rohrdanz, Katie M Martins, and John M Herbert. "A long-range-corrected density functional that performs well for both ground-state properties and time-dependent density functional theory excitation energies, including charge-transfer excited states". In: *The Journal of Chemical Physics* 130.5 (2009), p. 054112.

[255] Erich Runge and Eberhard KU Gross. "Density-functional theory for time-dependent systems". In: *Physical Review Letters* 52.12 (1984), p. 997.

[256] Shuping Huang et al. "Computational prediction for singlet-and triplet-transition energies of charge-transfer compounds". In: *Journal of Chemical Theory and Computation* 9.9 (2013), pp. 3872–3877.

[257] John P Perdew et al. "Density-functional theory for fractional particle number: derivative discontinuities of the energy". In: *Physical Review Letters* 49.23 (1982), p. 1691.

[258] CD van der Weij-de Wit et al. "Charge separation is virtually irreversible in photosystem II core complexes with oxidized primary quinone acceptor". In: *The Journal of Physical Chemistry A* 115.16 (2011), pp. 3947–3956.

[259] Yutaka Shibata et al. "Photosystem II does not possess a simple excitation energy funnel: time-resolved fluorescence spectroscopy meets theory". In: *Journal of the American Chemical Society* 135.18 (2013), pp. 6903–6914.

[260] Natalia P Pawlowicz et al. "Charge separation and energy transfer in the photosystem II core complex studied by femtosecond midinfrared spectroscopy". In: *Biophysical Journal* 93.8 (2007), pp. 2732–2742.

[261] Patrick Jordan et al. "Three-dimensional structure of cyanobacterial photosystem I at 2.5 Å resolution". In: *Nature* 411.6840 (2001), pp. 909–917.

[262] David J Vinyard and Gary W Brudvig. "Progress toward a molecular mechanism of water oxidation in photosystem II". In: *Annual Review of Physical Chemistry* 68 (2017), pp. 101–116.

[263] Keisuke Saito, A William Rutherford, and Hiroshi Ishikita. "Energetics of proton release on the first oxidation step in the water-oxidizing enzyme". In: *Nature Communications* 6.1 (2015), pp. 1–10.

[264] Yixin Zhao et al. "Improving the efficiency of water splitting in dye-sensitized solar cells by using a biomimetic electron transfer mediator". In: *Proceedings of the National Academy of Sciences* 109.39 (2012), pp. 15612–15616.

[265] Emmanuel Odella et al. "Proton-coupled electron transfer across benzimidazole bridges in bioinspired proton wires". In: *Chemical Science* 11.15 (2020), pp. 3820–3828.

[266] Peter Hamm, Robert A Kaindl, and Jens Stenger. "Noise suppression in femtosecond mid-infrared light sources". In: *Optics Letters* 25.24 (2000), pp. 1798–1800.

[267] AA Lanin et al. "Frequency-tunable sub-two-cycle 60-MW-peak-power free-space waveforms in the mid-infrared". In: *Optics Letters* 39.22 (2014), pp. 6430–6433.

[268] AA Lanin et al. "Multioctave, 3-18 μm sub-two-cycle supercontinua from self-compressing, self-focusing soliton transients in a solid". In: *Optics Letters* 40.6 (2015), pp. 974–977.

[269] EA Stepanov et al. "Solid-state source of subcycle pulses in the midinfrared". In: *Physical Review Letters* 117.4 (2016), p. 043901.

[270] CJ Fecko, JJ Loparo, and A Tokmakoff. "Generation of 45 femtosecond pulses at 3 μm with a KNbO3 optical parametric amplifier". In: *Optics Communications* 241.4-6 (2004), pp. 521–528.

[271] Agnė Marcinkevičiūtė et al. "A compact, self-compression-based sub-3 optical cycle source in the spectral range". In: *Journal of Optics* 19.10 (2017), p. 105505.

[272] Jinqing Huang, Alexander Parobek, and Ziad Ganim. "Octave-spanning mid-infrared pulses by plasma generation in air pumped with an Yb: KGW source". In: *Optics Letters* 41.21 (2016), pp. 4855–4858.

[273] DJ Cook and RM Hochstrasser. "Intense terahertz pulses by four-wave rectification in air". In: *Optics Letters* 25.16 (2000), pp. 1210–1212.

[274] Takao Fuji and Toshinori Suzuki. "Generation of sub-two-cycle mid-infrared pulses by four-wave mixing through filamentation in air". In: *Optics Letters* 32.22 (2007), pp. 3330–3332.

[275] Ki-Yong Kim et al. "Coherent control of terahertz supercontinuum generation in ultrafast laser–gas interactions". In: *Nature Photonics* 2.10 (2008), pp. 605–609.

[276] Poul B Petersen and Andrei Tokmakoff. "Source for ultrafast continuum infrared and terahertz radiation". In: *Optics Letters* 35.12 (2010), pp. 1962–1964.

[277] Takao Fuji and Yutaka Nomura. "Generation of phase-stable sub-cycle mid-infrared pulses from filamentation in nitrogen". In: *Applied Sciences* 3.1 (2013), pp. 122–138.

[278] Yutaka Nomura et al. "Phase-stable sub-cycle mid-infrared conical emission from filamentation in gases". In: *Optics Express* 20.22 (2012), pp. 24741–24747.

[279] Y Nomura et al. "Single-shot detection of mid-infrared spectra by chirped-pulse up-conversion with four-wave difference frequency generation in gases". In: *Optics Express* 21.15 (2013), pp. 18249–18254.

[280] L Bergé et al. "Ultrashort filaments of light in weakly ionized, optically transparent media". In: *Reports on Progress in Physics* 70.10 (2007), p. 1633.

[281] A Braun et al. "Self-channeling of high-peak-power femtosecond laser pulses in air". In: *Optics Letters* 20.1 (1995), pp. 73–75.

[282] Arnaud Couairon and André Mysyrowicz. "Femtosecond filamentation in transparent media". In: *Physics Reports* 441.2-4 (2007), pp. 47–189.

[283] James D Gaynor et al. "Fourier transform two-dimensional electronic-vibrational spectroscopy using an octave-spanning mid-IR probe". In: *Optics Letters* 41.12 (2016), pp. 2895–2898.

[284] Eran Edri et al. "Ultrafast charge transfer between light absorber and Co_3O_4 water oxidation catalyst across molecular wires embedded in silica membrane". In: *Journal of the American Chemical Society* 139.15 (2017), pp. 5458–5466.

[285] Won Jun Jo, Georgios Katsoukis, and Heinz Frei. "Ultrathin Amorphous Silica Membrane Enhances Proton Transfer across Solid-to-Solid Interfaces of Stacked Metal Oxide Nanolayers while Blocking Oxygen". In: *Advanced Functional Materials* 30.12 (2020), p. 1909262.

[286] Degao Wang et al. "A stable dye-sensitized photoelectrosynthesis cell mediated by a NiO overlayer for water oxidation". In: *Proceedings of the National Academy of Sciences* 117.23 (2020), pp. 12564–12571.

[287] Shahnawaz Rafiq and Gregory D Scholes. "Slow intramolecular vibrational relaxation leads to long-lived excited-state wavepackets". In: *The Journal of Physical Chemistry A* 120.34 (2016), pp. 6792–6799.

[288] E Vogel, A Gbureck, and W Kiefer. "Vibrational spectroscopic studies on the dyes cresyl violet and coumarin 152". In: *Journal of Molecular Structure* 550 (2000), pp. 177–190.

[289] Akihito Ishizaki and Graham R Fleming. "On the adequacy of the Redfield equation and related approaches to the study of quantum dynamics in electronic energy transfer". In: *The Journal of Chemical Physics* 130.23 (2009), p. 234110.

[290] Yuan-Chung Cheng and Graham R Fleming. "Dynamics of light harvesting in photosynthesis". In: *Annual Review of Physical Chemistry* 60 (2009), pp. 241–262.

[291] Akihito Ishizaki and Graham R Fleming. "Quantum coherence in photosynthetic light harvesting". In: *Annual Review of Condensed Matter Physics* 3.1 (2012), pp. 333–361.

[292] Dieter Rehm and Albert Weller. "Kinetics of fluorescence quenching by electron and H-atom transfer". In: *Israel Journal of Chemistry* 8.2 (1970), pp. 259–271.

[293] Albert Weller. "Photoinduced electron transfer in solution: exciplex and radical ion pair formation free enthalpies and their solvent dependence". In: *Zeitschrift für Physikalische Chemie* 133.1 (1982), pp. 93–98.

[294] JR Rumble. *CRC Handbook of Chemistry and Physics, 100th edn., 2019–2020*. 2019.

[295] Michael S Lynch et al. "Probing the Photoinduced Metal- Nitrosyl Linkage Isomerism of Sodium Nitroprusside in Solution Using Transient Infrared Spectroscopy". In: *Journal of the American Chemical Society* 133.14 (2011), pp. 5255–5262.

[296] Elvira R Sayfutyarova and Sharon Hammes-Schiffer. "Substituent Effects on Photochemistry of Anthracene–Phenol–Pyridine Triads Revealed by Multireference Calculations". In: *Journal of the American Chemical Society* 142.1 (2019), pp. 487–494.

[297] Joris J Snellenburg et al. "Glotaran: A Java-based graphical user interface for the R package TIMP". In: *Journal Statistical Software* 49.3 (2012), pp. 1–22.

[298] Katharine M Mullen, Ivo HM Van Stokkum, et al. "TIMP: an R package for modeling multi-way spectroscopic measurements". In: *Journal of Statistical Software* 18.3 (2007), pp. 1–46.

Appendix A

Additional Experimental and Theoretical Details for Chapter 2

A.1 Cresyl Violet

Results and Discussion

In order to demonstrate the role of vibrational coherences, or rather lack thereof, in 2DEV spectra, control experiments were performed on cresyl violet (CV) dissolved in deuterated methanol. CV was chosen because it is well-documented in the literature that when both two-dimensional electronic spectroscopy (2DES) and visible pump-visible probe spectroscopy have been applied to CV, strong vibrational coherences with a frequency of $\sim$590 cm^{-1} were observed.[89, 90, 287] However, in a 2DEV experiment, performed under the same broadband excitation conditions as in previous 2DES and visible pump-visible probe experiments (Figure A.1), no vibrational coherences were observed. In the following text, these results are presented along with a short discussion.

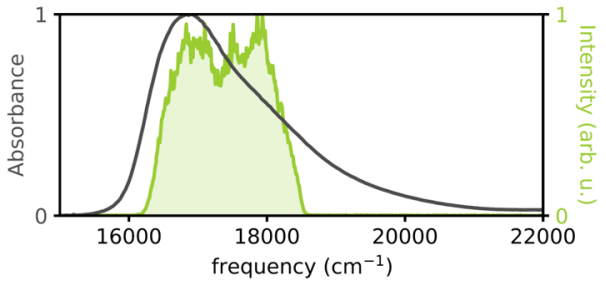

Figure A.1: Absorption spectrum of cresyl violet dissolved in deuterated methanol at 298 K (grey) together with laser excitation spectrum (green).

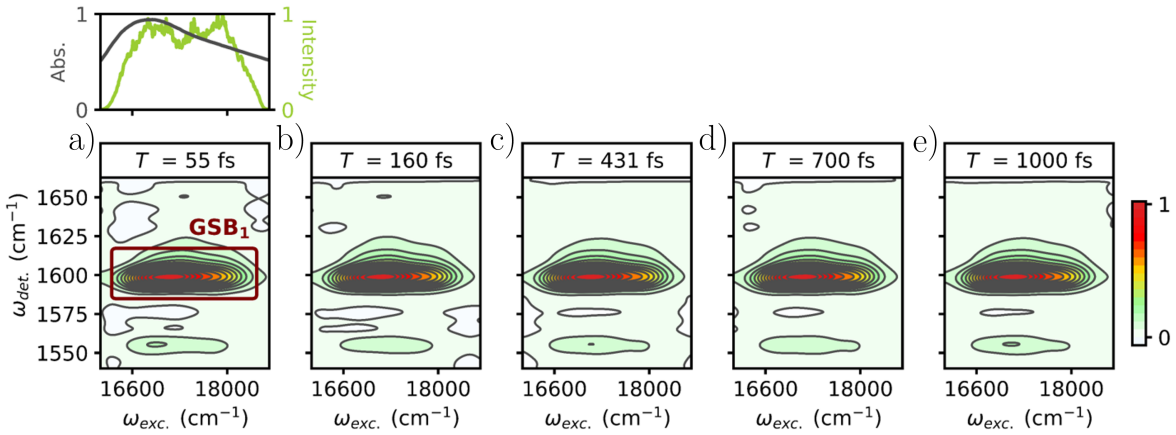

Figure A.2: a)-e) 2DEV spectra of cresyl violet at $T = 55$ fs, 160 fs, 431 fs, 700 fs, and 1000 fs, respectively. All spectra have been normalized to $T = 0$ fs. Contour levels are drawn in 6.6% intervals. The absorption spectrum and laser excitation spectrum are shown above a) and the main feature of interest, GSB_1, has been labeled in a).

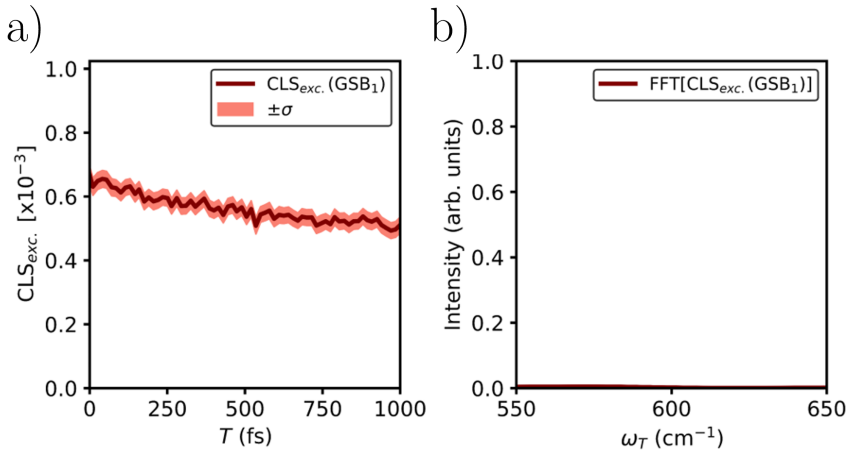

Figure A.3: a) $CLS_{exc.}$ dynamics of GSB_1 (dark red line) along with the standard error from the linear fits used to calculate the $CLS_{exc.}$ (light red shaded region). b) Power spectrum of the $CLS_{exc.}$ dynamics of GSB_1 centered around the region of interest, $\sim$590 cm^{-1}. In both a) and b), there is no evidence for wavepacket dynamics.

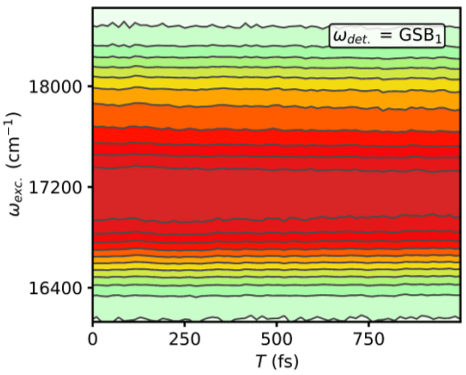

Figure A.4: To highlight the lack of oscillatory intensity dynamics in the 2DEV spectra of cresyl violet, slices were taken through GSB_1 and plotted as a function of waiting time, T. The colormap used here is identical to that of Figure A.2.

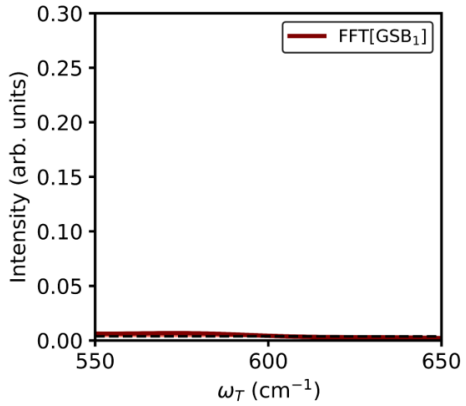

Figure A.5: Average power spectrum of GSB_1 (red) centered around the region of interest, $\sim$590 cm^{-1}, versus the average noise floor (black, dashed) calculated by taking the average power spectrum of the experimental noise. No wavepacket dynamics are evident.

Representative 2DEV spectra of CV are shown in Figure A.2. Throughout the remainder of the discussion, we will apply the same analysis as in Chapter 2 to the strong ground state bleach (GSB) feature labeled as GSB_1 in Figure A.2. The results of the center line slope (CLS) analysis for GSB_1 along the excitation axis are shown in Figure A.3a. It is immediately apparent that no oscillatory dynamics are present. To make this even more obvious, the power spectrum of the CLS is shown in Figure A.3b—there is absolutely no evidence for wavepacket dynamics in the CLS. To complete the analysis, we show slices through GSB_1 taken along the excitation axis and plotted as a function of waiting time, T, in Figure A.4 and we show the power spectrum of GSB_1 plotted along with the noise floor in Figure A.5. Once again, no oscillatory dynamics were observed, which demonstrates that the 2DEV spectra of CV do not exhibit the vibrational coherences that one would expect to see based on previous 2DES or visible pump-visible probe experiments. The reason that these vibrational coherences are not observable in this 2DEV experiment is because the probed higher frequency vibrational modes are not anharmonically coupled to the lower frequency modes[288] that are responsible for the appearance of the vibrational coherences in previous work. The result is that the probed modes are completely ignorant of the wavepacket dynamics. Therefore, these dynamics are absent from the CLSs and peak amplitudes. This conclusion has important implications for 2DEV spectroscopy—in the case where the probed vibrational modes are not anharmonically coupled to those that would be responsible for the appearance of vibrational coherences in a 2DES experiment, any observed oscillations in the CLS or peak amplitude in a 2DEV experiment will not be of purely vibrational origin, but rather must be electronic or vibronic in origin. In terms of the current study, the vibrational modes of chlorophyll pigments in the probed region (1525-1715 cm^{-1}) are not anharmonically coupled to lower frequency modes (i.e. the frequency region of the observed beats in the current study).[88] Therefore, the observed beats can not be vibrational in origin.

Methods

The same 2DEV experimental setup described in the Chapter 2 and elsewhere[2] was used for this experiment, however, the excitation and probe frequencies were adjusted accordingly. The visible excitation spectrum was centered at 17390 cm^{-1} and spanned 16129$\sim$18518 cm^{-1}, while the infrared (IR) probe spectrum was centered at 1587 cm^{-1}. The excitation energy was set at 250 nJ and the pump pulse duration was $\sim$8 fs.

A.2 Theoretical Modelling

The model presented in the main text features two electronically coupled monomers, each with one electronic degree of freedom (DOF) and one Franck-Condon active vibrational mode. The model parameters (labeled in Figure A.6) were chosen to be similar to those expected for LHCII and are as follows: $\epsilon_\beta - \epsilon_\alpha = 100$ cm^{-1}, $J = 100$ cm^{-1}, $\omega_{g,\alpha} = 1650$

cm^{-1}, $\omega_{e,\alpha} = 1560\ \text{cm}^{-1}$, $\omega_{g,\beta} = 1660\ \text{cm}^{-1}$, $\omega_{e,\beta} = 1550\ \text{cm}^{-1}$, and the Huang-Rhys factor, S, was set to 0.005 for both vibrational modes.[50, 52, 53] As in previous work[69, 83], the site basis is spanned by the nine states: $|\alpha_g^0\beta_g^0\rangle$, $|\alpha_g^1\beta_g^0\rangle$, $|\alpha_g^0\beta_g^1\rangle$, $|\alpha_e^0\beta_g^0\rangle$, $|\alpha_e^0\beta_g^1\rangle$, $|\alpha_e^1\beta_g^0\rangle$, $|\alpha_g^0\beta_e^0\rangle$, $|\alpha_g^0\beta_e^1\rangle$, and $|\alpha_1^0\beta_e^0\rangle$, where the subscript on α or β indicates whether or not the electronic DOF is excited (e for excited state or g for ground state) and the superscript indicates whether or not the vibrational DOF on monomer α or β is excited (1 for excited state or 0 for ground state). In the site basis, the electronic transition dipole matrix elements were set to $\frac{\mu_\alpha}{\mu_\beta} = -5$ in order to recover a linear absorption spectrum with reasonable qualitative agreement to LHCII in terms of the intensities of the two main Q_y bands, and the vibrational transition dipole matrix elements were all set to unity.

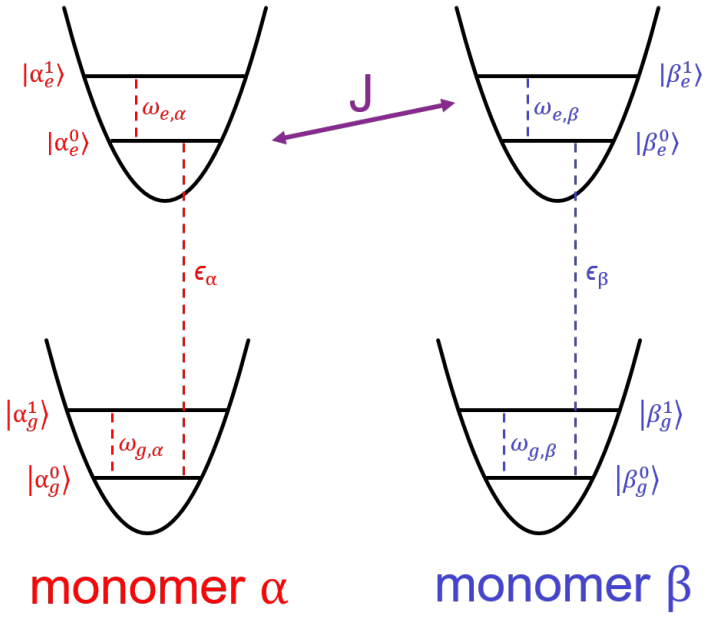

Figure A.6: In the model, the strength of electronic coupling between the electronically excited states of monomers α and β is given by J. Labeled are the various model parameters (energies of vibrational and electronic degrees of freedom for each monomer) and the states for each monomer.

The simulated 2DEV spectra (composed of the rephasing and nonrephasing excited state absorption and ground states bleach pathways[83]) were calculated using the Full Redfield quantum master equation.[289] The spectral density was taken to be of Drude-Lorentz form[43], where the reorganization energy, λ, was set to 35 cm^{-1} and the cutoff frequency, γ, was set to $\sim$106 cm^{-1} ($\gamma^{-1} = 50$ fs). These bath parameters were chosen as they are reasonable for pigment-protein complexes.[290, 291]

For all calculations, the temperature was set at 150 K, rather than 77 K, in order to ease computational demand. As the vibrational modes in this model were assumed to be localized spectators of the dynamics and were not populated until the third light-matter interaction, an electronic bath that induced energy fluctuations and population relaxation was used during the initial coherence time, $t_{\text{exc.}}$, and the waiting time, T, while a vibrational bath that only induced vibrational relaxation was used during the last coherence time, $t_{\text{det.}}$ (note: this would not be the proper treatment in the case where there was substantial electronic-vibrational mixing[67], however, the separation of the bath into discrete electronic and vibrational portions is valid for the parameter regime inhabited by in this model, which is essentially that of "D1" in Ref. [66]). The absorptive 2DEV spectra presented in the text were recovered by Fourier transforming along $t_{\text{exc.}}$ and $t_{\text{det.}}$ and combining the total rephasing and nonrephasing pathways. The spectra were calculated as a function of T from 0-708 fs in 12 fs steps.

In order to highlight the sensitivity of 2DEV spectra to electronic coupling, the 2DEV spectrum for $J = 0$ cm^{-1} (all other model parameters identical) is shown in Figure A.7. Through a comparison of Figure 2.3b and 2.3c to Figure A.7, it is evident that the two excited state absorption quartets arise as a result of electronic coupling.

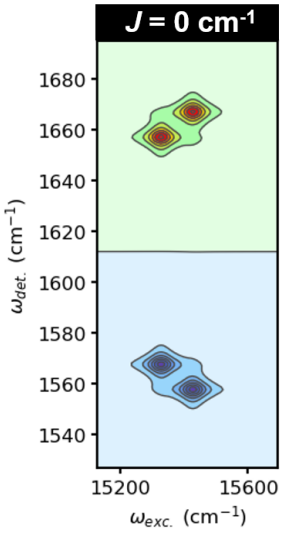

Figure A.7: When $J = 0$ cm^{-1}, the excited state absorption (ESA) quartet structure vanishes, leaving only one ESA feature on each non-interacting monomer. Positive features indicate ground state bleaches and negative features indicate ESAs.

A.3 Data Processing Details

As mentioned in Chapter 2.4, the experimental data was subjected to a Savitzky-Golay filter[95] for presentation in the main text, in order to emphasize the lower frequency oscillatory signals under discussion. In Figure A.8, we compare the both the filtered and unfiltered versions of the cross-power spectrum and beat frequency map presented in Figure 2.5. Upon comparison, it is evident that filtering leaves the oscillatory signals under discussion unaltered, rather, as intended, filtering only deemphasizes higher frequency signals.

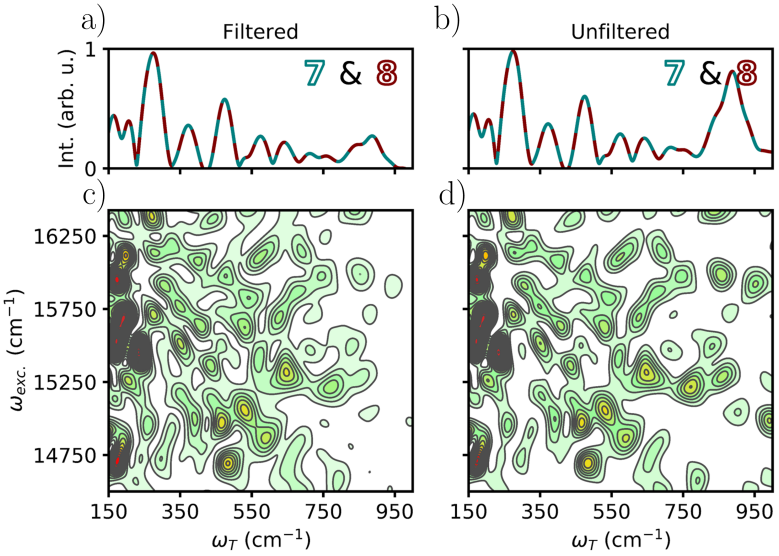

Figure A.8: a)-b) Filtered (as described in the Methods section) and unfiltered cross-power spectrum of the center line slope dynamics of excited state absorptions seven and eight. c)-d) Filtered (again, as described in Chapter 2.4) and unfiltered beat frequency map. Only peaks that survive the noise floor were plotted in c) and d) such that contour levels are drawn in 4% intervals starting from the top of the noise floor. The colormap indicates peak intensity, where intensity is shown to increase from green to red.

A more explicit comparison of the beat frequencies versus the noise floor is shown in Figure A.9. The noise floor was calculated by taking the average power spectrum of the experimental noise.

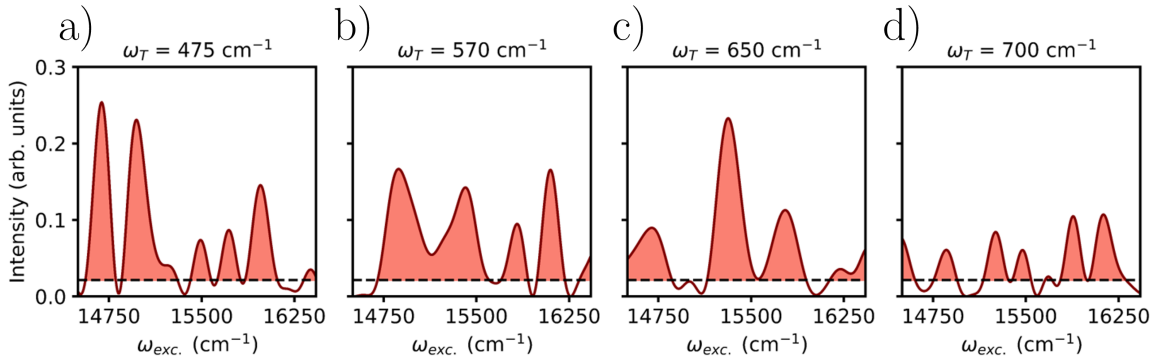

Figure A.9: a)-d) Selected beat frequencies of 475 cm^{-1}, 570 cm^{-1}, 650 cm^{-1}, and 700 cm^{-1} plotted as a function of excitation frequency shown against the average noise floor (black, dashed). Features that survive the noise floor are shaded in red.

A.4 Absorption Spectrum

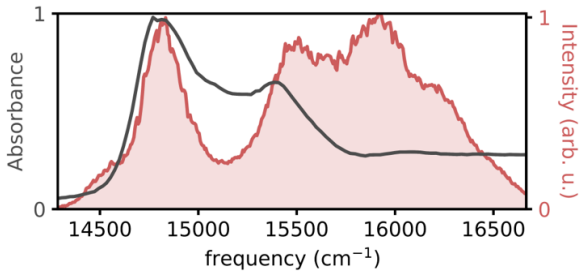

Figure A.10: Linear absorption spectrum of LHCII at 77 K (grey) together with laser excitation spectrum (red).

Appendix B

Fitting Results and Details for Chapter 3

$\omega_{\text{det.}}$ (cm^{-1})[a]	PA Component	A_0	A_1	τ_1 (fs)[b]	ω_1 (cm^{-1})	ϕ_1 (π)	A_2	τ_2 (fs)[c]	ω_2 (cm^{-1})	A_3	τ_3 (fs)
1690	$\perp$	0.42	-	-	-	-	-	-	-	-	-
	$\parallel$	0.17	−0.01	140±30	111±7	0.7±0.2	−0.001	-	240±20	0.01	330±120
1680	$\perp$	0.01	-	-	-	-	-	-	-	−0.01	600±200
	$\parallel$	0.19	−0.01	140±30	90±10	0.8±0.3	-	-	-	-	-
1670	$\perp$	−0.93	-	-	-	-	-	-	-	−0.01	600±200
	$\parallel$	−0.56	−0.01	190±30	106±5	1.1±0.2	−0.001	-	240±10	-	-

Table B.1: Fit parameters for the peak amplitude dynamics provided in Figures 3.2c, 3.2f, and 3.3c.

The fitting function employed is given by

$$f(t) = A_0 + A_1 \cos(2\pi\omega_1 t)\exp(-t/\tau_1) + A_2 \cos(2\pi\omega_2 t)\exp(-t/\tau_2) + A_3 \exp(-t/\tau_3)$$

convoluted with the instrument response function.

[a] Excitation frequency fixed at 17800 cm^{-1}.

[b] All errors indicate 1σ errors.

[c] Damping time unable to be fit precisely without smaller timesteps past 625 fs, but are likely >600 fs.

$\omega_{\text{det.}}$ (cm^{-1})	PA Component	A_0	A_1	τ_1 (fs)[a]	ω_1 (cm^{-1})	ϕ_1 (π)	A_2	τ_2 (fs)[b]	ω_2 (cm^{-1})
1670	$\parallel$	17821.70	-1.12	250±50	92±6	1.33±0.19	-0.14	-	240±20

Table B.2: Fit parameters for the excitation frequency distribution dynamics provided in Figure 3.3g. The fitting function employed is given by

$$f(t) = A_0 + A_1 \cos(2\pi\omega_1 t) \exp(-t/\tau_1) + A_2 \cos(2\pi\omega_2 t) \exp(-t/\tau_2)$$

convoluted with the instrument response function.

[a] All errors indicate 1σ errors.

[b] Damping time unable to be fit precisely without smaller timesteps past 625 fs, but are likely >600 fs.

Appendix C

Global Analysis Results and Details Chapter 5

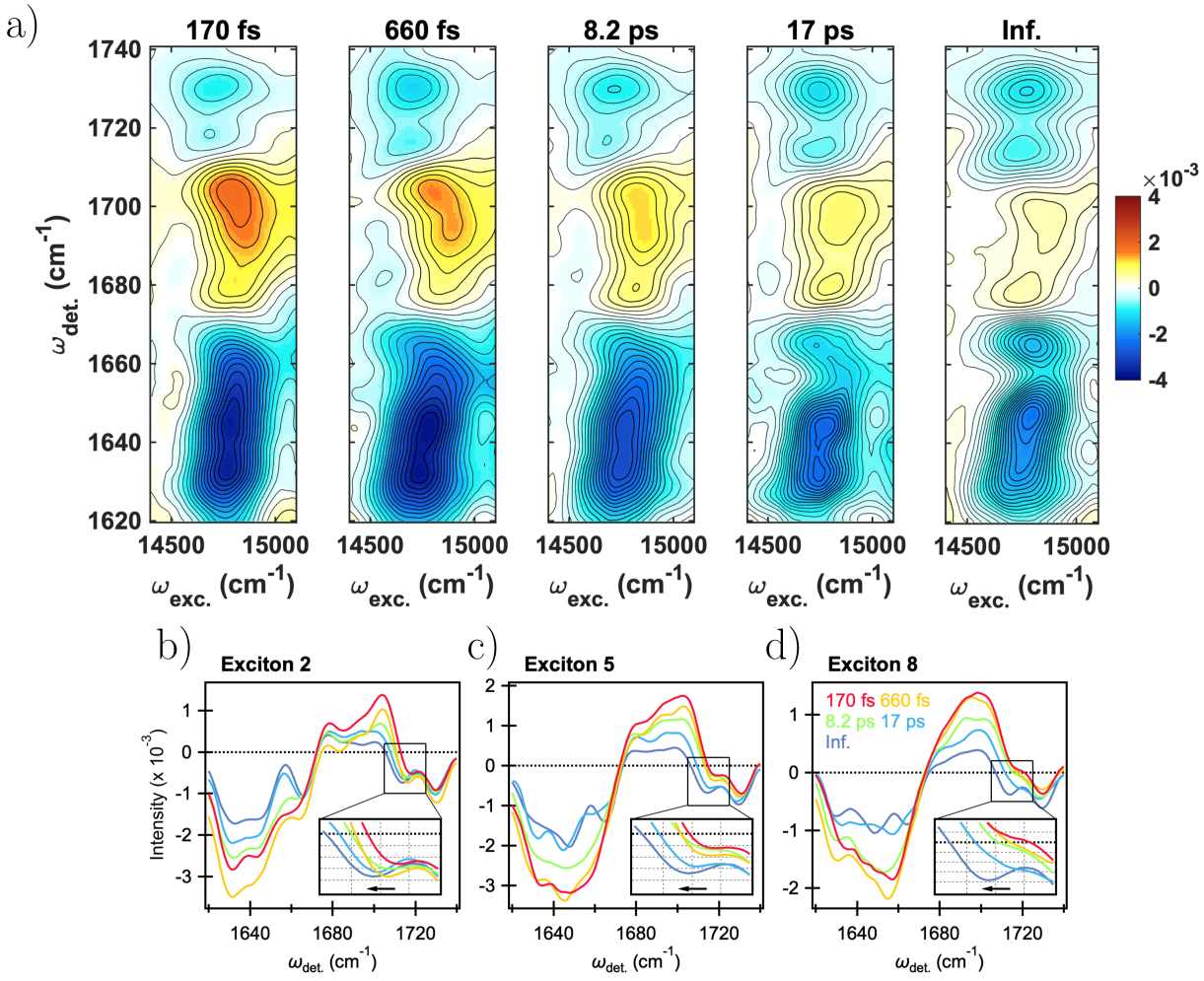

Figure C.1: a) Five components were required for a reasonable fit with time constants of 170 fs, 660 fs, 8.2 ps, 17 ps, and a non-decaying offset component (longer than detection time range of 100 ps). Each 2D-EADS evolves into the next one with the time constants listed above. Contour levels are drawn in 5% intervals. The time-dependent evolution of excitons 2, 5, and 8 are shown in b)-d), respectively. For the analysis, the detection ranges was selected to be $\omega_{\text{det.}}$ = 1620-1740 cm^{-1} because the dynamics in this range most fully reflect charge separation.

Appendix D

Additional Experimental and Theoretical Details for Chapter 6

D.1 Absorption Spectra

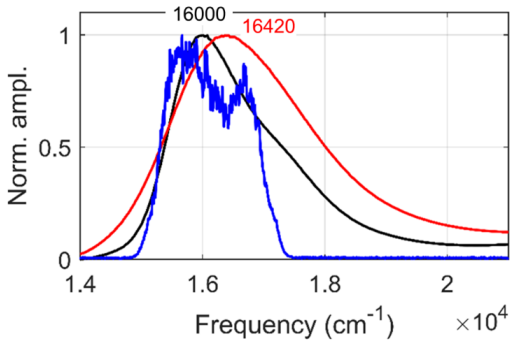

Figure D.1: Normalized electronic linear absorption spectra of InC in dDMSO (black) and D_2O (red). The blue curve represents the excitation spectrum used in transient IR and 2DEV experiments.

D.2 Fitting Results of Time Traces of Transient IR

The pump-probe transients for different vibrational bands (Figure 6.1b and 6.1c) of InC in dDMSO and D_2O are shown Figures D.2 and D.3-D.4, respectively. In each graph, the black circles represent experimental data points and solid blue line represents the exponential fit. The initial 200 fs of each transient were excluded from the fitting to avoid the coherent artifact.

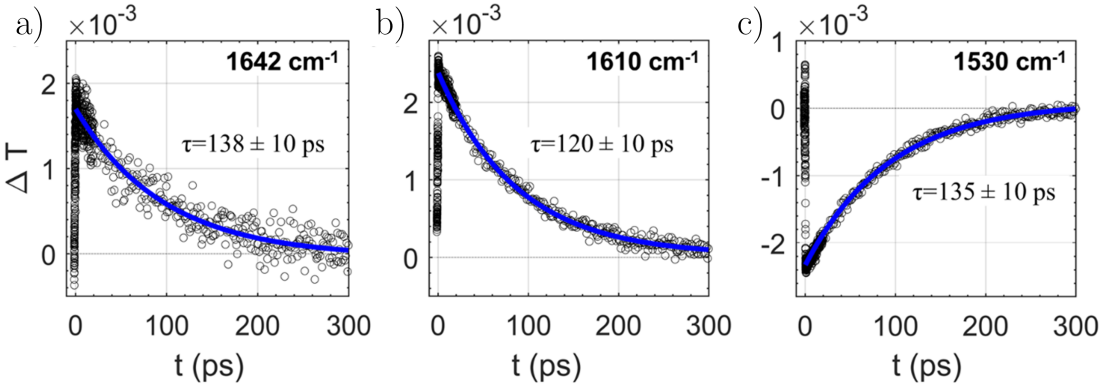

Figure D.2: Monoexponential fitting of the transients obtained in transient IR experiments of InC in dDMSO at detection frequencies of a) 1642 cm^{-1}, b) 1610 cm^{-1}, and c) 1530 cm^{-1}.

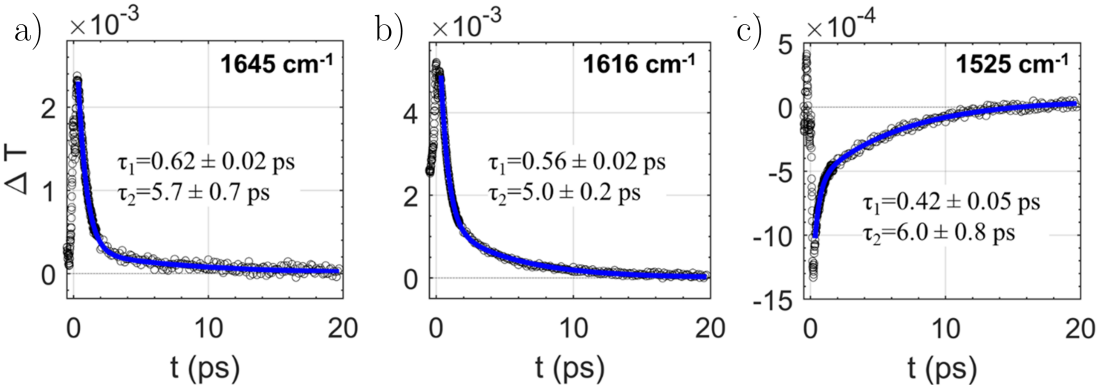

Figure D.3: Biexponential fitting of the transient obtained in transient IR experiments of InC in D_2O at detection frequency of a) 1645 cm^{-1}, b) 1616 cm^{-1}, and c) 1525 cm^{-1}.

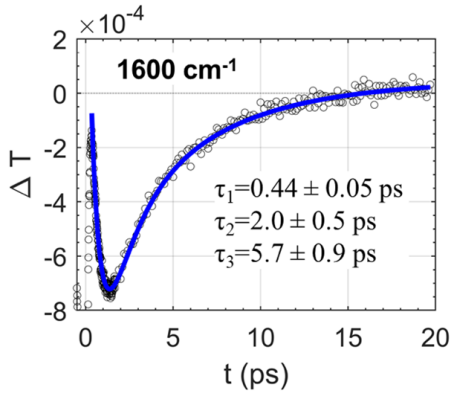

Figure D.4: Triexponential fitting (an exponential rise followed by a biexponential decay) of the transient obtained in transient IR experiments of InC in D_2O at detection frequency of 1600 cm^{-1}.

D.3 Theoretical Calculations

Regarding the vibrational frequency calculations, we utilize a scaling factor of 0.96 throughout.

Indigo	Total energy (Ha)	ΔE (eV)
keto-S_0 min	−875.7473	-
keto-S_1 FC	−875.6722	2.04
keto-S_1 min	−875.6816	−0.26
enol-S_1 min	−875.6706	0.30

Table D.1: TDDFT calculation of Indigo with 6-31+G* basis set at B3LYP level of theory.

Indigo	Total energy (Ha)	ΔE (eV)
keto-S_0 min	−2446.9650	-
keto-S_1 FC	−2446.8875	2.11
keto-S_1 min	−2446.8968	−0.25
enol-S_1 min	−2446.8859	0.30

Table D.2: TDDFT calculation of Indigo Carmine with 6-31+G* basis set at B3LYP level of theory.

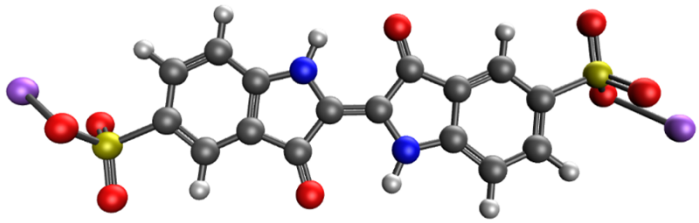

Figure D.5: The optimized geometry of keto-S_1 of InC calculated at the TDDFT/B3LYP/6-31+G* level of theory. The geometry is very similar to that of the keto-S_0 minimum shown in Figure 6.1d.

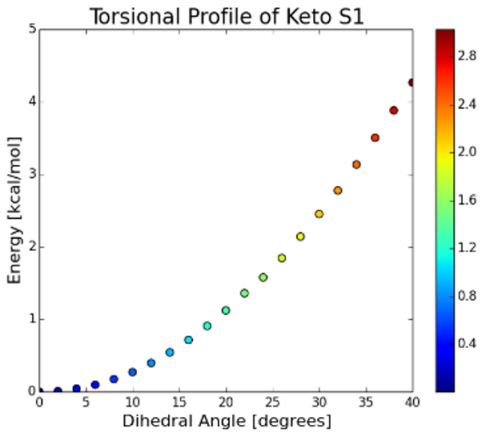

Figure D.6: The calculated energy relative to the planar configuration (dihedral angle = 0°) of the keto-S_1 minimum as a function of dihedral angle around the central C=C bond in Indigo. The corresponding dipole moments are shown via the color scale on the right. TDDFT/B3LYP/6-31+G* level of theory.

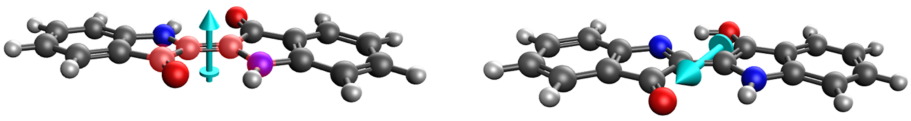

Figure D.7: Dipole moments, calculated at the TDDFT/B3LYP/6-31+G* level of theory, overlaid on (left) the keto-S_1 minimum geometry for Indigo, optimized with a 14° dihedral constraint involving the N−C−C−C atoms highlighted in red, and (right) enol-S_1 minimum. As given by excited-state geometry optimization calculations, the dipole moment vectors of the twisted keto-S_1 state and enol-S_1 minimum are (0.87, 0.02, 0.00) and (0.97, 1.54, −0.69), with magnitudes of 0.94 and 1.94 D, respectively. We argue in the main text that this significant change in direction and increase in magnitude is consistent with the change in sign of the CLS.

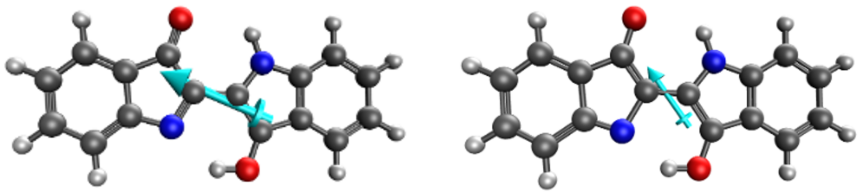

Figure D.8: Dipole moments overlaid on (left) the enol-S_1 minimum geometry for Indigo and (right) the S_1/S_0 MECP geometry. These calculations utilized the SF-TDDFT/BHHLYP/6-31+G* level of theory. As given by excited-state geometry optimization calculations, the dipole moment vectors of the enol-S_1 minimum and MECP are (−0.22, −1.80, 4.57) and (−0.11, −1.11, 0.83), with magnitudes of 4.92 and 1.39 D, respectively.

Appendix E

Additional Experimental and Theoretical Details for Chapter 7

E.1 Electrochemical Characterization

The free energy gap ΔG between the $BIPPF_{15}$ S_1 (0,0) band and the relaxed PET state was estimated by the Rehm-Weller equation[292, 293]

$$\Delta G = -E_{00} + E_{1/2}(BIPPF_{15}{}^{+}/BIPPF_{15}) - E_{1/2}(BIPPF_{15}/BIPPF_{15}{}^{-}) - \frac{e^2}{4\pi\varepsilon_0\varepsilon_s l}. \quad \text{(E.1)}$$

Here E_{00} is an energy difference between S_0 and locally excited states, $E_{1/2}(BIPPF_{15}{}^{+}/BIPPF_{15})$ and $E_{1/2}(BIPPF_{15}/BIPPF_{15}{}^{-})$ are midpoint potentials for the $BIPPF_{15}{}^{+}/BIPPF_{15}$ and $BIPPF_{15}/BIPPF_{15}{}^{-}$ redox couples, e is the elementary charge, ε_0 is the permittivity of vacuum, ε_s is a dielectric constant of the solvent, and l is a distance between donor and acceptor molecules. According to the equation, the free energy gap was estimated to be $\Delta G = -100$ meV. The parameters used for the estimation of ΔG are summarized in Table E.1.

E_{00} (eV)	E_{ox} (eV)	E_{red} (eV)	ε_s[294]	l (Å)
1.92	1.05	−0.83	36.6	6.4

Table E.1: Parameters used for the estimation of ΔG.

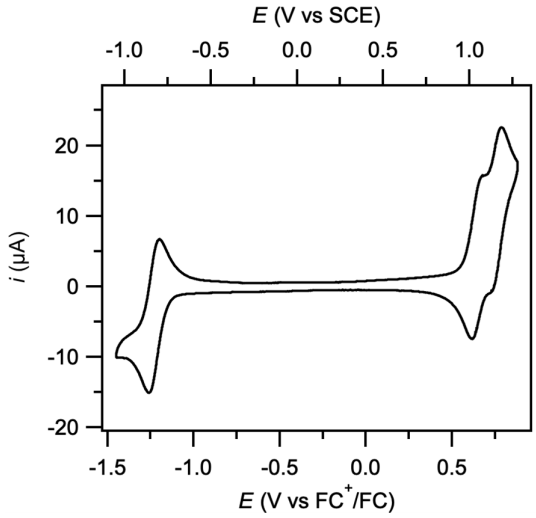

Figure E.1: Cyclic voltammetry of $BIPPF_{15}$. The midpoint potentials ($E_{1/2}$) for the $BIPPF_{15}^{+}$/$BIPPF_{15}$ and $BIPPF_{15}$/$BIPPF_{15}^{-}$ redox couples were estimated as the average of the anodic and cathodic peak potentials, yielding values of +1.05 and −0.83 V versus SCE, respectively.

E.2 Absorption Spectra

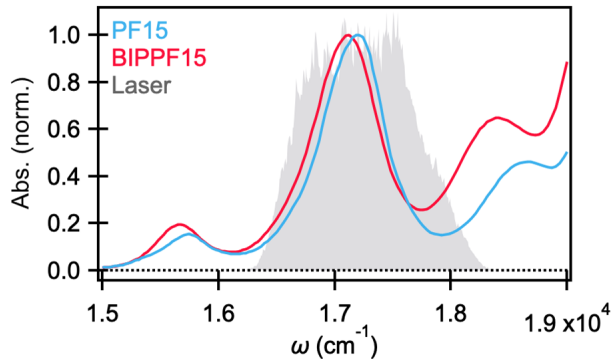

Figure E.2: Electronic absorption spectra of PF_{15} (blue) and $BIPPF_{15}$ (red). The spectrum of excitation laser pulse is also shown (gray).

E.3 Fitting Results of Time Traces of Transient IR

		A_0	A_1	τ_1 (ps)	A_2	τ_2 (ps)	A_3	τ_3 (ps)
1548 cm^{-1}	PF_{15}	0.01	−0.91	0.33±0.01	−0.08	>500	-	-
	$BIPPF_{15}$	0.15	0.26	19*	−0.23	65*	−0.35	290*
1597 cm^{-1}	PF_{15}	0.07	−0.61	0.25±0.02	0.31	0.39±0.3	-	-
	$BIPPF_{15}$	−0.1	0.12	13±1	−0.22	82±0	−0.64	270±0

Table E.2: Fit parameters for time traces of transient IR of PF_{15} and $BIPPF_{15}$ at 1548 cm^{-1} and 1597 cm^{-1}.

The fitting function employed is given by

$$f(t) = A_0 + A_1 \exp(-t/\tau_1) + A_2 \exp(-t/\tau_2)$$

or

$$f(t) = A_0 + A_1 \exp(-t/\tau_1) + A_2 \exp(-t/\tau_2) + A_3 \exp(-t/\tau_3)$$

convoluted with the instrument response function. All fixed values are indicated by *.

E.4 CLS Analysis of 2DEV Spectra

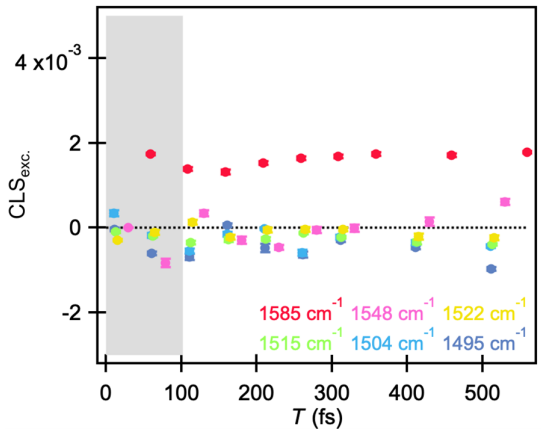

Figure E.3: CLS dynamics (with respect to the excitation axis) of PF_{15} in deuterated acetonitrile. The time range where visible and IR pulses overlap, <100 fs, is indicated by the shaded area. The error bars indicate the standard error of the CLS, obtained by a linear fit of the conditional average.[47]

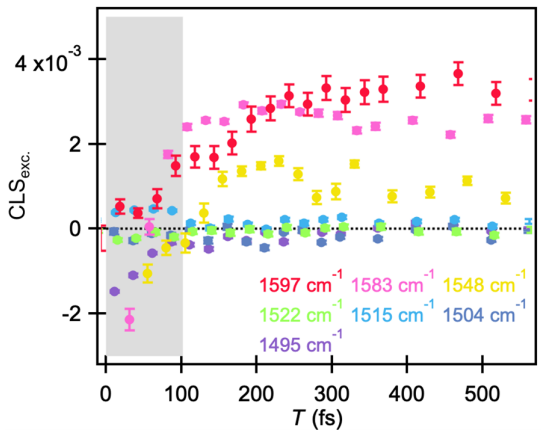

Figure E.4: CLS dynamics of $BIPPF_{15}$ in deuterated acetonitrile. The time range where visible and IR pulses overlap, <100 fs, is indicated by the shaded area. The error bars indicate the standard error of the CLS, obtained by a linear fit of the conditional average.[47]

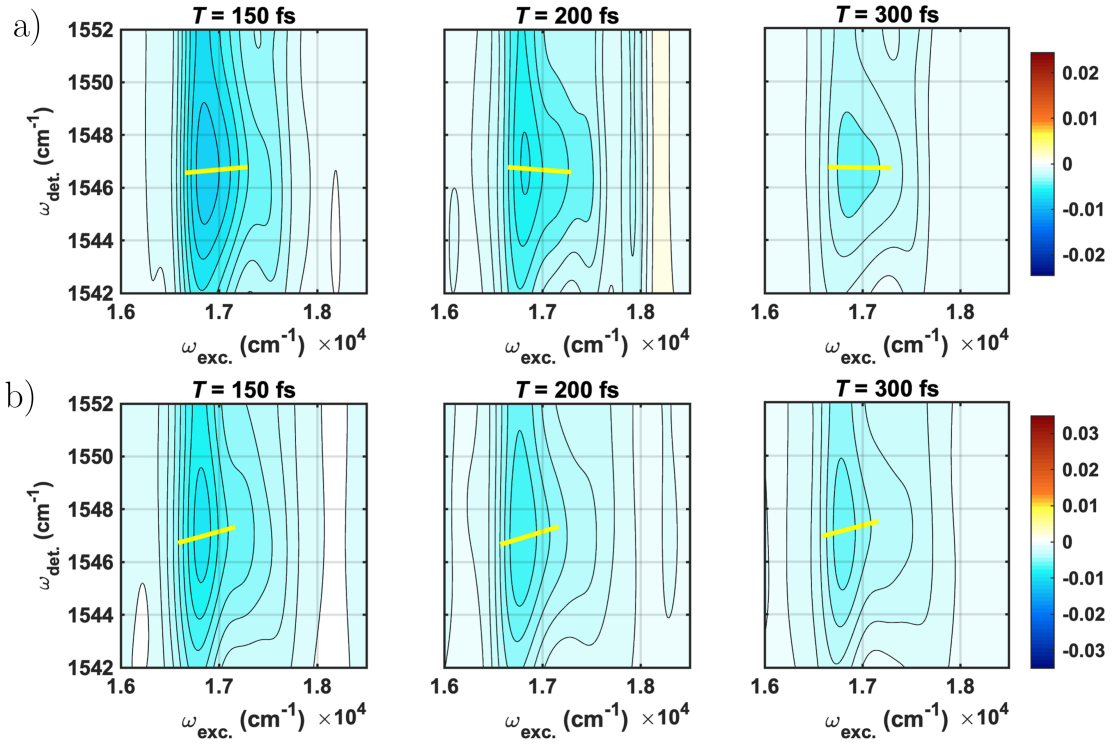

Figure E.5: Fitting result of $CLS_{exc.}$ for a) PF_{15} and b) $BIPPF_{15}$ in deuterated acetonitrile in the 1542-1552 cm^{-1} detection region. $CLS_{exc.}$ refers to the slope of the center line calculated with respect to the excitation axis.

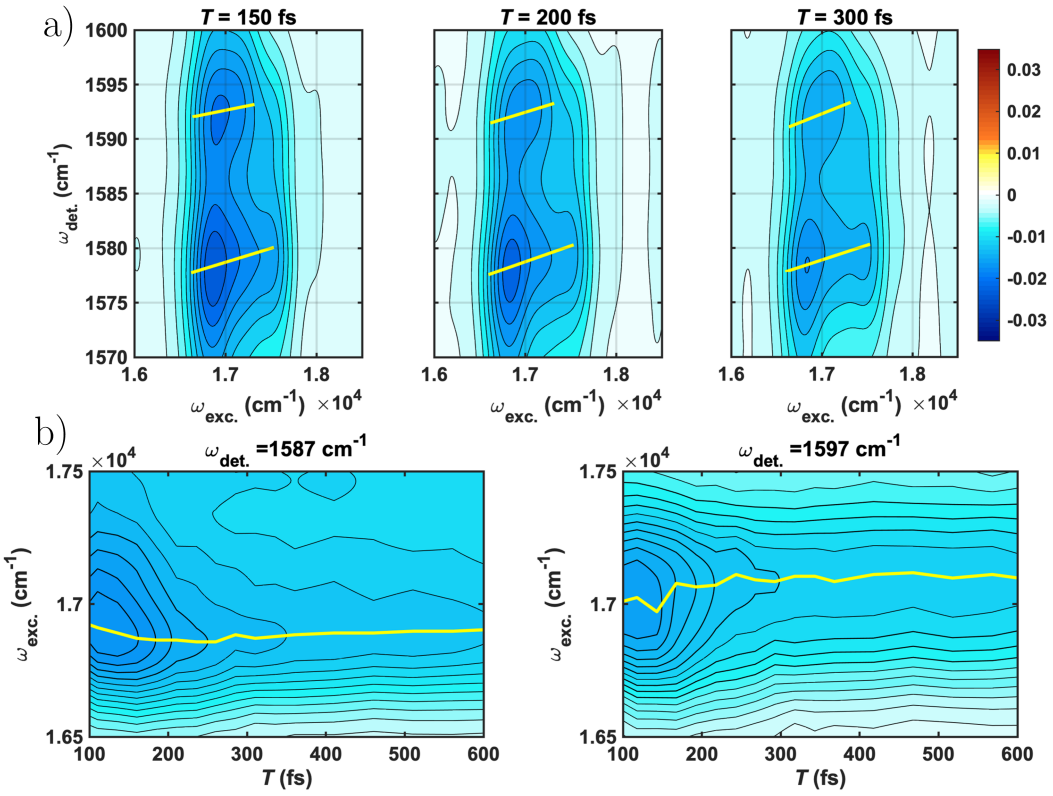

Figure E.6: a) Fitting result of $CLS_{exc.}$ for $BIPPF_{15}$ in deuterated acetonitrile in the 1570-1600 cm^{-1} detection region. b) 2DEV spectra as a function of waiting time along the excitation axis at a fixed detection frequency of 1587 cm^{-1} and 1597 cm^{-1}. The yellow line shows peak frequencies at each waiting time. The peak at lower detection frequency shows a red shift along the excitation axis while the peak at higher detection frequency shows a blue shift along the excitation axis, indicating the positive increase in the CLS dynamics.

E.5 Detailed Analysis of Transient IR Spectra of PF_{15}

Transient IR spectra of PF_{15} at short times showed positive and negative bands at 1589 cm^{-1} and 1581 cm^{-1}, respectively (Figure E.7) which decayed within 10 ps. These signals can be assigned to a vibration associated with the ester group (Figure 7.1) because no positive band was observed in the transient IR spectra of $BIPPF_{15}$ at 1580-1590 cm^{-1}. The rapid decay implies that these bands can be assigned to the overtone (2←1 transition) and the bleach (1←0) of the same vibrational mode on the electronic ground state. Similar rapid decay of an overtone on the electronic ground state is also observed by transient IR spectroscopy for NO and CN stretch frequencies in a sodium nitroprusside system.[295] As these signals completely disappear within a few tens of picoseconds, the transient IR spectra were compared at 50 ps (Figure 7.3c).

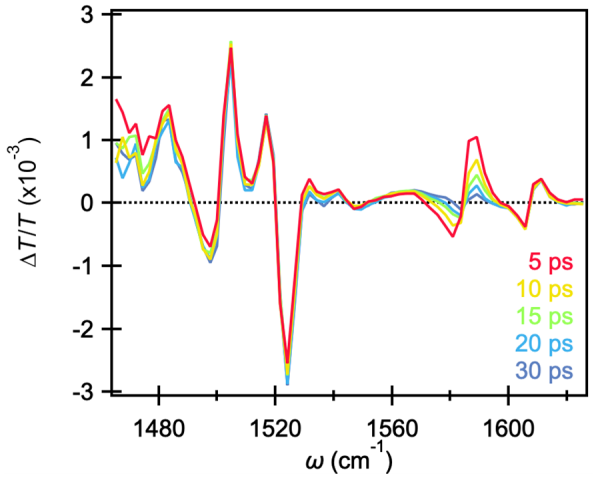

Figure E.7: Transient IR spectra of PF_{15} from 5-30 ps.

E.6 Possible States that Can Contribute to PCET Dynamics

There are six states relevant to photoinduced PCET (Figure E.8).[213, 215, 296] The excited electronic states include the locally excited state (LE) without proton transfer, the charge separated state (CSS) without proton transfer, the proton transferred-locally excited state (PT-LE), and the proton and electron transferred (PET) state. In addition, there are two ground states with or without proton transfer which are labeled as proton transferred-ground state (PT-GS) and ground state (GS), respectively. The NMR spectrum of $BIPPF_{15}$ indicates that the PT-GS is inaccessible from the GS.[223, 232] According to the energetics estimated by the midpoint potentials and the calculations, the CSS is not accessible with the current excitation wavelength. Time-resolved IR spectra showed both electron transfer (ET) and proton transfer (PT) bands at 1597 cm^{-1} and 1548 cm^{-1}, respectively, indicating that the PET state is lower in energy than the PT-LE state. The calculation with the OT-LRC-ωPBEh functional also predicts that, at the 93.1° geometry, the PET state is the lowest singlet excited state.

There are two possible relaxation pathways from PET state to GS, i.e. charge recombination (CR) to directly yield the GS or through the PT-GS requiring ground state PT (Figure E.8a and E.8b). As discussed in a later section, global and target analysis of the transient IR data suggests that the relaxation involves three major transient species, consistent with the latter pathway (Figure E.8b). It should be noted that the ET signal at 1597 cm^{-1} reflects the dynamics of the PET state although there is a possibility that the PT signal at 1548 cm^{-1} can reflect the PT-GS.

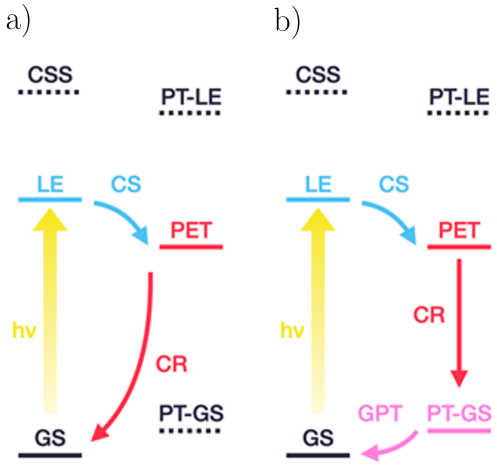

Figure E.8: Possible relaxation pathways of photoinduced PCET. a) The PET state directly returns to the GS through CR. b) CR of the PET state yields the PT-GS which is followed by ground state PT.

E.7 Detailed Analysis of Transient IR Spectra of $BIPPF_{15}$

Global and target analysis was performed to obtain reliable time constants by using the Glotaran software based on the R-package TIMP.[297, 298] Since the transient IR signal of $BIPPF_{15}$ did not exhibit fast dynamics on the timescale of a few hundreds of femtoseconds (Figure 7.3d and 7.3e and Table E.2), only the signal after 500 fs was analyzed. Singular value decomposition indicates that the system can be well described by three components (Figure E.9). The time constants obtained by global fitting with three components (plus constant offset) were 19 ps, 65 ps, and 290 ps. The first and third components (19 ps and 290 ps) can be assigned to CR and CS, respectively (inverted kinetics behavior), and are similar to the values obtained by the analysis at specific probe wavenumbers (Table E.2). The second time constant (65 ps) can be assigned to the ground state PT process.

Transient IR spectra at short times (Figure 7.3) clearly show that the PET state is formed immediately after the photoexcitation or is populated by an ultrafast pathway which proceeds within the instrument response time of ∼90 fs. The time traces of PT and ET bands provide more inside into the PET formation and show a small increase (rise) in the signal intensity with 19 ps (Figure 7.3d and 7.3e), indicating that the PET state is actually populated mainly via the slower relaxed PET formation pathway as the inverted kinetics dominate over the unrelaxed PET formation pathway. In either ultrafast PET formation case, the kinetics after 500 fs can be approximately described by the model shown in Figure E.10a in which LE and PET are initially populated by photoexcitation with the ratio 96:4. The branching ratio from LE to PET and Triplet/GS can be calculated from the fluorescence decay data of $BIPPF_{15}$ and PF_{15} to be ∼97:3 (∼290 ps versus ∼10 ns).

Kinetic simulations based on this model with k_{CS}^{-1} = 300 ps and k_{CR}^{-1} = 19 ps and the above indicated branching fit well experimental data and show that the PET state is populated up to ∼5% (maximum transient population) regardless of the initial population branching during the excitation pulse, as long as this initial population of PET does not exceed 5% (LE accordingly not less than 95%). Target analysis based on the model shown in Figure E.10a with the initial population of PET being 3-5% provided reasonable species associated spectra (SAS), and the results with 4% are shown in Figure E.10b (fitting results are shown in Figure E.11). As the amplitude of the second and third components are small, some artifact appears in the first spectrum at 1590 cm^{-1}, however, these spectra qualitatively reproduce the signature of each species even though all of them are mixed and do not represent completely pure species. The first spectrum shows intense spectral features similar to the transient IR spectrum of PF_{15} at 1460-1540 cm^{-1}, suggesting that this component can be reasonably assigned mostly to the LE state. The second spectrum shows clear PT and ET bands at 1548 cm^{-1} and 1597 cm^{-1}, respectively. The third spectrum shows a small negative band at 1548 cm^{-1} which can be assigned to the GS-PT signal. The fourth spectrum shows a positive signal over the entire detection range and can be assigned to the triplet state.[221] It can be seen that the population of the PET state basically stays

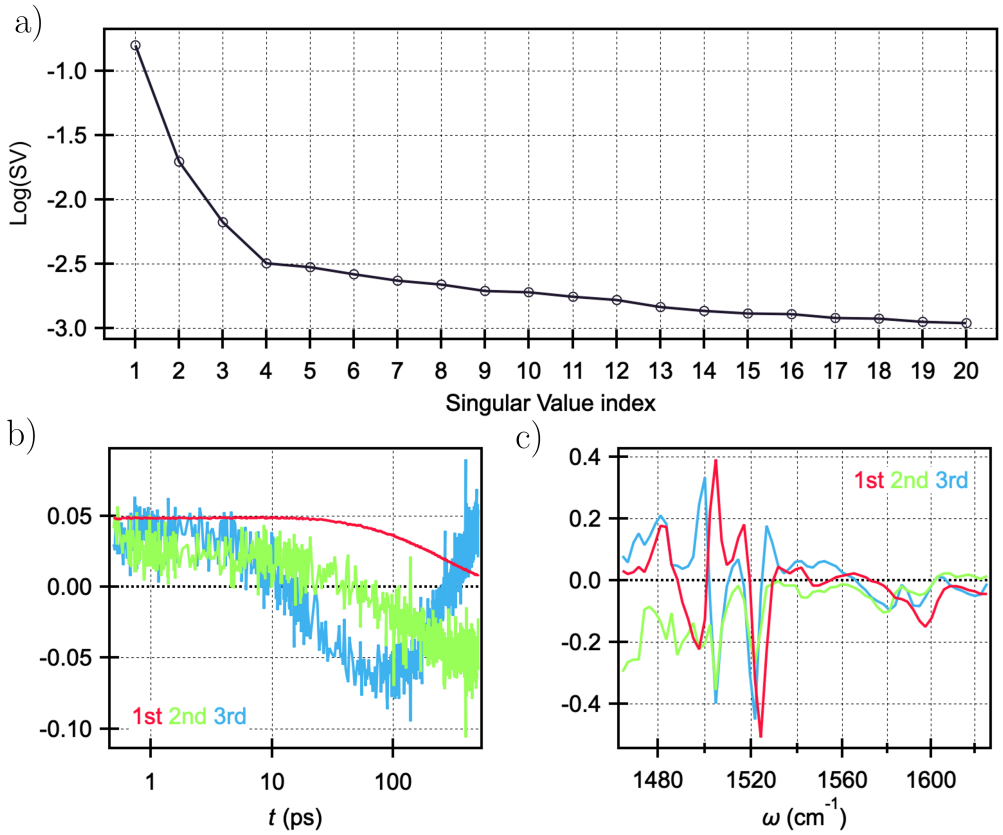

Figure E.9: Singular value decomposition of the transient IR signal of $BIPPF_{15}$. a) The first 20 singular values. b) The first three left singular vectors. c) The first three right singular vectors.

~4% at short times and slightly increases with time scale of k_{CR}^{-1} = 19 ps (Figure E.10c and E.10d). The population of PT-GS increases with tens of picoseconds, indicating that the contribution of the PT-GS to the PT signal at 1548 cm^{-1} is negligible in the observation time window of the CLS (less than 1 ps).

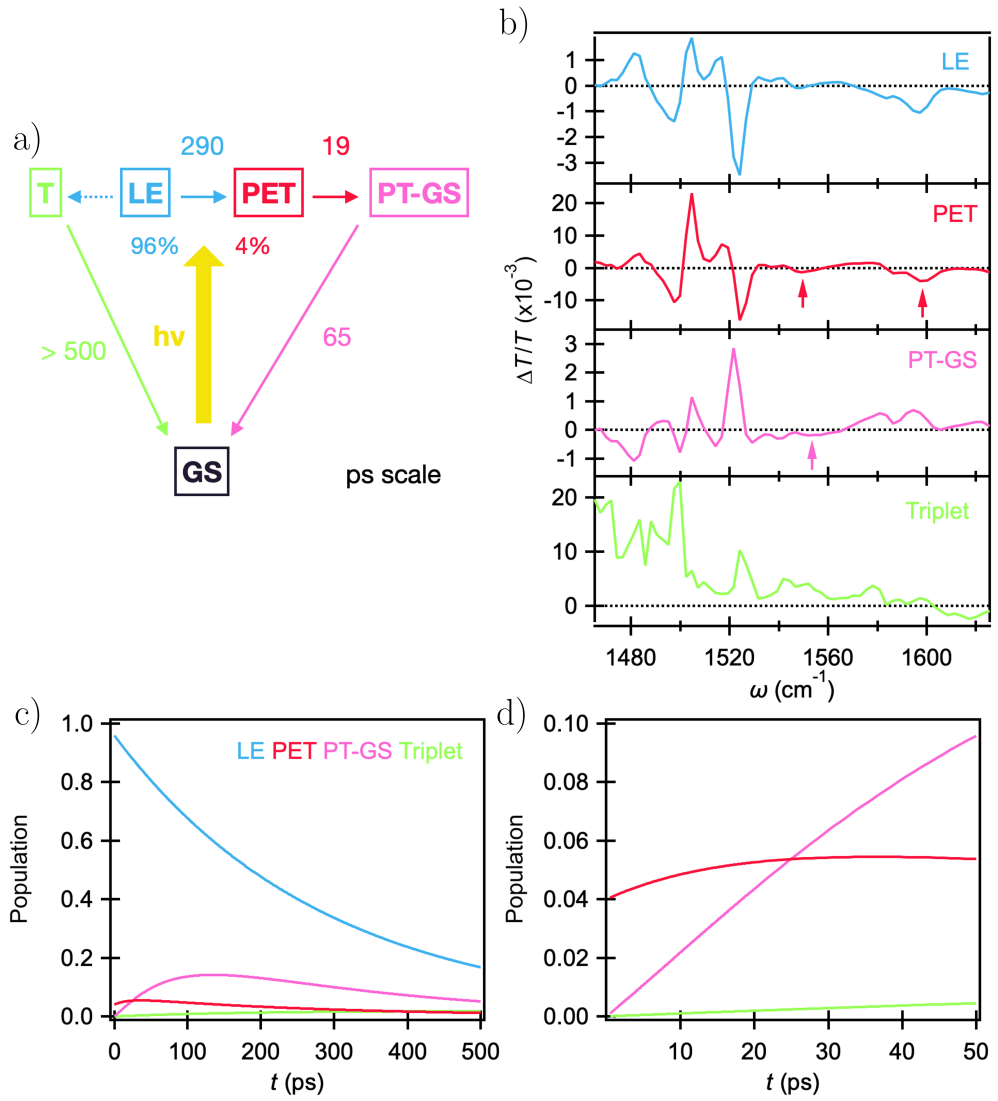

Figure E.10: a) Kinetic model used to analyze the transient IR data of $BIPPF_{15}$. Initial populations after excitation for the LE and PET states were assumed to be 9% and 4%, respectively. The LE state evolves to the PET (solid arrow) and triplet (dotted arrow) states. The PET state then evolves to PT-GS and eventually all populations return to the GS (solid arrows). b) Species associated spectra obtained by the model shown in a). c) and d) Population dynamics of the transient species in the time range at c) 0.5-500 ps and d) 0.5-50 ps.

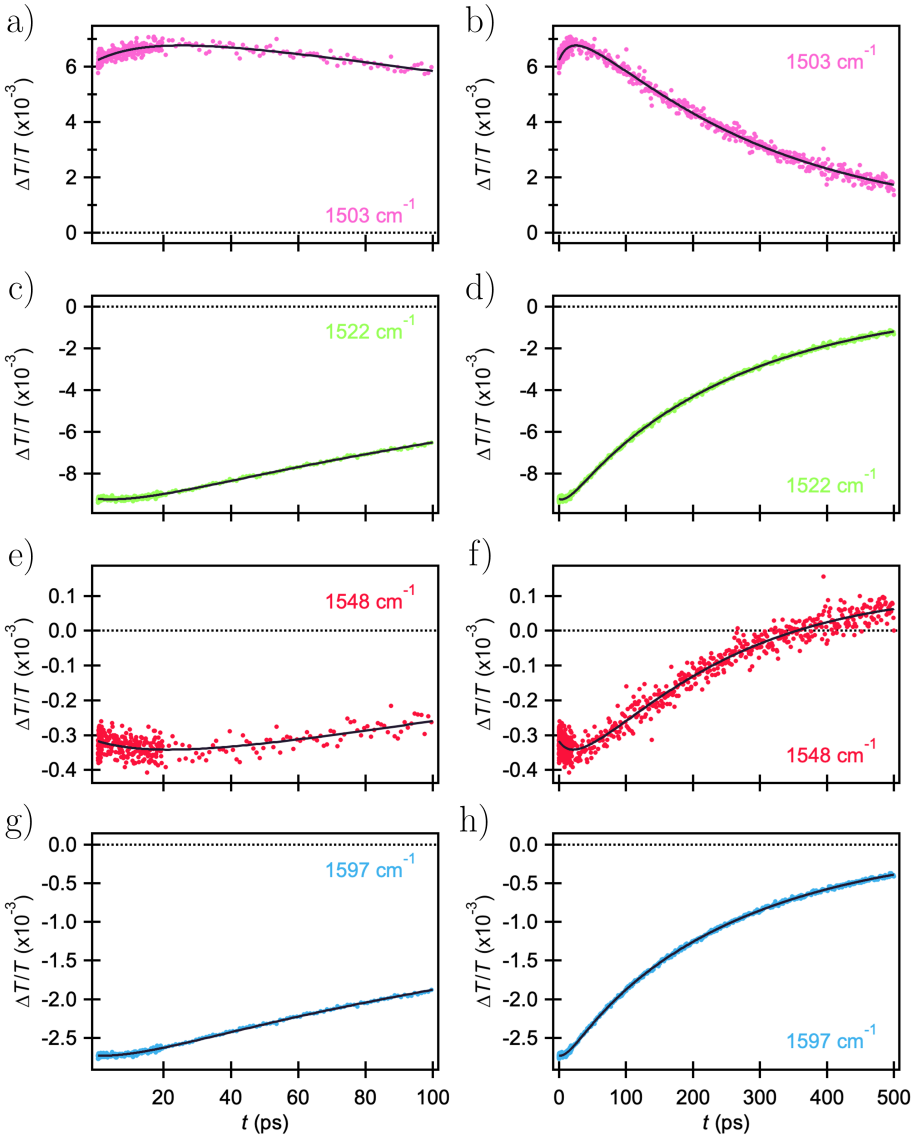

Figure E.11: Fitting results of global analysis of transient IR of $BIPPF_{15}$. Probe frequencies were a) and b) 1503 cm^{-1}, c) and d) 1522 cm^{-1}, e) and f) 1548 cm^{-1}, and g) and h) 1597 cm^{-1} in the time range of a), c), e), and g) 0.5-100 ps and b), d), f), and h) 0.5-500 ps.

E.8 Fluorescence Measurement

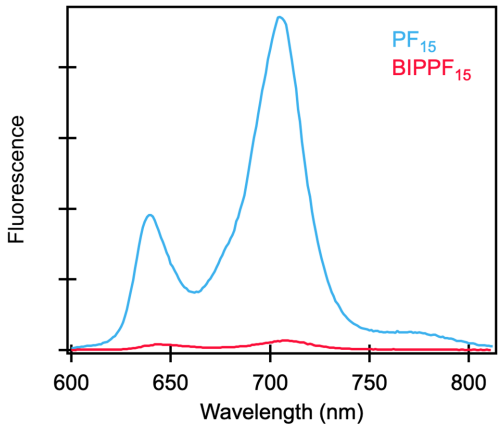

Figure E.12: Fluorescence spectra of PF_{15} and $BIPPF_{15}$ in acetonitrile. The integrated fluorescence intensity of $BIPPF_{15}$ was 1/30 compared to that of PF_{15}, indicating the excited state is quenched by ET.

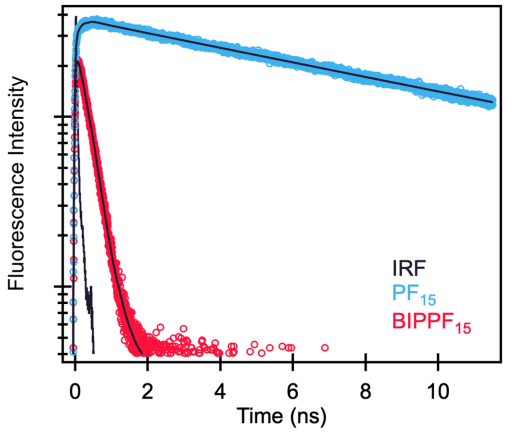

Figure E.13: Time-resolved fluorescence of PF_{15} and $BIPPF_{15}$ in acetonitrile with excitation at 583 nm and emission detection at 710 nm. Open circles: raw data. Solid lines: fit with 9.8 ns and 272 ps lifetimes for PF_{15} and $BIPPF_{15}$.

E.9 Summary of the Experimental Results

1) The transient IR spectra of PF_{15} and $BIPPF_{15}$ have significantly different spectral features at longer times. In addition to bands assigned to the ET and PT processes, the lifetime of the major transient in $BIPPF_{15}$ was 290 ps, which is much shorter than that of PF_{15}, indicating CS takes place on this time scale. The results of fluorescence measurements are consistent with this conclusion.

2) Transient IR spectra show two minor transients with time constants of 19 ps and 65 ps. SAS obtained by global and target analysis suggests that these two time scales can be assigned to CR and GS-PT, respectively.

3) Transient IR spectra at short times show that ET and PT signals appear immediately after photoexcitaion, indicating the PET state is prepared directly by photoexcitation or formed via an ultrafast pathway which proceeds within our instrument response time of ∼90 fs. The normalized signal intensities of the fluorescence lifetime measurements of $BIPPF_{15}$ and PF_{15} also support this conclusion. The ratio of LE to PET population at early times is estimated to be 96% to 4% by kinetics simulations and target analysis. The PET population produced via this ultrafast pathway displays normal dynamics with a 19 ps decay assigned to CR. Overall quantum yield of the PET state is 97% with 4% contribution via unrelaxed ultrafast pathway and 93% contribution via relaxed pathway from LE state, however, the PET state maximum transient population is only ∼5%.

4) The CLS dynamics shows a 120 fs rise, indicating a progressive increase in the dipole moment as supported by the electronic structure calculations. The five time scales are summarized in Figure 7.1d and in more detail in Figure 7.6.

E.10 Calculated Structures of $BIPPF_{15}$

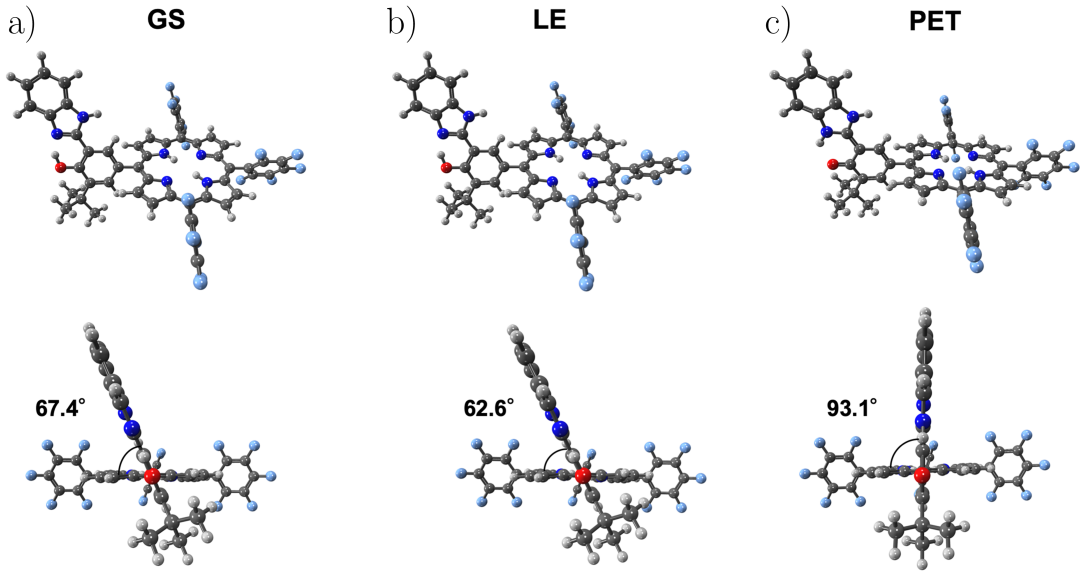

Figure E.14: Optimized structures of $BIPPF_{15}$ for a) GS, b) LE, and c) PET states.